DEPARTMENT OF
LIFE SCIENCES

NOVA SCHOOL OF
SCIENCE & TECHNOLOGY

SIMPLIFIED CHIP PROTOTYPING FOR IMPROVED SCREENING OF GENE-SILENCING THERAPEUTICS USING 3D CELL MODELS

ANA BEATRIZ BRITO DE OLIVEIRA
Master in Biotechnology

DOCTORATE IN BIOTECHNOLOGY
NOVA University Lisbon
February 2025

NOVA SCHOOL OF SCIENCE & TECHNOLOGY

DEPARTMENT OF LIFE SCIENCES

SIMPLIFIED CHIP PROTOTYPING FOR IMPROVED SCREENING OF GENE-SILENCING THERAPEUTICS USING 3D CELL MODELS

ANA BEATRIZ BRITO DE OLIVEIRA

Master in Biotechnology

Adviser: Pedro Miguel Ribeiro Viana Baptista
Full Professor, Nova School of Science and Technology - NOVA University Lisbon

Examination Committee:

Chair: Ana Cecília Afonso Roque,
Full Professor, Nova School of Science and Technology - NOVA University Lisbon

Rapporteurs: Duarte Miguel de França Teixeira dos Prazeres,
Full Professor, Instituto Superior Técnico (IST) – University of Lisbon

Catarina Raquel Fernandes Caneira,
Researcher, Institute of Systems and Computer Engineering for Microsystems and Nanotechnologies (INESC-MN)

Adviser: Pedro Miguel Ribeiro Viana Baptista,
Full Professor, Nova School of Science and Technology - NOVA University Lisbon

Members: Ana Cecília Afonso Roque,
Full Professor, Nova School of Science and Technology - NOVA University Lisbon

DOCTORATE IN Biotechnology

NOVA University Lisbon
February 2025

Simplified Chip Prototyping for Improved Screening of Gene-silencing Therapeutics Using 3D Cell Models

ACKNOWLEDGMENTS

Research is often considered a lonely endeavor, but for me, it has been the complete opposite. Therefore, there are many people to whom I owe my deepest gratitude.

I begin by thanking the Fundação para a Ciência e Tecnologia for funding this thesis (2020.07660.BD), in the scope of the project UIDP/04378/2020 and UIDB/04378/2020 of the UCIBIO Research Unit and the project LA/P/0140/2020 of the Associate Laboratory i4HB and project NANOHEAT (2022.04315.PTDC), and to NOVA School of Science and Technology, which provided all the resources for the development of this thesis.

I would like to sincerely thank my advisor, Prof. Pedro Baptista. Throughout all these years, your door was always open for me. You allowed this thesis to be my own while steering me in the right direction when I needed it, even though my stubbornness kept me from realizing it right away. Most importantly, thank you for always making me feel valued and helping me grow not only academically but as a person. To Prof. Alexandra, thank you for listening and for your kind ways of helping me whenever I reached out.

Thank you to my fellow companions on this journey—Daniela, Rubén, Margarida, Cinthya, Daniela Alexandre, André, Sandra, and Bilal —for the meaning you brought to each day. Thanks also to all the undergraduate, master's, and exchange students with whom I had the opportunity to learn. A heartfelt thank you to Daniela for the years of incredible friendship and for never letting me whine alone. To Rubén, for your care and for always finding ways to cheer me up. To my friends Maria Inês, Tânia, Bernardo, João, and Andreia, thank you for patiently listening to my endless cycles of highs and lows and for constantly pushing me forward.

To my parents and sister, words will never fully capture the depth of my gratitude, but I'll try. To my parents, thank you for your unwavering support and endless encouragement throughout my studies and for teaching me everything that academia never could. And to my little sister, the person you are and your unshakable belief in me have always inspired me to keep striving to do my best.

"And, when you can't go back, you have to worry only about the best way of moving forward."

Paulo Coelho, *The Alchemist*

ABSTRACT

Cancer research has long been hindered by the limitations of conventional 2D culture models, which fail to replicate the intricacies of the tumor microenvironment. This lack of complexity prevents accurate evaluation of cancer therapeutics, including gene-silencing approaches. The shortcomings of standard cancer models in recapitulating the dynamic microenvironment of tumors prompted the development of more physiologically relevant models. While Tumor-on-Chip systems show promise in addressing these challenges, their widespread adoption is limited due to technical complexity and high fabrication costs.

To overcome these barriers, this thesis presents a strategy to simplify the prototyping of ToC devices by focusing on accessible materials and fabrication processes. This work outlines a pathway to create efficient, reproducible, and cost-effective biochips suitable for cancer modeling and screening gene-silencing therapeutics. The objectives include synthesizing and characterizing gold nanoparticle conjugates, evaluating their gene silencing efficiency in 2D and 3D models, streamlining the biochip fabrication, and translating these findings to the final device.

The results provided insights into the differential behavior of nanoparticle uptake and resultant silencing efficiency between models. While 2D cultures exhibit faster uptake kinetics, 3D spheroids better mimic diffusional barriers and tumor heterogeneity, making them a more reliable model for evaluating nanoparticle-based therapies. The developed ToC device successfully reproduced these complexities, yielding promising results. Still, future work should aim to incorporate fluidic channels and immune cells to further enhance tumor microenvironment recapitulation, bridging the gap between preclinical models and *in vivo* complexity to improve therapeutic predictions.

Keywords: Tumor-on-Chip; Cancer models; Gene Silencing; Nanomedicine

RESUMO

A investigação sobre o cancro tem sido limitada pelas restrições dos modelos convencionais de cultura celular em 2D, que não conseguem replicar com precisão o complexo microambiente tumoral observado *in vivo*. Esta limitação compromete a avaliação eficaz de estratégias terapêuticas, incluindo terapia genética. As limitações das culturas 2D, como a incapacidade de mimetizar as interações celulares, as funções da matriz extracelular e gradientes de difusão, impulsionaram o desenvolvimento de modelos mais fisiologicamente relevantes. Embora os sistemas *Tumor-on-Chip* tenham demonstrado grande potencial na superação desses desafios, a sua utilização continua restrita devido à elevada complexidade técnica e aos custos substanciais de fabricação.

Esta tese introduz uma estratégia inovadora para simplificar a prototipagem de dispositivos adaptados à cultura de modelos tumorais, posteriormente aplicados a estratégias de silenciamento génico. Através da utilização de materiais e processos de fabricação acessíveis é demonstrada a criação de dispositivos eficientes, reprodutíveis e economicamente viáveis. Este estudo inclui a criação e desenvolvimento dos biochips, a síntese e caracterização de nanoconjugados de partículas de ouro, a avaliação da sua eficácia de silenciamento em modelos 2D e 3D, e a translação desses resultados para modelos ToC.

Os resultados revelam diferenças nos mecanismos de internalização dos nanoconjugados e, consequentemente, na eficácia do silenciamento. Enquanto as culturas 2D apresentam uma cinética de internalização mais rápida, os esferoides replicam com maior fidelidade as barreiras de difusão e a heterogeneidade tumoral. O modelo ToC desenvolvido, ainda que simplificado, reproduziu com sucesso os resultados obtidos em modelos convencionais. Estudos futuros deverão focar-se na incorporação canais de microfluídica e de componentes do sistema imune, para melhorar a modelação do microambiente tumoral e desta forma, colmatar a lacuna entre a simplicidade dos modelos convencionais e a complexidade do microambiente tumoral.

Palavras chave: *Tumor-on-Chip*, Modelos celulares, Silenciamento génico, Nanomedicina

CONTENTS

LIST OF FIGURES

LIST OF TABLES

ABBREVIATIONS

18S	18s Ribosomal RNA
2D	Two-Dimensional
3D	Three-Dimensional
AAAAn	Poly(A) Tail
ASCs	Adult Stem Cells
ASOs	Antisense Oligonucleotides
Au-S	Gold-Thiol Bond
AuNPs	Gold Nanoparticles
AuNPs-ASOs	Gold Nanoparticles Conjugated with Antisense Oligonucleotides
BCL2	B-Cell Lymphoma 2
BCR-ABL	Breakpoint Cluster Region - Abelson Murine Leukemia
BSA	Bovine Serum Albumin
CAF	Cancer-Associated Fibroblast
CAM	Chick Chorioallantoic Membrane
CAR-T	Chimeric Antigen Receptor T-Cell
Cas9	CRISPR-Associated Protein 9
cDNA	Complementary Dna
CML	Chronic Myeloid Leukemia
c-MYC	Proto-Oncogene MYC
copGFP	Copepod Green Fluorescent Protein
CRC	Colorectal Carcinoma
CRISPR	Clustered Regularly Interspaced Short Palindromic Repeats
CRISPR-Cas9	Gene Editing Tool
CRISPR-a	CRISPR Activation
CT	Cycle Threshold
CTLA-4	Cytotoxic T-Lymphocyte-Associated Protein 4
DLS	Dynamic Light Scattering
DNase	Deoxyribonuclease
DTT	Dithiothreitol
EPR	Enhanced Permeability and Retention
ECM	Extracellular Matrix
EDTA	Ethylenediaminetetraacetic Acid
EGFR	Epidermal Growth Factor Receptor
EMA	European Medicines Agency
ESCs	Embryonic Stem Cells
FDA	Food And Drug Administration
FBS	Fetal Bovine Serum
FRET	Förster Resonance Energy Transfer

GFP	Green Fluorescent Protein
GEMMs	Genetically Engineered Mouse Models
GelMA	Gelatin Methacrylate
HCC	Hepatocellular Carcinoma
HCT-116	Colorectal Cancer Cell Line
HER2	Human Epidermal Growth Factor Receptor 2
HUVEC	Human Umbilical Vein Endothelial Cells
ICP-AES	Inductively Coupled Plasma Atomic Emission Spectroscopy
iPSCs	Induced Pluripotent Stem Cells
KRAS	Kirsten Rat Sarcoma Viral Oncogene Homolog
LSPR	Localized Surface Plasmon Resonance
m7G	7-Methylguanosine (Typical 5' Cap on mRNA Molecules)
MCF7	Michigan Cancer Foundation-7 (Breast Cancer Cell Line)
miRNA	Micro RNA
mRNA	Messenger RNA
MRI	Magnetic Resonance Imaging
NP	Nanoparticle
PBS	Phosphate-Buffered Saline
PBMC	Peripheral Blood Mononuclear Cells
PC	Polycarbonate
PDMS	Polydimethylsiloxane
PFA	Paraformaldehyde
PEG	Polyethylene Glycol
PEGylated	Modified With Polyethylene Glycol
PEI	Polyethyleneimine
PLGA	Poly (Lactic-Co-Glycolic Acid)
PMMA	Polymethyl Methacrylate
PMSF	Phenylmethylsulphonyl Fluoride
PDOs	Patient-Derived Organoids
PDX	Patient-Derived Xenografts
PD-1	Programmed Cell Death Protein 1
PS	Polystyrene
qPCR	Quantitative Polymerase Chain Reaction
RNAi	Interference RNA
RNase H	Ribonuclease H
RT-qPCR	Real-Time Quantitative Polymerase Chain Reaction
SDS	Sodium Dodecyl Sulfate
shRNA	Short Hairpin RNA
siRNA	Small Interfering RNA
SPIONs	Superparamagnetic Iron Oxide Nanoparticles
TAE	Tris-Acetate-EDTA
TALENs	Transcription Activator-Like Effector Nuclease
TBST	Tris-Buffered Saline with Tween 20
TBS	Tris-Buffered Saline
TE	Tris-EDTA Buffer
TEM	Transmission Electron Microscopy
TME	Tumor Microenvironment
TNF-α	Tumor Necrosis Factor-Alpha
ToC	Tumor-On-Chip
UV-vis	Ultraviolet - Visible
VEGF	Vascular Endothelial Growth Factor
ZFN	Zinc Finger Nucleases

1

INTRODUCTION

The literature review presented in this chapter provides a contextualization of the thesis, which shall be more focused within each chapter. Also, some of the information discussed herein has been published, whole or in part, in the articles cited below. I reviewed and critically discussed the references cited in the text.

Oliveira, B.B., Fernandes, A.R., and Baptista, P.V. (2020). Nanotheranostics in Gene Therapy, *Advances in Cancer Nanotheranostics for Experimental and Personalized Medicine* 1(82). https://doi.org/10.2174/9789811456916120010007

Oliveira, B.B., Ferreira, D., Fernandes, A.R., and Baptista, P.V. (2023). Engineering gold nanoparticles for molecular diagnostics and biosensing. *WIREs Nanomedicine and Nanobiotechnology*, 15(1), e1836. https://doi.org/10.1002/wnan.1836

Cordeiro S., **Oliveira B.B.**, Valente R., Ferreira D., Luz A., Baptista P.V., and Fernandes A.R. (2024). Breaking the mold: 3D cell cultures reshaping the future of cancer research. *Frontiers in Cell and Developmental Biology,* 12:1507388. https://doi.org/10.3389/fcell.2024.1507388

1.1 Cancer Overview

A broad definition regards cancer as a combination of diseases characterized by the uncontrolled growth and spread of abnormal cells (1). Cancer cells are the result of several mutations in crucial genes that compromise their normal function, disturbing the cell cycle and leading to uncontrolled proliferation. Proto-oncogenes are responsible for the adequate control of cell division and growth, becoming oncogenes after genetic mutation. Conversely, tumor suppressor genes can work as a defense mechanism, but when mutated, they can allow uncontrolled cell division. Most of these molecular alterations are induced by direct mutations to the DNA, epigenetic changes of chromatin, or the result of altered expression patterns of regulatory pathways, both at the RNA and protein levels. Still, cells have highly effective DNA repair mechanisms that attempt to correct any physicochemical damage to DNA, such as base excision repair, nucleotide excision repair, or mismatch repair (2–4). While mostly preventing the onset of genome mutations, these mechanisms sometimes fail to correct the damage, and as a result, mutations prevail and accumulate.

Despite the wide acceptance of the impact of hereditary traits of cancer, about 90 to 95% of cancers develop due to environmental aspects and lifestyle (5–7). Currently, it is proposed that between 30% and 50% of cancer-related deaths are preventable by modifying lifestyle and avoiding exposure to major risk factors, including smoking, alcohol consumption, obesity, sedentarism, and chronic infections (6,8,9). Indeed, repetitive exposure to risk factors may increase the chances of cancer by augmenting the probability of mutations in the genome (10,11). Chemical compounds, especially those interacting with DNA, have a role in the formation of gene mutations. Carcinogenic substances influence the cytoplasm and nucleus of cells directly or indirectly and lead to genetic disorders and mutations. Other sources of gene mutations rely on radiation or infections such as *Human Papillomavirus* in cervical and oropharyngeal cancers, and *Helicobacter pylori* in stomach cancer (10).

Altogether, cancer is in the top ten causes of death worldwide and was responsible for almost 10 million deaths and around 20 million new cases in 2022 (12). Carcinomas are the most common type of cancer and thus, the one with the highest cancer-related deaths (**Figure 1.1**).

Demographic-based statistics indicate that new cases of cancer will increase by up to 77%, which translates to 35 million new cases per year, until 2050 (12). As so, improving the current anti-cancer therapies and screening protocols is of utmost importance. Still, advancing these protocols requires a deeper understanding of the mechanisms and pathophysiology of cancer, which should be further accompanied by the development of cancer models capable of accurately recapitulating these characteristics.

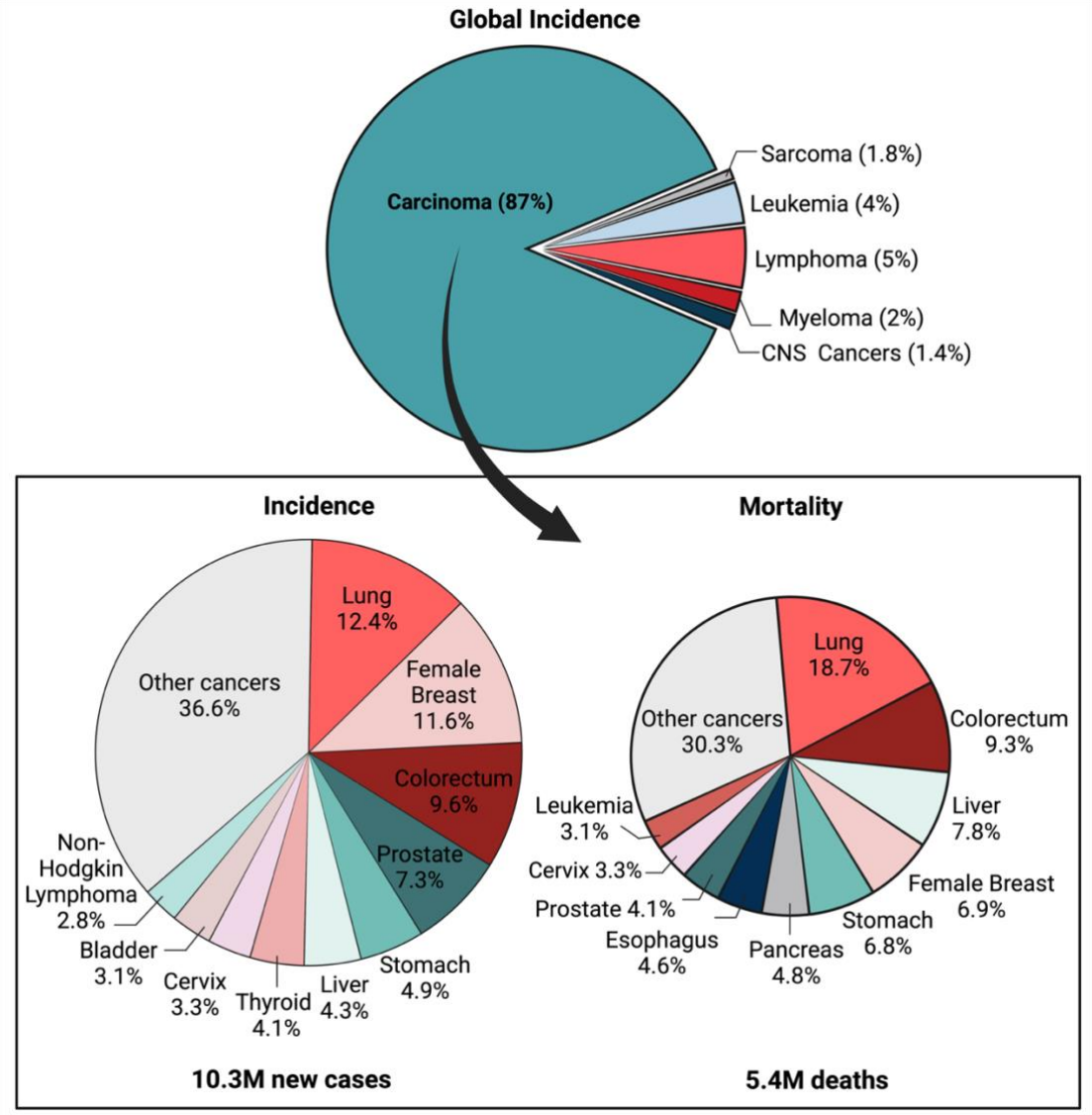

Figure 1.1. Incidence and mortality rates of different types of cancer worldwide.

1.1.1 Cancer Hallmarks

To guide cancer research and enhance the understanding of the underlying mechanisms of cancer progression, a concept addressed as Cancer Hallmarks was introduced. The hallmarks describe several functional capabilities acquired by human cells as they transition from normalcy to neoplastic growth states, more specifically capabilities that are crucial for their ability to form malignant tumors (13,14).

Initially, Hanahan Douglas and Robert Weinberg reported a set of six distinct hallmarks (14,15), comprising the capabilities for (1) Sustaining proliferative signaling; (2) Evading growth suppressors; (3) Resisting cell death (apoptosis); (4) Enabling replicative immortality; (5) Inducing angiogenesis; (6)

Activating Invasion and Metastasis. Later, two additional hallmarks (7) Reprogramming cellular metabolism and (8) Avoiding immune destruction; and two enabling characteristics (1) Genomic instability and mutation and (2) Tumor-promoting inflammation were added. Presently, all these traits have been sufficiently studied and are now regarded as part of the core set.

More recently, new studies have revealed other key players in cancer development and metastasis processes, from which were pointed new enabling characteristics involving "unlocking phenotypic plasticity," "non-mutational epigenetic reprogramming," "polymorphic microbiomes," and "senescent cells" (13).

1.1.2 Tumor Microenvironment

Behind some of these transformational processes is the Tumor Microenvironment (TME), which helps normal cells to become "rogue agents" and start promoting tumorigenesis. Most of the intricate processes supporting cancer progression are dependent on the interaction between TME and cancer cells (14,16). TME can be broadly defined as the combination of cellular and non-cellular components that surround cancer cells (**Figure 1.2**). The cellular part of TME comprises endothelial cells from the blood and lymphatic vasculature, adipocytes, pericytes, lymphocytes, cancer-associated fibroblasts (CAFs), and tumor-associated macrophages (17–20). Within the non-cellular part of TME, the extracellular matrix (ECM) is the predominant component. This complex network consists of various macromolecules, including growth factors, fibrous proteins (including collagen, elastin, and fibronectin), proteoglycans, glycoproteins, and cytokines (21–23). The ECM primarily supports the 3D structure, maintains tissue homeostasis, and regulates cell-to-cell and cell-matrix interactions, thereby influencing cell differentiation, survival, and proliferation. Besides the ECM, biochemical factors (*e.g.*, diffusion gradients of molecules, signaling factors, oxygen, and nutrients) and biophysical factors (*e.g.,* shear stress and interstitial flow) are also crucial for TME (24,25).

Overall, the TME is responsible for modulating processes related to cell invasion and metastasis, tumor growth, immune responses, and mechanisms of drug resistance. Therefore, owing to its importance in tumoral processes, researchers have been shifting the focus to explore new disease models capable of mimicking those interactions and also develop novel therapeutics targeting key TME players.

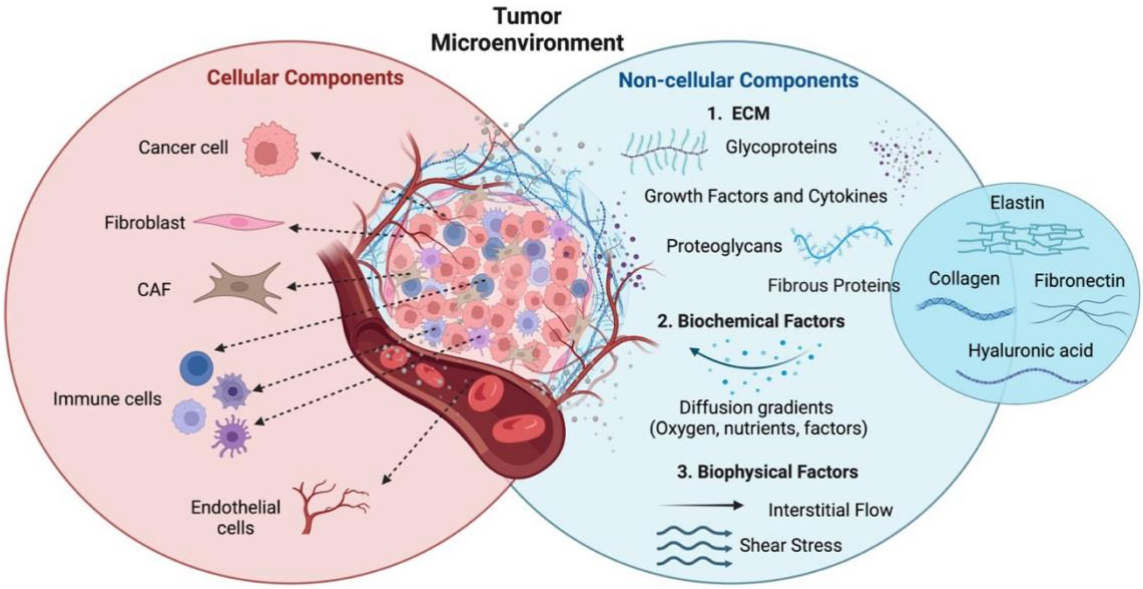

Figure 1.2. Representation of the TME components and their organization within the tumor mass.
Cellular (cancer cells, fibroblasts, immune and endothelial cells, and CAFs) and non-cellular (ECM, biochemical factors, and biophysical factors) components.

1.2 Cancer Therapeutics

Regardless of the scientific progress driven by advancements in molecular biology, biotechnology, and precision medicine, finding a cure for cancer is still the greatest challenge in medical research. Given the complexity and heterogeneous nature of cancer, achieving a "one size fits all" approach has proved impractical. As such, several methods were developed through the years in the hope of helping to win this battle. Currently, there is a broad range of treatment options that can be selected based on aggressiveness, molecular targets, mechanism of action, route of administration, specificity, cancer stage, side effects, and patient factors. Standard therapies like surgery, radiation therapy, and chemotherapy are generally more aggressive and less specific. Whereas novel therapies like targeted therapy, immunotherapy, and nanomedicine offer higher precision and can be tailored to individual patient profiles (**Figure 1.3**).

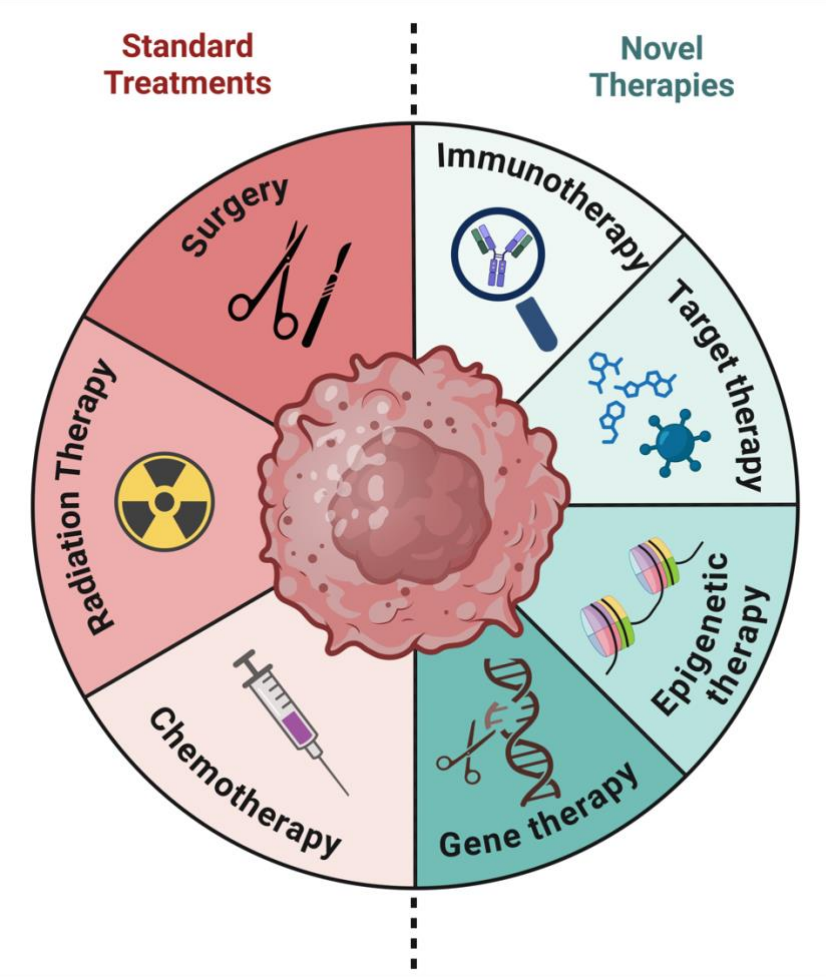

Figure 1.3. Current treatment modalities against cancer, divided into standard (left) and novel (right) therapies.

Standard Cancer Therapeutics

1.2.1 Surgery

Surgical tumor removal remains the oldest and most effective standalone cancer treatment, serving as the primary approach for most cancers (26). Early practices favored increasingly radical surgeries, which led to higher morbidity and mortality rates. Today, the focus has shifted to minimally invasive techniques that prioritize preserving form, function, and quality of life (26). Advances in surgical methods, such as robotic, laparoscopic, and reconstructive procedures, combined with multimodal therapies (adjuvant and neoadjuvant), have dramatically reduced postoperative mortality across all tumor types. For instance, gastric cancer mortality fell from 6% to 0.7%, lung cancer from 8.7% to 0.7%, and colorectal cancer from 7.4% to 5.9% (27–30). Recent progress has also enabled surgery to treat metastatic cancers effectively as part of multimodal therapy or to provide palliation when a cure is not possible (31–36). The development of specialized techniques, such as imaging and interventional radiology, has further advanced personalized surgery, achieving the critical goal of clear surgical

margins (37–39). However, cutting-edge approaches like intraoperative molecular imaging using isotopes and dyes remain financially prohibitive for widespread use.

1.2.2 Radiation Therapy

Radiation therapy is a cornerstone of cancer treatment, used as primary, adjuvant, or neoadjuvant therapy (40,41). It employs high-energy radiation to damage the DNA of cancer cells, inhibiting growth and shrinking tumors. Owing to their deep tissue penetration, X-rays are widely used for cancers such as breast, lung, prostate, and brain. Radiation is a primary treatment option for localized and early-stage cancers like prostate and laryngeal, while in advanced cases, it is used pre- or post-surgery to shrink tumors or target residual cells when complete tumor resection was not possible, as seen in head, neck, breast, and rectal cancers (42–45).

Combinatory therapies, such as radiation with chemotherapy, have shown improvements for cancers like lung, cervix, and head and neck (44). Additionally, advances in radiation technology, including dose fractioning and conformal techniques, aim to reduce toxicity and protect normal tissue. Ongoing research into molecular targeted therapies seeks to further enhance radiation's therapeutic effectiveness.

1.2.3 Chemotherapy

Surgery and radiation are effective for localized tumors but often fail against metastatic disease, which requires systemic therapies like hormonal therapy, immunotherapy, targeted therapy, and chemotherapy.

Since the 1940s, over 50 chemotherapeutic drugs have been developed, disrupting the cell cycle by damaging DNA or by targeting key components of cell division, leading to apoptosis(46), as seen for alkylating agents like cisplatin and anti-tumor antibiotics like doxorubicin, respectively (47–49). Chemotherapy regimens often combine drugs from different classes to achieve synergistic effects. However, a cure typically requires combining chemotherapy with surgery, either as adjuvant or neoadjuvant therapy, a standard practice for breast, colorectal, ovarian, and lung cancers.

Chemotherapy is effective against rapidly growing tumors like triple-negative breast cancer and lymphoma, though genetic factors like *KRas* mutations in colorectal cancer can influence drug response (48). Major challenges include side effects like anemia, hair loss, and nausea, as well as resistance mechanisms like altered metabolism and drug efflux (50–52). Therefore, new strategies for improved delivery and combination with other targeted therapies are being developed to overcome these challenges.

Novel Cancer Therapeutics

Surgery, radiation, and chemotherapy have long been the cornerstones of cancer treatment. While these remain essential for curing cancer, their aggressive nature, severe side effects, possibility for resistance and limited targeting have driven the development of new therapeutic approaches. These novel therapies are more targeted, inhibiting specific molecular targets or key oncogenic pathways, often with less toxicity and tailored to the individual characteristics of a patient's tumor.

1.2.4 Immunotherapy

A hallmark of cancer progression is the ability of cancer cells to evade the immune system, often accomplished through mechanisms like immune editing, T-cell signaling disruption, and enhanced immune tolerance. Currently, immunotherapies aim to stimulate effector (or repress counteracting) mechanisms of the immune system to recognize and destroy cancer cells, with strategies including checkpoint inhibitors, CAR-T cell therapy, and cancer vaccines.

Checkpoint inhibitors, such as pembrolizumab (targeting PD-1) and ipilimumab (targeting CTLA-4), block immune-suppressing proteins, enabling T-cell activation (53). These have shown success, with ipilimumab approved as a first-line treatment for metastatic melanoma (54,55). Similarly, CAR-T cell therapy engineers a patient's T cells to target cancer, achieving over 80% response rates in hematological cancers but facing challenges like toxicity and limited application in solid tumors due to the lack of specific targets (54). Cancer vaccines stimulate immune responses against cancer-specific antigens. Sipuleucel-T for metastatic prostate cancer and the oncolytic vaccine talimogene laherparepvec for unresectable melanoma, both with FDA and EMA approval, exemplify this approach (56–58).

Immunotherapy offers long-lasting responses and fewer side effects compared to conventional treatments. However, challenges like identifying specific tumor antigens limit broader application.

1.2.5 Targeted Therapies

Targeted cancer therapies offer a refined approach by focusing on specific molecules that drive tumor growth and progression, sparing most normal cells and reducing side effects compared to traditional chemotherapy. These therapies are primarily divided into small molecule inhibitors and monoclonal antibodies, both designed to disrupt cancer-specific pathways.

Small molecule inhibitors target intracellular enzymes and receptors. For example, imatinib inhibits the *BCR-ABL* tyrosine kinase in chronic myeloid leukemia (CML), achieving an 85% 8-year survival rate (59). Monoclonal antibodies, on the other hand, bind to cancer antigens on the cell surface or within tumor vasculature. Key examples include trastuzumab (Herceptin), which targets the HER2 receptor in breast cancer, and bevacizumab (Avastin), which inhibits VEGF to block angiogenesis (59–62).

Despite their precision, targeted therapies are not without challenges, including resistance mechanisms due to mutations or activation of alternative pathways and off-target effects.

1.2.6 Epigenetic Therapy

Epigenetic changes regulate gene expression without altering the DNA sequence through mechanisms like DNA methylation and histone modification (61,63). Recent studies have highlighted the role of epigenetic mechanisms in the onset of tumorigenesis, prompting the emergence of therapies aiming to reverse these modifications and restore normal cell function.

DNA methyltransferase inhibitors (*e.g.*, azacitidine, decitabine) reactivate tumor suppressor genes and are used for treating leukemia and myelodysplastic syndrome (63–65). Histone deacetylase inhibitors (*e.g.,* vorinostat, romidepsin) relax chromatin to restore gene expression, being approved for cutaneous T-cell lymphoma (66,67). While these have been proven effective in hematological cancers, progress in solid tumors is limited. Future research should explore other histone modifications and combine epigenetic therapy with other treatments to improve efficacy and overcome resistance.

1.2.7 Gene Therapy

Gene therapy was introduced three decades ago to treat diseases that were, until then, considered uncurable. Looking at publishing trends, it is fair to accept that science has entered a new era. Such is evidenced by the rising numbers of approved gene therapy products in the last ten years (68). Gene therapy involves various strategies to silence (downregulate), activate (upregulate), edit (repair), or delete (knockout) genes behaving in aberrant ways, offering targeted and personalized approaches to cancer treatment (69).

There are several systems to choose from, including interference RNA (RNAi) (70,71), antisense oligonucleotides (ASOs) (72,73), CRISPR/Cas9 (74–76), Transcription activator-like effector nucleases (TALENs) (77,78), and zinc finger nucleases (ZFNs) (79,80). These can be categorized into two distinct groups: DNA-targeted and RNA-targeted therapies, depending on the type of target molecule (**Figure 1.4**).

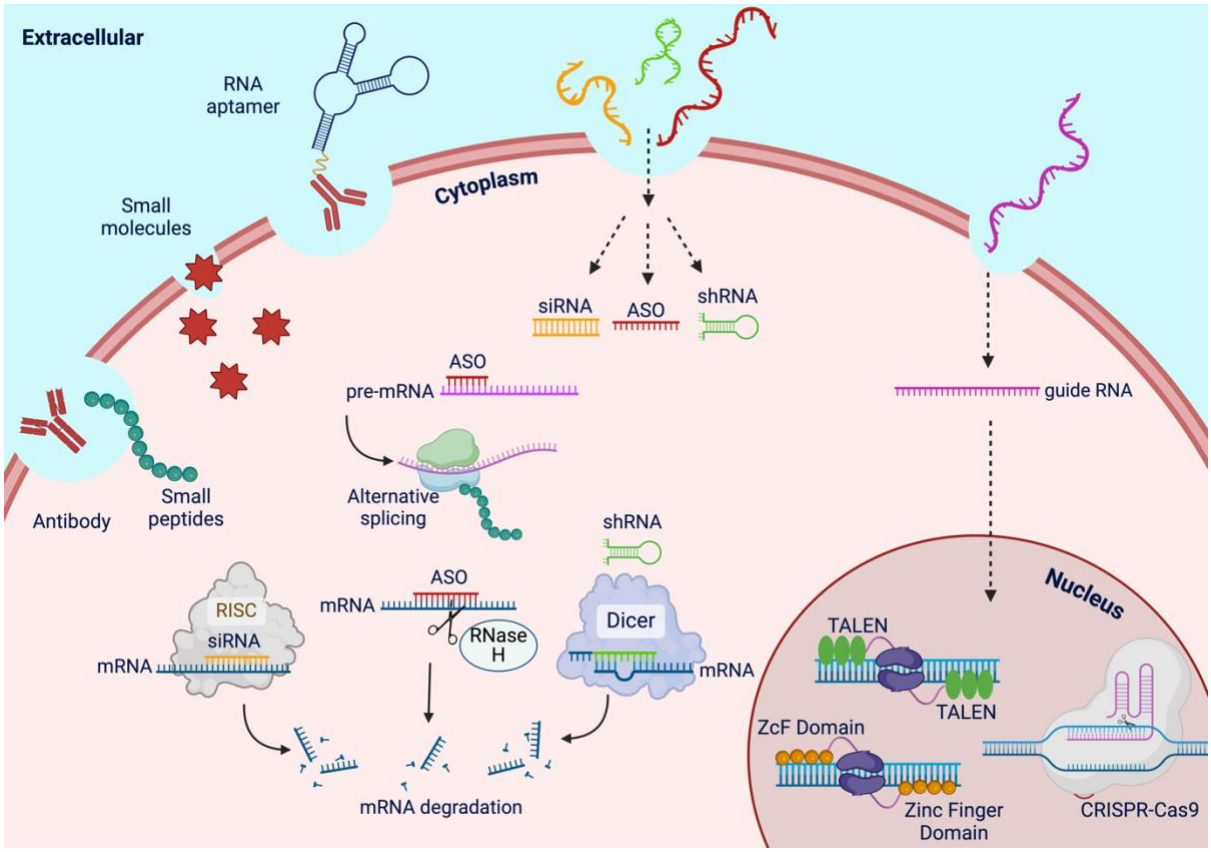

Figure 1.4. Mechanism of action of the several gene therapy schemes.
Gene editing and modulation therapies are expected to expand the range of druggable targets from proteins to RNAs and DNAs. Cell surface, extracellular, and intracellular proteins remain favorable targets for the development of small-molecule and protein (*e.g.,* antibody) therapeutics, as well as RNA aptamer drugs (Left). Still, most human genome sequences transcribed as functional ncRNAs largely outnumbered mRNAs to be translated into proteins. Both mRNAs and ncRNAs can be directly targeted by RNAi systems such as ASOs, shRNA, and siRNA (middle). Once introduced into cells, mRNA therapeutics may be developed for protein replacement/alternative splicing therapy or vaccination. In addition, guide RNAs (right) could be used along with other elements like mRNAs coding for the DNA binding domain of ZnF Nucleases and TALENs to directly edit the target gene sequences using CRISPR, Zinc Finger Nucleases and TALENs systems, respectively.

1.2.7.1 DNA-Targeted Therapy

DNA-targeted therapies, including CRISPR/Cas9, TALENs, and Zinc Finger nucleases, can directly modify cancer-related genes and pathways by creating double-strand breaks in DNA, enabling gene disruption or repair (81–83). For instance, TALENs can enhance T-cell function by disrupting the *PD-1* gene, boosting anti-cancer immunity in melanoma and lymphoma (84–89). Conversely, CRISPR/Cas9 has been used to knock out oncogenes or correct mutations in tumor suppressor genes (90–93). One example regards the editing of *EGFR* gene in non-small cell lung cancer, reversing mutational activation status and inhibiting tumor growth (94,95).

Gene replacement therapies, like CRISPR activation (CRISPR-a), can also introduce functional copies of tumor suppressor genes deleted (96), like *TP53*, into deficient cancer cells, and *REPRIMO* (97) in gastric cancer to overcome cancer dormancy (98). While these therapies hold great promise, ongoing research and clinical trials are essential to overcome challenges related to delivery, specificity, and resistance, ultimately improving their efficacy and safety for cancer patients.

1.2.7.2 RNA-Targeted Therapy

Contrary to DNA-targeted approaches that act by directly modifying genomic DNA, causing permanent changes, RNA therapies provide temporary modulation exerted at the transcriptional or translational level, therefore reducing long-term risks and offering greater flexibility for conditions like cancer, where gene expression is often deregulated due to epigenetic changes rather than DNA mutations (83,99,100). Additionally, while DNA-editing systems require delivery into the cell nucleus, posing challenges like protein instability and immune reactions, RNA therapies, including RNAi, mRNA therapies, and ASOSs (101–103), bypass the nuclear barrier, simplifying the delivery process(104–106).

RNAi introduces exogenous RNA sequences like small interfering RNA (siRNA) or short hairpin RNA (shRNA) molecules to target and signal for the degradation of specific mRNA transcripts. This mechanism exploits the endogenous RNAi mechanisms of micro-RNA sequences (miRNA), which are crucial for regulating gene expression, maintaining genomic stability, and defending against viral infections (107,108). RNAi systems have been successfully applied to silencing oncogenes, including *KRas* in colorectal cancer (CRC) (109–111).

Conversely, mRNA therapies involve the delivery of mRNA molecules into cells, enabling them to produce therapeutic proteins. This approach offers rapid development and customization to target specific genetic profiles. For example, Pfizer-BioNTech and Moderna COVID-19 vaccines prompted the production of the spike protein of the SARS-CoV-2 virus, eliciting an immune response (112–114). For cancer treatment, mRNA vaccines can be used to trigger the production of tumor antigens, stimulating the immune system to recognize and attack cancer cells (115–117).

ASOSs, on the other hand, exploit short, synthetic strands of nucleotides designed to bind to target mRNA molecules, preventing their translation into proteins (102,118). ASOSs have been used to target the *BCL2* gene (119), promoting increased apoptosis in chronic lymphocytic leukemia (120,121).

1.3 Antisense Oligonucleotides

Considering the value of gene modulation strategies, particularly in the context of cancer treatment, leveraging ASOSs-based approaches has the potential to improve the current treatment outcomes by offering a targeted approach to a specific patient's tumor type. Over the next sections, ASOSs mechanisms of action, targets, clinical applications, and benefits/challenges will be addressed in detail.

1.3.1 Mechanisms of Action and Structural Modifications

Antisense oligonucleotides are synthetic single strands of DNA or RNA designed to bind to an mRNA target by Watson-Crick base pairing. There are three major ways for ASOs to perform their modulatory effect: 1) signaling the RNA for degradation; 2) blocking translation; and 3) altering the splicing of pre-mRNA(122) (**Figure 1.5**).

Enzymatic RNA degradation is the most well-defined ASOs mechanism of action. Here, ASOs signals RNA for degradation by leveraging the RNase H activity, which recognizes RNA/DNA complexes and degrades the RNA part of the complex, resulting in mRNA degradation and downregulation of the target transcripts (73,123). Conversely, ASOs can prevent the mRNA translation into proteins by steric interference, preventing the bonding of the ribosome to the mRNA sequence. Finally, ASOs can also be designed to target specific regions of pre-mRNA molecules with regulatory effects, such as recruiting splicing factors. By targeting these regions, ASOs can alter the splicing patterns(124,125).

The mechanism of action that ASOs undertake is primarily dictated by their chemical structure. Several chemical modifications can be performed to promote a specific mechanism of action, improve the stability, binding affinity, and overall therapeutic efficacy (126), reduce immunogenicity, and increase their resistance to nucleases (101). These modifications can occur on the phosphate backbone, sugar rings, and 3' or 5' terminals of the oligonucleotide sequence (**Figure 1.5**).

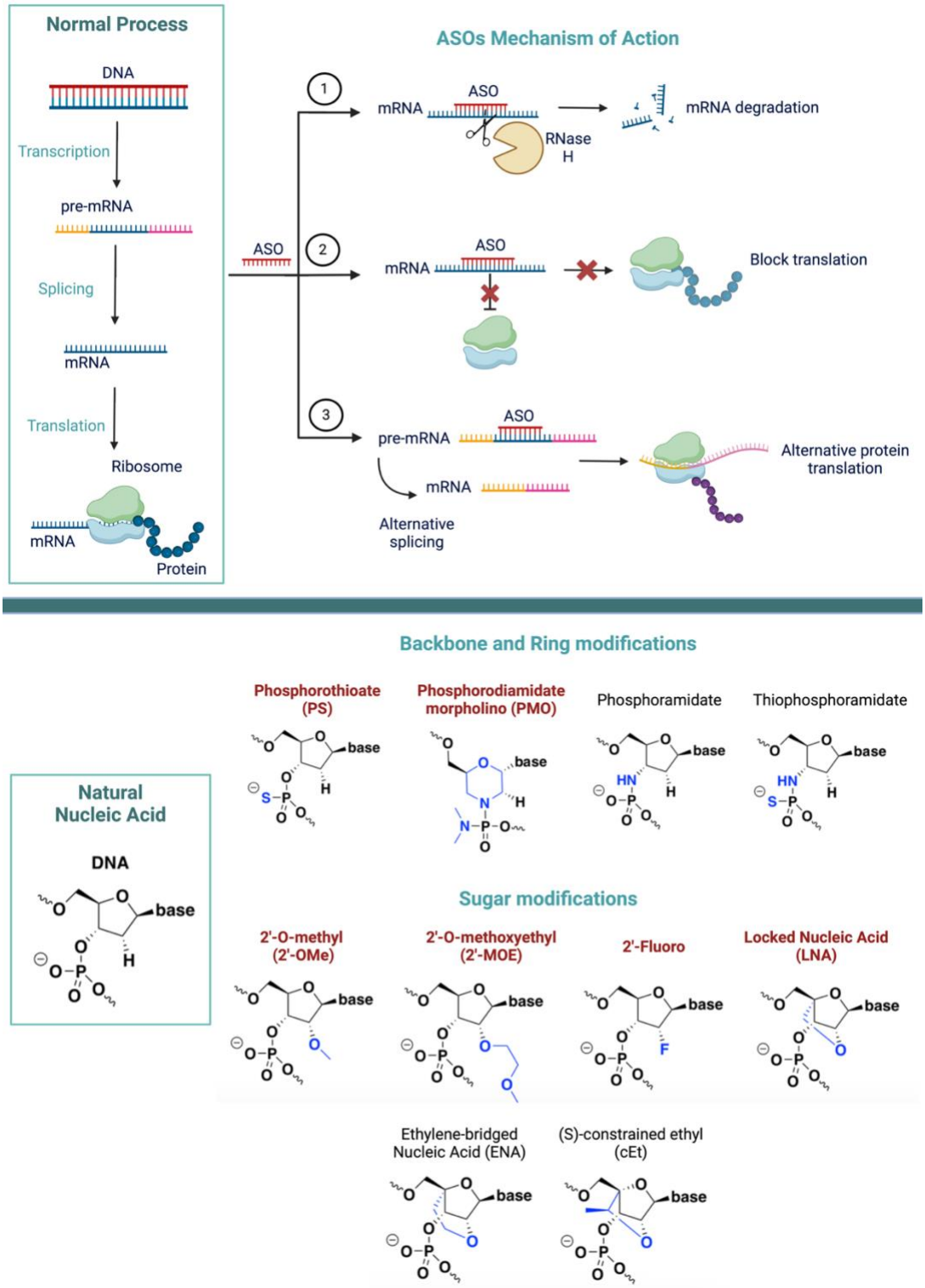

Figure 1.5. ASOs mechanisms of action (top) and common structural modifications (bottom).

1.3.2 ASOs in Clinical Trials

Among the 123 clinical trials completed on ASOs-based therapies, 60% are in Phase I, and the other 40% have entered Phase 2,3, or 4 for treating a variety of genetic disorders, including several types of cancer (127). These therapies work by binding to specific mRNA molecules, modulating gene expression either by degrading the target mRNA or by altering its splicing.

The first approved ASOs-based drug was Fomivirsen, targeting cytomegalovirus retinitis (CMV) in patients with AIDS (128,129). Among the FDA and EMA-approved ASOs-based therapies are Nusinersen (130,131), Eteplirsen (132), Casimersen (133), and Golodirsen (134) against Spinal muscular atrophy and Duchenne muscular dystrophy, respectively. These types of ASOs are commonly referred to as "splicing correcting" that act either by 1) skipping exons to produce truncated but functional proteins or 2) by modifying the splicing in pre-mRNA molecules (135). Second-generation ASOs called "Gapmers" or chimeric ASOs, such as Mipomersen and Inotersen, utilize RNAse H-mediated degradation to target disease-associated mRNAs (136,137).

Still, the majority of ASOs-based drugs are designed for targeting specific mutations or exons, enabling personalized therapies like Milasen, the first patient-customed ASOs developed for neuronal ceroid lipofuscinosis 7 (138). Additionally, ASOs are being investigated for cancer treatment, including Oblimersen, which targets *BCL-2* mRNA to enhance apoptosis (139–141); Trabedersen, which suppresses *TGF-β2* mRNA to mitigate tumor-promoting effects (142–144); and AZD9150, which inhibits *STAT3* mRNA to block pro-tumorigenic signaling, currently in Phase 2 trials (145,146).

1.3.3 ASOs-based Therapies: Benefits and Challenges

ASOs-based therapies offer significant advantages, including high specificity, rapid development based on target mRNA sequences, and the ability to modulate gene expression or alter splicing patterns in a patient-specific manner (147). Still, gene therapies, including ASOs, face challenges related to efficient delivery to target tissues, avoiding immune responses, and ensuring stability and long-term expression (148). To address these issues, chemical modifications (such as those reviewed before) have been introduced (149). Despite these efforts, off-target effects, immune responses, and limited delivery efficacy remain barriers to their clinical success, similar to challenges faced by other gene and immunotherapies. As so, exploring new delivery systems, such as those based on nanotechnology, is critical to overcoming these limitations and unlocking the full therapeutic potential of these novel cancer treatments.

1.4 Gold Nanoparticles in Cancer Therapy

The continuous advances in cancer research have prompted the development of a plethora of strategies for fighting cancer, such as those detailed before. From targeting specific molecular pathways to correcting mutated genes and their abnormal expression patterns, several tools are now available. Despite their value for cancer treatment, 95% of all new therapeutics show limitations regarding the poor pharmacokinetics, toxicity, and off-target effects, which have hindered wider clinical application (150). In the last years, a lot of effort has been put into developing effective, nontoxic, non-immunogenic, and noncarcinogenic vectors to deliver nucleic acids and drugs into cells, to achieve targeted delivery to specific areas in the body, minimizing their side effects and increasing their efficiency (151,152).

1.4.1 Nanotechnology and Nanomedicine

Nanotechnology is commonly addressed as the study and manipulation of materials at the nanometer scale (1 to 100nm) (153). At the nanoscale, materials exhibit unique properties that differ significantly from their bulk counterparts, primarily due to their reduced size, increased surface area-to-volume ratio, and predominance of quantum effects (154). When materials are confined to the nanoscale, they can display altered electrical, optical, mechanical, and chemical properties. For example, gold nanoparticles (AuNPs) turn red or purple instead of metallic yellow and have tunable optical properties based on their size and shape, making them useful in medical imaging and diagnostic applications (155). Similarly, the electrical conductivity of materials can change, as seen in carbon nanotubes and graphene, which possess exceptional conductivity and are being explored for advanced electronic devices (155).

Perhaps the greatest advantage of nanomaterials, particularly nanoparticles (NPs), is their size, which falls within the same range as biomolecules (153,156). This similarity in scale, coupled with their high surface area, allows improved catalytic properties, targetability, and interaction with their environment (157). Due to their reduced size, nanoparticles have the advantage of accumulating naturally in tumors by enhanced retention and permeability (EPR) effect (158). These advantages have not gone unnoticed, and nanotechnology was set to revolutionize the field of medicine, particularly in cancer therapy, by enabling unprecedented precision and effectiveness in diagnosis and delivery applications.

1.4.1.1 Types of Nanoparticles and Applications

Currently, a wide variety of nanoparticles are being investigated for cancer therapy, either for targeted delivery of therapeutics or as contrast agents for diagnostic applications. These nanoformulations can be divided into organic (polymeric, lipid-based, protein-based, dendrimers, and carbon-based) and

inorganic (*e.g.*, silica, quantum dots, and metallic) nanoparticles. Some of these have already been approved for clinical use (**Table 1. 1**) (159).

Table 1. 1. List of approved nanoformulations for cancer therapeutics.

Name	Type of NP	Active drug	Size	Target cancer	Ref
Doxil	Liposomal NP (PEGylated)	Doxorubicin	80-100 nm	HIV-associated Kaposi's sarcoma, ovarian cancer, metastatic breast cancer, multiple myeloma	(160)
Myocet	Liposomal NP	Doxorubicin	150 nm	Breast cancer	(161)
Onivyde	Liposomal NP (PEGylated)	Irinotecan	100 nm	Metastatic pancreatic cancer	(162)
Marqibo	Liposomal NP (non-PEGylated)	Vincristine	100 nm	Philadelphia chromosome; Negative acute Lymphoblastic leukemia	(163)
DaunoXome	Liposomal NP	Daunorubicin	45-80 nm	HIV-associated Kaposi's sarcoma	(164)
DepoCyt	Liposomal NP	Cytarabine	120 nm	Lymphomatous meningitis	(165)
MEPACT	Liposomal NP (non-PEGylated)	Mifamurtide		Osteosarcoma	(166)
Lipo-Dox	Liposomal NP (PEGylated)	Doxorubicin	180 nm	Kaposi's sarcoma breast and ovarian cancer	(167)
Oncaspar	Protein-based NP (PEGylated)	L-Asparginase	50-200 nm	Acute Lymphoblastic Leukemia	(168)

Zinostatin stimalamer	Polymer-protein conjugate NP	Styrene maleic anhydride neocarzinostatin (SMANCS)		Hepatocellular carcinoma	(169)
Copaxone	Polymeric NP	Glatiramer acetate	5 nm and 100nm	Multiple sclerosis	(170)
Eligard	Polymeric NP	Leuprolide acetate	260 nm	Prostate Cancer	(171)
Abraxane	Polymeric NP (Albumin-bound)	Paclitaxel	130 nm	Advanced non- small-cell lung cancer, metastatic pancreatic and breast cancers	(172)
Genexol-PM	Polymeric NP (micelle)	Paclitaxel	20-50 nm	Breast Lung and Ovarian cancer	(173)
NanoTherm	SPIONs (Iron oxide NPs)	-	20 nm	Thermal ablation glioblastoma	(174)
GastroMARK	SPIONs (Iron oxide NP coated with silicone)	-	400 nm	Imaging agent	(175)

Generally, organic nanoparticles are used as delivery vehicles for drugs, vaccines, chemotherapeutic agents, genes, and fluorescent dyes that enhance the bioavailability and stability of the payload, reduce side effects, and allow for controlled release (176,177). The choice of NP is dependent on the chemical properties of the transported molecule (177–179). For instance, liposomes can encapsulate both hydrophilic and hydrophobic drugs, protein-based NP usually carry hydrophobic drugs, whereas dendrimers are used to transport a multitude of compounds given their ability to bind multiple functional groups (180) (**Figure 1.6**).

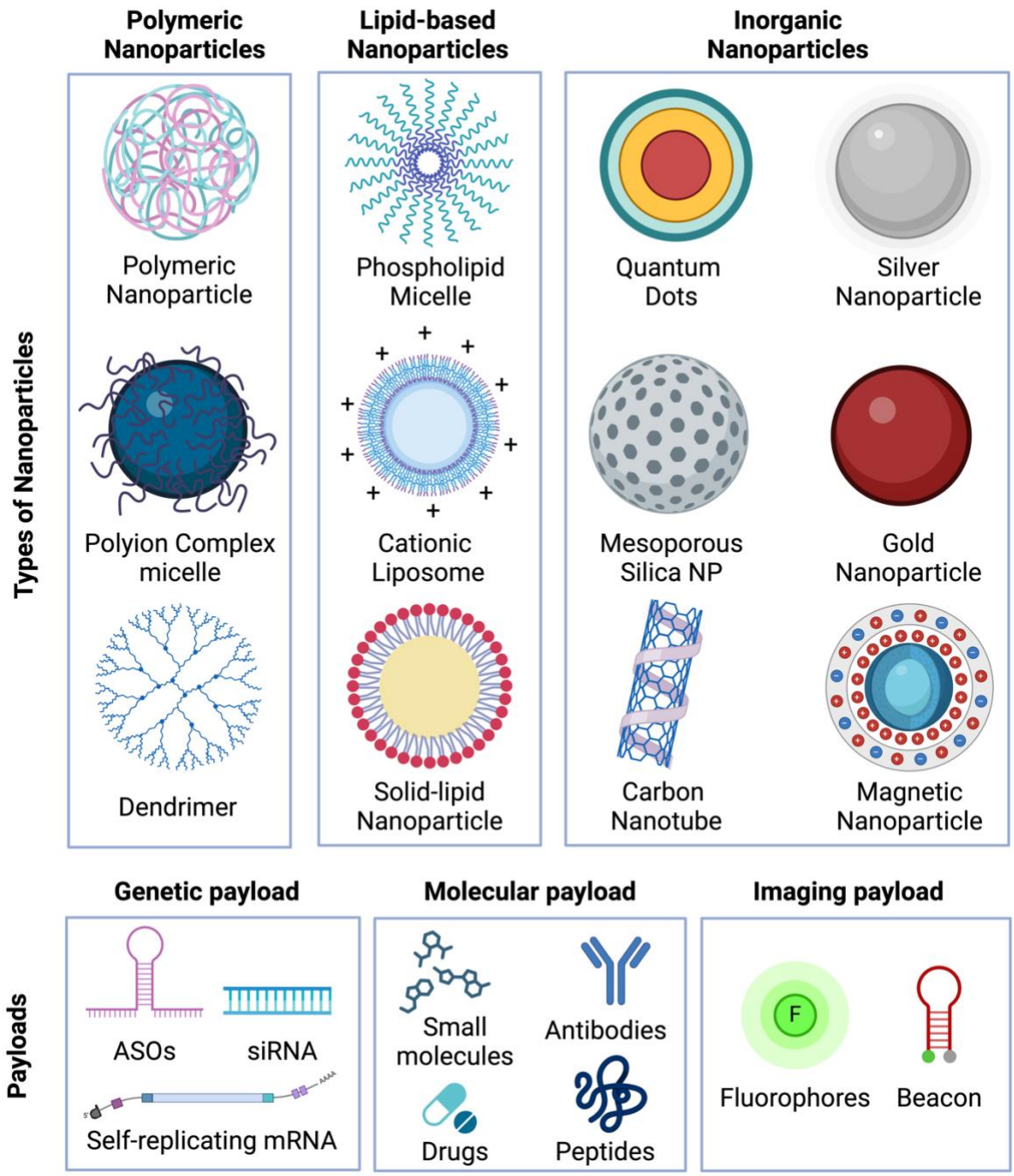

Figure 1.6. Types of nanoparticle systems and respective payloads.

Within the realm of inorganic nanoparticles, Silica nanoparticles are used either as delivery vehicles for therapeutic agents or as imaging tools by conjugation with fluorescent dyes (181). Quantum dots are highly valued for their unique optical properties, including size-dependent fluorescence, and are extensively used in imaging and diagnostic applications (182). They offer high-resolution imaging of biological tissues and real-time tracking of cellular processes.

Metal nanoparticles like iron, silver, and gold are more versatile, being applied as contrast agents, imaging probes, delivery vehicles, and photothermal agents (183). Particularly, Iron oxide nanoparticles are commonly used as contrast agents in magnetic resonance imaging (MRI) (184). Their magnetic properties also enable their use in hyperthermia treatment, where they generate heat to kill cancer cells when subjected to an alternating magnetic field. Conversely, Silver nanoparticles possess potent antimicrobial properties, making them useful in wound dressings, coatings for medical devices, and antibacterial agents (185). Gold nanoparticles are used in various biomedical applications, including targeted drug delivery, photothermal therapy, and contrast agents in imaging techniques (186,187). These applications will be discussed in more detail.

1.4.2 Gold Nanoparticles

Despite the variety of possible nanosystems, inorganic nanoparticles, particularly AuNPs, have been extensively studied due to their exquisite optical properties, ease of synthesis and surface functionalization, high surface-to-volume ratio, low toxicity, size/shape-related optoelectronic properties, and ability to enter cells and interact with target biomolecules (188). Most of these advantageous features derive from their morphology (*e.g.,* size, shape, solvent, surface ligands, core charge) and can be tuned by modulating some of these aspects (188,189). However, most limitations regarding AuNPs are related to the difficulty in controlling these same properties during scale-up (190).

1.4.2.1 AuNPs' Synthesis

Gold nanoparticles (AuNPs) were first synthesized in the 19th century by Michael Faraday and later simplified by Turkevich using the citrate reduction method (191,192). Depending on the synthesis process, pH of the solution, and type of passivating agents, a variety of sizes and shapes are possible. In a nutshell, two main approaches can be considered for the scale-up synthesis of AuNPs. Top-down, which breaks bulk material into nanoparticles using techniques like laser ablation and UV irradiation (193–196), and bottom-up, which forms nanoparticles from precursor molecules, as seen in the Turkevich and Brust methods (197). Bottom-up methods are preferred for biomedical applications due to their simplicity, cost-effectiveness, and uniformity (198,199). While chemical synthesis is efficient, its use of organic solvents raises concerns, making biological synthesis using bacteria, fungi, algae, or plants a cleaner, eco-friendly alternative (200–203).

1.4.2.2 Surface Functionalization

The high surface-to-volume ratio and surface chemistry make AuNPs good scaffolds for functionalization with a great variety of molecules, including polymers (*e.g.*, PEG, PEI) for enhanced circulation and stability or with recognition elements (*e.g.,* proteins, antibodies) for targeted delivery (204,205). During the synthesis, AuNPs can be stabilized with capping agents that assist in maintaining the repulsive forces between nanoparticles, ensuring the stability of the colloidal solution (206), such as sodium borohydride, sodium citrate, or ascorbic acid. Later, AuNPs can also be functionalized with surfactants and polymers (*e.g.,* PEG (207,208), PEI (209,210)), proteins like bovine serum albumin (BSA) (211), amino acids (212,213), oligonucleotides (214,215), antibodies, receptors, ligands, drugs and diverse similar particles (216). Among the several modifications, PEGylation is often employed to improve solubility, prevent aggregation, reduce immunogenicity, and extend circulation time by avoiding immune clearance (217–219). Despite the type of molecule, surface functionalization typically aims to alter the AuNP's physicochemical behavior, surface charge, improve biocompatibility, selectivity, and target-binding properties, and make them better compound carriers, which plays a crucial role in achieving the desired properties for biomedical applications (220).

Surface functionalization strategies can be divided into covalent and non-covalent-based methods. Regarding the first one, covalent coupling with thiol (Au-S) using sulfur-containing ligands, such as organothiols, disulfides, and cysteine groups has been the most reported, since thiol moieties offer higher stability when compared with other passivating agents (221) such as acyl group or coupling molecules containing amine groups (*e.g.*, antibodies). Otherwise, non-covalent interactions can be achieved by electrostatic interactions and physisorption of ionized ligands. Usually, this last type is used for drug loading since no specific bond cleavage is required to carry out efficient drug release (222).

1.4.3 AuNPs as Imaging Agents

Gold nanoparticles are also notable for their striking optical properties, driven by the localized surface plasmon resonance (LSPR) band (223). Spherical AuNPs between 5 and 100 nm show the LSPR in the visible region. However, size, shape, and surface changes can shift LSPR to other regions, such as near-infrared or ultraviolet, enabling applications like biosensing, *in vivo* imaging, and enhanced detection through Raman scattering (223–233). Owing to the high density of gold atoms, AuNPs can also serve as contrast agents in CT scans, X-ray imaging, and photoacoustic tomography (229–231,234). These tunable properties make them versatile tools in diagnostics and imaging applications (190,227,232,235–237).

1.4.4 AuNPs as Delivery Vehicles

Despite the wide variety of therapeutic options for cancer treatment (*e.g.,* chemotherapeutic drugs, siRNA, and ASOs), their efficacy is often limited by poor stability, solubility, high toxicity, nonspecific delivery, and short circulating half-lives (238). Nanoparticles, particularly AuNPs, have emerged as promising delivery systems due to their ability to enhance stability, enable targeted and controlled delivery, and reduce side effects.

1.4.4.1 Targeting Strategies

Therapeutic payloads can be delivered via passive or active targeting (239–241). Passive targeting leverages the EPR effect, where AuNPs accumulate in tumors due to their leaky vasculature caused by increased angiogenesis, inflammation, and cytokines (242). Particles between 10nm and 60nm in diameter are ideal for passive accumulation, enabling higher drug concentrations at the tumor site while reducing systemic toxicity and extending circulation time when compared to free drugs (241,243). However, the success of this strategy is highly influenced by tumor vascularization, angiogenesis, and heterogeneous blood flow, which can limit drug uptake and distribution.

Active targeting involves functionalizing AuNPs with specific ligands (*e.g.,* antibodies, peptides, sugars, and aptamers) to bind to tumor-specific receptors, inducing mediated endocytosis and intracellular drug release (244). These approaches typically involve ligand-receptor interactions, such as bombesin and somatostatin receptors and Luteinizing hormone-releasing hormone (228,245,246), or antibody-based targeting like EGFR and folate receptors (247). Lastly, stimuli-responsive systems, activated by triggers like pH, light, heat, or magnetic fields, further enhance drug delivery efficiency (248,249).

1.4.4.2 Therapeutic Payloads

AuNPs offer a promising platform for delivering various therapeutic agents, including chemotherapeutics, immunomodulators (250,251), ASOs, siRNA, and CRISPR-based gene-editing tools (252,253).

Inspired by the success of Doxil (liposomal nanoparticles with doxorubicin), AuNPs-drug conjugates like Doxorubicin (254), Paclitaxel (255), 5-Fluorouracil (256), Cisplatin (257) and Camptothecin (258) have been explored. For instance, Aurimune™ (a colloidal solution of 30 nm pegylated AuNPs conjugated with tumor necrosis factor-alpha (TNF-α)) has shown improved efficacy, reduced toxicity, and enhanced tumor accumulation in clinical trials (259,260).

AuNPs are also valuable for delivering nucleic acids, enhancing their stability, circulation half-life, and targeted delivery by protecting them against enzymatic degradation and minimizing off-target effects (261). In this regard, an AuNPs-siRNA conjugate has successfully crossed the blood-brain barrier and silenced cancer-related genes in glioblastoma patients, while preclinical studies highlight their potential in targeting oncogenes like *BCL2* and *KRas* (262,263). Additionally, AuNPs-CRISPR conjugates have demonstrated effective gene editing in various conditions, like muscular dystrophy and fragile X syndrome, underscoring their promise in cancer therapy (262,263).

Overall, AuNPs offer a robust platform for delivering therapeutic molecules with improved stability, specificity, and reduced toxicity. However, several of these nanoconjugates have shown unsuccessful results in clinical trials, either due to poor therapeutic efficiency or toxicity concerns (264,265). It has been suggested that some of these limitations may stem from the lack of cancer models that accurately mimic the characteristics of *in vivo* tumors, ultimately skewing the results of preclinical studies. Consequently, there has been a paradigm shift towards developing more reliable cancer models, which may better predict the outcomes observed in real patients.

1.5 Cell Models in Cancer Research

Despite the extensive efforts to unravel tumor behavior and develop anticancer therapies, most treatments fail when advanced to clinical trials. The main challenge in cancer research has been the absence of predictive cancer models, that accurately mimic the tumoral processes and response to treatments (266). The tumor microenvironment shows several human-specific physical and chemical properties sustaining cancer development, which cannot be fully recapitulated by the conventional 2D cell cultures or the *in vivo* animal models (267). These limitations have driven the development of novel *in vitro* cancer models, that get one step closer to the typical features of *in vivo* systems while showing better species relevance (266). In this section, the most commonly used cancer models will be overviewed, while pointing out their main characteristics and how these impact their performance as cancer models (**Table 1.2**).

Table 1.2. Brief description and main advantages and limitations of the most used cancer models.

Model	Description	Advantages	Limitations

Animal models	*In vivo* models where human tumors are implanted or induced in animals (commonly mice), or genetically engineered models that spontaneously develop cancer.	Provide a full biological context, including immune system interactions and systemic factors. Allows for studying metastasis, tumor progression, and immune responses. Essential for preclinical validation of therapeutics.	Expensive, time-consuming, and subject to ethical concerns. Differences between animal and human biology may reduce translational accuracy. Limited ability to perform high-throughput screening.
2D-cell monolayer	Cells from establish cell-lines or primary cells are cultured in a flat, 2D monolayer on plastic or glass surfaces.	Simple, cost-effective, easy to handle, well-established, allows for high-throughput screening.	Lacks the complexity of the 3D tissue architecture. Limited cell-cell and cell-matrix interactions, reducing physiological relevance. Lacks diffusion gradients and hypoxia. Static model.
3D Tumor spheroids	Cells from one or multiple cell-lines are cultured in 3D aggregates that mimic the structural organization of solid tumors.	Better recapitulation of the 3D architecture and cell-cell interactions. Presence of diffusion gradients of oxygen (hypoxia), nutrients and signal molecules. Closer to physiological tumor behavior than 2D cultures.	Limited complexity compared to *in vivo* tumors. More difficult to handle and less control over replicates (size and shape). Limited ability to incorporate stromal and immune components. Static model. Not all cells can form aggregates.

Organoids	3D cultures derived from patient's tumor tissue, retaining much of the architecture, genetic makeup, and heterogeneity of the original tumor.	High physiological relevance, mimicking patient-specific tumor characteristics. Useful for personalized medicine and drug screening. Preserves key features of tumor heterogeneity.	Technically complex, cumbersome and time-consuming to establish. Lacks standardized protocols for organoid formation and maintenance. High variability between organoid cultures. Lack of immune system components unless co-cultured. Static model
Organotypic Slice Culture	Uses native tumor tissue samples or constructs to recreate the 3D architecture of tumors and their native TME. Supportes multiple cell-types and incorporates extracellular matrix.	Physiologically relevant. Maintains cell-cell and cell-matrix interactions. Better simulation of tumor behavior and drug responses. Suitable for studying complex tissue interactions. Reflects the native mechanical and biochemical properties	Lacks vascularization and perfusion. Limited nutrient and oxygen supply. May not fully replicate dynamic tumor microenvironment Often limited to short-term studies due to viability issues Reproducibility and standardization can be challenging.
Tumor-on-Chip	Microfluidic devices that recreate a miniaturized TME by combining 3D cell cultures with fluid flow and mechanical forces.	Mimics both the 3D structure and physiological conditions, such as fluid flow and shear stress. Allows for dynamic study of drug transport, cell interactions, and mechanical cues. Can integrate multiple cell types and ECM components, creating a more realistic tumor model.	Technically challenging and requires specialized equipment and trained personel. High costs for materials and equipment. Lack of standardized protocols for platform development and operation. Limited scalability for high-throughput applications.

1.5.1 *In vivo* Models

In vivo models, including mice, zebrafish, Genetically Engineered Mouse Models (GEMMs), Xenograft models, and Patient-derived Xenografts, have been a cornerstone of cancer research for decades, providing invaluable insights into tumor biology, disease progression, and therapeutic responses (268). These models offer a living system in which researchers can study the complex interactions between cancer cells and their microenvironment, test new treatments, and explore mechanisms of drug resistance. The primary characteristics of animal models include their ability to replicate the three-dimensional structure of tumors, their dynamic physiological environment, and their ability to monitor tumor growth and metastasis over time (269). However, despite their utility, *in vivo* models also have limitations, particularly in accurately mimicking the specificities of human tumors (**Figure 1 .7**).

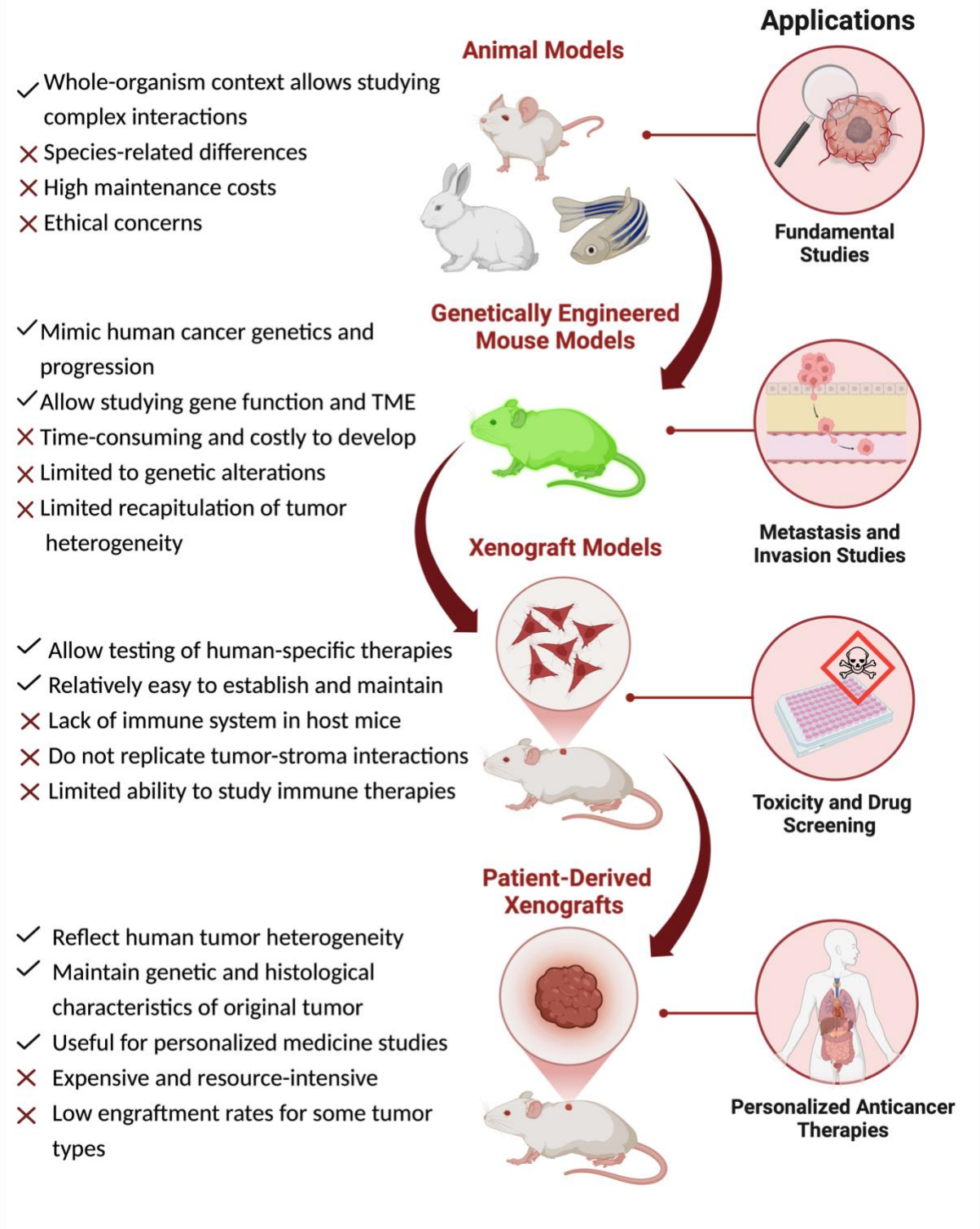

Figure 1 .7. Main *in vivo* models and their key advantages and limitations and main application in cancer research.

1.5.2 *In vitro* Models

In vitro models involve the study of cancer cells in a controlled, artificial environment outside a living organism. These models are fundamental in cancer research, providing simplified and accessible

systems to investigate cellular and molecular mechanisms, screen drug candidates, and understand tumor biology (270). Despite their limitations in fully replicating the complexity of *in vivo* tumors, *in vitro* models offer significant advantages in terms of reproducibility, cost-effectiveness, ease of manipulation, and human specificity (271) (**Figure 1.8**).

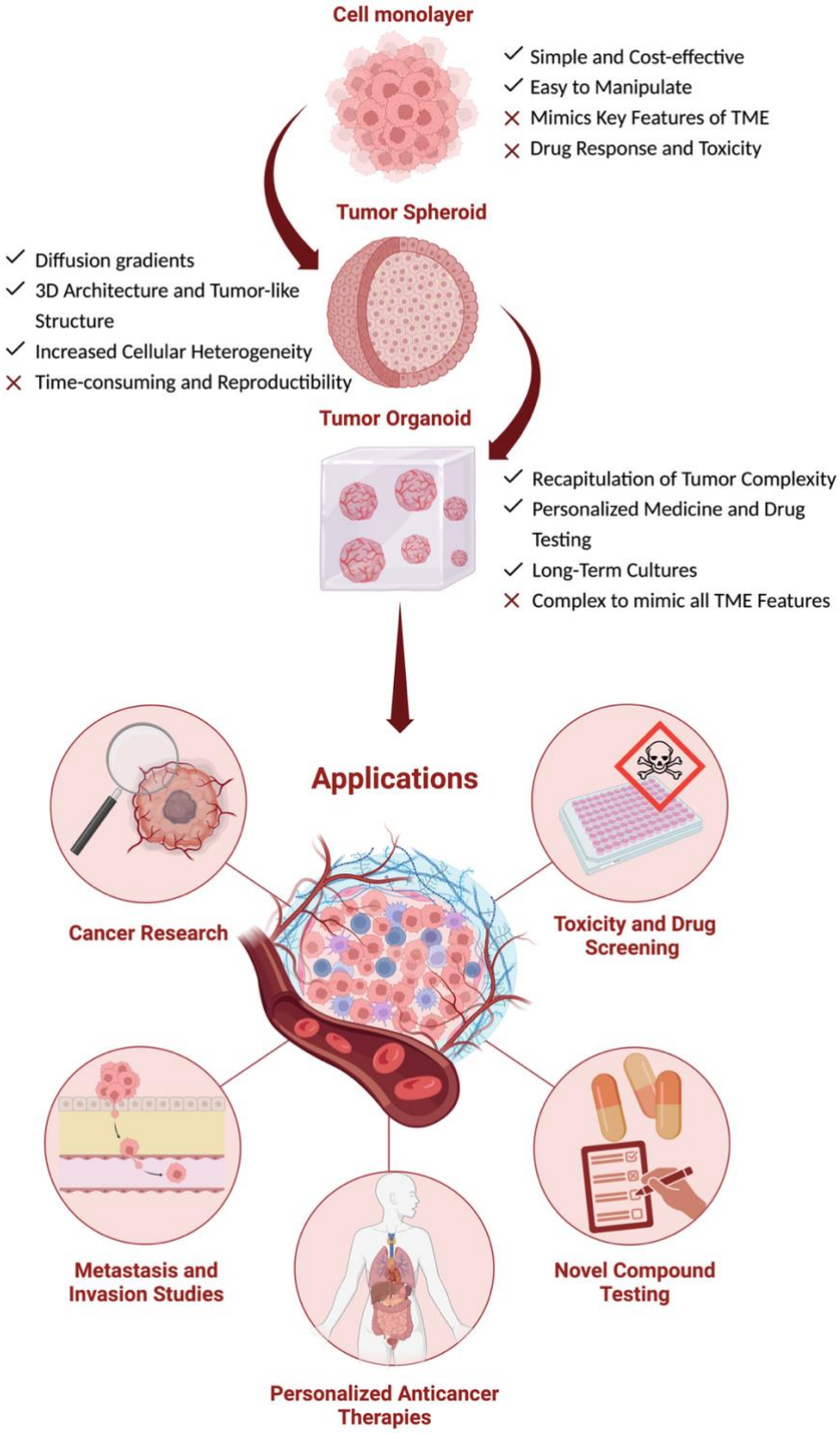

Figure 1.8. Main *in vitro* models and their key advantages and limitations and main application in cancer research.

1.5.2.1 2D Cell Cultures

2D cell cultures are the most traditional and widely used *in vitro* model. This method involves growing cancer cells, either primary or from established cell lines, on a flat, rigid surface such as petri dishes or culture flasks (272). Preclinical studies, particularly those based on drug screening, heavily rely on 2D cell monolayers due to their ease of implementation, cost-effectiveness, reproducibility, versatility, and compatibility with high-throughput screening (273–275). Still, these models do not fully recapitulate important features of the TME, including cell-to-cell and cell-matrix interactions and cellular heterogeneity (276). Moreover, when cultured as monolayers, tumor cells receive nutrients and oxygen indiscriminately, which does not occur in the *in vivo* environment, leading to changes in gene and protein expressions, metabolism, and proliferation kinetics (277–279). Altogether, these limitations add to the challenge of designing new target therapies (*e.g.,* cancer treatments) and accurately predicting drug responses. So, more advanced *in vitro* models have been developed to help improve the predictability of research results.

1.5.2.2 3D Cell Cultures

3D models are acknowledged as promising alternatives to conventional preclinical models, exhibiting increased recapitulative potential of the *in vivo* environment, and are suitable for large-scale screening (280,281). In 3D models, cells are cultured in ways to promote aggregation, leading to the creation of a 3D architecture. Besides the 3D architecture, these models can replicate numerous aspects found in native tumors, such as the occurrence of cell-to-cell and cell-matrix interactions, cell polarization, formation of oxygen, nutrient and pH gradients, *de novo* ECM deposition, and growth kinetics (275,282). What is more, recent studies reported that 3D models present similar gene expression patterns, drug resistance mechanisms, and activation status of signaling pathways to those observed *in vivo* (283,284). These features demonstrate the potential that 3D cultures hold as improved disease models.

Although it is improbable that these 3D cancer models will fully replace animal models at this time, they are anticipated to become a crucial intermediary between 2D *in vitro* and *in vivo* models (285). Such has been endorsed in the latest FDA Modernization Act 2.0, which admits the use of alternative models like spheroids and organoids in place of certain animal studies (286,287). By incorporating these advanced 3D models, researchers aim to provide clinically relevant data, enhance the translational effectiveness of preclinical studies, and ultimately improve treatment options for cancer patients while reducing the reliance on animal models (274).

1.5.2.2.1 Spheroids

Spheroids are widely used 3D cancer models due to their simplicity and adaptability (273). These microsized aggregates, derived from various cancers such as brain (288,289), breast (290,291), cervix (292,293), colon (294,295), lung (296,297), pancreas (298,299), and prostate (300,301), can consist of only tumor cells (homotypic spheroids) or include additional cell types like fibroblasts or immune cells (heterotypic spheroids) (273). Cell line-derived spheroids are easier to handle and suitable for high-throughput screening, while primary tissue-derived spheroids, despite challenges like limited lifespan, offer valuable insights into patient-specific responses (274).

Spheroids replicate key features of *in vivo* tumors, including strong cell-to-cell interactions and dense ECM, hampering the transport of nutrients, oxygen, and other soluble molecules, particularly in spheroids larger than 400 µm (273,277). This leads to the creation of distinct cell layers: an outer proliferative zone, a middle quiescent layer, and an inner hypoxic, necrotic core, resembling metastatic lesions and non-vascularized tumors (273,277,302). This heterogeneous and multilayered organization had a pivotal role in endorsing the application of spheroids as preclinical models in drug development and screening (287,291,308).

Spheroids can be generated using scaffold-free methods, including agitation, hanging drop, liquid overlay, and magnetic levitation (274), where cells self-organize and secrete ECM; or scaffold-based systems employing synthetic (*e.g.*, PEG, PLGA) or natural polymers (*e.g.,* collagen, alginate, GelMA) to mimic the ECM. Scaffold-free methods are simpler and more adaptable for high-throughput screening, while scaffold-based approaches enable more complex structures (273,274,303),

Although tumor spheroids offer a more precise depiction of tumor biology than traditional 2D models, they still face considerable challenges, including the lack of standardized protocols for generation of spheroids, leading to variability in size and composition across different laboratories (273,274), ultimately impairing the interlaboratory comparison of results and consistent reproduction of the findings. Furthermore, replicating the complex TME, including factors like vascularization and immune cell infiltration, remains an ongoing challenge (273).

1.5.2.2.2 Organoids

Organoids, unlike spheroids, self-organize and differentiate into tissue-specific cells, forming complex, renewable structures that mimic organ functions (304). Derived from sources like primary tissue biopsies, adult stem cells, embryonic stem cells, and induced pluripotent stem cells, their formation involves tissue dissociation, embedding in a 3D matrix (*e.g.,* Matrigel®), and incubation with media enriched with growth and differentiation factors tailored to the organoid type (305–308).

Organoids surpass 2D and spheroid models in replicating tumor microenvironments, improving accuracy in tumor behavior and patient-specific responses (309,310). However, they lack vascularization and complete microenvironment components, limiting their utility for immunotherapy studies. Challenges include sample acquisition, varying proliferative rates, optimization of growth factors, long culture times, and high costs. Additionally, batch variability and safety concerns hinder standardization (311–313).

Future advancements in tissue engineering, biomaterials, microfluidics, and standardized protocols could enhance organoid applications in drug development, regenerative medicine, and CRISPR-based gene editing (314–322).

1.5.2.3 Application of *in vitro* Models in Cancer Research

Owing to their ability to closely replicate biological systems, ease of manipulation, and species relevance, advanced 3D models are invaluable tools in cancer research, particularly for drug screening, personalized medicine, gene editing, and immunotherapy applications.

Drug development and screening are among the most promising uses of these models, enabling high-throughput drug testing, personalized regimen studies, and insights into drug resistance mechanisms (323,324). Studies comparing drug responses in spheroids and patient-derived organoids (PDOs) have demonstrated superior predictive accuracy compared to 2D cultures and xenograft mice models, with good consistency observed in comparison to original patient responses (324,325).

PDOs also hold significant promise for personalized treatments, drug response prediction, and biomarker identification (326–328), as evidenced by 17 studies testing tumor-specific responses using these models (329,330). Additionally, PDOs can be genetically modified using CRISPR/Cas9, a technique that has successfully corrected mutations in monogenic diseases, such as in intestinal organoids from cystic fibrosis patients (331).

In immunotherapy, models like BEHAV3D, which co-culture tumor organoids with CAR-T cells, have shown great potential for studying immune interactions, CAR-T cell efficacy, and treatment responses (332,333).

1.5.3 *Ex vivo* Models

Ex vivo models use freshly collected tissues to study cancer under controlled conditions, preserving the original tissue's architecture and microenvironment (284,349,350). They offer more physiological relevance than traditional cell cultures. Common examples include the chick chorioallantoic membrane

(CAM) assay, used to evaluate angiogenesis (334–336), and organotypic slice cultures, which replicate tumor heterogeneity and responses to therapies (337–348). These models support studies on drug effects, immune interactions, and gene therapies. However, challenges like short lifespan, sample variability, and maintenance complexity limit their broader application (349,350).

1.5.4 Limitations of Current Cancer Models

Even when considering the individual benefits of the previously described cancer models, significant limitations remain, particularly regarding the perfusion and vascularization of cells. Despite the ability of these advanced models to accurately mimic the 3D tissue architecture, replicate organ-level functionality, and simulate pharmacokinetic dynamics, they all share a fundamental limitation: their static nature. This is associated with major concerns, such as the accumulation of biochemical waste within the cell aggregates, the absence of mechanical properties of tumors, which can influence drug response, and the poor recapitulation of the immune response and vascularization (337–342). Altogether, this lack of dynamism can impact the predictivity of these models, potentially compromising the success of therapeutics when advanced to human trials (351).

All these limitations urged the need to develop new *in vitro* models for both basic and preclinical cancer research. These new models should consider that tumors are complex ecosystems dynamically evolving, hence not only focusing on recapitulating the TME but also the physicochemical properties and mechanical forces that native tumors face within a living organism. Given that all the aforementioned components have been shown to play a significant role in tumor progression, metastasis, and resistance to treatment (351,352).

1.6 Tumor-on-Chip

The leveraging of microfluidics and tissue engineering allowed to achieve an important milestone in cancer modeling: the development of Tumor-on-Chip (ToC) technology (353). ToC is a promising candidate to replace conventional experimental models, providing a more comprehensive and realistic model by integrating physical, chemical, mechanical, and biological cues of tumor development and metastasis (354,355). The implementation of ToC can bridge the gap between traditional cell cultures and *in vivo* animal models, offering unprecedented potential in the realms of drug discovery, cancer research, and personalized medicine (356–360).

ToC integrates microfluidics, biomaterials, and living cells to create micro-engineered environments that closely mimic the *in vivo* TME (**Table 1.3**) (361). These devices can simulate various physiological

conditions, such as nutrient and oxygen gradients (362,363), mechanical forces (364) and cellular interactions (365–367), providing a more accurate platform to enhance our understanding of cancer biology, reduce the time and cost associated with drug development, and improve clinical outcomes by enabling more effective and personalized treatment strategies (**Figure 1.9**) (356,360).

Table 1.3. Key components of ToC devices and their respective functionality.

Key components	**Functionality**
Microfluidic system	Enables precise control over fluids at the microscale. They facilitate the recreation of complex biological environments by controlling factors like nutrient gradients, shear stress, and oxygen levels.
Biological components	ToC systems support 3D cell growth with different cell types, which better replicates the architecture and function of real tumors. This includes proper cell-cell and cell-matrix interactions, as well as the development of environmental niches.
Materials	Chip materials: Poly(dimethylsiloxane) (PDMS), Polymethyl methacrylate (PMMA), Polycarbonate (PC), Hydrogels, glass and Paper-based, now joined by materials like polystyrene (PS). Scaffolds: Synthetic and biological materials like collagen, gelatin, alginate, Matrigel® are also used to simulate the ECM.

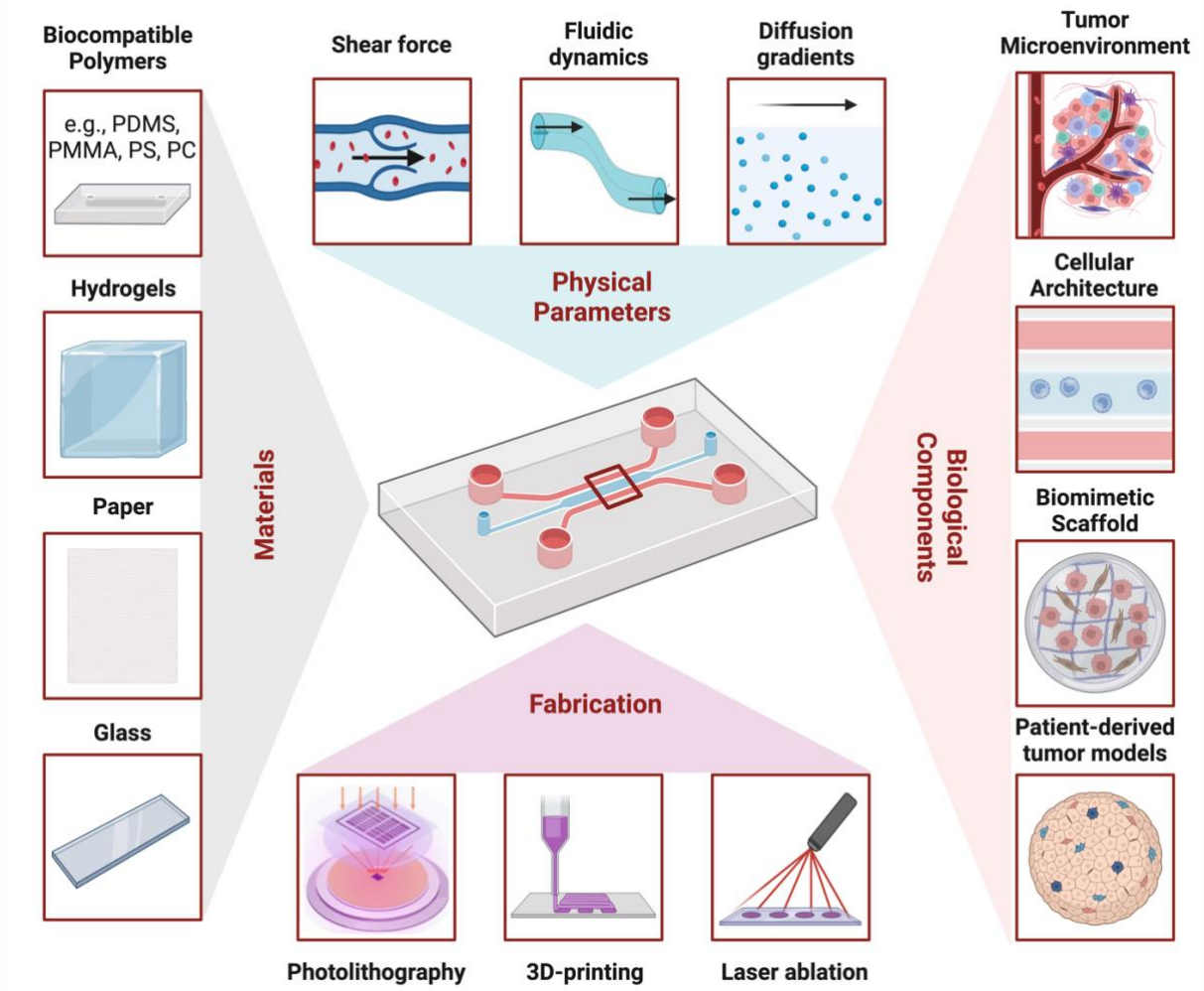

Figure 1.9. Key components of Tumor-on-Chip systems.

1.6.1 Biological Components

As mentioned in the previous sections, cancer is not solely defined by cancer cells but by the whole TME, including cellular and molecular components, ECM, as well as their complex interplay. Tumors have many biomechanical abnormalities such as elevated solid stress, interstitial pressure, and stiffness (368). One compelling feature of the ToC models is the possibility to finely control and thus, dissect the role of each parameter on cancer development and progression. Particularly, the different cell types and their spatial organization, the ECM properties, the generation of biochemical gradients, the control of the gaseous environment, and even the different mechanical forces at play.

1.6.1.1 Cell Sources

The complexity of TME can be closely mimicked in ToC models by integrating various cell types, such as stromal cells, immune cells, and endothelial cells to closely replicate the interactions and structure of actual tumors (369).

Cancer cell lines remain the primary tool for constructing cell models due to their cost-effectiveness, ease of use, and unlimited source of cells (370). Indeed, about 70% of all ToC systems have relied on the use of cancer cell lines (351,371). Even though its use theoretically allows easy comparison between the results obtained across different *in vitro* models, it is also well-known that cell lines do not completely represent *in vivo* tumors, since indeterminate transcriptomic, epigenetic, genetic, and phenotype changes may occur during cell immortalization (370).

A realistic approach to reconstitute the *in vivo* TME should include the use of primary cells directly extracted from fresh tissues or fluids with subsequent *ex vivo* culture. The other 30% of ToC models have reported the use of primary cells, mainly human peripheral blood mononuclear cells (PBMC), CAFs, or endothelial cells (*e.g.,* HUVECs) (372–375). Numerous ToC studies use PBMCs to study the effect of monocytes on cancer cell extravasation at different stages of their life cycle (372). Among the endothelial cells (ECs), HUVECs were by far the most well-represented source of ECs in vascularized ToC models (373,374). Still, the non-tumoral origin of HUVECs and PBMCs (extracted from healthy donors) impairs an exact mimic of tumor immune cell infiltration.

More recently, ToC models have been starting to incorporate patient-derived materials, creating biologically functional tissue mimetics where inter-tissue interactions can be reconstituted. Several cell sources can be exploited, including primary cells from surgical resections, biopsies, aspirates, and blood samples (376). One study has assessed the inter and intra-tumoral heterogeneity of breast cancer tissue using patient-derived spheroids cultured on ToC devices (377). Still, limitations regarding the isolation, availability, and viability of tumoral endothelial cells have been preventing the expansion of fully patient-derived vascularized ToC models (378), highlighting the need to develop novel and more efficient isolation protocols.

1.6.1.2 Cellular Architecture

Besides the variety of cell types, the spatial organization of the cells is a crucial factor in replicating the complex structure and function of the TME. Proper spatial arrangement ensures that cellular interactions (*e.g.,* cell-cell interactions) and the resulting biological processes (*e.g.,* cytokine secretion) closely mimic those *in vivo*. This complex network of interactions is known to influence tumor behavior and

drug response, thereby endorsing the importance of recapitulating the cellular architecture of tumors to enhance the physiological relevance of ToC models (379).

To mimic the heterogeneity of the TME, ToC devices utilize co-culture systems where two or more cell types are grown together in close proximity. These systems enable the study of interactions between cancer cells, stromal cells, endothelial cells, and immune cells. For instance, a glioblastoma ToC model might include glioblastoma cells, astrocytes, and microglia to replicate the brain tumor environment more accurately (380). Besides the variety of cell types, these can be grown in different conformations from simple monolayers to complex 3D architectures. Indeed, ToC systems often incorporate 3D structures such as spheroids, organoids, and other tissue-like constructs. For example, a breast cancer ToC model used a co-culture MCF-7 breast cancer cells with fibroblasts and endothelial cells to study how the presence of fibroblasts influenced the invasion and migration of cancer cells (381). In another study, a ToC system with dermal fibroblasts and HUVEC cells investigated the formation of vascular networks and their impact on drug delivery and efficacy (382).

Advanced microfabrication techniques are employed to design and construct ToC devices with precise spatial configurations that allow the creation of complex cell geometries and vascularized models. The designs commonly applied can be divided into five categories: compartmentalized chip, micro-well array, 2D chip, membrane chip, and lumen chip (383). Almost half of the ToC belongs to the "compartmentalized chips" category, which involves the compartmentalization of cells by their embedment in hydrogels (384–393). The "micro-wells array" is typically used for high-throughput applications since it allows studying multiple or replicated conditions, but often with limited cell complexity (394–399). The "2D chip" approach includes all different designs containing cell cultures as monolayers. These 2D models do not display *in vivo* stromal characteristics because their key point is to focus on technological advances, for instance, automation(400), control of oxygen (401), or shear stress (402). In "Membrane chips", the microchannels are separated by a porous membrane that allows cells (initially grown as a monolayer) to migrate through the membrane pores (403–409). A key feature of this device is the possibility of obtaining an air-liquid interface (allowing respiratory epithelial cell differentiation) (373). Although membrane chips were not often used for cancer studies, they are extensively applied in other pathologies (*e.g.,* infection-induced recruitment of immune cells, breathing-induced absorption of nanoparticles) (373). The category "lumen chip" consists of ToC in which a critical element is used to form lumen in hydrogels. This design is typically used to model blood vessels in tumors or to tightly pack cells in a cylindrical compartment (321,410–413).

Despite the advancements in cancer modeling offered by ToC systems, the complexity of designing and fabricating these devices, coupled with the need for precise control over multiple variables, makes it

difficult to create universally applicable models. Future research is focused on improving the scalability and reproducibility of ToC systems.

1.6.1.3 Scaffolds

The ECM is a crucial component of the TME, providing structural support and biochemical signals to cells (414). What is more, its composition varies according to the nature and state of the organs (415,416) and also during pathological conditions, such as tumor growth (417,418). Those dynamic changes not only affect cell differentiation, proliferation, survival, migration, and adhesion (419) but can also influence cell response to drugs by either enhancing their efficacy or promoting drug resistance (420). Given its modulatory effect on tumor behavior, ToC systems have focused on selecting and designing biomaterials to accurately reconstitute the extracellular matrix. The same principle is also applied to ToC coatings for 2D cell monolayers.

Collagen I is the main ECM component *in vivo* and is by far the most used hydrogel in ToC (being used in half of the ToC publications) (351). Additionally, other matrices like Matrigel®, fibrin gelatin, and agarose have been applied (421,422). Collagen provides tensile strength and structural integrity, Matrigel offers a complex mix of proteins and growth factors, and fibrin is used for its role in wound healing and cell migration. Nevertheless, the results of Matrigel-cultured cells should be carefully considered, given its influence on gene expression (423).

Overall, mimicking the *in vivo* ECM further enhances the physiological relevance of the ToC models. Besides supporting cell adhesion, proliferation, and differentiation, the choice of the matrix can be tailored to replicate specific tissue types and disease conditions, allowing for more accurate modeling of tumor biology.

1.6.2 Physicochemical Parameters

Besides the precise control over the spatial arrangement of different cell types, ToC devices integrate microfluidic channels that enable the manipulation of biochemical gradients (424), oxygen levels (425), pH (426), and mechanical forces (427), providing a dynamic environment that better simulates the *in vivo* conditions tumors.

Oxygen gradients, for instance, are crucial for replicating hypoxic regions within solid tumors, influencing cancer cell behavior and treatment resistance (363,428,429). Additionally, the acidity of tumors, often resulting from altered metabolic activities of cancer cells, can also be replicated in ToC

systems by controlling the pH of the microenvironment (430). This control is significant for studying tumor progression and the efficacy of pH-sensitive therapeutics (431). Finally, ToC platforms can apply mechanical forces such as shear stress and mechanical strain to cells, simulating the physical forces experienced *in vivo* (432,433). These forces influence cell behavior, including migration, invasion, and response to therapy (434,435). For example, shear stress applied through fluid flow can mimic blood flow within the TME, affecting endothelial cells and angiogenesis (436,437).

1.6.2.1 Microengineering Components

To achieve precise control over the physicochemical and ECM properties, as well as cellular organization and cell types, Tumor-on-Chip systems require extensive expertise in microengineering and microfabrication. A variety of materials and techniques are employed to replicate the dynamic environment of *in vivo* tumors (438). The design and functionality of these devices vary depending on the desired application and the tumor models being studied but generally include features such as microchannels, wells, and chambers to culture cells and tissues (439). Additionally, devices with increased complexity can also integrate sensors, controllers, and imaging modules (**Table 1.4**) (438). Altogether, this control allows for better prediction of how tumors will respond to therapies, providing valuable insights for drug development and personalized medicine.

Table 1.4. Description, function, and used materials of components of ToC devices that can be incorporated into a whole system.

Device part	Description	Function	Material / Type
Microfluidic Channels	Network of small channels through which fluids, cells, and nutrients flow.	Simulate blood flow, nutrient and oxygen transport within the TME and control shear force.	Typically made from PDMS, glass, or other biocompatible polymers.
Cell Culture Chambers	Specific regions where tumor cells are cultured.	House the tumor cells and recreate the 3D architecture of tumor tissues.	PDMS, hydrogels (collagen, Matrigel®), or other matrix materials to support 3D cell growth.
Biomimetic Extracellular Matrix	A scaffold that mimics the natural ECM of tissues.	Provide structural support and biochemical signals to cells, enabling 3D cell culture.	Collagen, gelatin, alginate, Matrigel®, and synthetic hydrogels.

Substrate or Base Material	The foundational layer on which the entire device is built.	Provide structural integrity and support for the microfluidic and cell culture components.	Glass, silicon, PDMS, and other rigid or semi-rigid materials.
Microenvironment Control Systems	Systems to control various environmental factors such as oxygen levels, pH, and temperature.	Closely mimic the physiological conditions of the TME.	Microfluidic pumps, valves, sensors, and heating elements.
Fluidic Pumps and Valves	Devices to control the flow of fluids within the chip.	Deliver nutrients, remove waste, and introduce drugs or other substances in a controlled manner.	Peristaltic pumps, syringe pumps, and on-chip micropumps.
Sensors and Detectors	Embedded sensors to monitor various parameters such as pressure, oxygen concentration, and pH.	Provide real-time feedback and ensure optimal conditions for cell growth and experimentation.	Optical sensors, electrochemical sensors, and biosensors
Imaging and Analytical Interfaces	Integrated systems for real-time imaging and analysis of cells and tissues.	Visualize cell behavior, track cell proliferation, and monitor drug responses.	Fluorescence microscopy, confocal microscopy, and other imaging methods.
Drug Delivery Systems	Mechanisms to introduce therapeutic agents or other substances to the cell culture chambers.	Test the effects of drugs on tumor cells in a controlled manner.	Microinjectors, diffusion-based systems, and integrated reservoirs.
Interfacing Components	Connections to external equipment such as microscopes, pumps, and computers.	Facilitate integration with analytical instruments and control systems for data acquisition and analysis.	Microfluidic connectors, electrical interfaces, and data ports.

1.6.3 Fabrication Processes

Typically, ToC devices are fabricated using advanced microfabrication techniques, including photolithography (440), soft lithography (441,442), 3D printing (443–445), and laser ablation (446,447). Each fabrication method offers unique advantages and drawbacks, making them suitable for different aspects of ToC device creation (**Table 1.5**). The choice of the technique depends on the specific requirements of the study, including precision, material compatibility, cost, and scalability. Integrating multiple techniques can often provide a balanced approach, leveraging the strengths of each to overcome individual limitations.

Table 1.5. Overview of the principal fabrication methods used to develop ToC devices.

Method	Description	Advantages	Limitations
Photolithography	Process used to transfer geometric patterns onto a substrate using light. It entails applying a photosensitive material known as photoresist to the substrate, exposing it to light through a mask, and developing the pattern by removing either the exposed or unexposed regions of the photoresist.	**High Precision and Resolution:** Capable of producing extremely detailed and accurate microstructures, essential for replicating complex biological environments. **Scalability:** Suitable for mass production, allowing for the creation of numerous identical chips. **Compatibility with Various Materials:** Applicable to a wide variety of materials, including polymers, silicon and glass enabling diverse applications.	**Cost:** High initial setup costs due to the need for cleanrooms and specialized equipment. **Material Limitations:** Not suitable for all biocompatible materials, particularly some soft hydrogels. **Complexity:** Requires multiple steps and precise alignment, increasing the complexity and potential for errors.

Soft lithography	Soft lithography uses a flexible elastomeric stamp (usually made of PDMS) to transfer patterns onto a substrate. The stamp is created by casting PDMS on a master mold, which contains the desired microstructure.	**Flexibility:** Can produce a variety of microstructures using soft, elastomeric materials like PDMS, which are biocompatible and transparent. **Cost-Effective:** Less expensive than photolithography, as it doesn't require cleanroom facilities for every step. **Ease of Use:** Simplified process that allows for rapid prototyping and modifications	**Resolution Limitations:** Lower resolution compared to photolithography, which may limit the precision of microstructures. **Deformation:** Elastomeric materials can deform under pressure, potentially altering the microenvironment. **Reproducibility:** Variability in the fabrication process can lead to inconsistencies between chips.
3D printing	3D printing creates objects layer by layer from a digital model. There are several methods available, such as stereolithography (SLA), fused deposition modeling (FDM), and digital light processing (DLP).	**Customization:** Allows for highly customizable and complex designs tailored to specific research needs. **Material Variety:** Can use various biocompatible materials, including hydrogels and biodegradable polymers. **Integration:** Enables the incorporation of multiple functionalities within a single device.	**Resolution:** Generally lower resolution compared to lithography, though this is improving with advances in technology. **Mechanical Properties:** Printed structures may lack the mechanical strength and stability required for some applications. **Speed:** Some 3D printing processes can be time-consuming, particularly for high-resolution or large-volume production.

Laser ablation	Laser ablation uses a focused laser beam to remove material from a substrate by vaporization or sublimation. It is a precise method for cutting or engraving microstructures.	**Precision:** High precision in cutting and structuring materials, useful for detailed microstructures. **Versatility:** Applicable to a wide range of materials, including metals, polymers, and ceramics. **Minimal Contact:** Non-contact process reduces contamination risk and preserves material integrity.	**Thermal Damage:** Potential for thermal damage to materials, which can affect biocompatibility. **Cost:** Requires expensive equipment and maintenance. **Scalability:** Less suitable for mass production compared to lithographic methods.

1.6.4 Materials

Materials commonly used include PDMS (448), hydrogels (449), and other biocompatible polymers (450,451). In the same manner as the fabrication methods, each material has its advantages and limitations, affecting its suitability for different applications. Generally, PDMS is the most popular material for its flexibility and ease of fabrication, but its chemical nature leads to the absorption of small hydrophobic molecules, narrowing its application in drug studies (452,453). Conversely, PMMA and PC provide better mechanical strength but lack gas permeability, limiting the oxygen supply to the cells (454–456). Hydrogels offer a realistic 3D environment but have stability and reproducibility issues (451,457,458). Glass provides excellent optical clarity but is brittle (459), while paper-based materials are low-cost and easy to handle but have poor optical properties for imaging, are less durable and offer less control over fluid flow (450,460). More recently, PS has also been explored due to its superior properties (461). Among them, the ease of fabrication with more consistent and predictable surface properties than PDMS and PMMA, while allowing effortless molding and surface-treatment to enhance cell adhesion or create specific patterns for cell growth. The excellent optical transparency, similar to glass, makes it suitable for high-resolution imaging and microscopy. Additionally, PS also shows high chemical resistance, comparable to PMMA and PC, outperforming PDMS, which can absorb small hydrophobic molecules. Overall, the choice of material often depends on the specific requirements of the experiment and the desired balance between ease of use, biocompatibility, and mechanical properties (450).

1.6.5 Tumor-on-Chip Applications in Cancer Research

The precise manipulation of the cellular environment in Tumor-on-Chip (ToC) models enhances the accuracy of tumor responses, making them valuable for drug screening, disease modeling, and personalized medicine (277,354,360,462–465). ToC models not only recapitulate physiologically relevant conditions (466) but also offer compatibility with a wide range of analytical methods and high-throughput formats. These features, along with the ability to produce patient-specific models and the relatively short experimental time, have contributed to the growing interest in ToC systems.

In cancer modeling, most ToC studies focus on the TME, particularly in metastasis (466,467), invasion (468), tumor heterogeneity (469), and cell-matrix interactions (470,471). These studies manipulate physiological parameters such as hypoxic gradients, ECM composition, and shear force, often using co-cultures of cancer cells with inflammatory cells (*e.g.*, macrophages), cancer-associated fibroblasts (CAFs), and endothelial cells, which play critical roles in tumor progression (383,470,472).

Beyond cancer modeling, ToC devices are increasingly used for high-throughput drug screening, allowing simultaneous testing of multiple drugs and dosages. This capability has made ToC a reliable tool for drug screening (315,473,474), drug validation (475), resistance (476,477), and toxicity studies (478,479). The customization potential of ToC devices to reflect the unique characteristics of individual patient tumors makes them particularly advantageous for personalized medicine (466). Unlike the "one-size-fits-all" approach of traditional oncology treatments, ToC enables the identification of the most effective and least toxic therapy for each patient (480). By incorporating patient-derived cells, ToC models can be used to test therapeutic responses and tailor treatment strategies (481–483). Additionally, individualized tumor chips can facilitate "micro"-clinical trials, enabling the testing of various drug doses, schedules, and combination therapies to guide clinical decisions.

1.6.6 Challenges and Considerations

ToC technology offers significant potential for personalized medicine, enabling rapid, automated results with just a few patient cells. However, technical challenges persist. Fabrication of these devices is complex, and standardized protocols are needed to ensure reproducibility and scalability. The integration of multiple cell types and components into a unified system poses additional difficulties, while the creation of reliable, homogeneous tumor models for comparative studies remains a key challenge. Furthermore, addressing intellectual property concerns related to device commercialization is essential (484,485).

1.6.7 Towards Widespread Adoption of ToC Technology

Before ToC technology can be widely adopted in cancer research, it must overcome those challenges and deliver consistent results. Given its interdisciplinary nature, researchers, physicians, and regulatory bodies need to make a joint effort to address the remaining challenges that have been preventing ToC models from becoming the future of cancer research. To do so, it is essential to validate ToC models through co-clinical trials, comparing drug responses in ToC systems with patient outcomes (474,486). Integrating patient-derived tissues with *in vivo* trials will demonstrate ToC's potential in drug development and personalized treatment.

What is more, to truly revolutionize cancer modeling, a shift towards accessible fabrication and design optimization of ToC platforms is essential. One promising approach is laser engraving thermosensitive polystyrene sheets, which offer biocompatibility, optical transparency, and ease of surface functionalization. The thermosensitive nature allows precise patterning without expensive photolithography equipment. Indeed, laser engraving eliminates the need for molds or clean-room settings, and since design modifications are computerized, adjustments for specific experiments can be easily performed. While the final devices may have minor imperfections, this method provides a cost-effective way to optimize and test prototypes before finalizing designs. By simplifying fabrication and reducing costs, this approach makes ToC devices more accessible, accelerating the development of accurate cancer models.

Finally, emerging technologies like advanced microfabrication, nanotechnology, and AI integration will further enhance ToC capabilities, optimizing data analysis, experimental design, and therapeutic strategies, advancing both pre-clinical and clinical research.

1.7 Scope of the Thesis

Gene therapy holds significant promise for cancer treatment by silencing activated oncogenes and modulating defective tumor-suppressor genes using tools like ASOs and siRNA, now joined by CRISPR technology. Despite advancements, their success in clinical trials and applications has been dependent on efficient vectorization towards selective sites, to help overcome enzymatic degradation and improve tissue availability and cell uptake. Among the vectorization strategies, those based on nanoparticles, particularly AuNPs, have been extensively exploited for delivering therapeutic nucleic acids, due to the simplicity of surface functionalization and biocompatibility. Still, the wide range of conceptual nanoscale platforms cannot be easily assessed in terms of toxicity and efficacy against cancer cells, due to the lack of accurate and predictive experimental models of human tumors. Tumor-on-Chip offers a

promising alternative for *in vitro* research, enhancing drug development and reducing animal testing. Yet, these systems are, from a user perspective, immensely complex to build and operate, and therefore inaccessible to the majority of researchers.

In this thesis, we aim to shift the paradigm towards the simplification of ToC devices, through innovative fabrication methods and materials like polystyrene, to broaden the application of ToC models. We propose developing a simplified chip prototype that creates 3D-cancer models mimicking tumor microenvironment, thereby improving the screening of gene silencing strategies based on functionalized gold nanoparticles (AuNPs@ASOs). The work is divided into four stages. The first two focus on identifying important cues to assess the therapeutic effects of silencing strategies in complex cancer models, while the latter stages involve developing and optimizing ToC devices to enhance the predictiveness of these outcomes.

1. Synthesis and characterization of AuNPs@ASOs nanoconjugates targeting a well-known oncogene (*c-MYC*), with interest in their stability in the culture media, cytotoxicity, and silencing effect on the target mRNA and protein.
2. Assess the requirements for advancing silencing strategies from simple 2D cultures to more complex 3D cancer models, with a focus on uptake rates, time-dependent silencing profiles, and dose escalation requirements.
3. Develop simplified ToC prototypes suitable for 2D and 3D cancer modeling, evaluating the effect of different designs and surface coatings.
4. Evaluate the suitability of the developed devices in reproducing the silencing effects observed in plate-based cancer models and provide insights into the requirements for improving the predictiveness of the achieved cancer models.

2

MATERIALS AND METHODS

All materials and methods shared across multiple chapters are presented in this section to avoid repetition and enhance readability. A full-detailed description of the methods is presented in the chapters.

2.1 Materials

2.1.1 Reagents

Table 2.1. List of chemical and biological reagents.

Name	CAS / Ref	Company
1× phosphatase inhibitor (PhosStop)	Ref 12352204	Roche, Switzerland
Absolute ethanol	64-17-5	PanReac, Germany
Acetic acid (Glacial)	64-19-7	Merck, USA
Acrylamide	79-06-1	Merck Millipore, USA
Agarose	9012-36-6	VWR, USA
Agarose with electrophoresis grade,	Ref MB02703	NZYTech, Portugal
Anti-mouse IgG, HRP-linked Antibody	7076	Cell Signaling Technology, USA
Anti-rabbit IgG (FITC) produced in goat	F9887,	Sigma-Aldrich, USA
Anti-rabbit IgG, HRP-linked Antibody	7074	Cell Signaling Technology, USA

BIOFLOAT™ FLEX coating solution	F202005	faCelitate, Germany
Bovine Serum Albumin (BSA)	MB04602	NZYtech, Portugal
Bromophenol Blue	115-39-9	Merck, USA
CellTiter 96® (MTS assay)	Ref 35810005	Promega, USA
CellTox™ Green cytotoxicity assay	Ref 8742	Promega, USA
Chloroform	67-66-3	Merck, USA
cOmplete™ Protease Inhibitor Cocktail	Ref 12352204	Roche, Switzerland
DTT (dithiothreitol)	3483-12-3	Thermo Scientific™, USA
Dulbecco's Modified Eagle Medium (DMEM)	Ref 41965062	Invitrogen, USA
Ellman's reagent (5,5-dithio-bis-(2-nitrobenzoic acid)	Ref 22582	Thermo Scientific™, USA
Ethanol (96%)	64-17-5	LabChem, USA
Ethylenediaminetetraacetic acid (EDTA)	25102-12-9	Merck, USA
Fetal Bovine Serum (FBS)	Ref 10131035	Invitrogen, USA
Ficoll PM400	26873-85-8	Sigma-Aldrich, USA
GelRed™	Ref 41003	Biotium, USA
Hoechst dye	H6024	Sigma-Aldrich, USA
Hydrochloric acid (HCL)	7647-01-0	Merck, USA
Isopropyl Alcohol (IPA)	7732-18-5	Fisher Chemical, USA
Minimum Essential Medium (MEM)	Ref 11140035	Gibco™, USA
Molico powdered milk light	-	Nestlé, Portugal

Mouse monoclonal Anti-β-Actin antibody	A5441	Sigma-Aldrich, USA
NP-40	9016-45-9.	Sigma-Aldrich, USA
NZY M-Mulv First-Strand cDNA synthesis kit	Ref MB17202	NZYTech, Portugal
NZYSupreme qPCR Green Master Mix	Ref MB41903	NZYTech, Portugal
One-step NZYSpeedy RT-qPCR Green kit	Ref MB34301	NZYTech, Portugal
Paraformaldehyde (PFA)	30525-89-4	Sigma-Aldrich, USA
PEG (O-(2-Mercaptoethyl)-O′-methyl-hexa(ethylene glycol)	Ref 672572	Sigma-Aldrich, USA
Pen Strep (Penicillin-Streptomycin (10,000 U/mL)	Ref 15150122	Gibco™, USA
Phenylmethylsulphonyl fluoride (PMSF)	329-98-6	Sigma-Aldrich, USA
Pierce 660nm Protein Assay Reagent	Ref 22660	Thermo Scientific, USA
Potassium chloride	7447-40-7	Merck, USA
Rabbit anti-c-MYC primary antibody Y69	ab32072	Abcam, UK
SDS (Sodium dodecyl sulphate	151-21-3	Sigma-Aldrich, USA
Sodium chloride	7647-14-5	Merck, USA
Sodium citrate	6132-04-3	Sigma-Aldrich, USA
Sodium Dodecyl Sulfate (SDS)	151-21-3	Merck, USA
Sodium Phosphate Dibasic	7758-11-4	Sigma-Aldrich, USA
Sodium Phosphate Monobasic	7778-77-0	Sigma-Aldrich, USA
Tetrachloroauric(III) acid	16961-25-4	Sigma-Aldrich, USA
Tris hydrochloride (Tris HCl)	1185-53-1	Sigma-Aldrich, USA
TRIS- acetate	6850-28-8	Santa Cruz, USA

Tris(hydroxymethyl)aminomethane (TRIS)	77-86-1	Sigma-Aldrich, USA
Triton X-100	9036-19-5	Sigma-Aldrich, USA
TrypLE Express reagent	Ref 12604021	Gibco, USA
Tween® 20	9005-64-5	Merck Millipore, USA
WesternBright ECL	K-12045	Advansta, USA
Xylene Cyanol FF	2650-17-1	BDH Chemicals, UK

2.1.2 Primer and Oligonucleotide Sequences

All primers and thiolated oligonucleotides were purchased from STAB Vida, Lda., Portugal.

Table 2.2. List of primers and ASOs.

Gene	Forward Primer	Reverse Primer	Product size
c-MYC	5'-TCTGAAGAGGACTTGTTGC-3'	5'-TTCAGTCTCAAGACTCAGC-3'	229 bp
copGFP	5'-TTCTACCACTTCGGCACCTA-3'	5'-TCCACCACGAAGCTGTAGTA-3'	335 bp
18S	5'-AGGGTTCGATTCCGGAGAG-3'	5'-GAATTACCGCGGCTGCTG -3'	215 bp
Antisense Oligonucleotides (ASOs) Sequence			
c-MYC	5' – GCGCCCATTTCTTCCAGATATCCTCGCTGGGCGC – 3'		
copGFP	5′-thiol- GCG CCC CGT ACT TCT CGA TGC GGG TGG GGC GC-3′		
Scramble	5'-TTTCGGGTTGACGTTAGCCGGATCTACCGAAA-3'		

2.1.3 Solutions

Ultrapure distilled water used in these solutions came from a Millipore water purification system (Merck Millipore, USA).

Table 2.3. List of solutions.

Name	Composition
AGE I	10 mM phosphate buffer pH=8 2% SDS
AGE II	10 mM phosphate buffer pH=8 1.5 M NaCl 0.01% SDS
Loading dye (6X)	0.25% Blue bromophenol 0.25% Xylene Cyanol 1.5 mg Ficoll
Membrane Blocking Solution	5% (w/v) milk solution Tris-buffered saline with 0.1% (v/v) Tween 20 (TBST).
Paraformaldehyde (PFA) 4%	4g of Paraformaldehyde 90mL of PBS 1X Incubate overnight at 65ºC Adjust the volume until 100mL Filtrate (0.22 µm) Store at -20ºC
Phosphate Buffer Saline (PBS) 1X	8g of NaCl 1.44g of Na_2HPO_4. 0.2g of KCl.

	0.24g of KH_2PO Bring the pH to 7.4 or 7.2 using HCl. Add distilled water until the total volume reaches 1L.
Phosphate Buffer ph8 (100mM)	20.214 g of K2HPO4 3.394 g of KH2PO4 Adjust solution to final desired pH using NaOH. Add distilled water until the volume is 1 L.
Protein Lysis Buffer	150 mM NaCl 50 mM Tris (pH 8.0) 5 mM EDTA 2% (v/v) NP-40 1× phosphatase inhibitor 1× protease inhibitor (cOmplete Mini) 1 mM PMSF 0.1% (w/v) DTT
SDS Loading Buffer 4X	0.2M of Tris 1M ph 6.5 (Stacking Buffer) 0.4M of DTT 4.3M of Glycerol 8.0% (w/v) of SDS 6mM of Bromophenol blue

Tris-acetate-EDTA (TAE) Buffer (50X)	2 M Tris-Acetate 0.05 M EDTA
Tris-EDTA (TE) pH 7.4	10 mM Tris base (pH 7.4) 1 mM EDTA (pH8) Sterilize by autoclaving and filtration (0.22 µm).
Tris-buffered saline (TBS) 10X	24g of Tris-HCL 5.6g of Tris-base 80g NaCl Add distilled water until the total volume reaches 1L. Bring the pH to 7.6.
Tris-buffered saline with 0.1% Tween® 20 detergent (TBST) 1X	100mL TBS 10X 1mL Tween-20 Add distilled water until the total volume reaches 1L.

2.1.4 Equipment

Table 2.4. List of equipment.

Name	Company
Balance Sartorius BP 610	Sartorius, USA
CO_2 Incubator	Leec, UK
CO_2 Laser Epilog Mini 24	Epilog Laser, USA
Electric Convection Oven	Princess, Holland
FEI Technai G2 Spirit TEM microscope	Thermo Scientific™, USA
Gel Doc XR+ Molecular Imager system	Bio-Rad, USA

Hot press SKU: 1005002084935618	PrintSymbol, Portugal
ICP-AES with 40.68 MHz RF generator and AS500 auto-sampler	Horiba, Ultima, Palaiseau, France
Infinite M200 Microplate reader	Tecan, Switzerland
JEOL, 1200EX electron microscope	Jeol, USA
Malvern Zetasizer	Malvern Panalytical, UK
Nanodrop 2000 Spectrophotometer	Thermo Scientific™, USA
Nanoparticle Analyzer SZ-100	Horiba Scientific, Japan
Nikon Eclipse Ti-U inverted microscope	Nikon, Japan
Pentax K100D Digital SLR Camera	Pentax, Japan
pH meter Basic 20 with combined glass electrode 5209	Crison, Spain
Qi1Mc digital camera	Nikon, Japan
Rotor-Gene Q 5plex HRM Platform	Qiagen, Germany
Rotor-Gene RG3000	Corbett, Australia
Scanning Electronic Microscopy model SU3800	Hitachi Ltd, Japan
SDS-PAGE Mini-PROTEAN®3 System	Bio-Rad, USA
Semi Dry Blotter	Cleaver Scientific, UK
Sigma 1-14 Microfuge (SciQuip, UK)	Sigma-Aldrich, USA
Sigma 3-16K, Centrifuge	Sigma-Aldrich, USA
Thermal Cycler MyCycler	Bio-Rad, USA
Ultrasonic Cleaner S30H	Elma, Germany
UVmini 1240 spectrophotometer	Shimadzu, Germany

Vortex MS 3 Digital	IKA, Germany
VWR Digital Heat Block	VWR, USA
Wide Mini-Sub Cell GT electrophoresis cell	Bio-Rad, USA

2.1.5 Consumables

Table 2.5. List of consumables.

Name	**Company**
24-well plate (Cat. No. 30024)	SPL Life Sciences, South Korea
25cm^2 culture flasks	VWR, USA
96-wells plate (Cat. No. 30096)	SPL Life Sciences, South Korea
Amersham Hybond 0.45 µm PVDF membrane	Amersham™, UK
BIOFLOAT™ 96-wells plate	faCellitate, Germany
BRAND™ Four-Clear Sided Disposable Cuvettes	Thermo Scientific™, USA
Hyperfilm™ ECL™ film	GE Healthcare, Portugal
Insulin syringe needle U-100, Omnican®	Braun, Germany
Malvern Panalytical Folded Capillary Zeta Cell	Malvern Panalytical, UK
NAP-5 column	Cytiva, Germany
Pall Acrodisc™ 32 mm Syringe Filter with 0.2um Supor™ Membrane	Pall, USA
PTFE Teflon plates	Amazon, Germany
Transparent polystyrene thermoplastic sheets “Shrinky-Dinks	K&B Innovations, USA

2.2 Methods

2.2.1 Gold Nanoparticles Synthesis and Functionalization

2.2.1.1 Gold Nanoparticles Synthesis

Gold nanoparticles were synthesized via the citrate reduction method, as described by Lee and Meisel. Briefly, a solution of 1 mM Tetrachloroauric (III) acid was boiled until it reached reflux conditions and quickly mixed with a heated solution of 38.8 mM of sodium citrate (285mg) for a final volume of 250mL. Upon the addition of the sodium citrate, the solution turned to a deep red color, indicating the formation of gold nanoparticles. The solution was heated under constant stirring for 25 minutes and then left to cool to room temperature. Once cooled, the obtained colloidal gold solution was filtered with a 0.2μm filter membrane and then protected from light with aluminum foil. The nanoparticles were stored at room temperature until further use.

2.2.1.2 Gold Nanoparticles Functionalization with PEG

AuNPs were subsequently functionalized with thiol-modified polyethylene glycol (PEG) to attain 30% of surface coverage. PEG molecules are typically attached to nanoparticles to enhance their stability, improve biocompatibility, and provide functional groups for further functionalization steps. In the present case, the thiol-modified PEG was added to the particles for improved stability and biocompatibility. The protocol for PEG functionalization exploits the high affinity of gold to thiol groups, leading to the formation of quasi-valent bonds between the PEG molecules and the AuNP's surface. Briefly, 10nM of citrate-capped AuNPs were incubated with an aqueous solution of 0.028% (w/v) SDS and 0.003 mg/mL of PEG and ultrasound for 10 seconds and then incubated for a period of 16h under low agitation (487). The unbound PEG molecules were removed through two centrifugations of 45 min at 14,000xg and 4ºC. The functionalization efficiency was assessed with Ellman's assay. Other coverage percentages can be easily achieved by adjusting the amount of PEG added to the AuNPs.

2.2.1.3 Gold Nanoparticles Functionalization with ASOs

AuNPs@30%PEG were further functionalized with antisense thiolated oligonucleotides (5′-thiol-(CH2)6-ssDNA oligo-3') harboring a complementary sequence to the target of interest and 6 reversely complementary nucleotides (underlined) in each 3' and 5' terminals, to create the stem-loop structure. For the specific silencing of the *c-MYC* gene (NCBI Reference Sequence: NG_007161.2), the probe sequence 5′-thiol- GCG CCC ATT TCT TCC AGA TAT CCT CGC TGG GCG C-3′ was used [AuNPs@Myc]. Conversely, the sequence 5'-thiol- GCG CCC CGT ACT TCT CGA TGC GGG TGG

GGC GC-3' [AuNPs@copGFP] was used for silencing the *copGFP* gene. Additionally, a control probe, with a sequence without any target on the human genome, was also functionalized on the particles 5′-thiol-TT CGG GTT GAC GTT AGC CGG ATC TAC CGA AA-3′ [AuNPs@Scramble]. The thiol groups on ASOs molecules were reduced with 0.1 M of DTT, followed by subsequent purification using a desalting NAP-5 column, according to the manufacturer's instructions. The referred ASOs sequences were added to the AuNPs@30%PEG in a ratio of 1:150 (AuNPs: oligonucleotides) for AuNPs@c-MYC and AuNPs@Scramble and 1:100 to AuNPs@copGFP. After AuNPs' incubation with the purified oligonucleotides, the ionic strength of the solution was gradually increased. As such, the Au-nanoprobes were first incubated for 20 minutes with AGE I solution at a final concentration of 10 mM phosphate buffer (pH=8) and 0.01% (w/v) SDS. Secondly, AGE II was added in appropriate volumes to achieve a final concentration of 10 mM phosphate buffer (pH=8), 0.05 M NaCl, and 0.01% (w/v) SDS. Serial additions of AGE II were performed to attain final concentrations of 0.1, 0.2, and 0.3 M of NaCl. Upon each AGE addition, a step of 10 sec of ultrasounds and 20 min incubation under agitation were performed. After the final AGE II addition, the solution was incubated in the dark for 16h at room temperature under agitation. The excess of oligonucleotides was removed by two centrifugations of 1h at 15,500xg. The supernatants were recovered, and the amount of oligonucleotide was quantified using a NanoDrop. The number of ASOs bonded to the AuNPs' surface was determined by subtracting the number of ASOs present in the supernatants recovered from the NPs washes from the initial amount of ASOs incubated with NPs (488–490).

2.2.1.4 Gold Nanoparticles Characterization

All gold nanoparticles and nanoconjugates (AuNPs@Citrate, AuNPs@30%PEG, AuNPs@c-MYC, AuNPs@copGFP, and AuNP@Scramble) were analyzed by UV-visible (UV-vis) spectroscopy, Dynamic Light Scattering (DLS), zeta potential, Transmission Electron Microscopy (TEM) and gel electrophoresis. The UV-vis absorption spectra were obtained in the range of 400–800nm with 1cm path quartz Suprasil® cuvettes. Then, the colloidal gold concentration was determined using the absorption at 520nm and assuming a molar absorptivity for the plasmon resonance band maximum (520nm) of 2.33×10^{8} $M^{-1}cm^{-1}$. The hydrodynamic diameter of nanoparticles was obtained with DLS by performing 3 measurements of 30 seconds in 2mL disposable plastic cuvettes with four clear sides, using a scattering angle of 90º at 25ºC. Similarly, zeta potential measurements were obtained by performing 5 measurements of 30 seconds at 25ºC, using a Malvern Panalytical Folded Capillary Zeta Cell. The AuNPs formulations were diluted in milliQ water to a final concentration of 4 nM in 1.1mL prior to DLS and Zeta potential analysis. TEM measurements were performed in Switzerland by Dr. Eva Susnik, using a Tecnai Spirit Transmission electron microscope (491). The obtained TEM images were then used to calculate the core diameters and size distributions using ImageJ software (https://imagej.net/,

version 1.53a). For the migration analysis, 15µL of each gold formulation was mixed with 30% glycerol and then loaded into a 0.5% agarose gel. The electrophoresis was run for 40 minutes at 70mV. Finally, the stability of the Au-nanoconjugates in cell medium (DMEM) and different phosphate buffer concentrations and pH was also assessed by DLS and UV-vis spectroscopy.

2.2.2 Cell Culture

2.2.2.1 2D and 3D Cell Culture Maintenance

HCT-116 (ATCC® CCL-247™) tumor cell line purchase from American Type Culture Collection (ATCC®, USA) and MCF-7 constitutively expressing *copGFP* (MCF-7/copGFP) (Cat# AKR-211) purchased to Cell Biolabs (Cell Biolabs Inc, USA) were grown in Dulbecco's Modified Eagle Medium (DMEM) and supplemented with 10% (v/v) Fetal Bovine Serum (FBS) and 1% (v/v) Pen Strep. MCF-7/copGFP cells were also supplemented with 1% Minimum Essential Medium (MEM). Both cell lines were maintained in 25cm^2 culture flasks at 37°C in a 99% (v/v) humidified atmosphere of 5% (v/v) CO_2 (CO_2 Incubator. Cell passage was performed anytime cells reached 80% of confluency.

HCT-116 spheroids were prepared according to Baek et al. (492). Cells were seeded at a density of 5 × 10^3 cells per well in a super-low attachment U-shape 96-well culture plate and grown for 3 days.

2.2.2.2 Seeding Conditions for Plate-based Silencing Assays

For 2D-cell challenge assays, HCT-116 cells were seeded at a density of 1 × 10^5 cells per well in 24-well plates and incubated for 24h on a CO_2 Incubator to allow cell adherence. Conversely, for 3D-cell challenge assays, spheroids seeded at a density of 5 × 10^3 cells per well were used on the third day of growth. Before incubating the cells/spheroids with the nanoconjugates, the medium was removed from the wells and replaced by a solution with medium and the respective nanoconjugate in the referred concentrations. After the designated period of incubation, the supernatant was removed from the wells, and the cells were detached using TrypLE Express and further centrifuge for 5 min at 500xg (2D cells) or 5 min at 1,000xg (spheroids). The obtained pellet was either used for RNA/protein extraction or Inductively Coupled Plasma mass spectrometry (ICP-MS).

2.2.2.3 Seeding Conditions for Chip-based Silencing Assays

For cell seeding into the biochip, cells are detached from the 25cm^2 culture flasks using Triple Express and centrifuged at 500xg for 5 min. The pellet was resuspended in 1mL of DMEM medium, and the cells were counted using a hemacytometer. For on-chip 2D cell culture, each biochip's well was incubated with 1x10^4 cells, and for 3D cultures, the seeding was performed using 5x10^3 cells per well.

The biochips were then placed on a petri dish half-filled with distilled water at 37ºC in a CO_2 incubator. To promote spheroid formation, the biochips were placed in a circular shaker at 100xg for 1.5 hours. This process was repeated for the length of spheroid growth (3 days).

Before incubating the cells/spheroids with the Au-nanoconjugates, the medium was withdrawn from the reservoirs using an insulin needle, and then the respective concentration of each nanoconjugate was diluted in DMEM medium and infused back into the reservoirs of the biochip.

2.2.3 Cell Viability Assays

2.2.3.1 MTS Assay

To assess the cell viability of 2D cell cultures, either grown on plate-based or within the biochips, the MTS assay was used. Briefly, cells were seeded at a density of 1×10^4 cells/well (biochip and 96-wells plate) and allowed to grow for 24h. In the case of growth curves, cultures were also allowed to grow for longer periods. If challenged with Au-nanoconjugates, then the additional challenge time was also considered. Before exposing the cells to MTS reagents, the supernatant was completely removed from the wells/reservoirs. The MTS reagent was then diluted in culture media (1:5) and added to the cells. After 45 min of incubation in a CO_2 Incubator at 37°C, the supernatant was collected from each well in the biochip and placed on a 96-well plate, then the absorbance at 490nm was measured on a microplate reader. Controls were performed by incubating the MTS reagent with only DMEM medium and DMEM with the Au-nanoconjugates.

2.2.3.2 CellTox Assay

For the assessment of cell viability on spheroids, the CellTox™ Green cytotoxicity assay was performed, following the manufacturer's recommendations. Briefly, following spheroid incubation with the Au-nanoconjugates, the culture medium was removed and replaced by CellTox™ Green dye 1X prepared on DMEM medium, without phenol red, and incubated for 24h. Images of the spheroids were then acquired using the FITC filter (excitation at 480/30 nm and emission at 535/45 nm) with 800ms of exposure time. The CellTox Green dye enters cells with compromised membrane integrity and becomes fluorescent after binding to DNA. The fluorescent signal is proportional to the binding of the dye to the DNA of cells with compromised membranes; hence, it can be used to infer the cell viability (493,494). For 100% of cell death control, spheroids were fixated with 4% PFA solution in PBS; following the PFA addition, spheroids were incubated for 20 min at room temperature. The ImageJ software was used to measure the green fluorescence intensity (mean fluorescence x area) of the total spheroid by delimiting its periphery. The fluorescence intensity was normalized to the background's fluorescence

(of the corresponding image). The final cell viability was attained by normalizing the corrected fluorescence intensity of each condition to the 100% cell death control (spheroids fixated with PFA).

2.2.4 Gene Silencing Conditions

2.2.4.1 Challenge Conditions for Plate-based Cultures

Gene silencing assays were conducted by incubating cells, either in 2D or 3D configurations, with various concentrations of Au-nanoconjugates for different durations (challenge time). For simplicity, the Au-nanoconjugate concentrations mentioned here refer to the ASOs concentrations that cells were exposed to. Since the ASOs are functionalized on the AuNPs' surface, an equivalent concentration of gold was also introduced to the cells. However, this gold concentration was only considered for the AuNPs@30%PEG controls. In these controls, the amount of AuNPs added matched the gold concentration in the silencing conjugates (AuNPs@c-MYC, AuNPs@copGFP, and AuNPs@Scramble).

To assess the silencing effect of the Au-nanoconjugates on the *c-MYC* gene, HCT-116 cells were incubated with 3 different nanoconjugates: AuNPs@c-MYC, AuNPs@PEG, AuNPs@Scramble. The cells were exposed to different doses (20nM, 30nM, 33nM, 40nM, 54nM, 70nM and 88nM – concentration of ASOs, corresponding to 0.17nM, 0.25nM, 0.28nM, 0.34nM, 0.45nM, 0.59nM and 0.74nM of gold, respectively) and the incubation times (3h, 6h, 12h, 18h and 24h). Conversely, the silencing effect of *copGFP* was performed using the MCF-7/copGFP cell line. These cells were also exposed to different doses of nanoconjugates (20nM, 50nM, and 100nM – concentration of ASOs, corresponding to 0.13nM, 0.32nM, and 0.64nM, of gold, respectively) and the incubation times (6h and 24h). For both genes, an AuNPs@PEG control was performed simultaneously so that the concentration of gold matched the one used on AuNPs@copGFP [AuNPs@PEG], AuNPs@c-MYC [AuNPs@PEG M], or AuNPs@Scramble [AuNPs@PEG S]. All experiments (plate and biochip) also have a "Cells" or "Spheroids" control, where only DMEM medium was added to the wells.

2.2.4.2 Challenge Conditions for Chip-based Cultures

For the silencing assays on biochip, the cells, either 2D or 3D, were challenged for 6 hours using different gold nanoconjugates. HCT-116 cells were incubated with 54nM of AuNPs@c-MYC (corresponding to 0.38nM of gold), for specific silencing of the *c-MYC* oncogene, while MCF-7/copGFP cells were incubated with 20nM of AuNPs@copGFP (corresponding to 0.13nM of gold) for specific silencing of *copGFP* gene. Additionally, both cell types were incubated for 6 hours with AuNPs@PEG, matching the gold concentration to each of the silencing nanoconjugates, as a control.

All experiments (plate and biochip) also have a "Cells" or "Spheroids" control, where only DMEM medium was added to the wells.

2.2.5 Evaluate the Effect of the Challenging in RNA Expression

2.2.5.1 RNA Extraction Protocol

For plate-based cultures, the RNA from HCT-116 and MCF-7/copGFP 2D-cell cultures was performed using 2 wells (of 24-well plates) for each condition. Whereas, for the spheroid cultures, a total of 8 spheroids were used. For chip-based cultures, a total of 8 reservoirs were used per condition. For all culture systems, the supernatant was removed from the wells/reservoirs, and cells were detached from the plate/biochip using TrypLE™ Express Enzyme (1X), which was incubated for 5 min or 20 min at 37ºC for plate-based and biochip systems, respectively. The pellets were then centrifuged for 5 min at 500xg (2D cells) or 1,000xg (spheroids), and then RNA was extracted using NZYol reagent, following the manufacturer's specifications.

After extraction, the integrity of the RNA was assessed by electrophoresis in a 1% agarose gel, and the concentration of the RNA was quantified on NanoDrop.

2.2.5.2 RNA Expression Analysis (RT-qPCR)

2.2.5.2.1 *c-MYC* Expression Analysis

For *c-MYC* RT-qPCR, the RNA was diluted to 10ng/µL, from which 1µL was used as the template for the 1-step RT-qPCR reaction, using the One-step NZYSpeedy RT-qPCR Green kit. A 229-base pair (bp) fragment of the human *c-MYC* proto-oncogene (Ac. No. NM_002467) and a 215 bp fragment of the human *18S* N5 ribosomal RNA (Ac. No. NR_003286) were amplified using the primers listed in **Table 2.2**. The reaction mixture was prepared following the manufacturer's specifications, containing 400nM of each primer, 1X One-step NZYSpeedy qPCR Green master mix, 0.4µL of NZYRT mix, 10ng of RNA, and DEPC-treated water up to 10µL. The amplification was conducted using the following thermal conditions: 50ºC for 20 min (Reverse transcription step), 95ºC for 3 min (Denaturation step) followed by 40 cycles of 95ºC for 30 sec and 60ºC for 50 sec. The obtained PCR products were then analyzed in a 1.5% agarose gel electrophoresis stained with 1X GelRed.

2.2.5.2.2 *copGFP* Expression Analysis

For the amplification reaction of *copGFP*, complementary DNA (cDNA) was produced in a separate reaction, using 100ng of RNA and following the manufacturer's recommendations for the NZY M-Mulv First-Strand cDNA synthesis kit. The concentration of cDNA was quantified in a Nanodrop and diluted

for 100ng/µL, which was used as the template in the subsequent RT-qPCR amplification. The amplification reactions of *copGFP* and *18S* (intern control of gene expression) were performed using the NZYSupreme qPCR Green Master Mix, with the primers listed in **Table 2.2**. The reaction mixture was prepared following the manufacturer's specifications, containing 500nM (*copGFP*) or 600nM (*18S*) of each primer, 1X NZYSupreme qPCR Green Master Mix, 100ng of cDNA, and DEPC-treated water up to 10µL. The amplification was conducted using the following thermal conditions: 95ºC for 5 min (Denaturation step) followed by 40 cycles of 95ºC for 30 sec, 52ºC for 30 sec, 72ºC for 45 sec, and a final extension step of 7 min at 72ºC. The obtained PCR products were then analyzed in a 1.5% agarose gel electrophoresis stained with 1X GelRed.

2.2.5.3 Analysis of the Silencing Results

The silencing potential of the anti-c-MYC and anti-copGFP Au-nanoconjugates was assessed via the $2^{-\Delta\Delta CT}$ method. For each experience, both *c-MYC* or *copGFP* (target gene) and *18S* (reference gene) were amplified, and the respective Cycle Threshold (CT) values were acquired using the Corbett Rotor-Gene 6000 version 1.7 Software, setting a threshold of 0.0015. The delta CT (△CT) was calculated for each control (CT_{target}—CT_{18S}), and the delta delta CT (△△CT) was calculated by subtracting the △CT from the respective control (495). The results were analyzed using one-way ANOVA (Kruskal–Wallis test) and non-parametric t-test (Mann-Whitney test) with GraphPad Prism Version 8.0.1 (244) software. Bars on graphs represent the average result of at least 3 biological replicates with 3 technical replicates and error bars the respective Standard Error Mean (SEM) value or Standard Deviation.

2.2.6 Protein Expression Analysis

The silencing effect of the Au-nanoconjugates on protein expression was also assessed, either by Western-blot technique (HCT-116 plate-based culture systems) or Immunofluorescence staining for biochip cultures (HCT-116 and MCF-7/copGFP).

2.2.6.1 Western-blot

Proteins were extracted from HCT-116 cells, either seeded in a 24-well plate (2 wells per condition) or from spheroids (10 spheroids per condition). The 2D cells were detached with Triple Express, whereas the spheroids were simply recovered from the wells. The pellet was then washed with PBS 1X, resuspended in lysis buffer, and incubated overnight at -80ºC. Then, the whole-cell extracts were sonicated following a sequential increase in intensity: 10 pulses at 60% intensity (repeat 5 times), 15 pulses at 70% intensity (repeat 15 times), and 10 pulses at 80% intensity (repeat 10 times). Following the sonication, the extracts were centrifuged at 10,000xg for 5 min at 4ºC. The supernatant was

recovered, and protein concentration was determined using the Pierce 660nm Protein Assay Reagent, following the manufacturer's specifications. Then, 20µg of total protein extracts were incubated for 5 min at 70ºC with the SDS loading buffer and then separated by SDS-PAGE in a 5% acrylamide gel. The electrophoretic transfer was performed using the semi-dry transfer method for 1h at 120mA. The proteins were transferred onto a 0.45 µm PVDF membrane. Next, the blocking was performed for 2 h at room temperature with 5% (w/v) milk solution in TBST Buffer 1X. The incubation of membranes with antibodies was performed following the manufacturer's instructions: overnight incubation at 4ºC with the 1:1000 dilution of primary antibody against c-MYC, and 1h at room temperature for 1:500 dilution of anti-β-actin antibody. Membranes were washed with TBST and incubated with the appropriate secondary antibody (1:2000 of Anti-rabbit IgG for c-MYC and 1:3000 of Anti-mouse IgG for β-actin) conjugated with horseradish peroxidase. WesternBright ECL was applied to the membranes, and the signal was acquired in a dark room using a Hyperfilm™ ECL™ film, with 1 minute of exposure time for c-MYC protein and 15 seconds for β-actin.

2.2.6.2 Immunofluorescence

The silencing effect of the Au-nanoconjugates was also assessed at the c-MYC and copGFP protein levels via immunofluorescence microscopy. Following the challenge, cells were fixated either on the biochip or in a 24-well plate using a solution of 4% paraformaldehyde and incubated for 20 minutes at room temperature. Subsequently, cells were permeabilized with 0.1% (v/v) Triton X-100 solution for 10 minutes at room temperature. Next, the blocking step was performed with 1% (w/v) BSA in a PBST solution, incubated for 30 min at room temperature. For HCT-116 cells, the primary antibody [Rabbit anti-c-MYC antibody (1:100 dilution)] was incubated overnight at 4 ºC. After overnight incubation, cells were washed 3 times with PBST solution and then incubated with the respective secondary antibody [Anti-rabbit IgG (FITC) produced in goat (1:100 dilution)] for 1 hour at room temperature. The secondary antibody was washed 3 times with PBS 1X. Finally, both cell lines were stained with 7.5 µg/mL of Hoechst dye (for nucleolus staining) for 15 min at room temperature. Following the incubation with Hoechst dye, cells were washed 3 times with PBS 1X.

2.2.7 Microscopy Imaging

The fluorescence images were acquired with a Ti-U eclipse inverted microscope (Nikon, Tokyo, Japan) and respective software NIS Elements Basic software vs. 3, using the DAPI filter (excitation at 360/40nm and emission at 460/50nm) with 200ms of exposure time for Hoechst dye, and the FITC filter (excitation at 480/30 nm and emission at 535/45nm) with 2 sec of exposure time of FITC beacon. The FITC filter was also used to detect the fluorescence of CellTox Green dye in the spheroid's viability

assays (as described in previous sections). ImageJ software was used to obtain the CTCF values of each fluorescence channel (Green for c-MYC and copGFP proteins; Blue for Hoechst dye). The CTCF values were obtained using the formula: CTCF= Integrated Density – (Area of selected cell x Mean fluorescence of the background). The final fluorescence ratio was obtained by dividing each condition by its control.

Brightfield microscopy using a Ti-U Eclipse inverted microscope (Nikon, Tokyo, Japan) and respective software NIS Elements Basic software vs. 3.1 (Nikon, Tokyo, Japan) was used to assess the cell adhesion to the biochip.

Additionally, Scanning Electronic Microscopy (SEM) (model SU3800, Hitachi Ltd., Tokyo, Japan) was also performed on the biochips. For this, $1x10^4$ cells from HCT-116 and MCF-7/copGFP cell lines were seeded into the biochip and then placed on a CO_2 incubator at 37ºC for 24 hours. Following the cell fixation protocol, all the liquid content of the wells was removed. Then, the top two layers of the biochip were removed, and the biochip was sputtered with gold for 90 seconds at a pressure of 0.1 torr, using a current between 10 and 20 mA and a voltage of about 1kV under an argon environment. The images detected either the secondary electrons (SE mode) or backscattered electrons (BSE mode) under a high vacuum and with an accelerating voltage between 20kV and 30kV. For the non-conductive biochips (without gold sputter), only SE mode was used.

2.2.8 Biochip Fabrication

The biochips' patterns were defined on Inkscape vector image software (License: GNU GPLv2) and then engraved on transparent polystyrene thermoplastic sheets "Shrinky-Dinks" using a CO_2 laser machine, with 40W of power, 10.6 μm of wavelength and 0.254 m/s writing speed, at 1000 ppi (pulses per inch). The biochip is composed of 5 layers with 8 small chambers suitable for 8 independent experiments. The cuts were performed using the following laser specifications: cut specification (vector) – Laser power: 80%; Speed: 40%; and Frequency: 500 Hz.

The top layers (1 and 2) have 8 pairs of inlets/outlets with different sizes: a smaller one (⌀ 0.18cm) for medium and cell perfusion through an insulin syringe needle and a larger one (⌀ 0.52cm) for aeration. This top layer was reinforced (2) for stability and to prevent sinkholes. The middle layers (3 and 4) have 8 all-in-depth microchambers with a diameter of 1.80cm and 0.71cm, respectively. The bottom layer (5) works as a sealer and provides a surface for cell adhesion. Each layer is cut into thin, flexible polystyrene sheets in a rectangular shape with 12.91cm x 7.75cm (width x height). After patterning, each layer was aligned and placed between two slabs of Teflon. The assembled unshrunk layered sheets were thermally bonded on a hot press, with the temperature set at 110ºC (approximately the glassy transition

temperature of PS ~100ºC) for 100 seconds with the top layer facing down, followed by another 100 seconds with the top layer facing up. If necessary, an extra seal between the layers was performed by only pressing the edges for 60 seconds. After the thermal bonding, the biochips were placed for 4 minutes in an oven at 155°C over a Teflon plate. After shrinkage, the biochips were allowed to cool down at room temperature for 2 minutes. After this step, the biochip shrunk to around 60% of its original size, and its height increased around 6-fold. The biochip's final size is 5.08 x 3.11 x 0.83cm (w x l x h). Due to the increase in the depth of the biochip, each microchamber has a capacity of roughly 80µL. All the measurements were performed using an analogic caliper.

2.2.9 Biochip Preparation

Before cell seeding, biochips need to be sterilized and treated to improve or prevent cell adherence. For this, each microchamber was infused with ethanol 70% (v/v) and placed under UV light for 1 hour. Then, the ethanol was removed, the chambers were washed with mQ water, and the biochip was air-dried in a laminar flow chamber. Next, the microchambers are infused either with DMEM medium supplemented with 1% (v/v) antibiotic/antimycotic and 10% (v/v) Fetal Bovine Serum to improve cell adherence (2D cell cultures) or with BIOFLOAT™ FLEX coating solution to prevent cell adherence (3D cultures) and incubated for 24 h at 37ºC on a CO_2 incubator.

3

GENE SILENCING WITH ASOS-BASED SYSTEMS

Part of this chapter was originally published in the following paper:

- **Oliveira B.B**, Fernandes A.R, and Baptista P.V,. (2024). Assessing the gene silencing potential of AuNP-based approaches on conventional 2D cell culture versus 3D tumor spheroid. *Frontiers in Bioengineering and Biotechnology*. 12:1320729. doi: 10.3389/fbioe.2024.1320729

  In this work, I was responsible for synthesizing and functionalizing all nanoconjugates, as well as conducting experiments to characterize their stability and silencing efficiency. I performed the cell culture experiments, viability (MTS) assays, and challenges, following established group protocols. Additionally, I optimized and performed assays for gene expression (RT-qPCR) and protein expression (Western blot) analysis. I also carried out all data analysis and statistical evaluations.

3.1 Introduction

Nanoparticles exhibit exceptional physicochemical properties for delivery applications due to their small size and high surface-to-volume ratio, enabling one-to-one molecular interactions and extensive surface functionalization that can be tailored for targeting, stability, and therapeutic purposes (186,496,497).

Gold nanoparticles stand out in biomedical applications, including delivery and bioimaging, due to their biocompatibility, low toxicity, and versatile surface for grafting recognition elements, ligands, and biomolecules (497). The surface chemistry of AuNPs is critical for colloidal stability and, thus, uptake and therapeutic efficacy. In this regard, polyethylene glycol is the most used coating agent, offering enhanced stability, biocompatibility, reduced immune responses and minimizing the side effects of therapeutic molecules like drugs or nucleic acids (186,498,499).

In cancer therapy, AuNPs functionalized with antisense oligonucleotides show promise by stabilizing and improving the delivery of these gene-silencing agents, which can be tailored to inhibit oncogene expression (500,501), including *c-MYC*, a key tumorigenesis driver (502,503). The therapeutic benefits of *c-MYC* silencing have been highlighted by ongoing research and clinical trials, showing potential in suppressing tumor growth and proliferation, decreasing the metastatic potential of cells, and increasing their sensitivity to other therapies like radiation, chemotherapy, and targeted drugs (504–508). Pre-clinical studies have been exploiting several methods to achieve effective gene silencing, such as ASOs, RNAi technologies, and CRISPR-based systems (509–511).

ASOs strategies silence genes by forming RNA-DNA complexes that end up triggering RNA for degradation, inhibiting translation, or modifying the splicing patterns, effectively suppressing target mRNA and protein levels (512–515). However, challenges such as stability, targeted delivery, and immune effects limit their clinical success. Advances in nanotechnology aim to address these issues, offering refined delivery systems to aid ASOs-based therapies and pave the way for personalized and effective cancer treatments (516) (**Figure 3.1**).

In this chapter, an anti-c-MYC ASOs vectorization system based on gold nanoparticles is presented. The stability of the nanoconjugates in different conditions was thoughtfully investigated. Then, the silencing efficacy of the nanoconjugate was evaluated on mRNA and protein levels using an *in vitro* 2D model of colorectal carcinoma (HCT-116 cells).

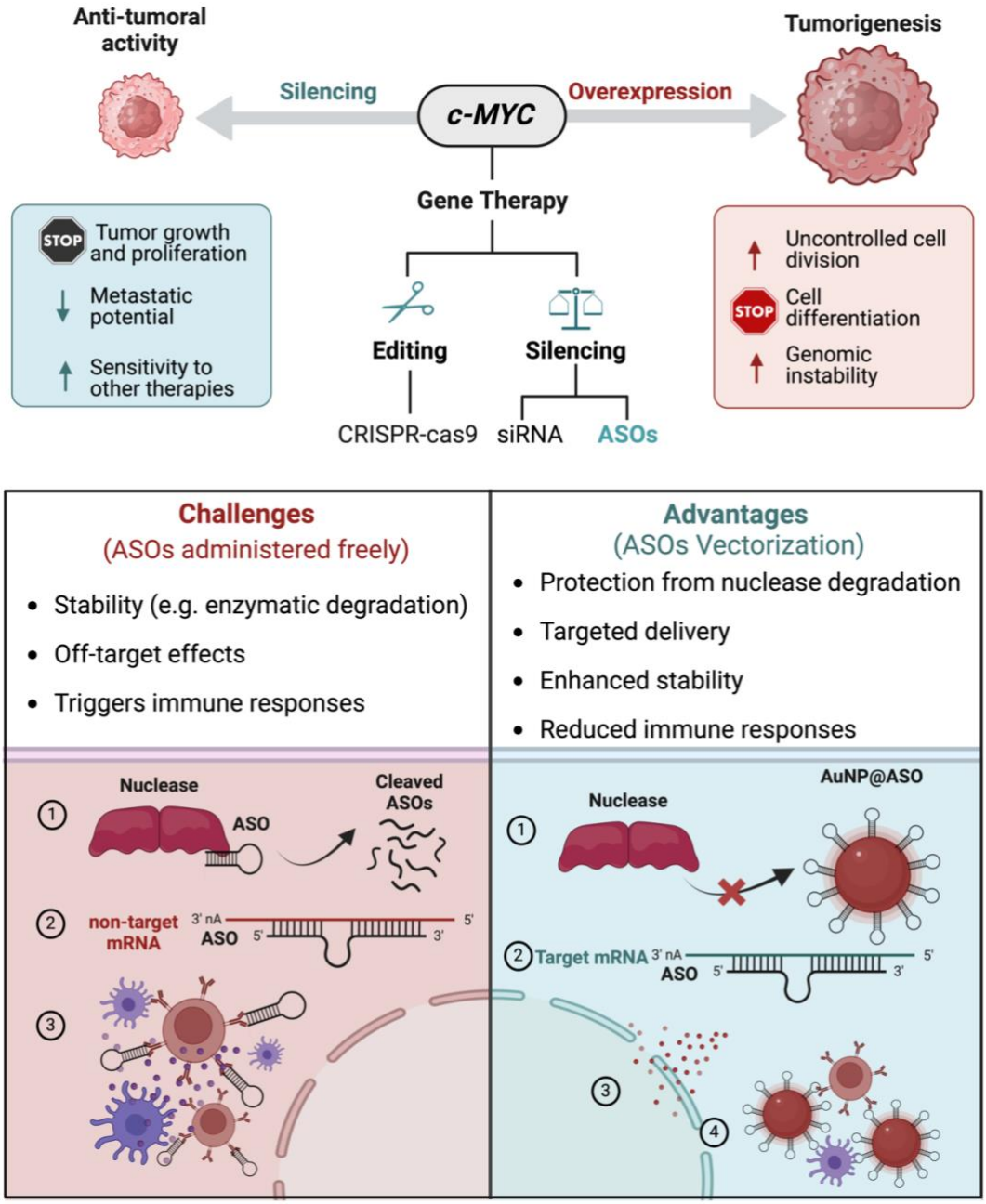

Figure 3.1. Importance of *c-MYC* downregulation in cancer cells and gene therapy systems undergoing research. Despite their therapeutic potential, there are several limitations regarding stability and efficient delivery. Nanotechnology offers several benefits by vectorizing these systems. Of relevance in this work is the functionalization of ASOs onto the AuNPs surface for enhanced stability and cellular uptake.

3.2 Methods

To improve the readability and comprehension of the present chapter, only the most relevant methods are detailed below. For more information regarding other methods and statistical analysis see Section **2.2.**

3.2.1 Gold Nanoparticles Synthesis and Functionalization

3.2.1.1 Gold Nanoparticles Synthesis

Gold nanoparticles with a diameter of ~12nm (±1) were synthesized via the citrate reduction method, as described by Lee and Meisel (517). Briefly, a solution of 1 mM Tetrachloroauric (III) acid was boiled until it reached reflux conditions and then quickly mixed with a heated solution of 38.8mM of sodium citrate (285mg) for a final volume of 250mL. Upon the addition of the sodium citrate, the solution turned to a deep red color, indicating the formation of gold nanoparticles. The solution was heated under constant stirring for 25 minutes, after which it was left to cool to room temperature. Once cooled, the obtained colloidal gold solution was filtered with a 0.2um filter membrane and then protected from light with aluminum foil. The nanoparticles were stored at room temperature until further use.

3.2.1.2 Gold Nanoparticles Functionalization with PEG

AuNPs were subsequently functionalized with thiol-modified polyethylene glycol (PEG) to attain 30% of surface coverage. PEG molecules are typically attached to nanoparticles to enhance their stability, improve biocompatibility, and provide functional groups for further functionalization steps. In the present case, the thiol-modified PEG was added to the particles for improved stability and biocompatibility. The protocol for PEG functionalization exploits the high affinity of gold to thiol groups, leading to the formation of quasi-valent bonds between the PEG molecules and the AuNP's surface. Briefly, 10nM of citrate-capped AuNPs were incubated with an aqueous solution of 0.028% (w/v) SDS and 0.003mg/mL of PEG, and ultrasound for 10 seconds and then incubated for a period of 16h under low agitation (518). The unbound PEG molecules were removed through two centrifugations of 45 min at 14,000xg and 4ºC. The functionalization efficiency was assessed with Ellman's assay. Other coverage percentages can be easily achieved by adjusting the amount of PEG added to the AuNPs.

3.2.1.3 Gold Nanoparticles Functionalization with ASOs

AuNPs@30%PEG were further functionalized with antisense thiolated oligonucleotides (5′-thiol-(CH2)6-ssDNA oligo-3') harboring a complementary sequence to the target of interest and 6 reversely complementary nucleotides (underlined) in each 3' and 5' terminals, to create the stem-loop structure. For the specific silencing of the *c-MYC* gene (NCBI Reference Sequence: NG_007161.2), the probe sequence 5′-thiol- GCG CCC ATT TCT TCC AGA TAT CCT CGC TGG GCG C-3′ was used [AuNPs@c-MYC]. Conversely, a control probe, with a sequence without any target on the human genome, was also functionalized on the particles 5′-thiol-TT CGG GTT GAC GTT AGC CGG ATC TAC CGA AA-3′ [AuNPs@Scramble]. The thiol groups on ASOs molecules were reduced with 0.1M

of DTT, followed by subsequent purification using a desalting NAP-5 column, according to the manufacturer's instructions. The referred ASOs sequences were added to the AuNPs@30%PEG in a ratio of 1:150 (AuNPs: oligonucleotides) for AuNPs@c-MYC and AuNPs@Scramble. After AuNPs' incubation with the purified oligonucleotides, the ionic strength of the solution was gradually increased. As such, the Au-nanoprobes were first incubated for 20 minutes with AGE I solution at a final concentration of 10mM phosphate buffer (pH=8) and 0.01% (w/v) SDS. Secondly, AGE II was added in appropriate volumes to achieve a final concentration of 10mM phosphate buffer (pH=8), 0.05M NaCl, and 0.01% (w/v) SDS. Serial additions of AGE II were performed to attain final concentrations of 0.1, 0.2, and 0.3M of NaCl. Upon each AGE addition, a step of 10 sec of ultrasounds and 20 min incubation under agitation were performed. After the final AGE II addition, the solution was incubated in the dark for 16h at room temperature under agitation. The excess of oligonucleotides was removed by two centrifugations of 1h at 15,500xg. The supernatants were recovered, and the amount of oligonucleotide was quantified using a NanoDrop. The number of ASOs bonded to the AuNPs' surface was determined by subtracting the number of ASOs present in the supernatants recovered from the NPs washes from the initial amount of ASOs incubated with NPs (490,519,520).

3.2.1.4 Gold Nanoparticles Characterization

All gold nanoparticles and nanoconjugates (AuNPs@Citrate, AuNPs@30%PEG, AuNPs@c-MYC, AuNPs@copGFP, and AuNPs@Scramble) were analyzed by UV-vis spectroscopy, DLS, zeta potential, TEM, and gel electrophoresis. The UV-vis absorption spectra were obtained in the range of 400–800nm with 1cm path quartz cuvettes. Then, the colloidal gold concentration was determined using the absorption at 520nm and assuming a molar absorptivity for the plasmon resonance band maximum (520nm) of 2.33×10^{8} $M^{-1}cm^{-1}$. The hydrodynamic diameter of nanoparticles was obtained with DLS by performing 3 measurements of 30 seconds in 2mL disposable plastic cuvettes with four clear sides, using a scattering angle of 90º at 25ºC. Similarly, zeta potential measurements were obtained by performing 5 measurements of 30 seconds at 25ºC. The AuNPs formulations were diluted in milliQ water to a final concentration of 4nM in 1.1mL prior to DLS and Zeta potential analysis. TEM measurements were performed by Dr. Eva Susnik at Dolphe Merkle Institute, University of Fribourg, Switzerland. The obtained TEM images were then used to calculate the core diameters and size distributions using ImageJ software. For the migration analysis, 15µL of each gold formulation was mixed with 30% glycerol (v/v) and then loaded into a 0.5% agarose gel. The electrophoresis was run for 40 minutes at 70mV. Finally, the stability of the Au-nanoconjugates in DMEM and different phosphate buffer concentrations and pH were also assessed by DLS and UV-vis spectroscopy.

3.2.1.5 Gold Nanoparticles Stability Assay

The stability of the Au-nanoconjugates was assessed by incubating 1nM of each nanoconjugate in different solutions: Milli-Q water, PBS 1X, DMEM, and DMEM + 10% FBS (medium used for cell cultures). Each nanoconjugate was incubated in 1mL of each solution for 0h or 24h at 37ºC, using the CO_2 incubator. Following the incubation period, UV-vis spectroscopy and DLS were performed. The data obtained from each technique was then treated and compared against standard controls (AuNPs in water – 0h).

3.2.2 Cell Culture

3.2.2.1 Seeding Conditions for Gene Silencing Assays

For cell challenge assays, HCT-116 cells were seeded at a density of 1×10^5 cells per well in 24-well plates and incubated for 24h on a CO_2 incubator to allow cell adherence. Before cell incubation with the nanoconjugates, the medium was removed from the wells and replaced by a solution with medium and the respective nanoconjugate in varied concentrations. Initial assessments were performed using ASOs concentrations ranging from 20nM to 70nM, corresponding to 0.17nM to 0.60nM of gold in the nanoconjugates, respectively. Later, the optimal concentration was set as 54nM. To simplify the reading, the concentrations referred to in the results section always report the concentration of ASOs, even for the nanoconjugate without ASOs (AuNPs@PEG). The concentration of AuNPs@PEG matched the concentration of gold present in AuNPs@c-MYC (AuNP@PEG M) or AuNPs@Scramble (AuNPs@PEG S) at the given concentration of ASOs used.

To optimize the challenge time, the nanoconjugates were incubated with the cells for varied periods: 3h, 6h, 12h, 18h, and 24h. The optimal challenge time was then defined at 6 hours of incubation. After the designated period of incubation, the supernatant was removed from the wells, and the cells were detached using TrypLE Express and further centrifuged for 5 min at 500xg. The obtained pellet was either used for RNA/protein extraction or Inductively Coupled Plasma mass spectrometry (ICP-MS). The detailed protocol for RNA extraction is detailed in *Section* **2.2.5.1.**

3.2.2.2 MTS Assay

The cytotoxicity of the Au-nanoconjugates was assessed with the MTS assay. Briefly, cells were seeded at a density of 1×10^4 cells/well (96-well plate) and allowed to grow for 24h. Then, cells were challenged with each of the Au-nanoconjugates in different concentrations (20nM, 30nM, 40nM, 54nM, and 70nM) for different periods (3h, 6h, 12h, 18h, and 24h). After the designated incubation period, the supernatant was completely removed from the wells. The MTS reagent was then diluted in culture media (1:5) and

added to the cells. After 45 min of incubation in a CO_2 incubator at 37°C, the absorbance at 490nm was measured on a microplate reader. Controls were performed by incubating the MTS reagent with only DMEM medium and DMEM with the Au-nanoconjugates.

3.2.3 Assess the Silencing Efficiency of the Au-nanoconjugates

3.2.3.1 *c-MYC* mRNA Expression Analysis

For *c-MYC* RT-qPCR, the RNA was diluted to 10ng/µL, from which 1µL was used as the template for the 1-step RT-qPCR reaction, using the One-step NZYSpeedy RT-qPCR Green kit. A 229-base pair (bp) fragment of the human *c-MYC* proto-oncogene (Ac. No. NM_002467) and a 215 bp fragment of the human *18S* N5 ribosomal RNA (Ac. No. NR_003286) were amplified using the primers listed in **Table 2.2** in Chapter 2. The reaction mixture was prepared following the manufacturer's specifications, containing 400nM of each primer, 1X One-step NZYSpeedy qPCR Green master mix, 0.4µL of NZYRT mix, 10ng of RNA, and DEPC-treated water up to 10µL. The amplification was conducted using the following thermal conditions: 50ºC for 20 min (Reverse transcription step), 95ºC for 3 min (Denaturation step) followed by 40 cycles of 95ºC for 30 sec and 60ºC for 50 sec. The obtained PCR products were then analyzed in a 1.5% agarose gel electrophoresis stained with 1X GelRed.

The silencing potential of the Au-nanoconjugates was assessed via the $2^{-\Delta\Delta CT}$ method and Relative change. Details are described in Chapter 2, section **2.2.5.3.**

3.2.3.2 c-MYC Protein Expression Analysis

Proteins were extracted from HCT-116 cells seeded in a 24-well plate (2 wells per condition). Cells were detached with Triple Express and centrifuged for 5 min at 500xg. The pellet was washed with PBS 1X, resuspended in lysis buffer, and incubated overnight at -80ºC. Then, the whole-cell extracts were sonicated following a sequential increase in intensity: 10 pulses at 60% intensity (repeat 5 times), 15 pulses at 70% intensity (repeat 15 times), and 10 pulses at 80% intensity (repeat 10 times). Following the sonication, the extracts were centrifuged at 10,000xg for 5 min at 4ºC. The supernatant was recovered, and protein concentration was determined using the Pierce 660nm Protein Assay Reagent, following the manufacturer's specifications. Then, 20µg of total protein extracts were incubated for 5 min at 70ºC with the SDS loading buffer and then separated by SDS-PAGE in a 5% acrylamide gel. The electrophoretic transfer was performed using the semi-dry transfer method for 1h at 120mA. The proteins were transferred onto a 0.45µm PVDF membrane. Next, the blocking was performed for 2h at room temperature with 5% (w/v) milk solution in TBST. The incubation of membranes with antibodies was performed following the manufacturer's instructions: overnight incubation at 4ºC with the 1:1000

dilution of primary antibody against c-MYC, and 1h at room temperature for 1:500 dilution of anti-β-actin antibody. Membranes were washed with TBST and incubated with the appropriate secondary antibody (1:2000 of Anti-rabbit IgG for c-MYC and 1:3000 of Anti-mouse IgG for β-actin) conjugated with horseradish peroxidase. Then, the WesternBright ECL was applied to the membranes, and the signal was acquired in a dark room using a Hyperfilm™ ECL™ film, with 1 minute of exposure time for c-MYC protein and 15 seconds for β-actin.

3.3 Results and Discussion

3.3.1 Au-nanoconjugates Characterization

The synthesized citrate-capped AuNPs were conjugated with PEG aiming for a surface coverage of 30% to provide increased biocompatibility and stability while allowing available surface for further conjugation with the desired ASOs (521–525). For the specific silencing of the *c-MYC* oncogene, a thiolated-ssDNA oligonucleotide harboring a sequence targeting a region of *c-MYC* was functionalized onto the AuNPs@30%PEG nanoconjugates, attaining a final functionalization of roughly 100 chains of oligo per particle (**Figure 3.2,** panel A). Additionally, a scramble (sequence without homology in the human genome) ssDNA oligonucleotide was used as the control for the specificity of the anti-c-MYC oligo. Each step of the conjugation was monitored by TEM, DLS, Zeta potential measurements, and UV-vis spectroscopy (**Figure 3.2**).

A

	AuNP@Citrate	AuNP@30%PEG	AuNP@c-MYC	AuNP@Scramble
Size ± SD(nm) TEM	12 ± 1	12 ± 1	12 ± 1	12 ± 1
Size ± PDI (nm) DLS	17.83 ± 0.18	20.74 ± 0.18	36.58 ± 0.16	34.28 ± 0.17
Zeta Potential ± SD (mV)	-49.1 ± 6.12	-52.7 ± 11.10	-48.0 ± 7.13	-55.8 ± 12.80
Functionalization (Nº molecules)		8.4E+5 ± 2.2E+3	113 ± 12	112 ± 14

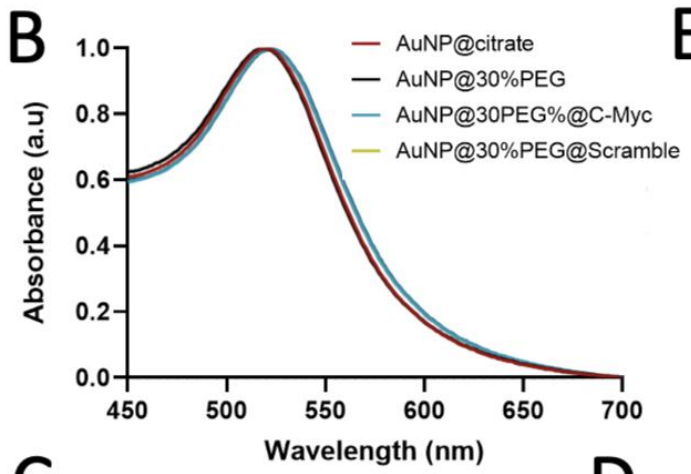

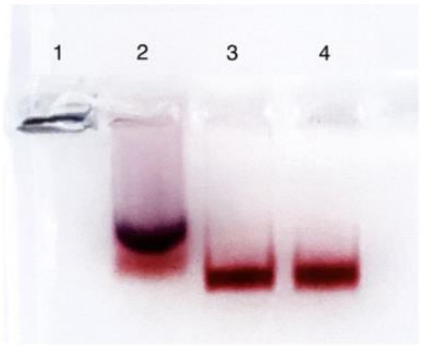

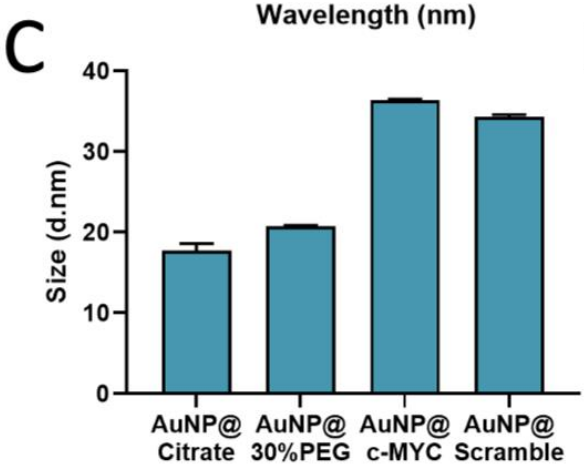

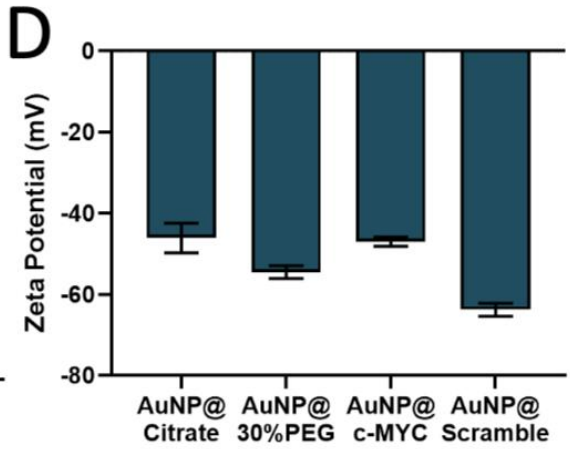

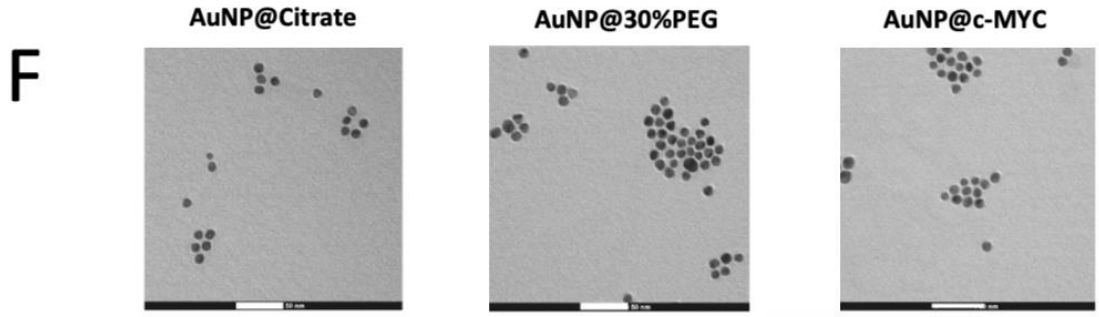

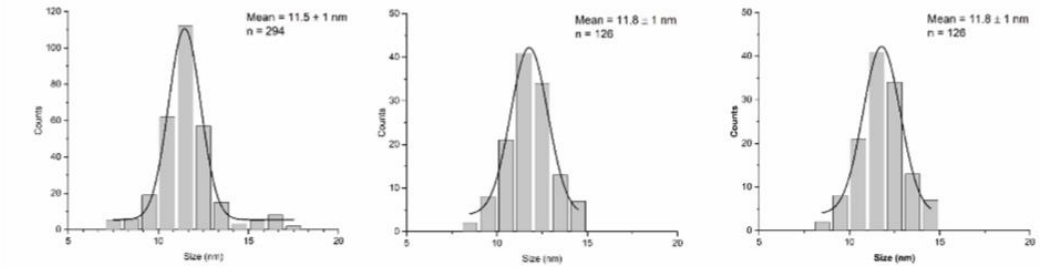

Figure 3.2. Characterization of Au-nanoconjugates by UV-Vis spectroscopy, DLS, and Zeta-potential. **(A)** Characterization data of all Au-oligonucleotide conjugates, regarding size by DLS and TEM, Zeta potential, and number of molecules functionalized in the particle's surface. **(B)** Normalized UV-vis spectroscopy results. All nanoconjugates have shown the maximum peak corresponding to the Surface Plasmon Resonance (SPR) peak at 520 ± 2nm. **(C)** Dynamic Light Scattering (DLS) results of different nanoconjugates. **(D)** Zeta potential results of different nanoconjugates. The error bars represent the standard deviation for 3 different batches of particles, each with 3 independent measurements. **(E)** Agarose gel electrophoresis of AuNPs**.** Electrophoresis was performed using a 0.5% agarose gel and run at 70mV for 40 minutes. Each lane contains 15uL of the respective AuNPs solution and 25uL of glycerol 30% (used as loading buffer). Legend: Lane 1. AuNPs@Citrate; Lane 2. AuNPs@30%PEG; Lane 3. AuNPs@c-MYC; Lane 4. AuNPs@Scramble. **(F)** Representative transmission electron microscopy (TEM) of AuNPs@Citrate, AuNPs@30%PEG, and AuNPs@c-MYC. **(G)** Corresponding histograms showing the size distributions determined from transmission electron micrographs.

Upon each step of functionalization, the SPR peak suffers a slight red-shift (**Figure 3.2,** panel B), associated with an increase in the size of Au-nanoconjugates, which was corroborated by the hydrodynamic diameter measured by DLS, which occurs due to an increase in the number of the molecules conjugated to their surface: AuNPs@Citrate (17.83 ± 0.18nm) < AuNPs@30%PEG (20.74 ± 0.18nm) < AuNPs@30%PEG@c-MYC (36.58 ± 0.16nm) ~ AuNPs@30%PEG@Scramble (34.28 ± 0.17nm) (526) (**Figure 3.2,** panel C). Additionally, the overall surface charge of the particles decreased when measured by Zeta potential. Given the negative nature of oligonucleotide chains, conferred by phosphate groups, this further suggests the binding of the oligonucleotides to the particles' surface (527) (**Figure 3.2,** panel D). Altogether, these results indicate modifications at the surface of the AuNPs, which can be associated with successful functionalization of the AuNPs with equivalent physical features. TEM measurements further support that surface functionalization is occurring, given that the core of the particles remained unchanged being around 12 ±1nm (**Figure 3.2,** panel F and G). These results were also corroborated via an agarose gel electrophoresis (527) (**Figure 3.2,** panel E). The different electrophoretic mobility indicates the presence of oligonucleotides on the AuNPs@c-MYC and AuNPs@Scramble nanoconjugates, noticeable by the higher migration toward the positive electrode. For AuNPs@30%PEG, migration was inferior since these nanoconjugates exhibit a more neutral surface charge (as shown by the Zeta potential measurements). Due to the ionic strength of the electrophoresis buffer, AuNPs@Citrate particles aggregated immediately. These large aggregates could not penetrate the agarose matrix and were retained in the well, which further underscores the importance of surface functionalization for improved stability (528).

The stability of nanoformulations is crucial for enhanced cell penetration and efficient ASOs delivery. All the nanoconjugates show a strong surface charge (-50 to -68mV), which has been reported as a good indicator of the stability of the colloidal solution (**Figure 3.2,** panel D) (529,530).

However, AuNPs are extremely sensitive to their chemical environment, and several parameters can affect their stability. For instance, certain pH ranges and ionic strengths can alter their surface charge, leading to reduced electrostatic repulsion and, therefore, increased aggregation (531,532). This change is often accompanied by a shift in color from red (stable AuNPs) to blue/ purple (aggregation) due to an increase in the particles' size. Additionally, proteins and biomolecules can adsorb onto the surface of AuNPs, causing either stabilization (steric hindrance) or aggregation (bridging flocculation), which can change the size or color of the colloidal solution, depending on the nature of the interaction (532–534). Given the chemical complexity of culture media and cellular microenvironment, stability studies of each nanoconjugate in different solutions were performed to further assess this matter (**Figure 3.3** and **Figure 3.4**).

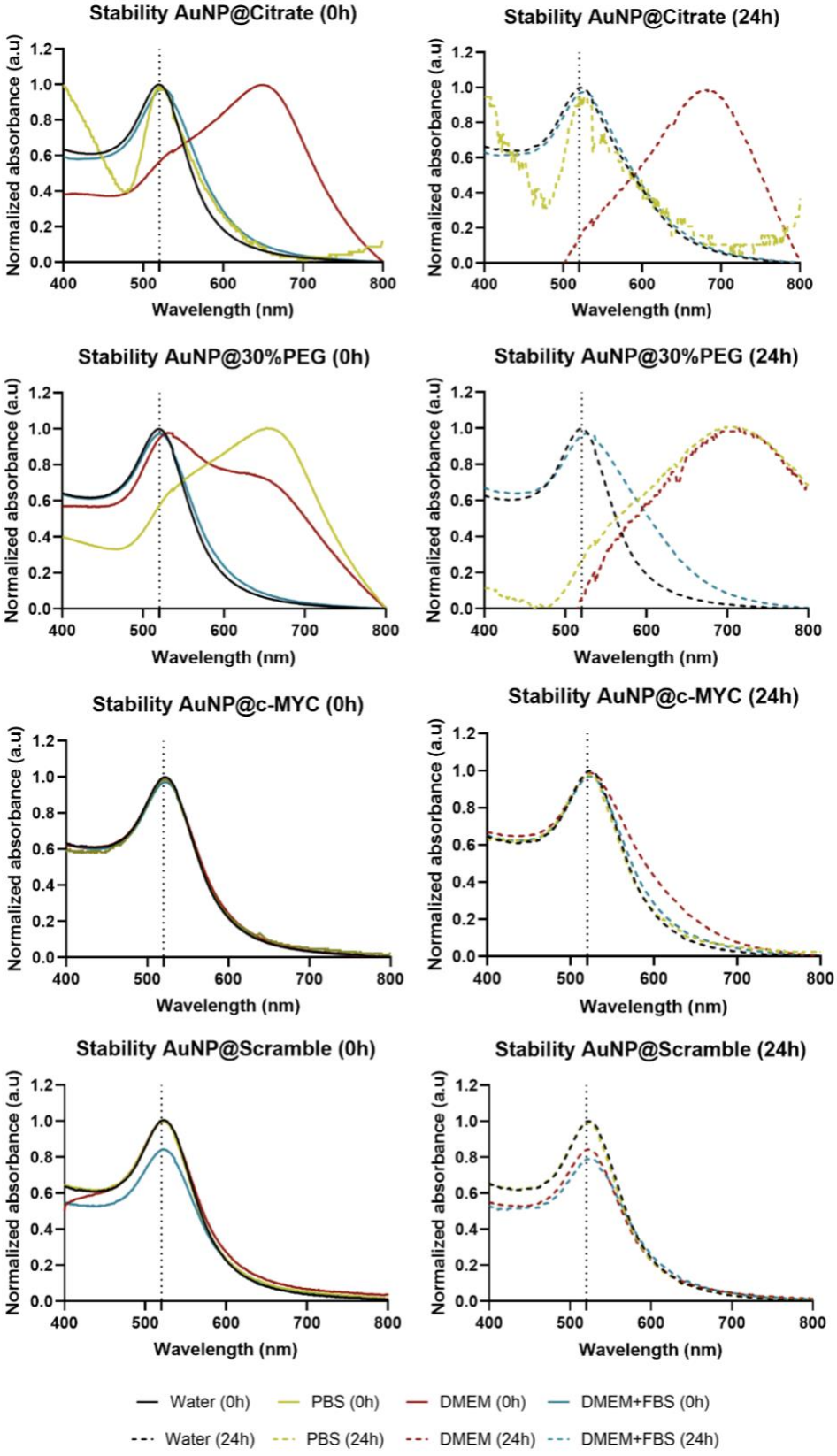

Figure 3.3. Stability of Au-nanoconjugates obtained by UV-vis spectroscopy upon incubation for 24h at 37ºC in different solutions.

Water (–), PBS1X (–), DMEM medium (–), and DMEM+10%FBS, before (full line) and after incubation (dotted line) at 37ºC for 24h. All the graphs show a dotted line at X=520, the typical value of the SPR band for spherical AuNPs.

The results showed that nanoconjugates with increased surface functionalization, such as AuNPs@c-MYC and AuNPss@Scramble, exhibited higher stability to changes in the surrounding chemical environment. The size of these nanoconjugates remained consistent, showing minimal alterations upon incubation with solutions of higher ionic strength (PBS 1X) and various chemical compositions (DMEM and DMEM+10% FBS) (**Figure 3.3** and **Figure 3.4**). This stability is due to their fully occupied surfaces, which thwart charge destabilization and prevent further interactions with other proteins and biomolecules. In contrast, AuNPs@30%PEG, with only 30% of the surface covered by PEG, still has room for new interactions, leading to a size increase when incubated with protein-rich solutions like DMEM and DMEM+10% FBS (**Figure 3.4**). Without stabilizing molecules (*e.g.*, PBS 1X), the disruption in surface charge leads to aggregation. A similar effect occurs with AuNPs@Citrate, which rapidly aggregates when dispersed in solutions with high salt content (*e.g.,* PBS 1X) and few stabilizing molecules (*e.g.,* DMEM). These data underscore the importance of surface coverage with both PEG for stabilization and biocompatibility and ASOs for maintaining good colloidal stability in various chemical environments (535,536).

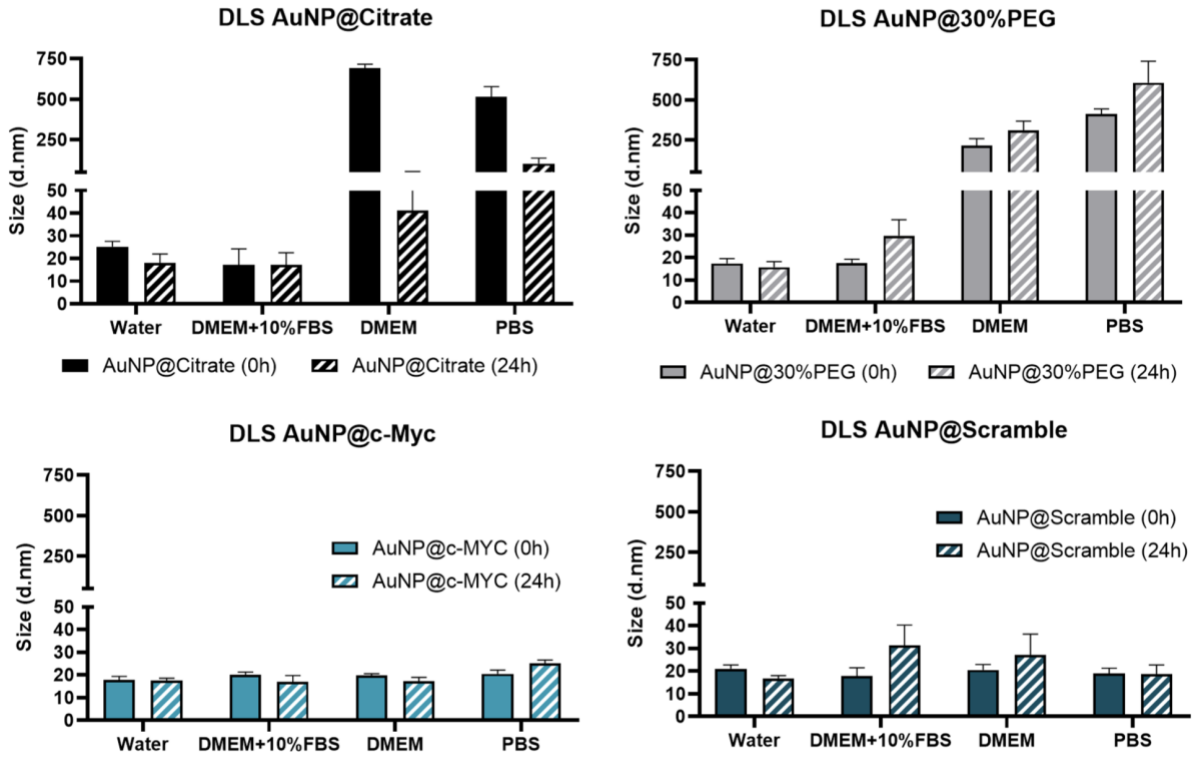

Figure 3.4. Hydrodynamic size of each nanoconjugate.
DLS results were obtained before (full bars) and after (stripped bars) incubation with different solutions. The bars are the average result of 3 measurements and the error bars de corresponding Standard Error Mean (SEM).

After confirming the stability of the developed nanoconjugates in the most suitable cell culture media (DMEM+10% FBS), the next steps focused on evaluating the silencing potential of the anti-c-MYC nanoconjugate.

3.3.2 *c-MYC* Gene Silencing in 2D Cell Models

The silencing potential of the gold nanoformulations was firstly assessed in a 2D colorectal cell model (HCT-116) by challenging cells for 6 hours with different concentrations of the anti-c-MYC ASO, ranging between 20nM to 70nM, corresponding to 0.17nM to 0.60nM of gold nanoconjugates, respectively. This range aligns with literature on gene silencing strategies using ASOs and siRNA, which commonly report interfering oligonucleotide concentrations between 20nM and 200nM (514,524,537,538).

All the concentrations of AuNPs@c-MYC show a silencing effect on the *c-MYC* gene when analyzed by the $2^{-\triangle\triangle CT}$ method (**Figure 3.5,** panel A) (539). The optimal concentration of the Au-oligonucleotide conjugate should result in a silencing effect with AuNPs@c-MYC ($2^{-\triangle\triangle CT} < 1$), while controls exhibit

no impact on the cells ($2^{-\Delta\Delta CT}$ >= 1). This criterion helped determine the most effective concentration of the Au-nanoconjugate for this model. The decrease in expression of the *c-MYC* gene is highlighted by the relative change shown in the heatmap (**Figure 3.5,** panel B).

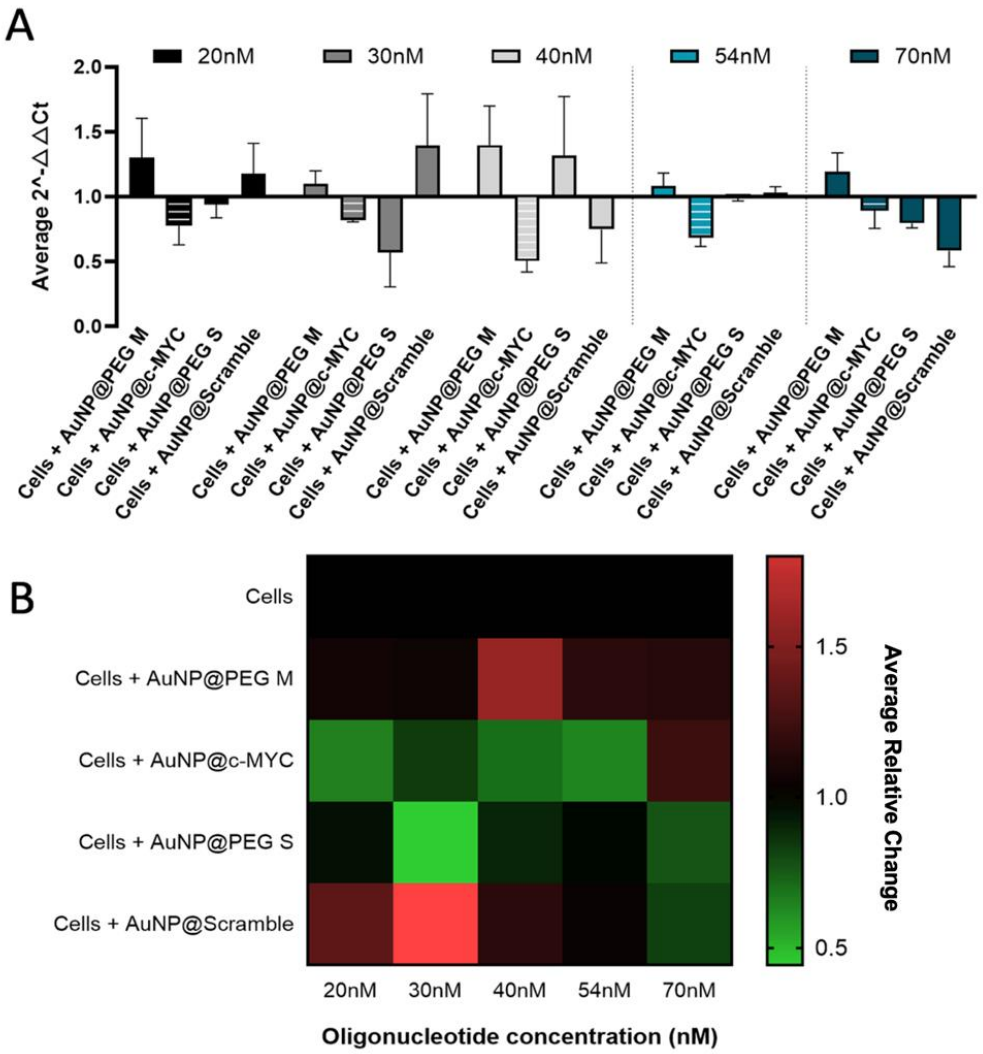

Figure 3.5. 2-ΔΔCT and Relative Change results of *c-MYC* silencing using concentrations of anti-c-MYC oligonucleotide ranging between 20nM to 70nM for 6 hours of incubation.
(A) Average $2^{-\Delta\Delta CT}$ results of *c-MYC* silencing. Full bars represent the experiment controls for cells incubated with (medium only, AuNPs@30%PEG M/ S and AuNPs@Scramble), while striped bars represent the result for the cells challenged with AuNPs@c-MYC ASO. Cells were incubated with the respective AuNPs-oligo at a concentration of 20nM (■), 30nM (■), 40nM (■), 54nM (■), and 70nM (■). Bars are the result of 3 independent biological replicates, and the error bars are the respective Standard deviation. **(B)** Average relative change results of *c-MYC* silencing. Each line represents the different AuNPs-oligo controls, and the columns show the concentration at which each ASO was incubated in the cells. Relative change results between 0.5 and 1 (gene silencing) are represented by green tones (from brighter to darker shades), relative change values equal to 1 are represented in black, and values between 1 and 1.8 (gene overexpression) are represented in red tones (from darker to brighter). Relative change values are the average result of 3 independent biological replicates.

The results imply no correlation between the concentration of the Au-oligonucleotide conjugate and the resulting gene silencing. This lack of correlation may be attributed to several factors, including the turnover time of mRNA molecules and the concentration dependence of cellular uptake and intracellular trafficking mechanisms. The last can lead to variations in the distribution of nanoconjugates within the cell, potentially resulting in different localization patterns that do not necessarily enhance interaction with the target mRNA molecule (540–542). Furthermore, the intracellular processing mechanisms of Au-nanoconjugates may not scale linearly with the dose. Additionally, the nanoparticles could influence the regulatory networks of genes associated with cell proliferation and growth (*e.g., c-MYC*) (543,544).

Considering the aforementioned information, the most promising silencing conditions were observed with 20nM and 54nM of oligo, achieving 21% and 28% of *c-MYC* silencing, respectively. However, a stronger off-target effect was noted in the controls (AuNPs@PEG and AuNPs@Scramble) corresponding to the 20nM nanoconjugate (**Figure 3.5**). Consequently, 54nM was chosen for subsequent studies (514).

Next, the cytotoxicity of these Au-nanoformulations was assessed by MTS assay (**Figure 3.6**). The results show no cytotoxicity for the range of concentrations used (0.17nM, 0.25nM, 0.34nM, 0.45nM, and 0.59nM of gold, corresponding to the oligo concentrations reported before). This is in line with the available information regarding the biocompatibility and absence of acute toxic effects of AuNPs with sizes between 10 and 60nm, either using *in vitro* or *in vivo* models (545–554). Nevertheless, it is important to note that the cytotoxicity effects of AuNPs depend on size, shape, coating agents, dose used as well as the number of cells exposed at a given concentration, which are not always reported (555,556).

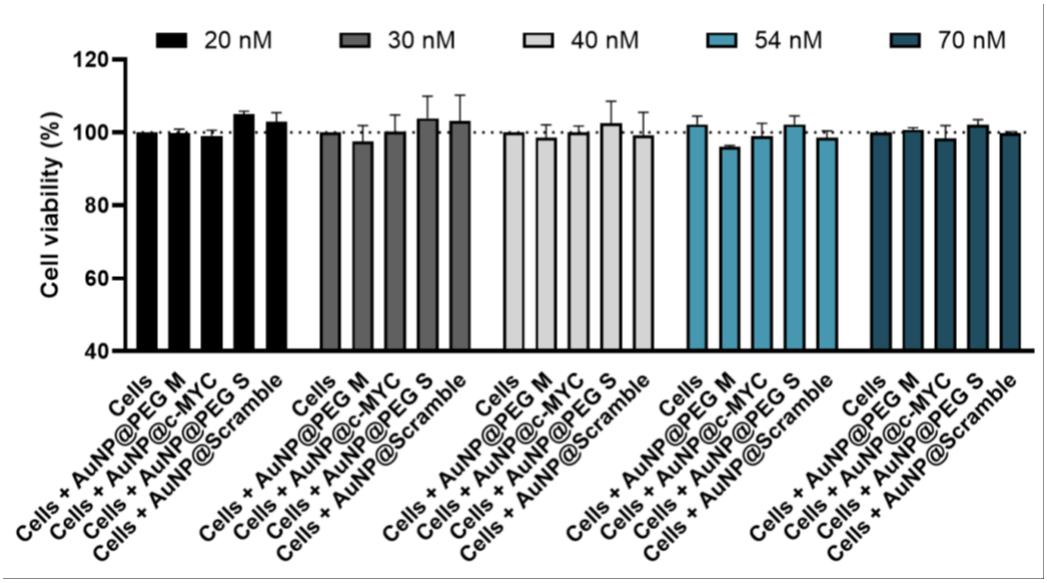

Figure 3.6. MTS assay results after 6 hours of challenge with each nanoconjugate.
Bars represent the normalized cell viability to the "Cells" control for the incubation with Au-oligonucleotide conjugate at a concentration of 20nM (■), 30nM (■), 40nM (■), 54nM (■), and 70nM (■). Bars are the result of 3 independent biological replicates with 2 technical replicates, and the error bars are the respective standard deviation.

Taking the concentration of 54nM, exposure time profiles were performed for 3, 6, 12, 18, and 24 hours (**Figure 3.7**). Data show a pronounced *c-MYC* downregulation when cells are exposed to 54nM of AuNPs@c-MYC for 6 and 12 hours, attaining a silencing effect of 33% and 23%, respectively. Besides, for these time points, the controls (AuNPs@PEG and AuNPs@Scramble) do not have a significant effect on the *c-MYC* expression.

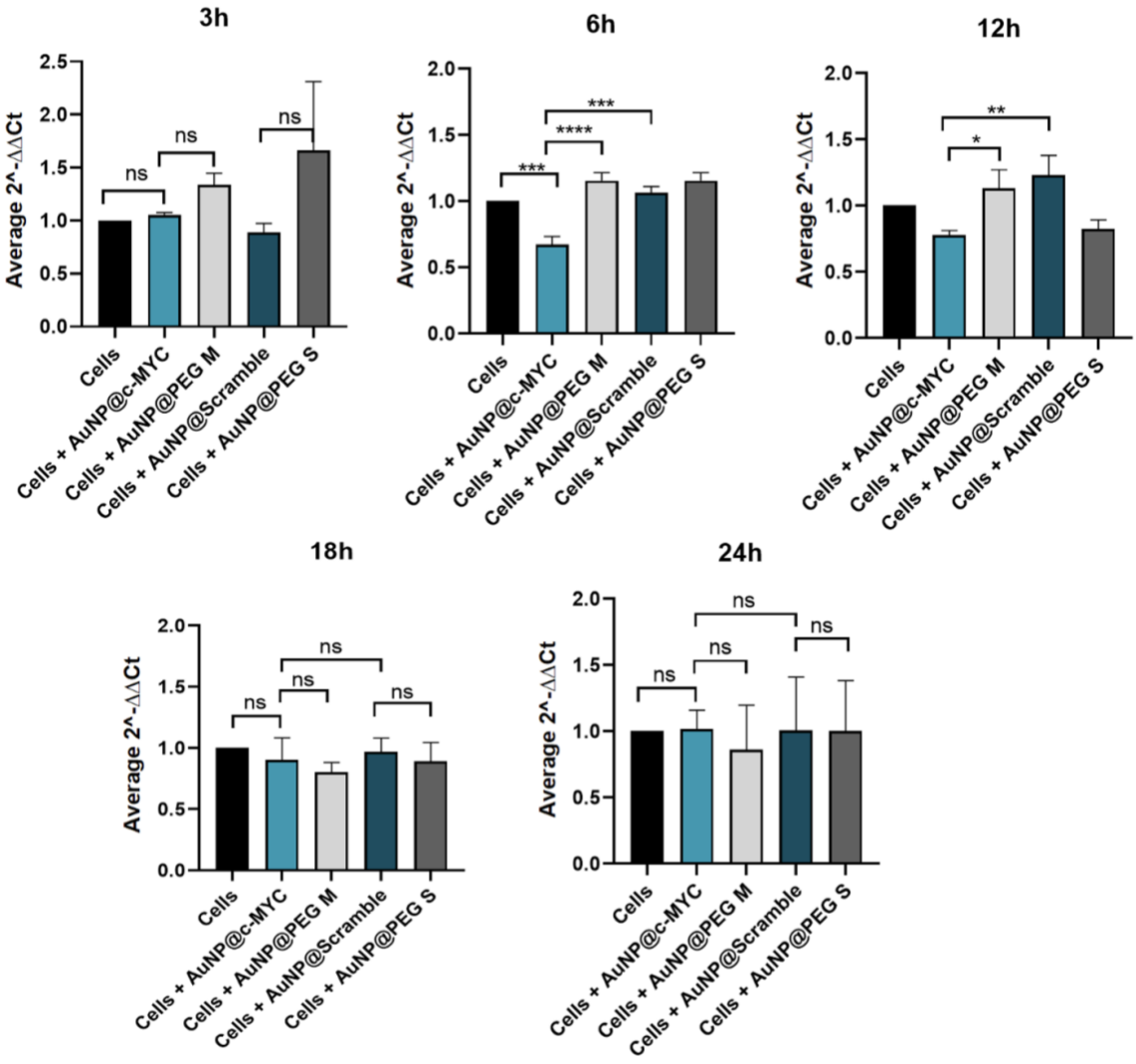

Figure 3.7. 2-△△CT results of *c-MYC* silencing for 3, 6, 12, 18, and 24 hours with Au-nanoconjugates incubation with cells, using 54nM of concentration.
Full bars represent the average result of 3 biological replicates, for the cells with the incubation with only medium (■), AuNP@c-MYC (■), AuNP@PEG M (■), AuNP@Scramble (■) and AuNP@PEG S (■) for either 3h, 6h, 12h, 18h and 24h. Error bars represent the Standard Error Mean. Statistical analysis was performed using One-way ANOVA and the Mann-Whitney test, Results were considered statistically significant for p values < 0.05. (*) represents $p \leq 0.0323$, (**) represents $p \leq 0.0021$, (***) represents $p \leq 0.0002$ and (****) represents $p < 0.0001$.

Once more, the cellular viability after incubation with 54nM of Au-nanoconjugates was assessed across different incubation periods (**Figure 3.8**). The results indicate no significant effect on cell viability between 3 and 12 hours of exposure (557). However, at 18 hours, a slight increase in cell viability was observed, potentially linked to elevated mitochondrial activity resulting from cellular stress responses or due to the cell duplication rate (558). By 24 hours, a decrease in cell viability is evident, suggesting that prolonged exposure to the nanoconjugates may induce cytotoxic effects (547,553).

The MTS assay, a standard method for assessing cell viability in 2D cultures, relies on the mitochondrial reduction of tetrazolium into formazan, assuming metabolic activity directly correlates with viability (559,560). However, this can lead to inaccuracies, as compounds affecting mitochondria without causing cell death may skew results, and cytotoxic agents that do not impair mitochondrial function might be overlooked (559,560). To improve reliability, combining MTS with direct assays like Trypan Blue or alternative methods such as LDH release, flow cytometry, or immunofluorescence is recommended (561–564).

In this work, the focus was on advancing the proposed gene silencing system to more complex cancer models, where many of the aforementioned assays are not compatible. Thus, the MTS assay was chosen for its compatibility and ease of comparison with the viability method further used in 3D-cell models.

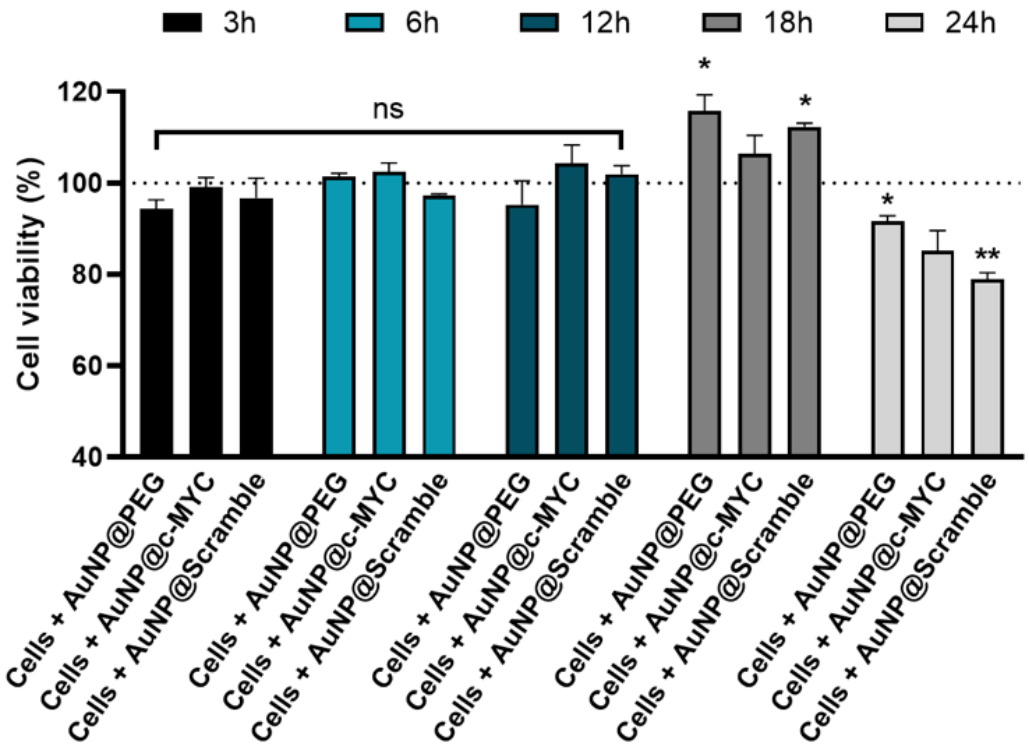

Figure 3.8. MTS assay results for cell incubation with 54nM of Au-nanoconjugates after 3, 6, 12, 18, and 24 hours of challenge.
Bars represent the normalized cell viability to the "Cells" control for the incubation with each Au-oligonucleotide conjugate after an incubation period of 3h (■), 6h (■), 12h (■), 18h (■), and 24 h (■). Bars are the result of 3 independent biological replicates with 2 technical replicates, and the error bars are the respective Standard deviation. Statistical analysis was performed to assess cell viability differences in relation to "Cells control" represented by the dotted line at 100%, using One-way ANOVA; the results were considered statistically significant for p values < 0.05. (*) represents $p \leq 0.0323$, (**) represents $p \leq 0.0021$.

3.3.3 c-MYC Protein Silencing in 2D Cell Models

Considering these initial calibration studies, the best incubation condition was set for 6h with 54nM of AuNPs@c-MYC for a 37% silencing of the *c-MYC* oncogene. Several biological and technical replicates were performed to assess the robustness of the chosen condition (**Figure 3.9**) (565–568). The results pointed to efficient and reproducible *c-MYC* silencing across all replicates (**Figure 3.9,** panel C).

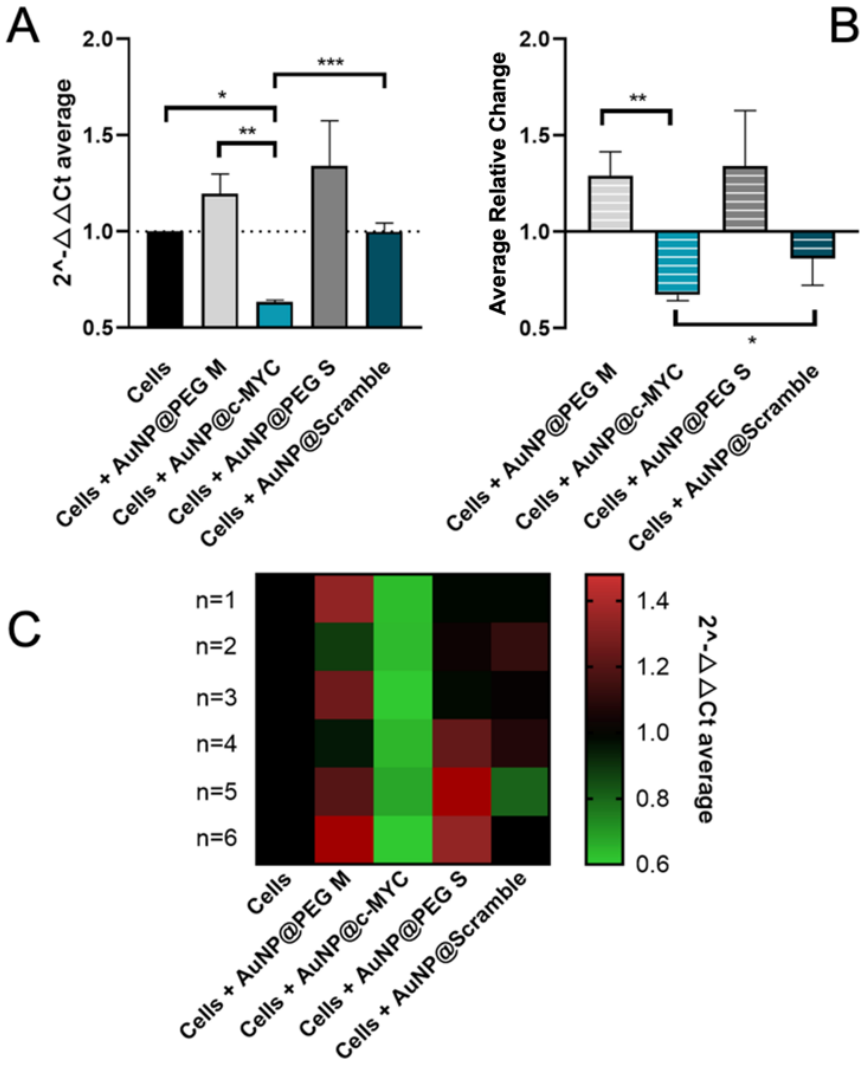

Figure 3.9. *c-MYC* silencing using 54nM of Au-nanoconjugates for 6 hours of challenge time.
(A) Average $2^{-\Delta\Delta CT}$ results and **(B)** Average relative change of *c-MYC* silencing. Full bars represent the $2^{-\Delta\Delta CT}$ and striped bars the relative change for each condition control: (■) cells incubated with medium only, (■) AuNPs@30%PEG M, (■) AuNPs@c-MYC, (■) AuNPs@PEG S and (■) AuNPs@Scramble. Bars are the result of 6 independent biological replicates, and the error bars are the respective Standard Error Mean. **(C)** Heat-map representation of the average $2^{-\Delta\Delta CT}$ results of *c-MYC* silencing. Each column represents the different Au-oligonucleotide conjugate controls, and the lines represent the results of each biological replicate. $2^{-\Delta\Delta CT}$ values between 0.6 and 1 (gene silencing) are represented by green tones (from brighter to darker shades), $2^{-\Delta\Delta CT}$ values

equal to 1 are represented in black, and values between 1 and 1.5 (gene overexpression) are represented in red tones (from darker to brighter). Statistical analysis was performed using One-way ANOVA and the Mann-Whitney test, Results were considered statistically significant for p values < 0.05. (*) represents $p \leq 0.0323$, (**) represents $p \leq 0.0021$ and (***) represents $p \leq 0.0002$.

Next, the silencing effect with the chosen conditions was also studied at the protein level (**Figure 3.10**). The results show that the silencing effect occurs not only at the mRNA level, but it also translates into the protein level, causing a 43% decrease in the c-MYC protein expression. Studies have already reported on the decreased expression of MYC protein upon the mRNA silencing with ASOs-based therapeutics (515,569). However, the final silencing activity might be influenced by the different uptake dynamics due to cell proliferation rate, mRNA target site, and ASOs modifications (570). As such, a deeper analysis of the silencing profiles in more complex cell models, such as 3D-tumor spheroids, might help to better elucidate this matter.

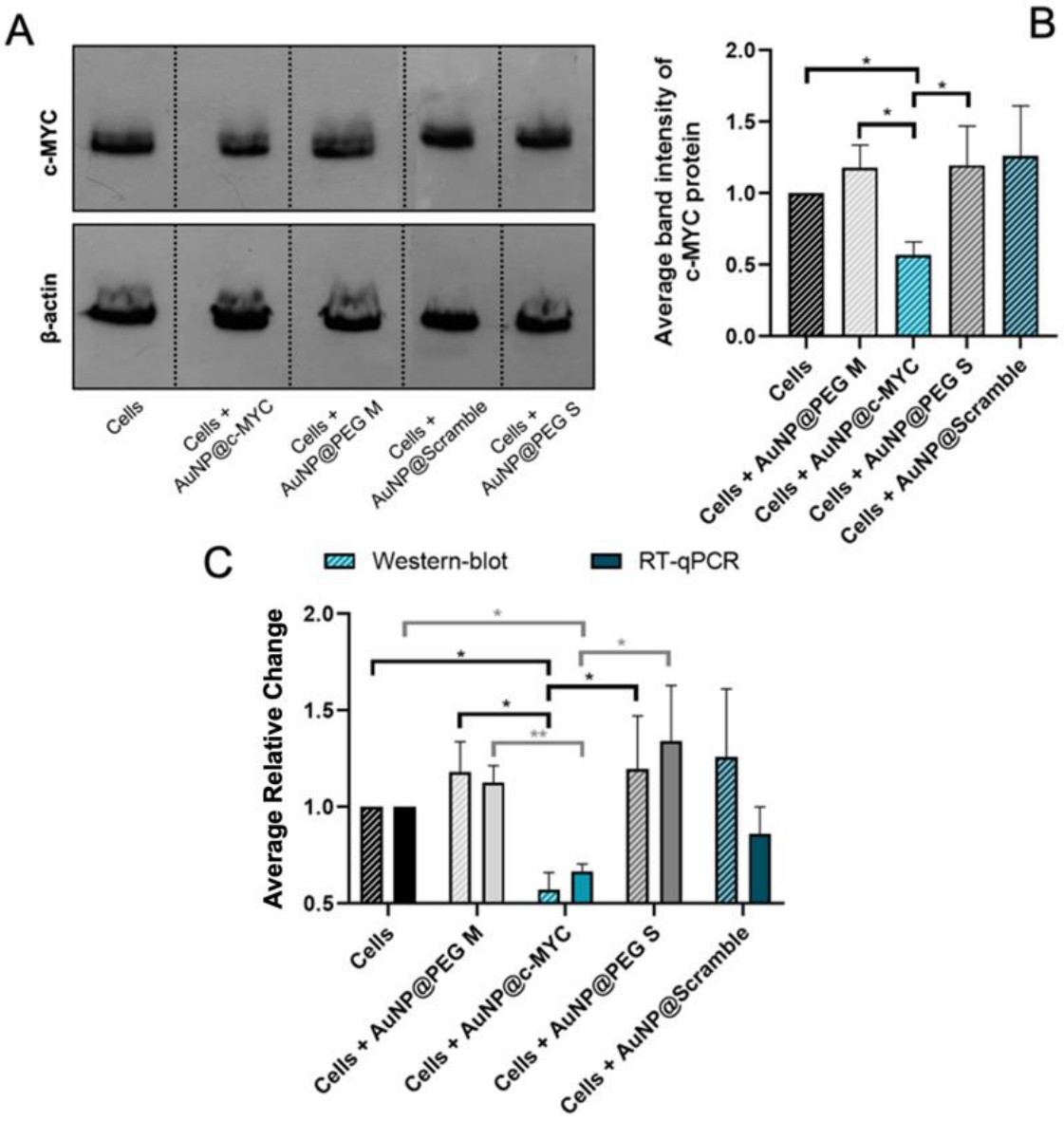

Figure 3.10. *c-MYC* silencing at the protein level using 54nM of Au-nanoconjugates for 6 hours of challenge time. **(A)** Representative image of a Western-blot membrane for the detection of c-MYC (top line) and β-ACTIN (bottom line) proteins after incubation with the respective Au-oligonucleotide conjugates using the previously optimized conditions. **(B)** Average results for the band intensity obtained for c-MYC protein (normalized to the respective β-Actin control) in 3 independent Western-blot experiments. **(C)** Average relative change results of *c-MYC* silencing obtained on mRNA level by RT-qPCR and protein level by Western-blot. Striped bars represent the results of Western-blot and full bars the results of RT-qPCR, for each experiment control: (■) cells incubated with medium only, (■) AuNPs@30%PEG M, (■) AuNP@c-MYC, (■) AuNPs@PEG S and (■) AuNPs@Scramble. Bars are the result of at least 3 independent biological replicates, and the error bars are the respective Standard Error Mean. Statistical analysis was performed using One-way ANOVA and the Mann-Whitney test, Results were considered statistically significant for p values < 0.05. (*) represents $p \leq 0.0323$ and (**) represents $p \leq 0.0021$.

3.4 Conclusions

This chapter presented the development of a vectorization system for an antisense oligonucleotide targeting *c-MYC*, a key oncogene implicated in multiple cancers (503,571,572). The Au-nanoprobe demonstrated good colloidal stability for 24 hours in various environments, ensuring its suitability as a delivery vehicle. Among the tested conditions (20–200nM oligonucleotides from 3-24h of incubation), the developed nanoconjugate achieved a 37% reduction in *c-MYC* mRNA, with corresponding protein suppression, aligning with the reported silencing efficiencies for similar systems (573). The controls showed no significant impact, confirming the specificity of the system.

Overall, the treatment did not induce notable cytotoxicity, as validated by viability assays, further supporting its potential for therapeutic applications. Effective *c-MYC* silencing is crucial, as its overexpression drives tumorigenesis, promoting proliferation and treatment-resistant cancers (571,572). While a 40–80% reduction is typically required for therapeutic impact (567,568), the results achieved here provide a strong foundation for further optimization. Given the challenges in clinical translation, including delivery efficiency and off-target effects (509,574), advancing this system in more complex tumor models will be essential to evaluate its uptake dynamics, long-term effects, and potential for improving ASOs-based cancer therapies.

4

TRANSITIONING GENE SILENCING FROM SIMPLE 2D TO MORE COMPLEX 3D MODELS

Part of the data enclosed in this chapter was originally published in the following issue:

- **Oliveira B.B**, Fernandes A.R, and Baptista P.V,. (2024). Assessing the gene silencing potential of AuNP-based approaches on conventional 2D cell culture versus 3D tumor spheroid. *Frontiers in Bioengineering and Biotechnology*. 12:1320729. doi: 10.3389/fbioe.2024.1320729

I was responsible for the cultivation and maintenance of all cell models and cell lines, as well as their characterization and viability assessments, following protocols previously optimized by the research group. Additionally, I designed, conducted, and optimized all experiments related to gene silencing, including subsequent analyses of gene expression using RT-qPCR and protein expression via Western-blot. Data analysis and statistical evaluation of all results were performed independently by me.

4.1 Introduction

Three-dimensional cell culture relying on tumor spheroids has become a critical tool for modeling malignant tissue due to the ease of manipulation, range of possible conditions, relatively low cost when compared to *in vivo* assays, and capability to mimic physiological conditions. Still, the great majority of cancer studies, particularly those reporting on nanoparticle-based gene silencing therapeutics, are heavily dependent on traditional 2D cell culture models (575,576).

2D cultures are characterized by cell adherence and growth in the form of a monolayer on a culture flask/petri dish or attached to any other plastic surface, with considerable ease of manipulation and low-cost maintenance (577). Still, they fall short of representing the real cell-cell interactions in a tumor mass (578–581). Furthermore, the 2D static monolayer system allows unlimited access to oxygen, nutrients, metabolites, and signaling molecules, which diverge from the real conditions faced by cells on growing tumor masses (283,292,582). As such, 3D *in vitro* aggregates of tumor cells, also known as spheroids, have been proposed as better models to mimic tumor behavior and microenvironment (583). This 3D arrangement of cells gets one step closer to the typical features of *in vivo* systems, such as proper cell-cell and cell-matrix interactions, creation of environmental "niches", morphology and division preservation, diversification of phenotypes and polarity, as well as different access to oxygen, nutrients, metabolites and signaling molecules (584–586). Spheroids have been used as models for colon, breast, pancreatic, and other cancer diseases to aid in the discovery of new anti-cancer therapeutics, as well as in toxicological screening and developmental biology studies, offering a more representative platform for studying therapeutics in a tissue-like context (275,578).

The use of 3D cell models for the evaluation of gene silencing strategies vectorized by nanoparticles is a promising technique for studying gene function, understanding disease mechanisms, and developing targeted therapies (273). Still, the translation of AuNPs-based approaches from conventional 2D cell culture models to more physiologically relevant 3D tumor models has proven challenging (576). This underscores the need to optimize delivery efficiency, achieve specific and efficient gene targeting, and address potential off-target effects. The lack of such understanding is likely a key reason why many gene silencing strategies have failed when advanced to clinical trials (587,588).

As so, it is of utmost importance to extend the current knowledge on nanoparticle-based gene silencing approaches supported on 2D cell cultures to the more realistic 3D spheroids. The effective translation between 2D to 3D-cell models requires a deeper understanding of the differences in the internalization mechanisms, cell-to-cell communication, extracellular matrix interactions, and diffusion gradients that might hinder the uptake efficiency and internalization kinetics of particles, ultimately impacting the

therapeutic/silencing outcome (589). Understanding these alterations is vital for successful gene silencing studies, not only improving the accuracy and relevance of experimental results but also aiding in the development of innovative strategies for targeted gene therapies in complex tissue-like environments (**Figure 4.1**).

Herein, we used the previously developed gold nanoconjugates targeting the *c-MYC* oncogene in a more complex 3D cell model of colorectal cancer to calibrate the silencing efficiency upon the increase in cellular complexity. Characterization of the silencing profiles pointed out the underlying differences in gene silencing efficiency between 2D and 3D cultures and the impact of the cellular microenvironment, spatial organization, and cell-cell interactions on the effectiveness of gene silencing strategies utilizing AuNPs.

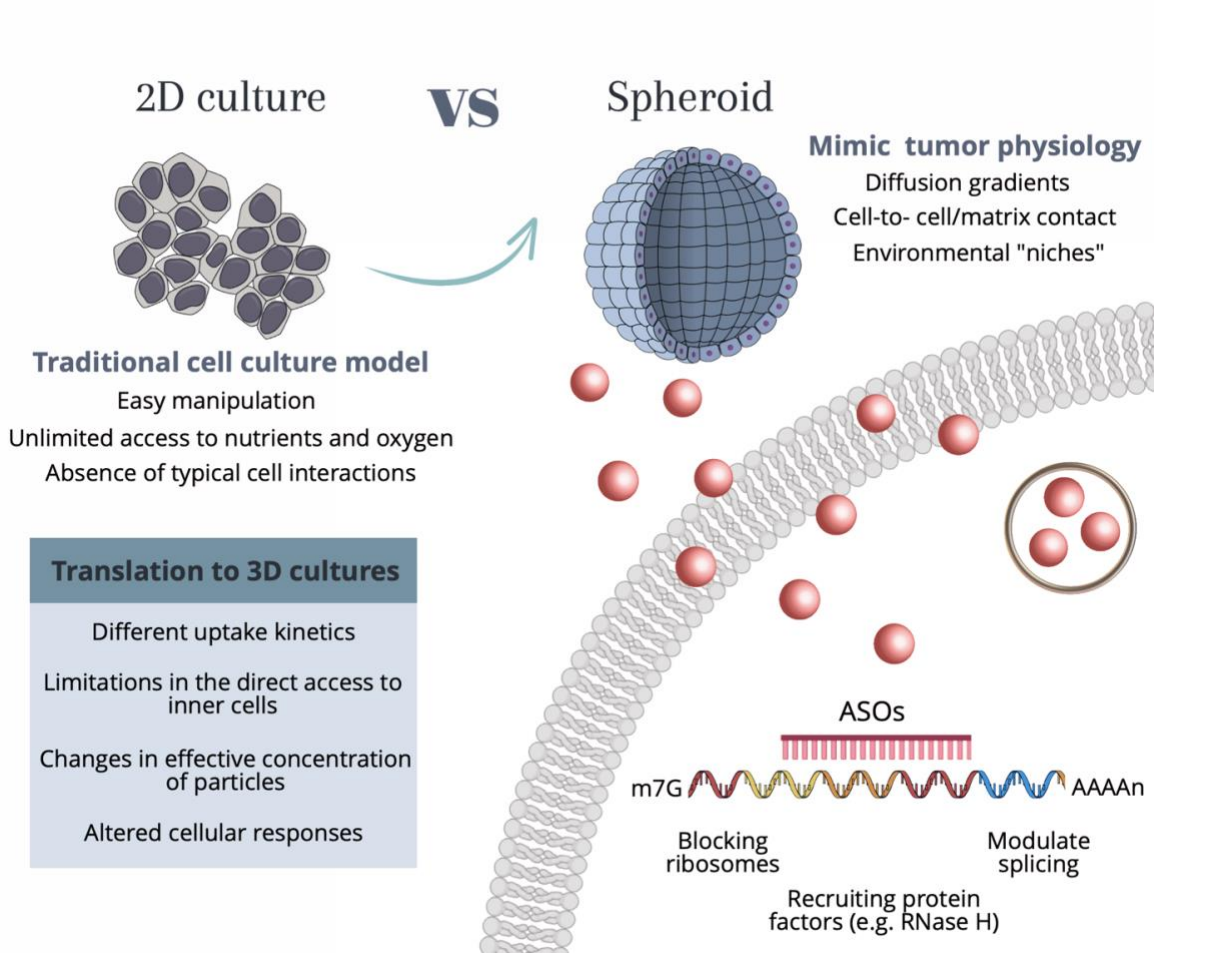

Figure 4.1. Main characteristics of each cell culture model and considerations for translating experiments to 3D tumor spheroids.
2D cell culture methods allow for easy and cost-effective manipulation. However, they present shortcomings related to unlimited access to nutrients and oxygen, as well as the lack of typical cell-cell interactions. Conversely, spheroids allow the recapitulation of the native structure of cells by creating diffusion gradients, cell-cell interactions, and environmental "niches" that allow cell heterogeneity. Independent of the cell culture method, the internalization of AuNPs by human cells occurs through a range of different mechanisms, among them phagocytosis, micropinocytosis, and receptor-mediated endocytosis, which use different receptors and cellular

signaling pathways. These mechanisms are dependent on the size and type of nanoparticles. For AuNPs with diameters <100nm (such as the ones used in the present work), the internalization mainly occurs by receptor-mediated endocytosis. Upon the entry of the Au-nanoconjugates in the cell, AuNPs can be arrested in vesicles such as lysosomes and further signaled for destruction, or the anti-sense DNA domain might be released and bind to the complementary mRNA site, performing the gene modulation by either blocking the ribosomes, recruiting protein factors (*e.g.*, RNase H) or modulate the splicing. Abbreviations: m7G – 7-methylguanosine (typical 5' cap on mRNA molecules); AAAAn – poly(A) tail; ASOs – Antisense oligonucleotide sequence.

4.2 Methods

To improve the readability of the present chapter, only the most relevant and newly introduced methods are detailed below. For detailed information regarding other methods and statistical analysis see Chapter **2.2.**

4.2.1 Spheroid Growth and Maintenance

HCT-116 spheroids were prepared according to Baek et al. (492). Cells were seeded at a density of 5 × 10^3 cells per well in a super-low attachment U-shape 96-wells culture plate and grown for 3 days while incubated at 37°C in a 99% (v/v) humidified atmosphere of 5% (v/v) CO_2 (CO_2 Incubator.

The size of the spheroids was assessed by brightfield microscopy for 16 days. For spheroids grown for more than 3 days, the medium was renewed every 4 days. The number of cells per spheroids was counted with the Trypan-Blue Exclusion Assay. Every day, 4 spheroids were collected and disintegrated with TrypLE™ Express Enzyme (1X), which was incubated for 20 min at 37ºC. Then, the pellet was centrifuged for 5 min at 1,000xg and resuspended in 50µL of PBS 1X. The cell suspension was diluted with Trypan-blue reagent (1:1 dilution) and placed in a hemocytometer for cell counting.

4.2.2 Conditions for Gene Silencing Assays on Spheroids

To assess the effect of the Au-nanoconjugates on *c-MYC* silencing on HCT-116 spheroids, these were incubated with 3 different nanoconjugates: AuNPs@c-MYC, AuNPs@PEG, AuNPs@Scramble. Spheroids were initially exposed to 54nM of ASOs (corresponding to 0.45nM of gold) for different incubation times (3h, 6h, 12h, 18h, and 24h). Additionally, spheroids were also exposed to 33nM of oligo (corresponding to 0.28nM of gold) to match the ratio of particles per cell when 2D cells are challenged with 54nM. The opposite condition was also studied: 2D cells challenged with the same ratio of particles per cell when spheroids are incubated with 54nM (88nM of oligo in 2D-cells). All these concentrations were assessed for different incubation times (3h, 6h, 12h, 18h, and 24h) to understand the uptake dynamics and silencing profiles across both models.

For both ASO-containing nanoconjugates, an AuNPs@PEG control was performed simultaneously so that the concentration of gold matched the one used AuNPs@c-MYC [AuNPs@PEG M] or AuNPs@Scramble [AuNPs@PEG S]. All experiments also have a "Spheroids" control, where only DMEM medium was added to the wells.

4.2.3 Viability Assay (CellTox) on Spheroids

For the assessment of cell viability on spheroids, the CellTox™ Green cytotoxicity assay was performed, following the manufacturer's recommendations. Briefly, following spheroid incubation with the Au-nanoconjugates, the culture medium was removed and replaced by CellTox™ Green dye 1X prepared on DMEM medium, without phenol red, and incubated for 24h. Images of the spheroids were then acquired using the FITC filter with 800ms of exposure time.

The CellTox Green dye enters cells with compromised membrane integrity and becomes fluorescent after binding to DNA. The fluorescent signal is proportional to the binding of the dye to the DNA of cells with compromised membranes; hence, it can be used to infer the cell viability (493,494). As such, for 100% of cell death control, spheroids were fixated with 4% paraformaldehyde solution in PBS 1X. Following the PFA addition, the spheroids were incubated for 20 minutes at room temperature. ImageJ software was used to measure the green fluorescence intensity (mean fluorescence x area) of the total spheroid by delimiting its periphery. The fluorescence intensity was normalized to the background's fluorescence (of the corresponding image). The final cell viability was attained by normalizing the corrected fluorescence intensity of each condition to the 100% cell death control (spheroids fixated with PFA).

4.2.4 ICP-AES

The presence of gold inside the cells was assessed by Inductively Coupled Plasma Atomic Emission Spectrometry (ICP-AES). AuNPs@c-MYC nanoconjugates were incubated with HCT-116 cells in 2D culture (54nM and 88nM) and spheroids (54nM and 33nM) for 3h, 6h, 12h, 18h, and 24h. After incubation, the supernatant was recovered, and then cells were detached from the wells as described before. For the spheroids, a 5-minute centrifugation at 1,000xg was performed to separate the spheroids from the medium. Then, cellular pellets and supernatants were incubated overnight with *Aqua Regia*. The samples were then analyzed by ICP-AES to assess the gold content, and the amount of gold per cell was calculated. A total of 4 wells (24-well plate) and 20 spheroids were used per condition for the 2D and 3D cell cultures, respectively. The service of ICP-AES for elemental detection of gold atoms was performed by Dr. Carla Rodrigues at Laboratório de Análises at the Chemistry Department of NOVA School of Sciences and Technology.

4.3 Results and Discussion

4.3.1 *c-MYC* Gene Silencing on Tumor Spheroids

The translation of nanoparticle-based gene silencing approaches from 2D to 3D-cell models relies on adjusting conditions to consider differences in AuNP's internalization and diffusion into the 3D structure, which play an important role in dictating silencing efficacy (590). In 2D-cell cultures, AuNPs passively diffuse onto cells, whereas in 3D-cell models, the architecture and organization in the three-dimensional matrix presents additional challenges, i.e., cells must penetrate multiple cell layers to reach the target (591–593). This usually involves adjusting the dose and incubation time of administration/challenge.

Firstly, the same concentration range of Au-nanoconjugates previously tested on 2D-cell cultures (20nM to 70nM) was used to evaluate the cytotoxic effect on the spheroids (**Figure 4.2**). As for the 2D model, the nanoconjugates showed no toxicity effect on cells. However, some level of spheroid disintegration is observed upon incubation with the nanoconjugates, which may be related to the disruption of cell-cell interactions by AuNPs. It has been shown that, upon interaction with proteins or integrins on the cell surface, AuNPs may interfere with these intercellular connections, impacting the stability of spheroids (565).

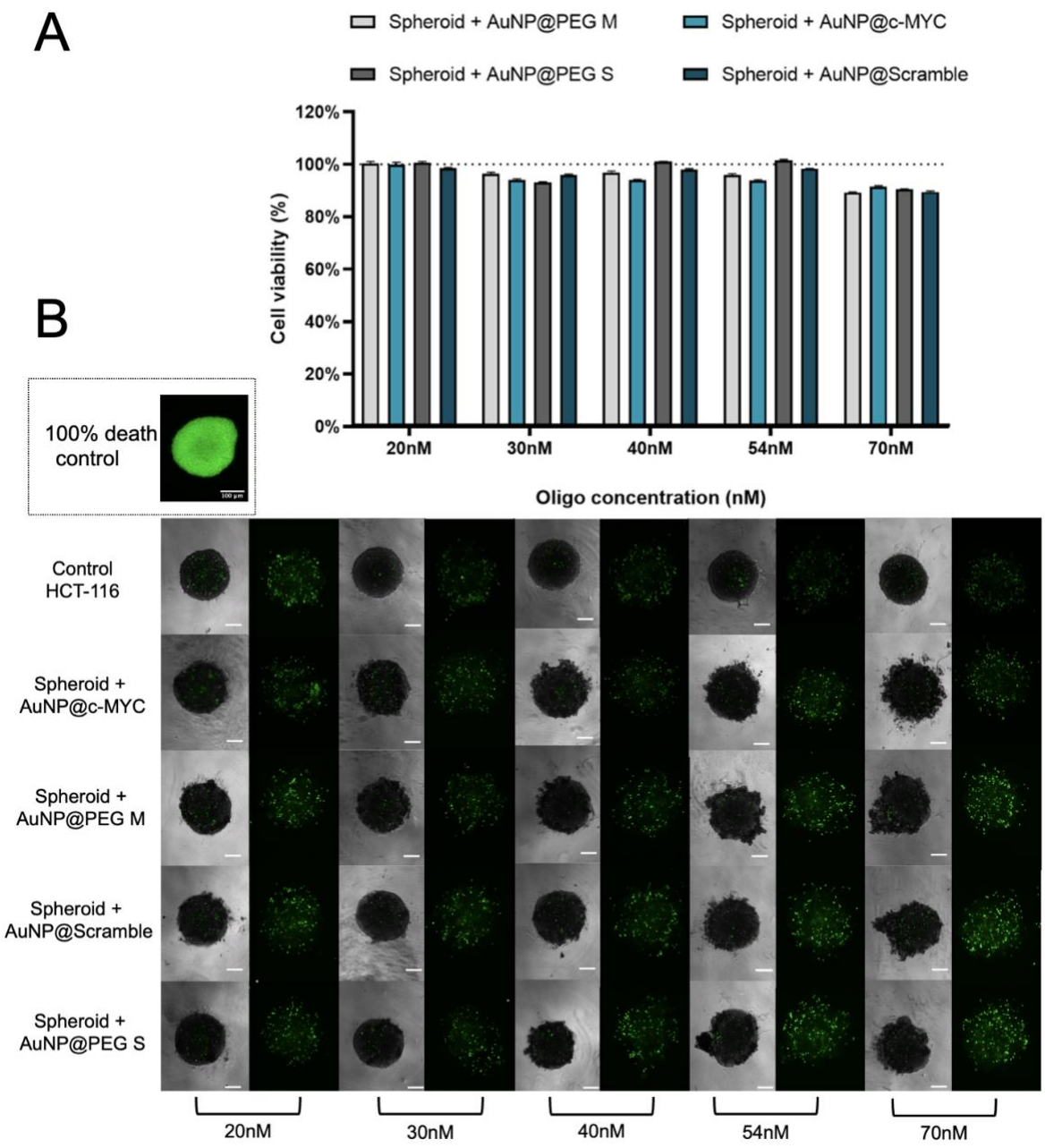

Figure 4.2. Cell viability of spheroids after 6 hours of challenge with each nanoconjugate.
(A) Bars represent the normalized cell viability when spheroids are incubated for 6h with (■) AuNPs@30%PEG M, (■) AuNPs@c-MYC, (■) AuNPs@PEG S, and (■) AuNPs@Scramble. at different concentrations: 20nM, 30nM, 40nM, 54nM and 70nM. Bars are the average result of 10 independent spheroids, and the error bars are the respective Standard deviation. The results were obtained by measuring the green fluorescence intensity (mean fluorescence x area) of the total spheroid by delimiting its periphery and then normalizing to the fluorescence of the background (of the corresponding image). The final cell viability was attained by normalizing the corrected fluorescence intensity of each condition to the 100% cell death control (spheroids fixated with PFA). (**B**) Spheroids stained with CellTox^{TM} Green dye after incubation with different concentrations of each nanoprobe. The spheroid on the inset represents a typical 100% cell death control, attained after fixation with PFA. Composite image obtained through the overlap of the brightfield image with the green channel using the 4x objective, followed by only the image attained with the green channel. All the images contain a scale bar of 100µm.

Next, the silencing potential using the optimal ASOs concentration previously set for the 2D-cell culture model (54nM) was assessed in spheroids (**Figure 4.3**). Similarly to the observed in 2D-models, the silencing effect is only observable for 6 and 12h. From both conditions, challenging spheroids for 6 hours with 54nM has been shown to provide the maximal silencing potential, leading to a decrease of 33% in the *c-MYC* expression.

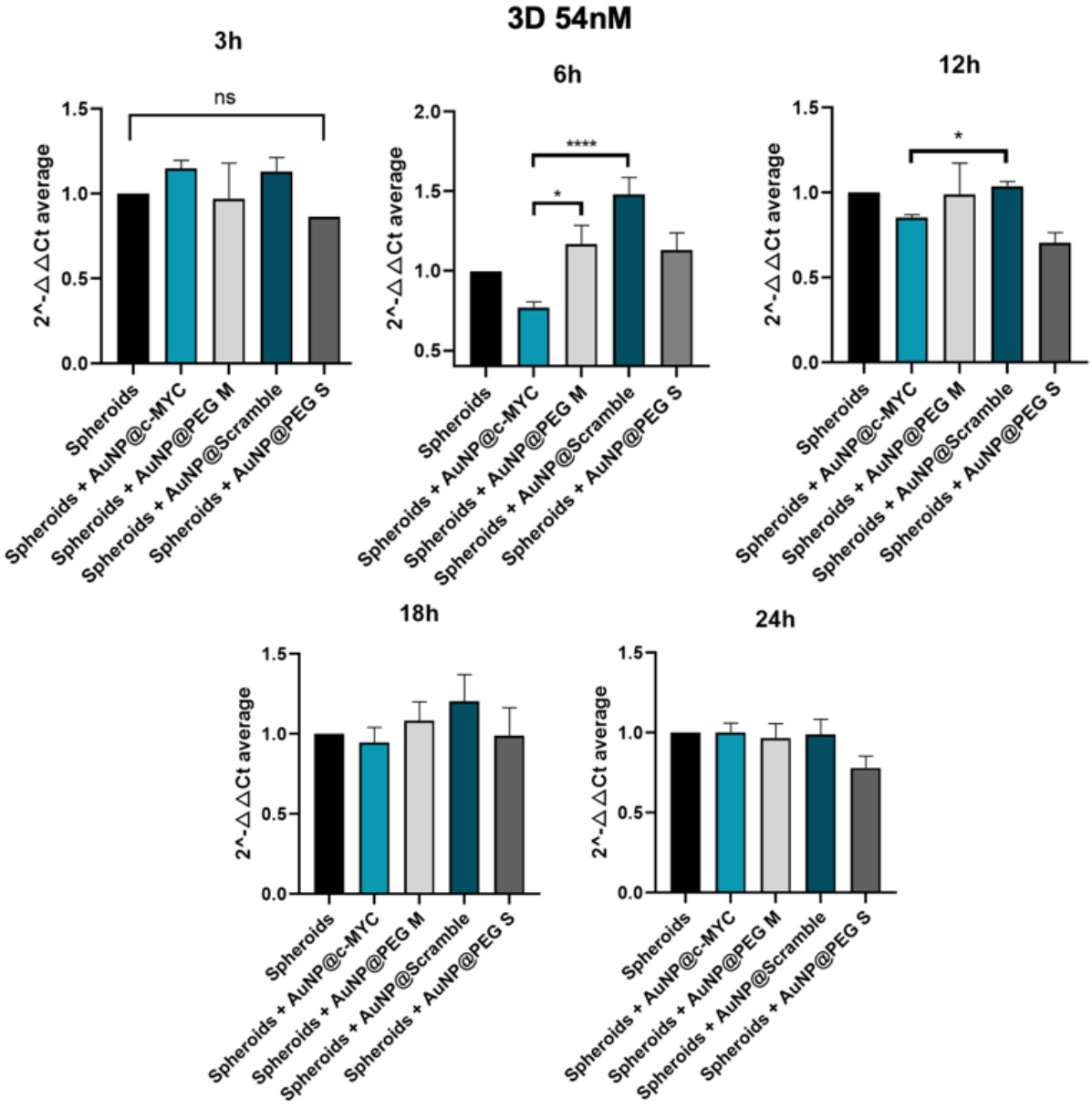

Figure 4.3. 2-△△CT results of spheroid challenge with 54nM of Au-oligonucleotide conjugates at different incubation periods.
Bars are the result of at least 3 independent biological replicates, and the error bars are the respective Standard Error Mean. Statistical analysis was performed using One-way ANOVA and the Mann-Whitney test, Results were considered statistically significant for p values < 0.05. (*) represents $p \leq 0.0323$, (**) represents $p \leq 0.0021$, (***) represents $p \leq 0.0002$ and (****) represents $p < 0.0001$.

Then, to corroborate this result, several biological replicates were performed (**Figure 4.4**). Data shows a robust silencing effect of 33%, observable across 8 independent biological replicates (**Figure 4.4**, panels A and B), similar to that attained for the 2D-cell model (37%) (panel C) (565–568).

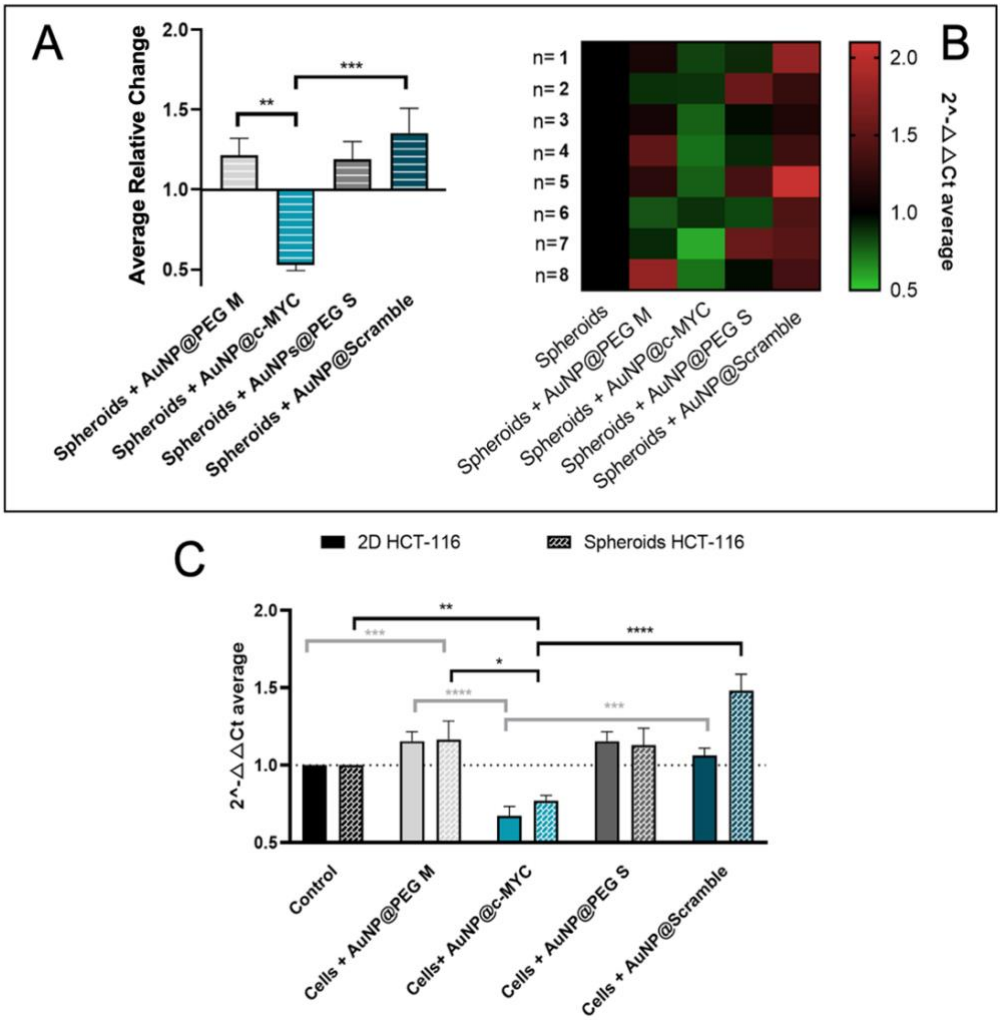

Figure 4.4. *c-MYC* silencing on HCT-116 spheroids upon 6h of incubation with 54nM of oligonucleotide. **(A)** Average relative change and **(B)** Heat-map representation of the average $2^{-\Delta\Delta CT}$ results of *c-MYC* silencing on spheroids. Each column represents the different Au-oligonucleotide conjugate controls, and the lines represent the results of each biological replicate. $2^{-\Delta\Delta CT}$ values between 0.5 and 1 (gene silencing) are represented by green tones (from brighter to darker shades), $2^{-\Delta\Delta CT}$ values equal to 1 are represented in black, and values between 1 and 2 (gene overexpression) are represented in red tones (from darker to brighter). **(C)** Comparison between the silencing results on 2D and 3D-cell culture models. Full bars represent the $2^{-\Delta\Delta CT}$ values obtained for 2D-cell culture and the dotted bars the spheroids, for each control: (■) Cells incubated with medium only, (■) AuNPs@30%PEG M, (■) AuNPs@c-MYC, (■) AuNPs@PEG S and (■) AuNPs@Scramble. Bars are the result of 8 independent biological replicates, and the error bars are the respective Standard Error Mean. Statistical analysis was performed using One-way ANOVA and the Mann-Whitney test, Results were considered statistically significant for p values < 0.05. (*) represents $p \leq 0.0323$, (**) represents $p \leq 0.0021$, (***) represents $p \leq 0.0002$ and (****) represents $p < 0.0001$.

4.3.2 c-MYC Protein Silencing in 3D Models

The silencing effect of the developed nanoprobe in combination with the chosen conditions was also studied at the protein level. Similarly to what was observed in 2D models, in spheroids, the AuNPs@c-MYC also reduced expression of the target protein by 47% (**Figure 4.5**), corresponding to the same silencing efficiency observed on the mRNA level (**Figure 4.5,** panel C) – considering the relative change values.

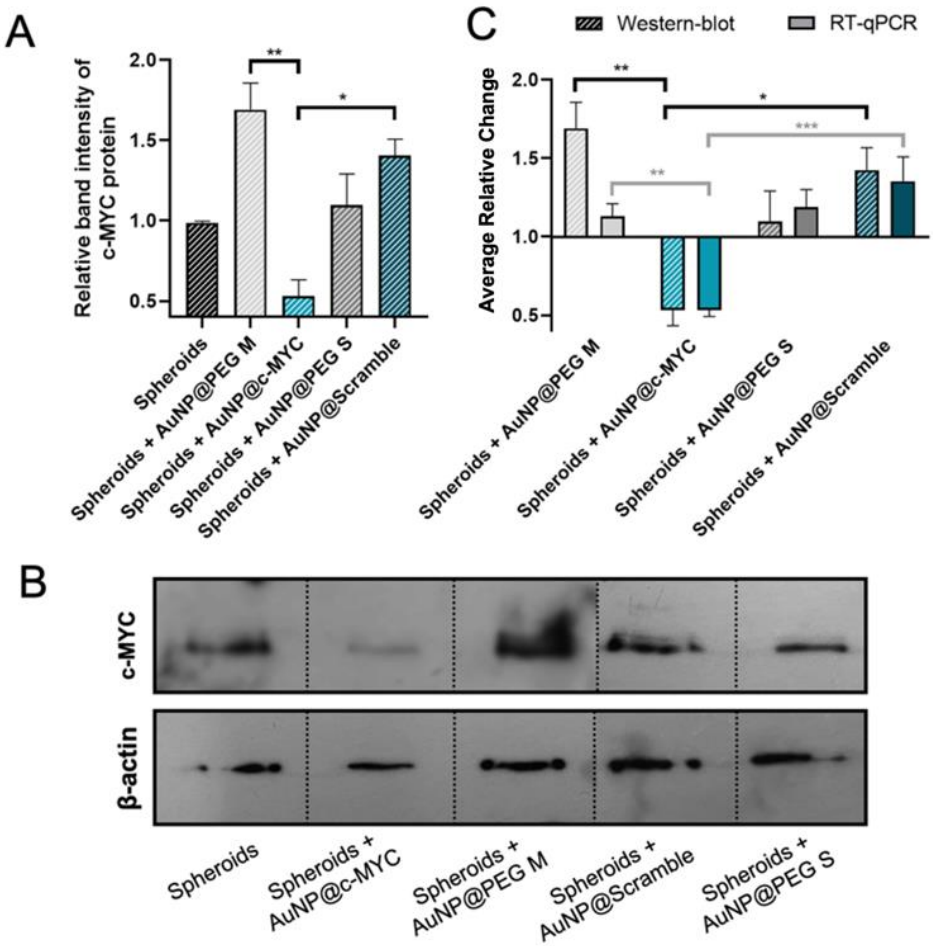

Figure 4.5. Expression of c-MYC protein on spheroids upon 6h of incubation with 54nM of oligonucleotide. **(A)** Average results for the band intensity obtained for c-MYC protein (normalized to the respective β-Actin control) in 3 independent Western-blot experiments. **(B)** Representative image of a Western-blot membrane for the detection of c-MYC (top line) and β-ACTIN (bottom line) proteins after incubation with the respective Au-oligonucleotide conjugates. **(C)** Average relative change of *c-MYC* silencing obtained on mRNA level by RT-qPCR and protein level by Western-blot. Striped bars represent the results of Western-blot and full bars the results of RT-qPCR, for each experiment control: (■) spheroids incubated with medium only, (■) AuNPs@30%PEG M, (■) AuNPs@c-MYC, (■) AuNPs@PEG S and (■) AuNPs@Scramble. Bars are the result of at least 3 independent biological replicates, and the error bars are the respective Standard Error Mean. Statistical analysis was performed using One-way ANOVA and the Mann-Whitney test, Results were considered statistically significant for p values < 0.05. (*) represents $p \leq 0.0323$, (**) represents $p \leq 0.0021$ and (***) represents $p \leq 0.0002$.

Overall, a similar silencing effect was obtained for mRNA and protein levels (**Figure 4.6**) in both 2D (mRNA – 37% vs protein – 43%) and 3D (mRNA – 43% vs protein – 47%) models, respectively. Still, a more detailed analysis of the silencing profiles in both models reveals that the silencing effect is more marked for the 3D than for the 2D model when analyzed by the relative change (normalized to AuNPs@Scramble).

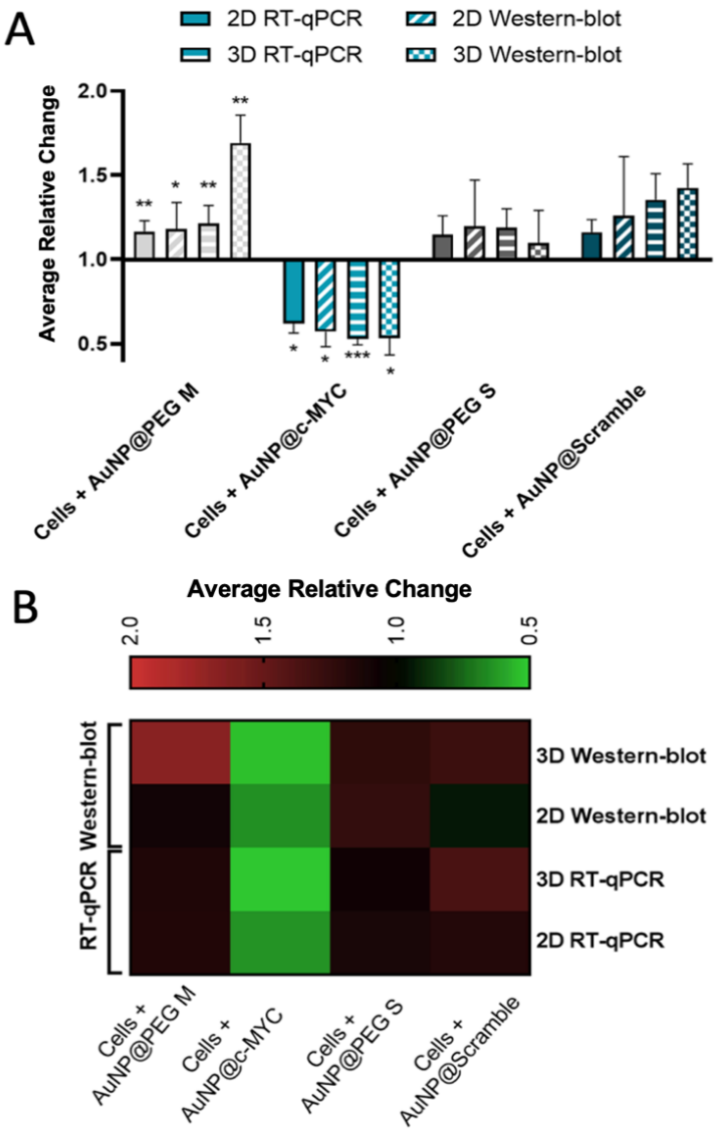

Figure 4.6. *c-MYC* silencing on 2D and 3D cell models.
Average relative change results of the *c-MYC* silencing of mRNA and protein in both 2D and 3D spheroids. Full bars represent the average relative change RT-qPCR values of the *c-MYC* silencing obtained for the 2D model, stripped bars the results for the 3D model, bars with diagonal stripes indicate Western-blot data of the 2D model, and checkered bars for the 3D model. Cells were incubated with different Au-nanoconjugates; the controls are represented by different colors: (■) AuNPs@30%PEG M, (■) AuNPs@c-MYC, (■) AuNPs@PEG S, and (■) AuNPs@Scramble. Bars are the result of at least 3 independent biological replicates, and the error bars are the respective Standard Error Mean. Statistical analysis was performed using One-way ANOVA and the Mann-Whitney test, Results were considered statistically significant for p values < 0.05. (*) represents $p \leq 0.0323$, (**) represents $p \leq 0.0021$ and (***) represents $p \leq 0.0002$. **(B)** Heat-map representation of the average relative change. Each column represents the different Au-oligonucleotide conjugates controls, and the lines represent the results

obtained with Wester-blot and RT-qPCR for both 2D and 3D cell models. Values between 0.5 and 1 (gene/protein downregulation) are represented by green tones (from brighter to darker shades), values equal to 1 are represented in black, and values between 1 and 2 (gene/protein overexpression) are represented in red tones (from darker to brighter).

However, when comparing conditions by the $2^{-\triangle\triangle CT}$ method, the opposite is observed, i.e., a silencing of 37% for the 2D-cell cultures and 33% for the 3D spheroids. Such apparent disparities might be due to *c-MYC* overexpression when spheroids are incubated with AuNPs@Scramble (**Figure 4.6** panel B**, line 3 x column 4**). Since the relative change is calculated using AuNPs@Scramble as a reference, the slight increase in *c-MYC* levels triggered by AuNPs@Scramble may lead to an overestimation of the silencing potential attained with AuNPs@c-MYC. Since no significant increase in gene expression occurs when 2D-cells are exposed to the AuNPs@Scramble (**Figure 4.6** panel B, **line 4 x column 4**), this does not have such an impact on the calculation of silencing efficacy (33% for $2^{-\triangle\triangle CT}$ method and 37% for relative change).

These data seem to indicate that despite the maximum silencing potential obtained with the same conditions (54nM of ASOs for 6 hours of incubation) in both models, the cells react differently to AuNPs exposure depending on whether they are cultured in 2D or 3D structures, which might be due to inherently different uptake mechanisms, ultimately causing distinct molecular responses (594–596). This is even more interesting when we consider the function of *c-MYC* on the modulation of cell proliferation, and it needs further investigation. When cells are grown as a monolayer on a flat surface, nanoparticles typically have direct access to the cells and can easily diffuse through the media and reach the cell membrane. Nanoparticles may then be internalized via passive diffusion or endocytosis, depending on their surface properties and the specific cellular uptake mechanisms involved (597). Conversely, nanoparticle uptake in spheroid models is influenced by their structure and cellular composition, including the extracellular matrix density and the barrier effect of the outer cell layers, which restricts direct access to cells in the inner layers, increasing the cellular heterogeneity and promoting oxygen and nutrient gradients (598). Together, these factors alter nanoparticle diffusion rate, mobility, distribution within the spheroid, and, ultimately, uptake efficiency.

4.3.3 Dose and Time-dependent Silencing across Models

Understanding these differences and the way they affect the internalization rate of particles is crucial when designing experiments and interpreting results in the context of gene silencing studies (599). Accordingly, the time-dependent silencing profiles for both cell models were compared when using the settled concentration of AuNPs@c-MYC (54nM) (**Figure 4.7**).

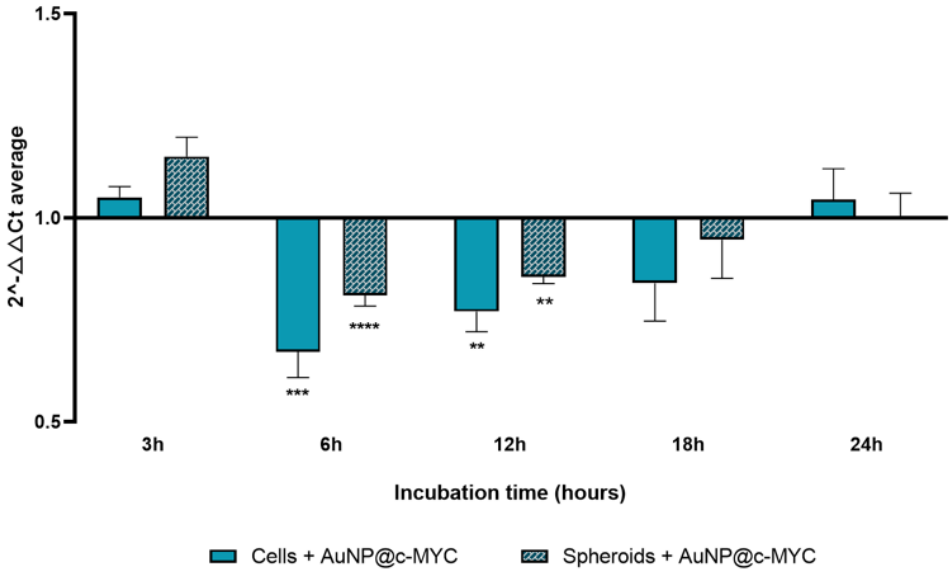

Figure 4.7. *c-MYC* silencing for 54nM of AuNP@c-MYC on 2D and 3D cell models over different incubation times.
The average $2^{-\Delta\Delta CT}$ values when using the AuNP@c-MYC nanoconjugate on 2D-cell culture are represented by (■), and the results for the 3D-cell culture model are presented by (■). Bars are the result of at least 3 independent biological replicates, and the error bars are the respective Standard Error Mean. Statistical analysis was performed using One-way ANOVA and the Mann-Whitney test, Results were considered statistically significant for p values < 0.05. (*) represents $p \leq 0.0323$, (**) represents $p \leq 0.0021$, (***) represents $p \leq 0.0002$ and (****) represents $p < 0.0001$.

The silencing profiles for 54nM of AuNPs@c-MYC seem to support the hypothesis of the effect played by the nanoparticle's internalization rate in the resulting silencing capability (**Figure 4.7**). Both models show a similar silencing profile over time, with the maximum silencing occurring at 6 hours, from which a gradual decay occurs until 18 hours of incubation (minimum silencing effect), after which *c-MYC* expression returns to basal levels. The same profile is also observable when analyzing the silencing potential with the relative change method (**Figure 4.8**). However, it is also noticeable that there is a *c-MYC* overexpression when spheroids are incubated with AuNPs@Scramble, which ends up causing an overestimation of the silencing effect of AuNPs@c-MYC on spheroids in comparison to the 2D-cell models.

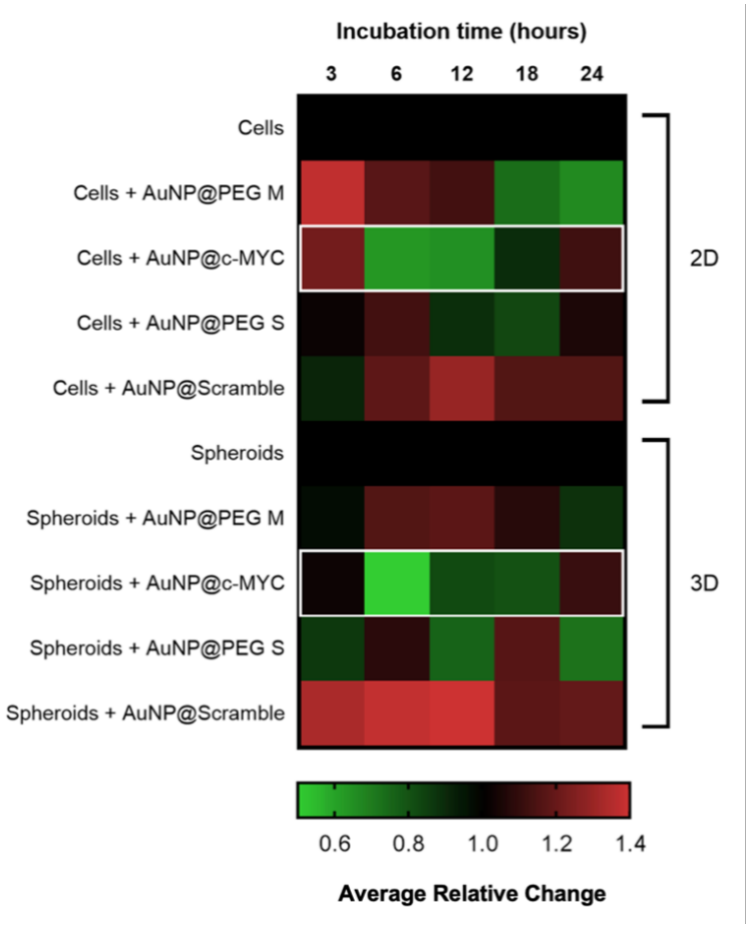

Figure 4.8. *c-MYC* silencing using 54nM of oligonucleotide on 2D and 3D cell models over different incubation times.
Heat-map representation of the average relative change for the incubation for 3h, 6h, 12h, 18h, and 24h with 54nM of each Au-nanoconjugate in 2D and 3D cell models. Each column represents a different incubation time, and the lines are the results obtained for each Au-oligonucleotide conjugate. Values between 0.5 and 1 (gene/protein downregulation) are represented by green tones (from brighter to darker shades), values equal to 1 are represented in black, and values between 1 and 1.4 (gene/protein overexpression) are represented in red tones (from darker to brighter).

Regardless of the analysis method used ($2^{-\Delta\Delta CT}$ or Relative change), a reduction in silencing efficiency is expected in spheroids compared to 2D models when the same conditions are applied across both models. This expectation arises from the increased cellular barriers and the presence of diffusion gradients in spheroids (594–596), which collectively hinder the uptake of nanoconjugates and consequently reduce the silencing effect. However, previous data do not indicate significant differences in silencing potential, either in terms of efficiency or time-dependent profiles. Therefore, a deeper investigation into unaccounted factors that may contribute to these results was undertaken.

When assessing the therapeutic effect of compounds, it is crucial to match the dose relative to the mass or number of cells across all models under study. This practice ensures the reliability and reproducibility

of the results, allowing for an accurate interpretation of the compound's efficacy and safety (600). Dose-response studies, determination of the therapeutic index, and identification of toxicity thresholds heavily depend on consistent and precise dosing (601–603). Over- or under-dosing can lead to misleading conclusions about the compound's safety profile and maximum efficacy (604). Additionally, successful clinical translation of pre-clinical studies is often hindered by the difficulty in accurately adjusting the dosage to achieve safe and effective results in human trials (605,606). Given that the scope of this work is to facilitate the transition of AuNPs-based silencing approaches from simple 2D cell cultures to more complex and reliable models, thereby accelerating the translation of pre-clinical findings to clinical applications, the initial step involved analyzing the number of cells in each model (**Figure 4.9**).

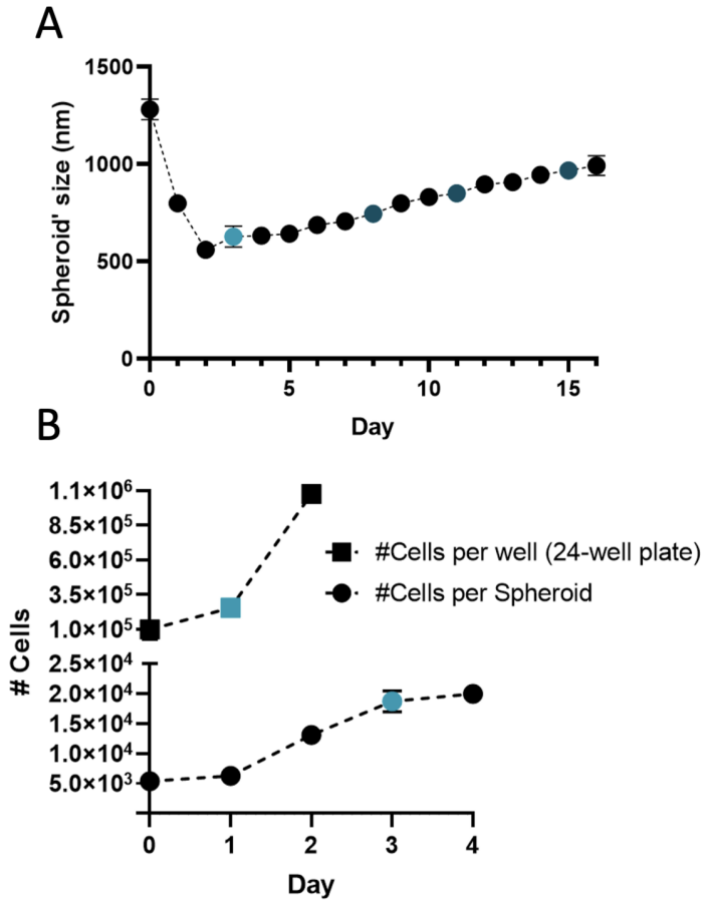

Figure 4.9. Growth of HCT-116 cells in both 2D and spheroid models.
(A) Size of HCT-116 spheroids over the days**.** The results are an average of the Ferret's diameter of 10 independent spheroids. The error bars are the respective standard deviation. The measurements were performed on microscope images acquired using a Ti-U Eclipse inverted microscope (Nikon, Tokyo, Japan) and further analyzed on Image J software. (●) represents the average size of a spheroid at 3 days of growth (condition used for the gene silencing assays) and (●) represents the spheroid's size on the days when the cell culture medium was exchanged to allow continuous growth. **(B)** Average number of HCT-116 cells in a 24-well plate well (■) and per spheroid (●) over the days. Blue represents the day each model was used for the challenge assays. The error bars are the respective standard deviation.

It should be noted that, thus far, the same concentration of ASOs – 54nM was used to challenge cells in both models. However, a spheroid of 3 days contains around $1.9x10^4$ cells, and each 24-well contains $2.5x10^5$ cells (more than 13 times the number of cells in a spheroid) (**Figure 4.9**). Meaning that each cell in a spheroid was being exposed to 2.6 times more nanoparticles (and therefore oligo) than a cell grown in 2D-culture. More precisely, a cell in the spheroid was exposed to roughly $1.5x10^6$ particles, whereas for the same concentration of oligo (54nM), a cell in 2D-cell culture was exposed to $5.8x10^5$ particles (**Figure 4.10,** panel A).

Further experiments were calibrated to attain the same ratio of particles per cell (**Figure 4.10**). To match the number of AuNPs that each cell in a spheroid is exposed to, when using 54nM of oligo, the 2D models have to be exposed to 88nM of anti-c-MYC oligo (**Figure 4.10,** panel B). Conversely, to assess the opposite condition (spheroids with the same number of particles per cell as the one used in the 2D-cell culture), 33nM of anti-c-MYC nanoconjugate was incubated with the spheroids (**Figure 4.10,** panel C). As for the initial studies, these concentrations were tested for 3h, 6h, 12h, 18h, and 24h of incubation on each cell model (see **Figure 4.11** and **Figure 4.12** for silencing results with the respective controls).

Exposing 2D-cultures to $1.5x10^6$ nanoparticles per cell (88nM of oligo) showed an earlier silencing effect, starting at 3h and lasting until 12h after the challenge, attaining an average silencing level of 55% in this time frame (**Figure 4.10,** panel B and **Figure 4.11**). This is a far more pronounced silencing effect than that attained for the standard ratio of $5.8x10^5$ particles per cell (54nM of oligo in the 2D model), where noticeable silencing only occurs between 6h (41%) and 12h (35%) of incubation, resulting on approximately 38% of silencing (**Figure 4.10,** panel C). Conversely, when using the same ratio ($1.5x10^6$ particles per cell) in 3D spheroids (54nM), the silencing effect seems to be delayed, only starting after 6h of incubation, for the maximum silencing level (47%), decreasing to 18% at 12h and 18h of incubation (**Figure 4.10,** panel B).

For spheroids exposed to $5.8x10^5$ particles per cell (33nM of oligo), the silencing effect also remains from 6 hours (38%) to 18 hours (7%) of incubation (**Figure 4.12**), while showing a closer match with the silencing profile obtained for 2D cell cultures (54nM of oligo) (**Figure 4.10,** panel C). Additionally, the silencing effect on spheroids seems to be more efficiently sustained over time (27% of silencing (33nM) versus 18% (54nM) at 12h) with this smaller ratio of particles. However, the maximum silencing potential (still occurring at 6h of incubation) decreased in comparison to the results obtained with $1.5x10^6$ particles per cell (54nM), resulting in a change from 47% (54nM) to 38% (33nM).

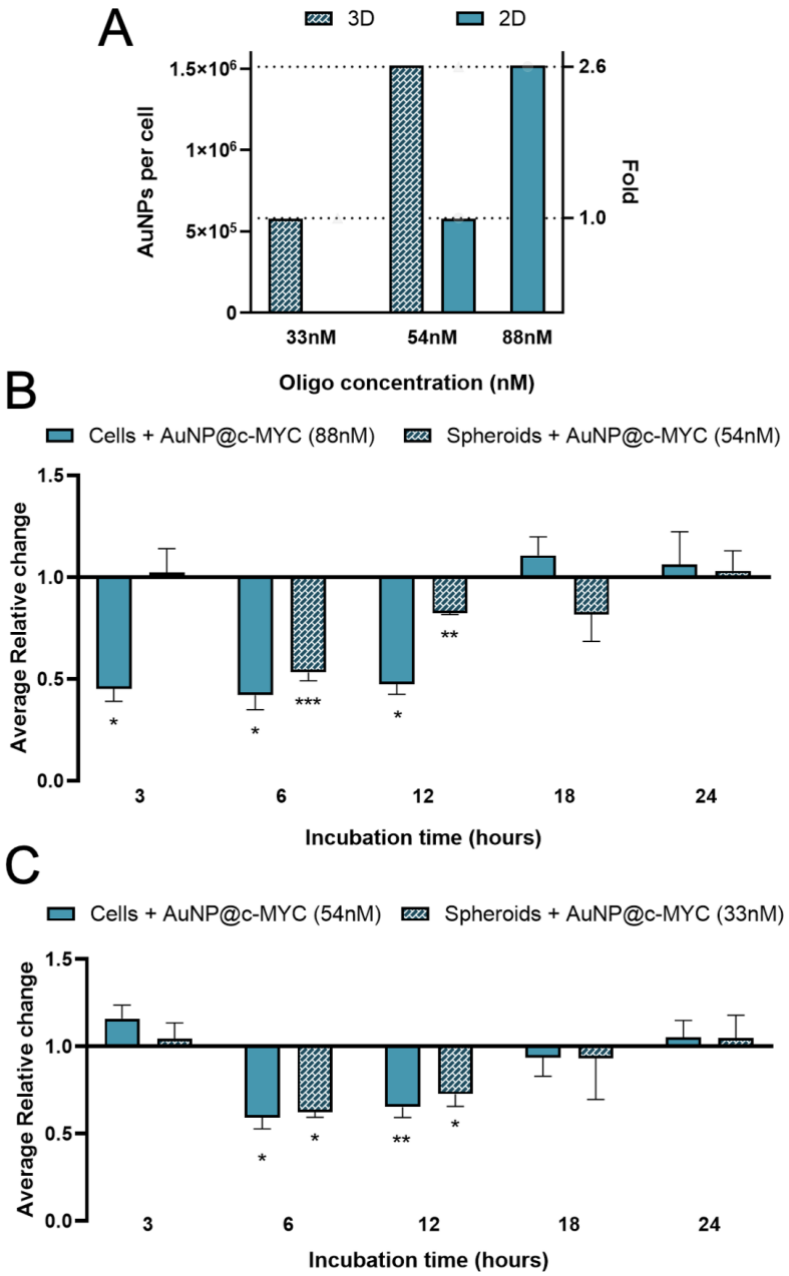

Figure 4.10. *c-MYC* silencing on 2D and 3D cell models over different incubation times.
(A) Number of particles per cell for the different ASOs concentrations in each cell model. Full bars (■) represent the 2D-cell model, and checkered bars (■) represent the spheroid model. (**B)** Relative change of the *c-MYC* silencing in both 2D-cells (88nM of ASOs) and spheroids (54nM of ASOs), attaining on the 2D-cell model the same ratio of particles per cell as used in spheroids. (**C)** Relative change of the *c-MYC* silencing in both 2D-cells (54nM of ASOs) and spheroids (33nM of ASOs), attaining on spheroids the same ratio of particles per cell as used in 2D-cell culture. The results of the 2D-cell culture are represented by (■), and the results for the 3D-cell culture model are presented by (■). Bars are the result of at least 3 independent biological replicates, and the error bars are the respective Standard Error Mean. Statistical analysis was performed using One-way ANOVA and the Mann-Whitney test, Results were considered statistically significant for p values < 0.05. (*) represents $p \leq 0.0323$, (**) represents $p \leq 0.0021$ and (***) represents $p \leq 0.0002$.

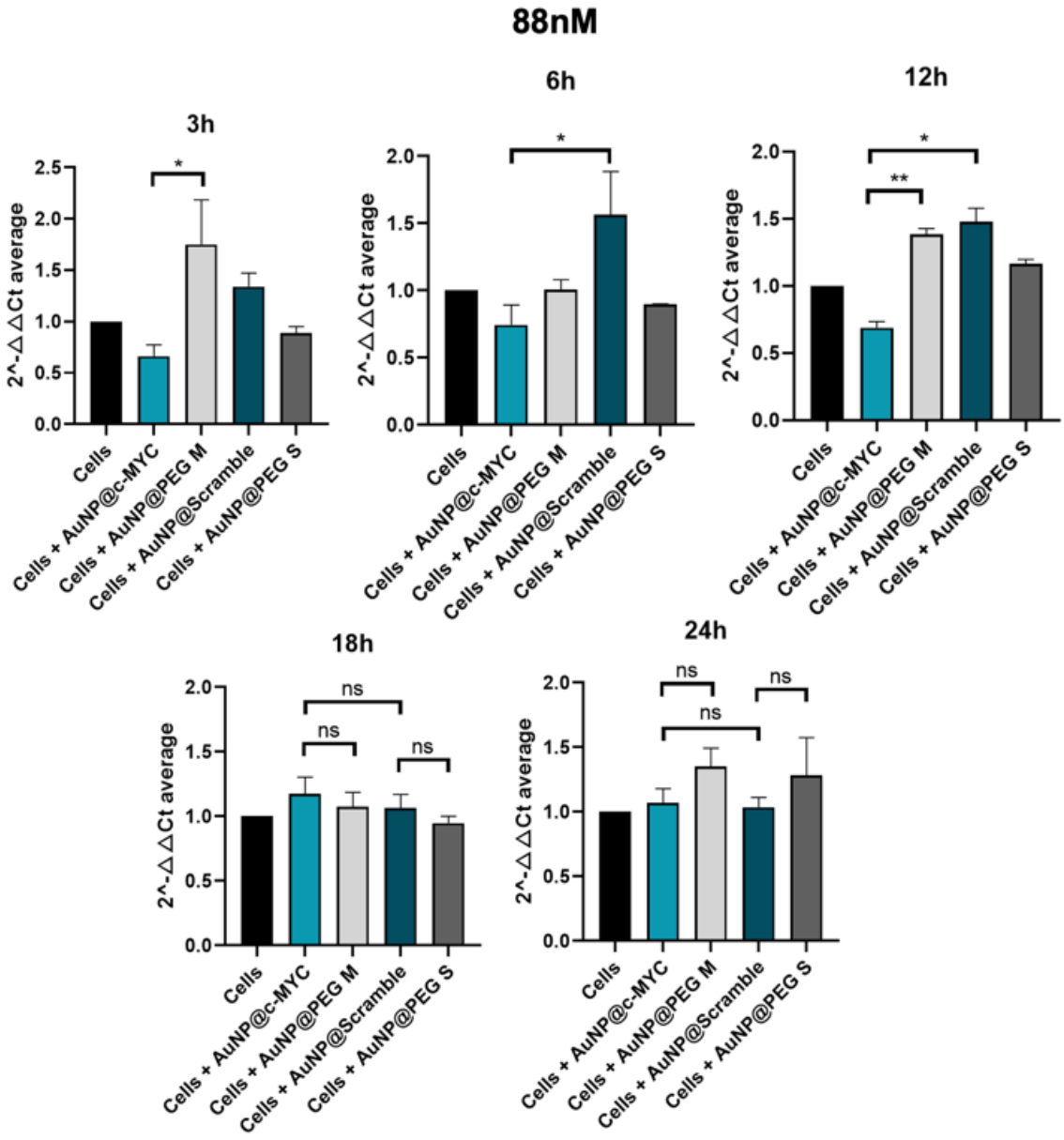

Figure 4.11. 2-△△CT results of 2D cell culture challenge with 88nM of Au-oligonucleotide conjugates at different incubation periods.
Bars are the result of at least 2 independent biological replicates, and the error bars are the respective Standard Error Mean. Statistical analysis was performed using One-way ANOVA and the Mann-Whitney test, Results were considered statistically significant for p values < 0.05. (*) represents $p \leq 0.0323$ and (**) represents $p \leq 0.0021$.

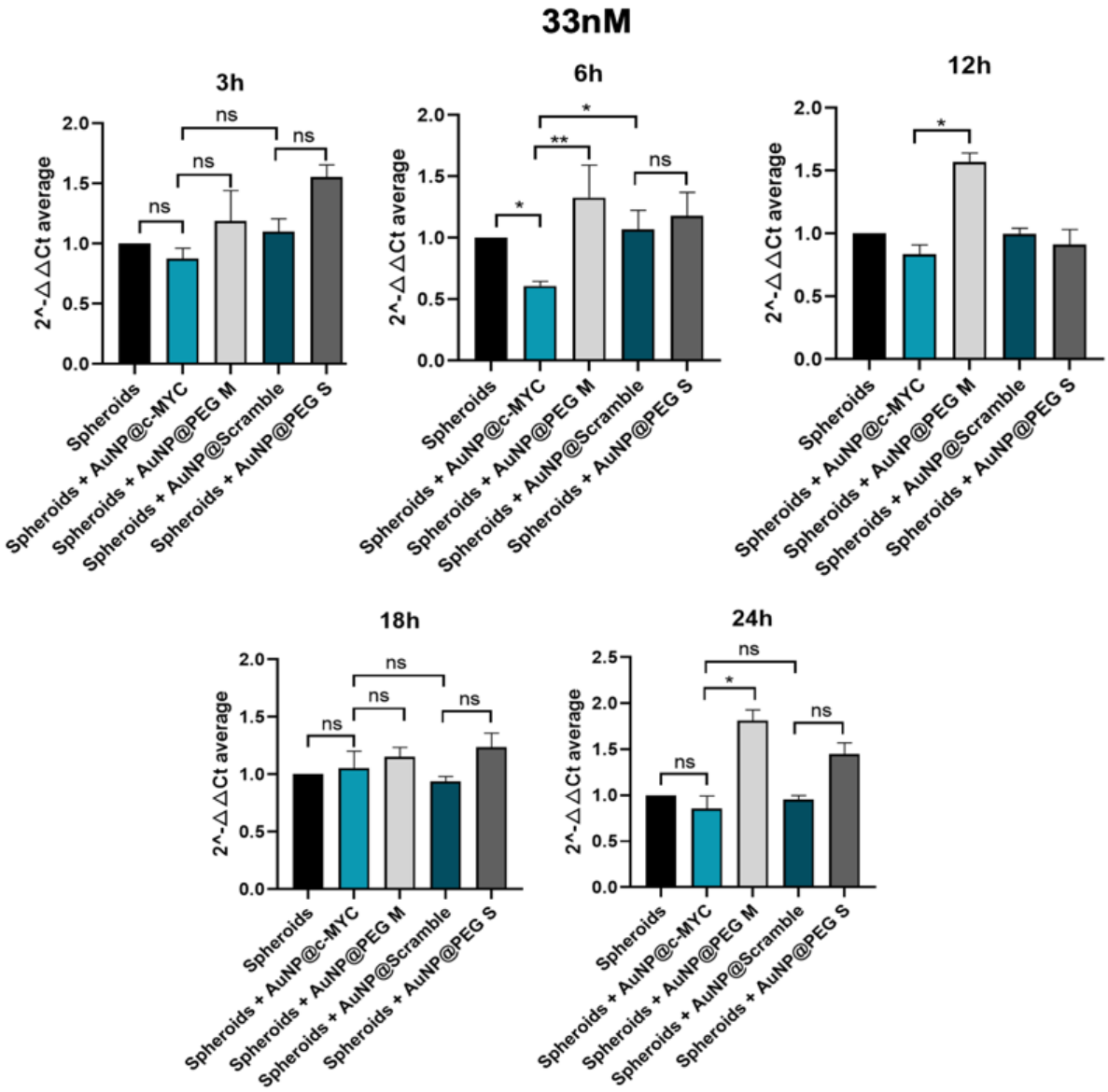

Figure 4.12. 2-△△CT results of spheroid culture challenge with 33nM of Au-oligonucleotide conjugates at different incubation periods.
Bars are the result of at least 2 independent biological replicates, and the error bars are the respective Standard Error Mean. Statistical analysis was performed using One-way ANOVA and the Mann-Whitney test, Results were considered statistically significant for p values < 0.05. (*) represents $p \leq 0.0323$ and (**) represents $p \leq 0.0021$.

Together, these data support the relevance of Au-nanoconjugate penetration into complex structures, which influences the number of nanoparticles per cell and, thus, the duration and efficiency of gene silencing (607,608). To further characterize this issue, the effective amount of gold in the cell fraction was determined by ICP-AES for 2D and 3D models challenged with anti-c-MYC nanoconjugate for 3h, 6h, 12h, 18h, and 24h (**Figure 4.13**).

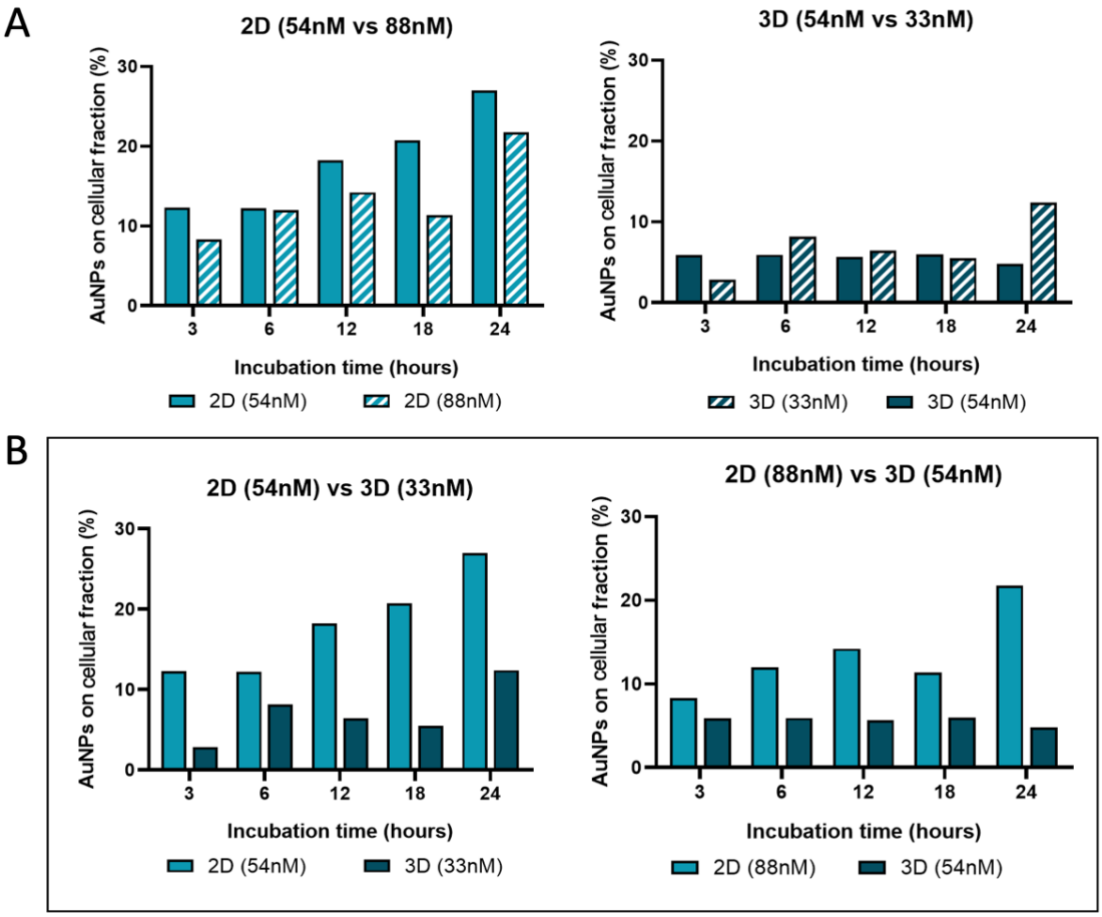

Figure 4.13. Gold content in the cell fraction.
ICP-AES was used to determine the gold content on the cellular fraction of 2D cultured cells and 3D spheroids after incubation with AuNPs@c-MYC nanoconjugates for 3h, 6h, 12h, 18h, and 24h. **(A)** Percentage of Au-nanoconjugates detected in the cellular fraction after incubation with 2D cells using 54nM (■) and 88nM (◪) (Left) or with Spheroids using 54nM (■) and 33nM (◪) (Right). (**B)** Comparison of the percentage of Au-nanoconjugates detected in the cellular fraction 2D cells and Spheroids with the same ratio of particles per cell. Left: $5x10^3$ particles per cell – (■) represents 2D-cultured cells with 54nM and (■) Spheroids with 33 nM. Right: $13x10^3$ particles per cell – (■) represents 2D-cultured cells with 88nM and (■) Spheroids with 54 nM.

Data show that the average number of AuNPs in 2D cultured cells is higher when compared to cells cultured as 3D spheroids for any given ratio of initial NP/cell exposure, which is in accordance with previous studies on this matter (590). Also, the number of AuNPs on the cellular fraction of 2D-cell culture seems to increase with the incubation time, except for 18 hours, which could be related to the duplication rate for HCT-116 cells (609). Additionally, regardless of being 2D or 3D cultured cells, data show a higher uptake efficiency (on both culture schemes) with the ratio of $5.8x10^5$ particles per cell (33nM of oligo on 3D and 54nM of oligo on 2D) when compared to $1.5x10^6$ particles per cell (54nM of oligo on 3D and 88nM of oligo on 2D) (**Figure 4.13**). This phenomenon where lower concentrations of AuNPs have better uptake than higher concentrations might be associated with individual cellular

response mechanisms and nanoparticle-cell interactions, such as saturation of cellular uptake mechanisms (607,608).

The cellular uptake of AuNPs occurs through various mechanisms, including phagocytosis, micropinocytosis, and receptor-mediated endocytosis (RME), with the pathway depending on nanoparticle size and type (610–616). AuNPs <100 nm are primarily internalized via RME, including caveolae-mediated, clathrin-mediated, and independent pathways (612,615,616). These mechanisms have limited capacity, leading to saturation at higher nanoparticle concentrations, which reduces uptake efficiency (616–618).

Higher nanoparticle concentrations also decrease the cell membrane's surface area-to-AuNPs ratio, hindering uptake, while lower concentrations promote better membrane interactions. Additionally, increased concentrations promote aggregation, limiting effective nanoparticle availability for uptake, whereas well-dispersed lower concentrations enhance cell contact (607). Particle size is crucial, with 27–30 nm AuNPs showing the fastest receptor-mediated endocytosis due to optimal membrane wrapping (618,619). These findings highlight the need for precise dose optimization before progressing to complex cell models.

4.4 Conclusions

In this chapter, we assessed the silencing efficiency of the previously developed AuNPs-ASOs strategy as it was advanced from a simple 2D cell culture to more complex 3D tumor spheroid models. Highlighting that both the concentrations of ASOs and nanoparticles, as well as the time point of analysis, can significantly influence gene silencing efficacy.

The results indicated similar *c-MYC* silencing efficiency in both cell models. However, this similarity was achieved possibly due to a 2.6 increase in particle-to-cell ratio in the 3D models, compensating for the higher cell density in 2D cultures. This surplus of particles in spheroids likely helps overcome challenges related to different uptake dynamics and increased diffusional barriers. Data on gold content showed that regardless of particle dosage, spheroids consistently exhibited lower particle uptake than 2D models. Both models demonstrated that nanoparticle accumulation is proportional to incubation time, with longer exposure leading to higher internalization. Still, the maximum silence efficiency was always attained at 6 hours of incubation. A deeper analysis revealed a dose-dependent silencing effect in 2D models, where increased nanoconjugate dose led to earlier and more intense silencing. In contrast, in 3D models, a reduced dose resulted in a more sustained silencing effect and higher silencing efficiency.

5

CRAFTING SIMPLIFIED DEVICES FOR TUMOR-ON-CHIP MODELS

Part of the data enclosed in this chapter was originally published in the following issue:

- **Oliveira, B.B**., Fernandes, A.R. and Baptista, P.V., (2024). Shrinking Cancer Research Barriers: Crafting Accessible Tumor-on-Chip Device for Gene Silencing Assays. *Advanced Engineering Materials,* 2402254. https://doi.org/10.1002/adem.202402254

I was responsible for the conceptualization *and* design of the devices as well as their production. In addition, I optimized the device designs, fabrication processes, and operating conditions to ensure their functionality and reproducibility. I also carried out the establishment and refinement of cell culture conditions tailored to the device, along with subsequent optimizations to improve performance and experimental outcomes.

5.1 Introduction

Tumor-on-chip technology is a cutting-edge method for replicating the tumor microenvironment *in vitro*, serving as an alternative to *in vivo* models (579,620,621). These microfluidic devices enable the use of increasingly complex cell models, ranging from 2D to 3D spheroids and tumoroids (315,361,469,622–625). Various parameters can be precisely adjusted, offering significant advantages over traditional *in vitro* systems, such as more intricate geometries, better control of microenvironmental factors, enhanced functionality, and high throughput (355,486). Despite these benefits, optimizing ToC designs remains challenging, and the fabrication processes can be cumbersome and costly.

Traditionally, creating microfluidic devices involves methods like photolithography (626,627), hot embossing (628,629), or injection molding (630) with materials such as polymers, gels, and organic monolayers, with PDMS being the most used (355,453,631,632). These manufacturing techniques require clean-room facilities, specialized equipment, highly trained personnel, and long fabrication times, making the process expensive and time-consuming (633). Additionally, PDMS has various limitations, such as gas permeability, which can affect long-term cell culture stability (461). Finding materials that balance biocompatibility, optical transparency, and mechanical properties while integrating multiple functionalities like fluid flow, cell culture, and real-time monitoring into a single device adds to the complexity (634). Additionally, scaling up production and developing standardized protocols for ToC devices remains challenging.

A shift towards more accessible ToC technology is crucial to fully realize its potential (635). Streamlining design and prototyping through innovative techniques and materials can reduce fabrication complexity and speed up production times (355,636). This would facilitate the creation of simplified ToC prototypes, helping identify the optimal design for specific biological applications.

Polystyrene (PS) has emerged as a promising material for microfluidics, especially for cell-culture devices, due to its excellent biocompatibility, ease of surface functionalization, optical transparency, heat resistance, and cost-effectiveness (637–639). Utilizing direct laser-writing micromachining on thermosensitive PS offers a novel, low-cost, and rapid fabrication method with non-contact characteristics, in contrast to photolithography (637,640–642). This method reduces the production time from two weeks to ten minutes and allows for easy pattern alterations at no extra cost, enabling personalized and iterative device optimization tailored to specific experimental needs, such as testing multiple therapeutic strategies and dosage screening, with better preclinical predictability and resource efficiency (355,361,466,643,644).

This chapter details an innovative process for fabricating biochips using thermo-retractile polystyrene sheets, commercially known as Shrinky Dinks® (645). The entire fabrication process is completed in under ten minutes through direct CO_2 laser engraving, followed by thermal bonding and heat-shrinking, creating the first fully PS device for cell culture without the need for precision machinery, mask production, or clean rooms (**Figure 5.1**). This method enables high-throughput production of devices suitable for rapid and cost-effective testing of multiple designs. These biochips were initially tested with 2D cultures of two distinct cancer cell lines to assess the biochips' biocompatibility and potential for further application with more complex cancer models.

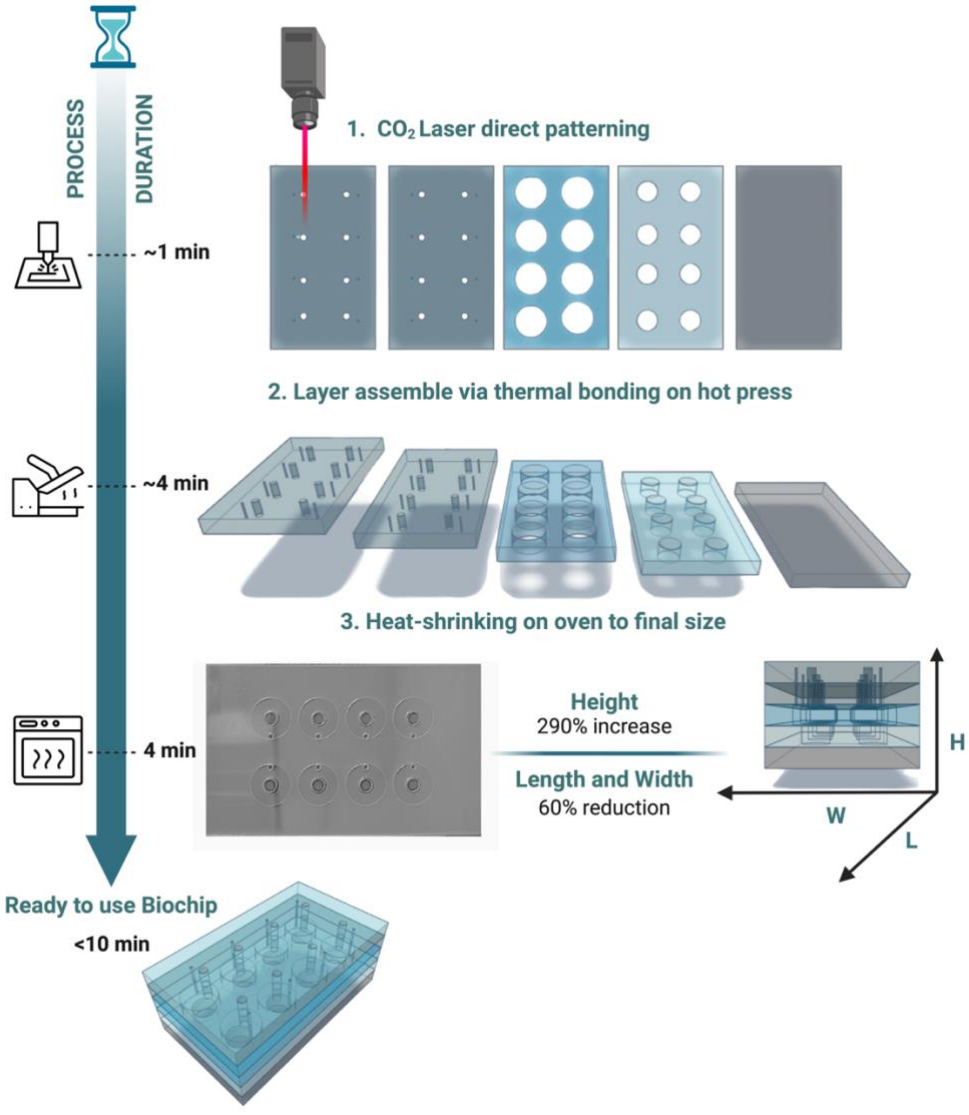

Figure 5.1. Fabrication processes for biochip manufacturing.
Functional biochips can be fabricated in under 10 minutes involving three simple steps: 1) use a CO_2 laser cutting machine to directly engrave the desired pattern onto polystyrene sheets; 2) assemble the patterned layers through thermal bonding on a hot press; 3) shrink the biochip to its final size on a conventional oven.

5.2 Methods

To improve the readability of the present chapter, only the most relevant and newly introduced methods are detailed below. For detailed information regarding other methods and statistical analysis see **Chapter 2.2Methods**.

5.2.1 Biochip Fabrication

The biochips' patterns were defined on Inkscape vector image software (License: GNU GPLv2) and then engraved on transparent polystyrene thermoplastic sheets "Shrinky-Dinks" using a CO_2 laser machine, with 40W of power, 10.6µm of wavelength and 0.254m/s writing speed, at 1000ppi (pulses per inch). The final biochip is composed of 5 layers with 8 small chambers suitable for 8 independent experiments. The cuts were performed using the following laser specifications: cut specification (vector) – Laser power: 80%; Speed: 40%; and Frequency: 500Hz. The operation of CO_2 was performed in FabLab (NOVA School of Sciences and Technology) with the supervision and help of Susana Neves.

The top layers (1 and 2) have 8 pairs of inlets/outlets with different sizes: a smaller one (⌀ 0.18cm) for medium and cell perfusion through an insulin syringe needle and a larger one (⌀ 0.52cm) for aeration. This top layer was reinforced (2) for stability and to prevent sinkholes. The middle layers (3 and 4) have 8 all-in-depth microchambers with a diameter of 1.80cm and 0.71cm, respectively. The bottom layer (5) works as a sealer and provides a surface for cell adhesion. Each layer is cut into thin, flexible polystyrene sheets in a rectangular shape with 12.91cm x 7.75cm (width x height). After patterning, each layer was aligned and placed between two slabs of Teflon. The assembled unshrunk layered sheets were thermally bonded on a hot press, with the temperature set at 110ºC (approximately the glassy transition temperature of PS ~100ºC) for 100 seconds with the top layer facing down, followed by another 100 seconds with the top layer facing up. If necessary, an extra seal between the layers was performed, only pressing the edges for 60 seconds. After the thermal bonding, the biochips were placed for 4 minutes in an oven at 155°C over a Teflon plate. After shrinkage, the biochips were allowed to cool down at room temperature for 2 minutes. After this step, the biochip shrunk to around 60% of its original size, and its height increased around 6-fold. The biochip's final size is 5.08 x 3.11 x 0.83cm (w x l x h). Due to the increase in the depth of the biochip, each microchamber has a capacity of roughly 80µL. All the measurements were performed using an analogic caliper.

5.2.2 Biochip Preparation

Before cell seeding, biochips need to be sterilized and treated to improve or prevent cell adherence. For this, each microchamber was infused with ethanol 70% (v/v) and placed under UV light for 1 hour. Then, the ethanol was removed, the chambers were washed with Milli-Q water, and the biochip was air-dried in a laminar flow chamber. Next, the microchambers are infused either with DMEM medium supplemented with 1% (v/v) antibiotic/antimycotic and 10% (v/v) Fetal Bovine Serum to improve cell adherence (2D cell cultures) and incubated for 24 h at 37ºC on a CO_2 incubator.

5.2.3 Cell Seeding and Growth on Biochip

For cell seeding into the biochip, cells are detached from the $25cm^2$ culture flasks using Triple Express and centrifuged at 500xg for 5 min. The pellet was resuspended in 1mL of DMEM medium, and the cells were counted using a hemacytometer. For on-chip 2D cell culture, each biochip's well was incubated with $1x10^4$ cells using an insulin syringe. The biochips were then placed on a petri dish half-filled with distilled water at 37ºC in a CO_2 incubator.

5.2.4 Cell Viability on Biohip

To assess the cell viability of 2D cell cultures grown in the biochips, the MTS assay was used. Briefly, cells were seeded at a density of 1×10^4 cells/reservoir (biochip) and allowed to grow for 24h. In the case of growth curves, cultures were also allowed to grow for longer periods. Before exposing the cells to MTS reagents, the supernatant was completely removed from the reservoirs. The MTS reagent was then diluted in culture media (1:5) and added to the cells, filling the totality of the wells. After 45 min of incubation in a CO_2 Incubator at 37°C, the supernatant was collected from each well in the biochip and placed on a 96-well plate, and the absorbance at 490nm was measured on a microplate reader. Controls were performed by incubating the MTS reagent with only DMEM medium.

5.2.5 Scanning Electronic Microscopy

Scanning Electronic Microscopy (SEM) (model SU3800, Hitachi Ltd., Tokyo, Japan) was performed on the biochips. For this, $1x10^4$ cells from HCT-116 and MCF-7/copGFP cell lines were seeded into the biochip and then placed on a CO_2 incubator at 37ºC for 24 hours. Following the cell fixation protocol, all the liquid content of the wells was removed. Then, the top two layers of the biochip were removed, and the biochip was sputtered with gold for 90 seconds at a pressure of 0.1 torr, using a current between 10 and 20 mA and a voltage of about 1kV under an argon environment. The images detected either the secondary electrons (SE mode) or backscattered electrons (BSE mode) under a high vacuum and with

an accelerating voltage between 20kV and 30kV. For the non-conductive biochips (without gold sputter), only SE mode was used.

The SEM microscopy and transactional cuts of the device were performed with the help of MSc. Pedro Rendas (Mechanical Department from NOVA School of Sciences and Technology).

5.3 Results and Discussion

Current fabrication processes and materials of microfluidic devices for cell culture entail several drawbacks, such as high cost, time, and labor, which makes it difficult to optimize the design via an experiment-based iteration manner. Herein, we report a simple and cost-effective approach to produce biochips in under 10 minutes using thin, flexible sheets of polystyrene.

5.3.1 Biochip Production

The biochip fabrication process involved the utilization of biaxially oriented thermo-sensitive polystyrene sheets commercially available under the name Shrinky Dinks®, which were then cut with the desired pattern using a CO_2 laser, assembled by thermal bonding, and then heat-shrunk to their final size (**Figure 5.2,** panel A). Leveraging this unique property of PS enables the patterning of minute dimensions while surpassing the necessity for precision machinery, typical of nanofabrication processes. Ultimately allowing the entire manufacturing process to be completed in under 10 minutes.

The settings of the CO_2 laser (cutting speed, laser power, and beam frequency) were assessed to perform the cut of the wells in the PS sheets without damaging the nearby material. The laser cutting process is divided into 3 types: melt shearing, vaporization, and chemical degradation. The cutting mechanism for thermoplastics, including polystyrene, is melt shearing (646), meaning the laser beam will melt the incident area, and the molten material is ejected by the shearing action of a stream of assist gas acting coaxially with the beam (647). From the several settings tested, the condition used was 0.206 m/s of writing speed and 32W of laser power. The layers were then assembled on a hot press set at 110ºC, a temperature slightly above the glassy transition temperature of PS (~100ºC) (648). Exposing polymers like PS to such conditions gives them rubber-like properties, which translates into a slight softening of the material that allows the layers to bond to each other (649), allowing the production of a device solely using PS slabs.

Unlike many other polymers which soften, melt, or even decompose under elevated temperatures, thermo-sensitive PS undergoes significant shrinkage while maintaining its original mass (638,642,650) (**Figure 5.2,** panel B). Our preliminary assessments showed that there is a shrinkage to the biochip's

surface area of approximately two-thirds of its original size, accompanied by an increase in thickness by a factor of 6 (**Figure 5.2,** panel C) (651,652). This level of shrinkage was considered for the subsequent design optimization steps. As such, all the patterns were initially designed and engraved with dimensions 2.5 higher than the desired final size.

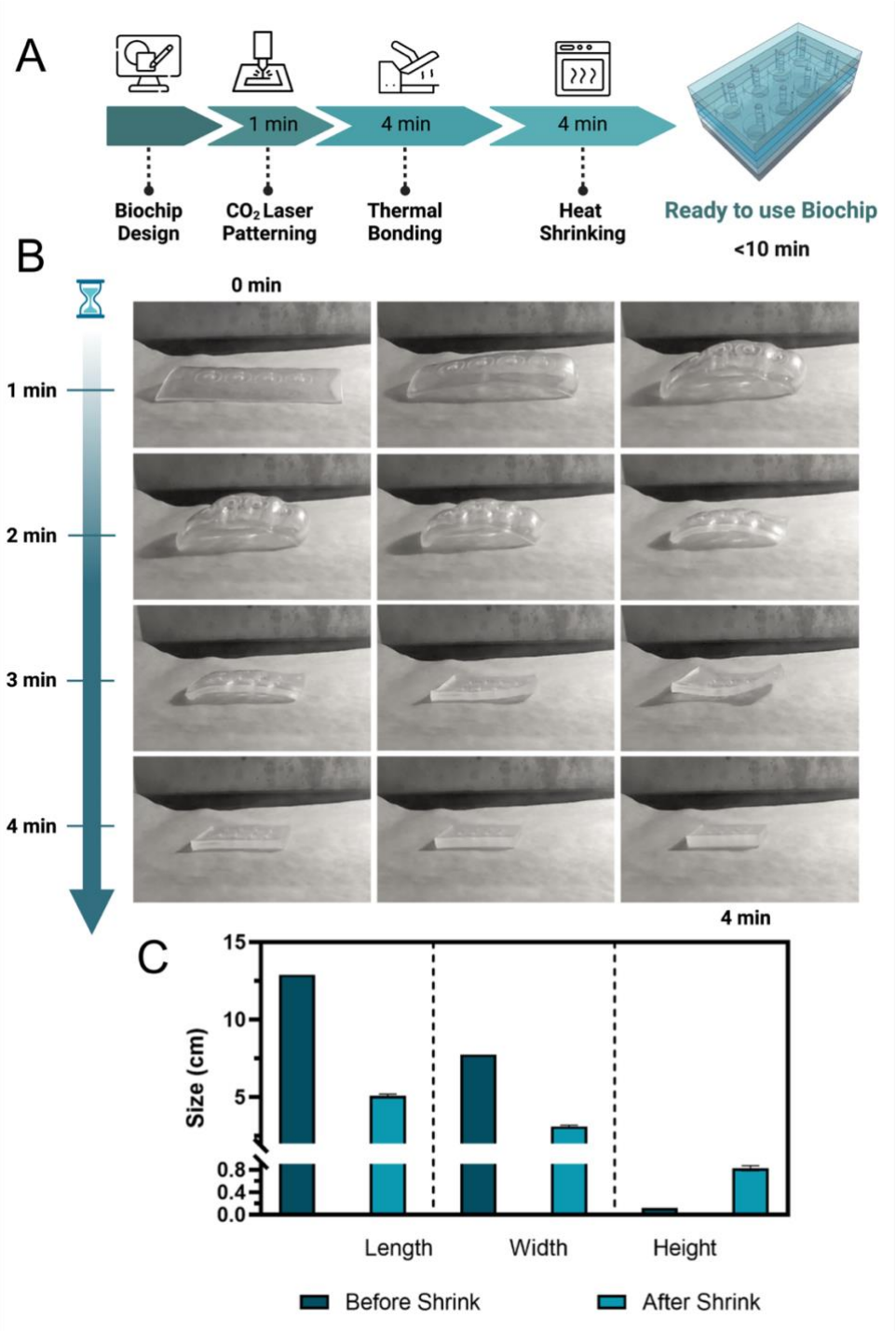

Figure 5.2. Biochip's fabrication process.
(**A**) Chronogram with the steps involved in the fabrication of the biochips. (**B**) Time-lapse pictures of the shrinking process. The images were obtained with a GoPro 11 Hero action camera. **(C)** Biochip dimensions before and after

the shrinkage process**.** All 3 dimensions (length, width, and height) were measured using an analogic caliper. The bars show the average result for the measurement of 30 biochips, before (■) and after (■) the shrinkage. The error bars show the corresponding standard deviations.

5.3.2 Design Optimization

The initial step in pattern design typically involves establishing the device's purpose and main features, such as the number of cells, type of model, culture duration, and experimental assays. For simplification, the first design focused solely on assessing the biocompatibility of the biochip material with cell maintenance and growth. This design featured a single culture chamber occupying most of the device, with channels for cell infusion and medium perfusion. The biochip consisted of three layers: the top layer with four inlets/outlets, the middle layer containing a pair of microchannels (⌀ = 100µm) for continuous medium perfusion, and an all-depth culture chamber (28.2mm x 14.4mm, w x h), and the bottom layer providing the surface for cell attachment and additional microchannels for cell seeding and detachment (**Figure 5.3**).

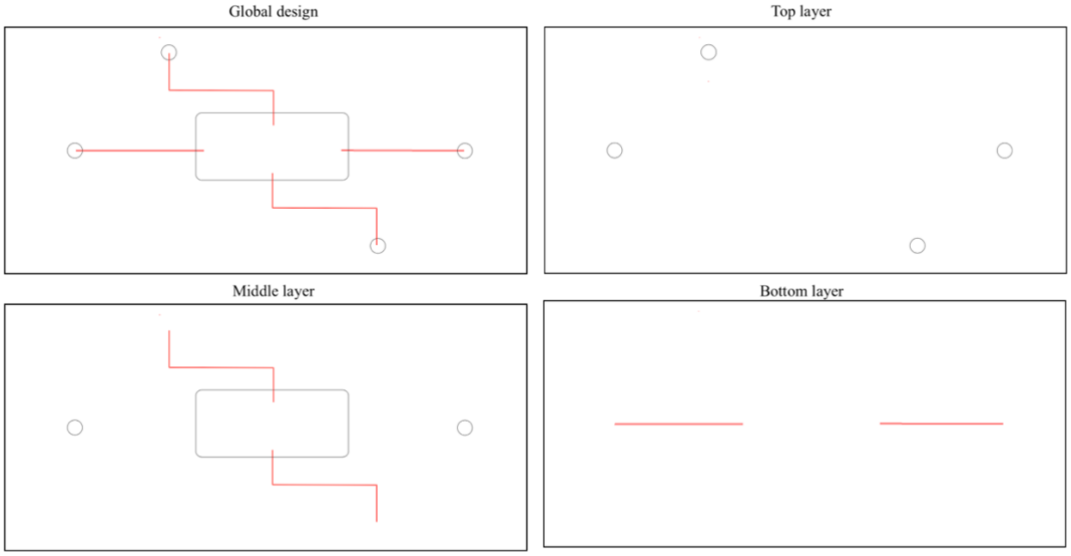

Figure 5.3. Patterning of the first conceptualized biochip.
(Black) represents cutting mode, (Red) engraving mode. Microchannels are designed with two parallel lines spaced by 0.1336 mm, which, after heat shrunk, give rise to 100µm channels. The chamber was designed for a final size of 28.2 mm x 14.4 mm (w x h).

Given the ease of design alteration, variants of this initial design were proposed to address common operational limitations. One such limitation is channel clogging during device infusion with the cell suspension (653). To mitigate this, a design with funnel-like channels for cell seeding was developed. By increasing the width of the microchannels, cells could more easily migrate to the chamber, preventing clogs (**Figure 5.4**).

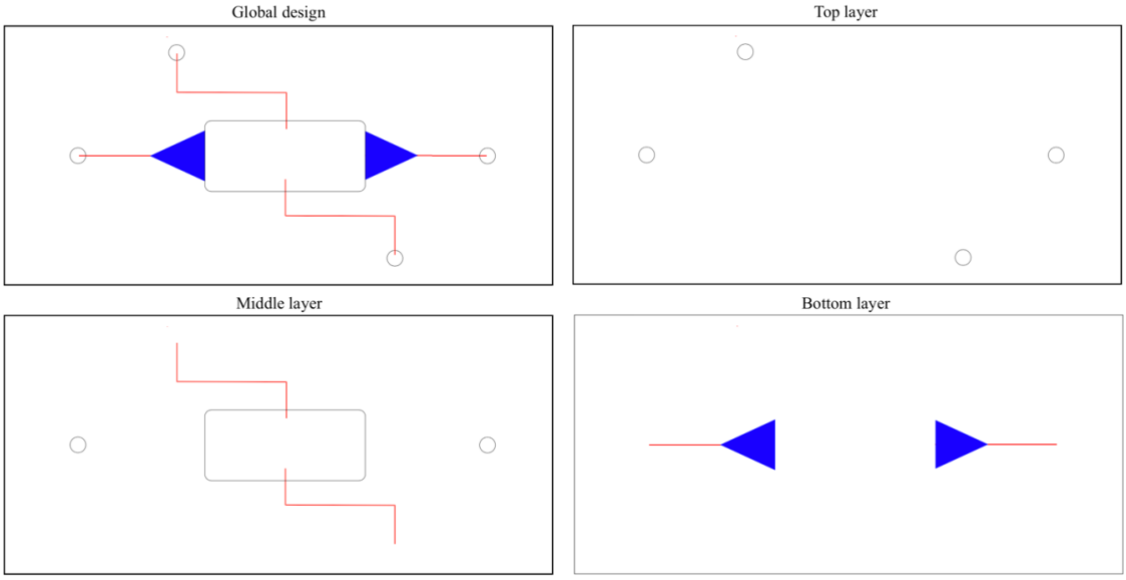

Figure 5.4. Patterning of the biochip with funnel-like channels.
(Black) represents cutting mode, (Red) engraving mode, and (Blue) rast mode.

Both designs exhibited sinkholes in the culture chamber, likely due to insufficient support. To address this issue, a series of designs were attempted, each targeting possible reasons for chamber collapse. Variations in chamber shape and orientation were explored (**Figure 5.5**).

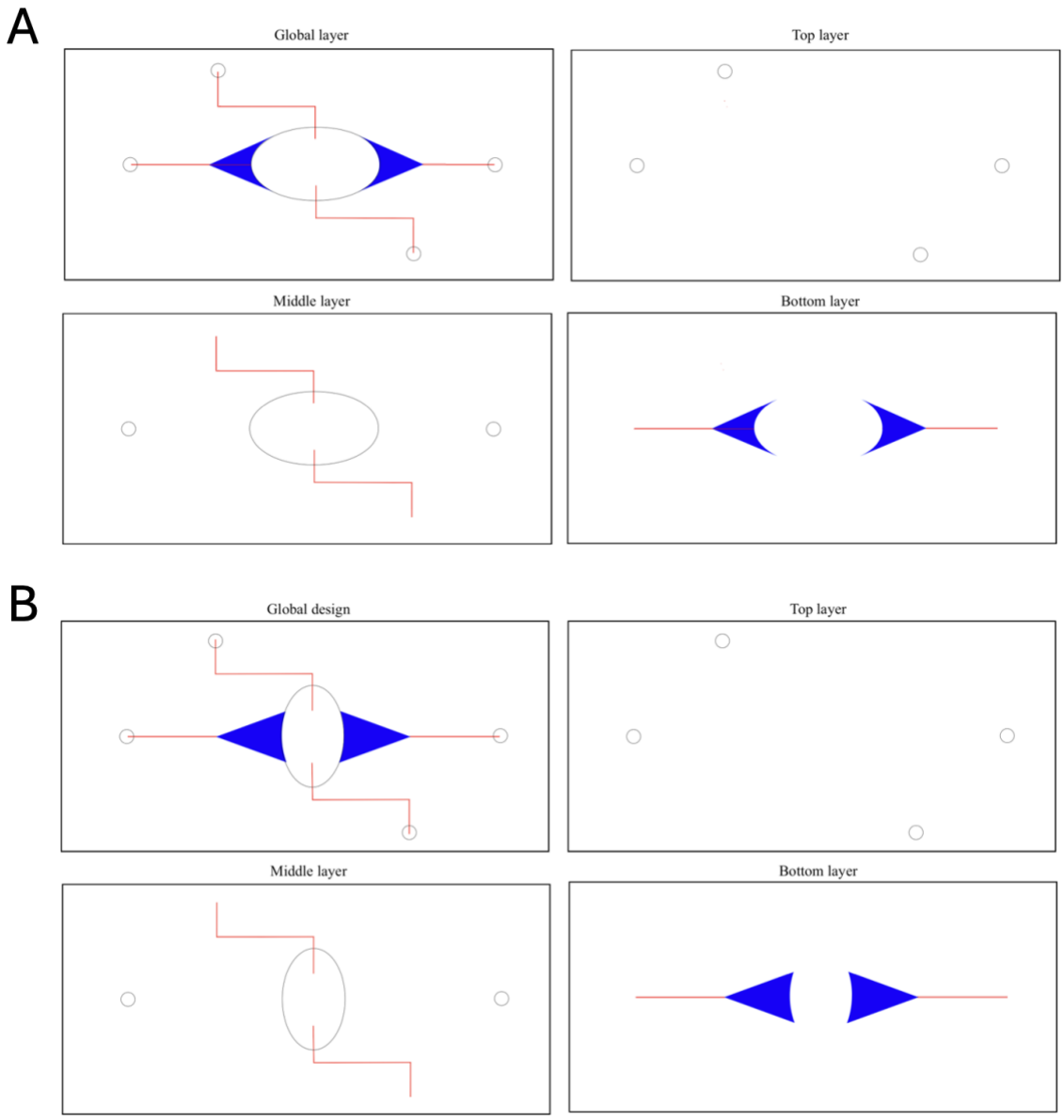

Figure 5.5. Variations of the first design to solve the sinkhole formation in the culture chamber.
Schematic representation of chip design with funnel-like channels, either by changing the shape (A) or the orientation (B) of the microchamber. (Black) represents cutting mode, (Red) engraving mode, and (Blue) rast mode. The chamber was designed for a final size of 25.4 mm x 14.5 mm (w x h).

Without successfully resolving the collapse issues, more drastic changes were implemented, including reducing the size (**Figure 5.6,** panel A) and altering the shape of the culture chamber (**Figure 5.6,** panels B and C) by incorporating support "pillars" and changing the shape (square vs. rectangular) and size of the device (**Figure 5.6,** panels B and C).

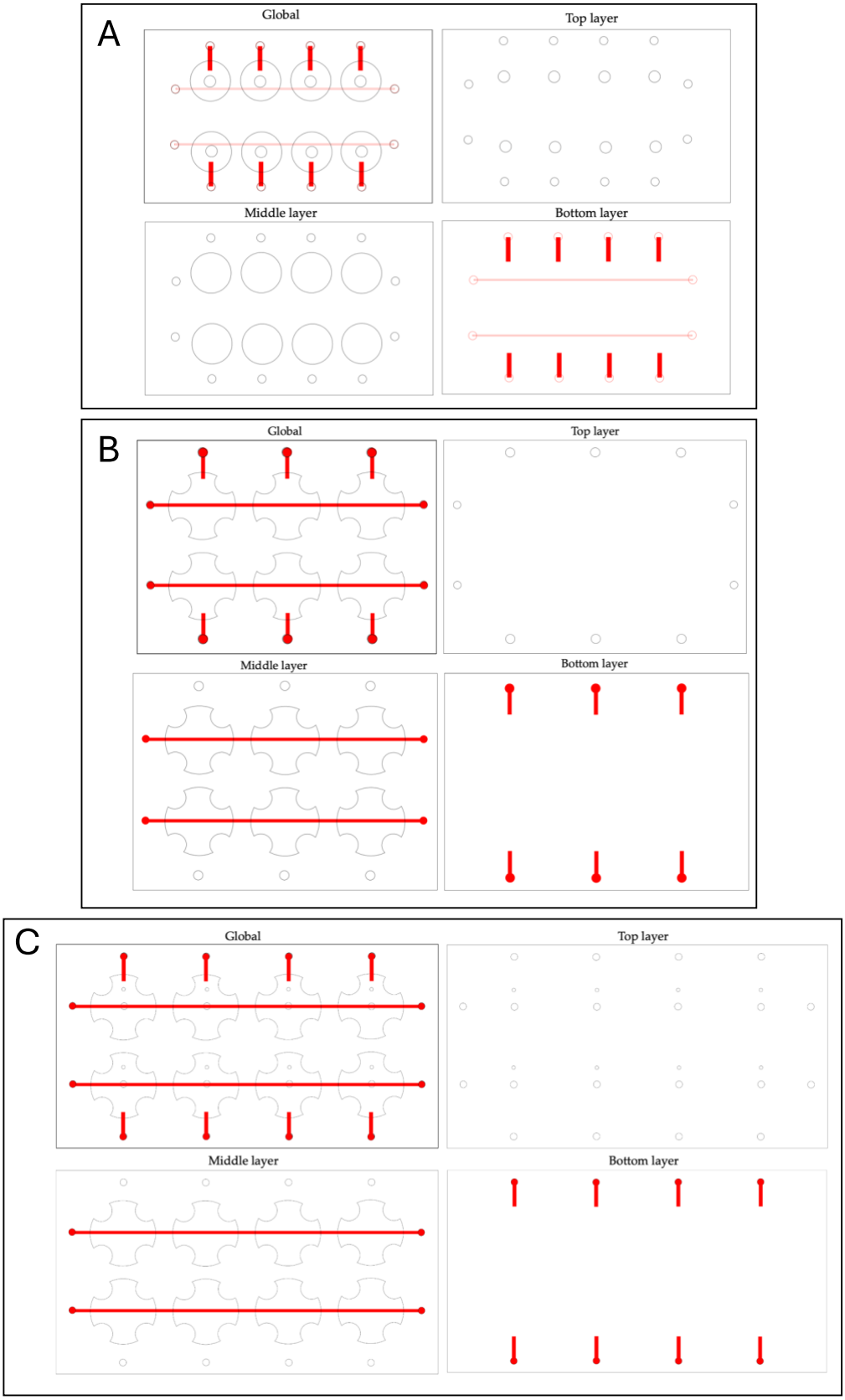

Figure 5.6. Patterning of the biochips conceptualized to prevent sinkholes.

(Black) represents cutting mode, (Red) engraving. (**A**) The microchip was designed by cutting 4 layers of rectangular shape with 129.06 x 77.50 mm (w x h), for a final size of 5.4 x 3.02 cm (w x h). Each of the 8 culture chambers has a diameter of 18.06 mm (7 mm final size). The microchannels for medium perfusion have two parallel lines spaced by 0.52 mm, which, after heat shrunk, give rise to 200 µm channels, and the channels for cell recovery were designed with a thickness of 2.38 mm aiming at a final width of 900 µm. (**B**) The microchip was designed for increased size and a lower w x h ratio. Square-like patterns were cut with dimensions of 178.30 x 127.07 mm (w x h), aiming for a final size of 7.0 x 5.0 cm (w x h). Each of the 6 culture chambers has a diameter of 40.0 mm (15.6 mm final size). The microchannels for medium perfusion have two parallel lines spaced by 1.86 mm, which, after heat shrunk, give rise to 720 µm channels, and the channels for cell recovery were designed with a thickness of 2.38 mm aiming at a final width of 900 µm. (**C**) Each layer is composed of rectangles measuring 232.97 x 124.39 mm (w x h), for a final size of 9.1 x 4.86 cm (w x h). Each of the 8 culture chambers has a diameter of 40.0 mm. The microchannels for medium perfusion have two parallel lines spaced by 1.86 mm, which, after heat shrunk, give rise to 720 µm channels, and the channels for cell recovery were designed with a thickness of 2.38 mm aiming at a final width of 900 µm.

Although these designs did not eliminate the sinkholes, they offered valuable insights for further improvements. One key finding was the need to incorporate additional ventilation holes to prevent bubbles from forming inside the chambers. Moreover, using a rectangular shape consistently improved the device's overall straightness. Finally, reducing the size of the device enhanced its stability and reproducibility, likely due to the increased strength per cm^2 applied during the layer bonding process (**Figure 5.7)**.

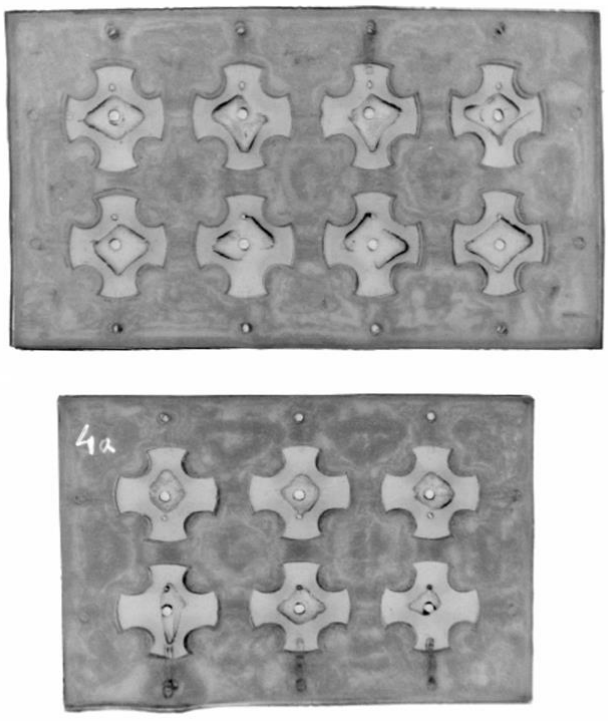

Figure 5.7. Biochips are designed with different culture chambers and sizes after shrinkage.
The images were obtained on a transilluminator using the bright light mode. The defects observable in the center of each culture chamber are caused by the sinkholes, leading to optical defects.

To address the issue of sinkholes while maintaining a similar volume capacity to 96-well plates, it was necessary to reduce the size of both the device and culture chambers while increasing their height. This was achieved by adding an additional layer with in-depth cuts for the chambers. However, this modification further weakened the support of the top layer, causing sinkholes to persist. To resolve this, an additional top layer with the same pattern was introduced, increasing the thickness of the sealer layer. This enhancement significantly improved the device's overall stability and effectively eliminated the sinkhole problem (**Figure 5.8**).

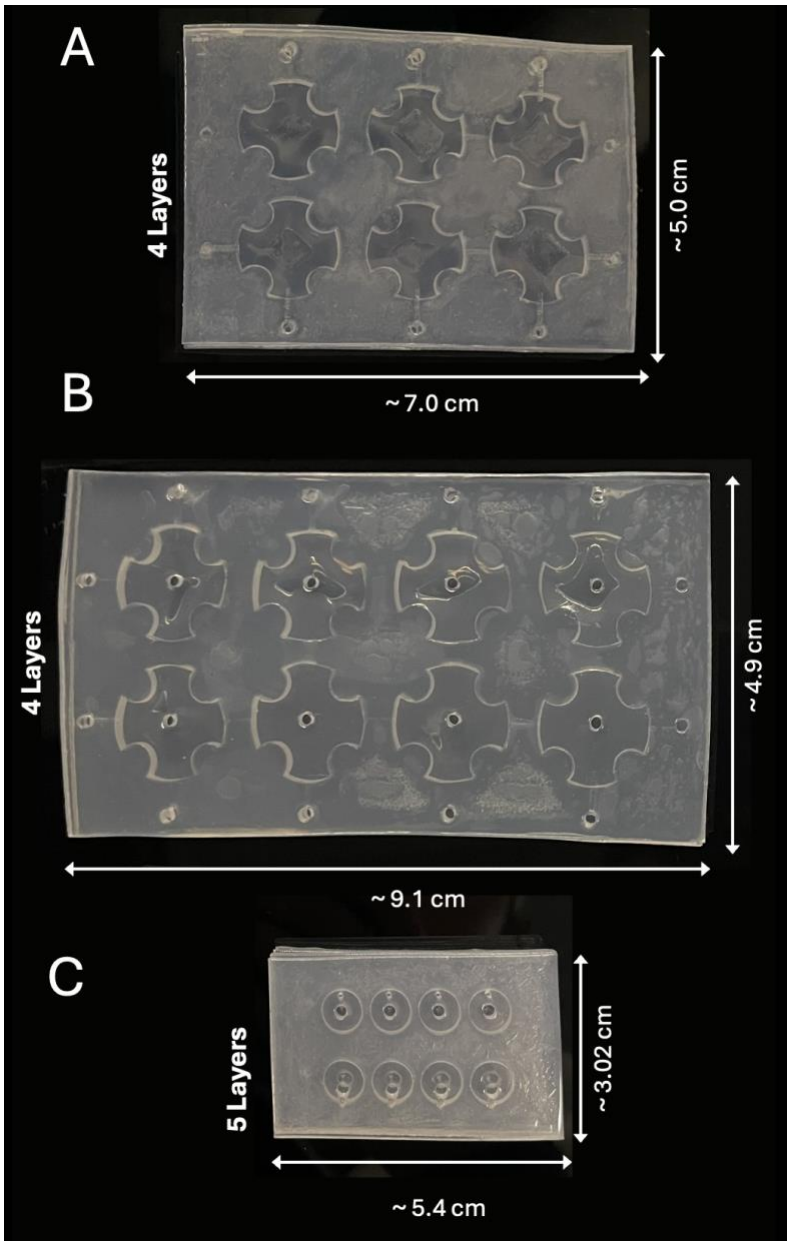

Figure 5.8. Biochip size after shrinkage.
The images were obtained with the camera of an iPhone 12 Pro. The defects in the center of each culture chamber on chips A and B are caused by the sinkholes, causing the optical defects. Chip C does not present sinkholes in

any of the wells due to the addition of an extra layer (5 layers) and the overall reduction in the size of the chip and culture chambers.

To focus on improving the stability of the biochip and eliminating sinkholes, a simplified design was developed, omitting the microchannels for medium perfusion. Instead, individual inlets/outlets were added to each microwell for medium infusion using an insulin needle (smaller holes in Layers 1 and 2) (**Figure 5.9**).

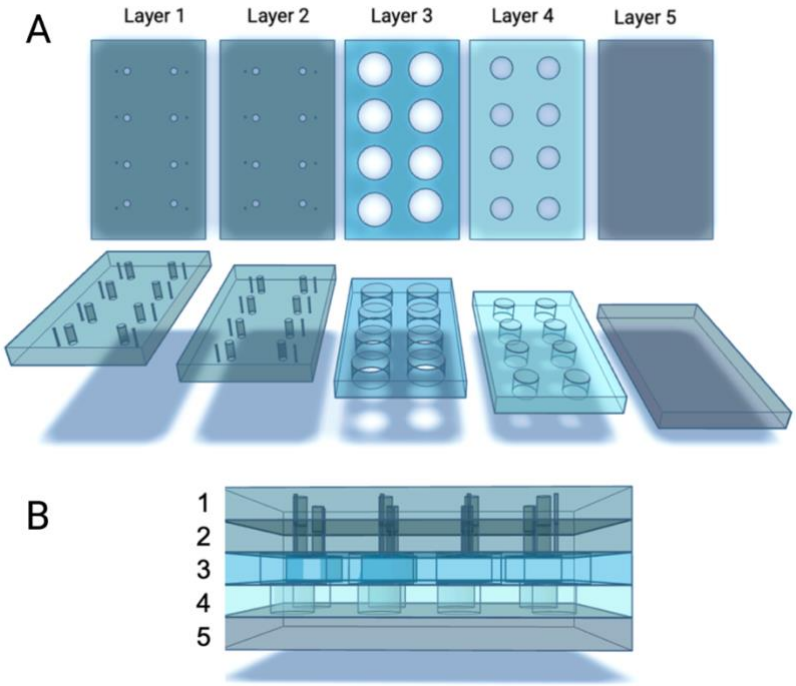

Figure 5.9. Schematic representation of the final design.
(**A**) Schematic representation of layer partnering and assembly order. Layer 1 and 2 - Top layers (Layer 2 for enhanced stability); Layer 3 – All in-depth wells with higher diameter; Layer 4 – All in-depth wells with lower diameter to promote cell aggregation; Layer 5 – Sealer and surface for cell adherence. (**B**) Cross-section view of the assembled layers.

Having accomplished the production of a functional device, the next steps were aimed at assessing the biocompatibility of the biochip's material with cell maintenance and growth. Since the inclusion of microchannels added unnecessary complexity to the device's operation, the simplified design was chosen for subsequent studies. To facilitate data correlation from on-chip assays, the size of the culture chambers was adjusted to match the volume capacity of a standard 96-well plate (100µL). Consequently, the biochip design incorporated reservoirs with a surface area of approximately 0.32cm², consistent with the wells in a standard 96-well plate. Considering the previous shrinkage results, the PS slabs were engraved with proportions 2.5 times larger than the desired final size (Width = 7 75cm; Length = 12.9cm; Height = 0.13cm) (**Figure 5.10**) (651,652). After shrinking, the biochips showed an isotropic reduction of 60 % regarding the original width and length dimensions (Width = 3.11 ± 0.08cm; Length

= 5.08 ± 0.10cm), accompanied by a corresponding 6-fold increase in height (Height = 0.83 ± 0.04cm) Overall, the proposed design yields the formation of reservoirs with a surface area similar to that of the wells on a 96-wells microplate (0.38±0.02cm^2), entailing a volume of approximately 80.9 ± 0.5µL (**Figure 5.10,** panel C).

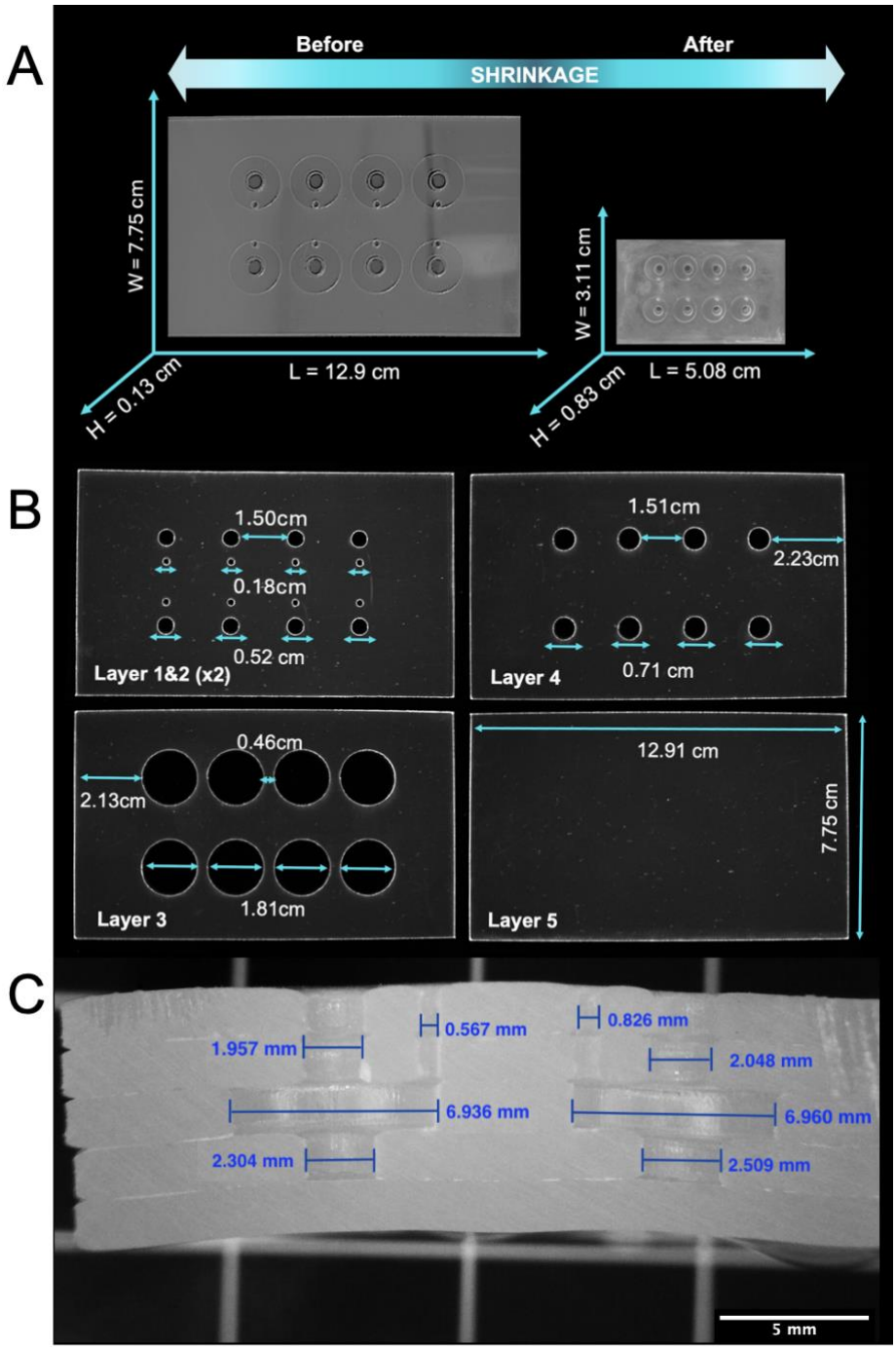

Figure 5.10. Biochip patterning and size characterization before and after the shrinking process.
(**A**) Size of the biochips before and after the shrinking process. The images of the biochip were obtained using the camera of an iPhone 11Pro. (**B**) Size of the patterns of each layer of the biochip before the shrinking. The images of the layers were obtained on a transilluminator using the bright light mode. (**C**) Image a transversal section of

the biochip after shrinkage with the measurements of the chambers. The image was obtained using a high-resolution camera.

This design facilitated the correlation of data with conventional 96-well plates while preventing cross-contamination between wells and promoting the formation of typical cell-cell interactions in 3D structures. These conditions were achieved by incorporating independent reservoirs with a U-shaped configuration. Since the biochip was devised to optimize cell seeding and proliferation kinetics for both 2D and 3D cell models, the next steps involved assessing suitable sterilization and surface functionalization processes for cell culture.

5.3.3 Biochip Surface Modification

The surface characteristics of a chip influence cell adherence and viability, which are crucial for cell morphology, physiology, and cell responses. To improve cell adherence, one may alter the surface topography, chemistry of the materials, and mechanical stiffness. Herein, we tested two different approaches: i) topographical changes, such as grooves, ridges, or patterns (easily crafted with laser ablation) were created on the bottom of the reservoir to increase the roughness of the surface and provide more anchoring points, facilitating cell adherence and promoting cell alignment. However, the creation of this uneven surface topography also reduced the optical transparency of the reservoirs, leading to optical defects that impaired the acquisition of microscopic images with fair quality (647); and ii) chemical alteration of the surface through coating with functional groups, biomolecules, extracellular matrix proteins, or immobilizing cell-adhesive peptides have been reported to provide essential cues for cell attachment and proliferation (654). To this end, DMEM medium supplemented with 10 % (v/v) FBS was added to the reservoirs of the biochip, 24 hours before cell seeding. FBS contains hundreds of different components, including growth and attachment factors, hormones, and extracellular matrix proteins, which collectively enhance cell attachment, proliferation, and survival (655,656) (**Figure 5.11**).

FBS has been proposed as a simple agent for coating surfaces in cell culture. When used as a coating, FBS forms a bioactive surface that closely mimics the natural extracellular matrix, promoting the adhesion of tumor cells to the biochip's substrate. This improved adhesion is critical for maintaining cell viability and morphology, enabling the cells to exhibit more physiologically relevant behaviors (**Figure 5.11,** panel A). Additionally, FBS coating supports the establishment of cell-cell and cell-matrix interactions, which are crucial for studying tumor growth, metastasis, and drug responses. Therefore, FBS coating significantly enhances the reliability and functionality of tumor-on-chip devices, making them invaluable tools for cancer research and therapeutic development (361,657).

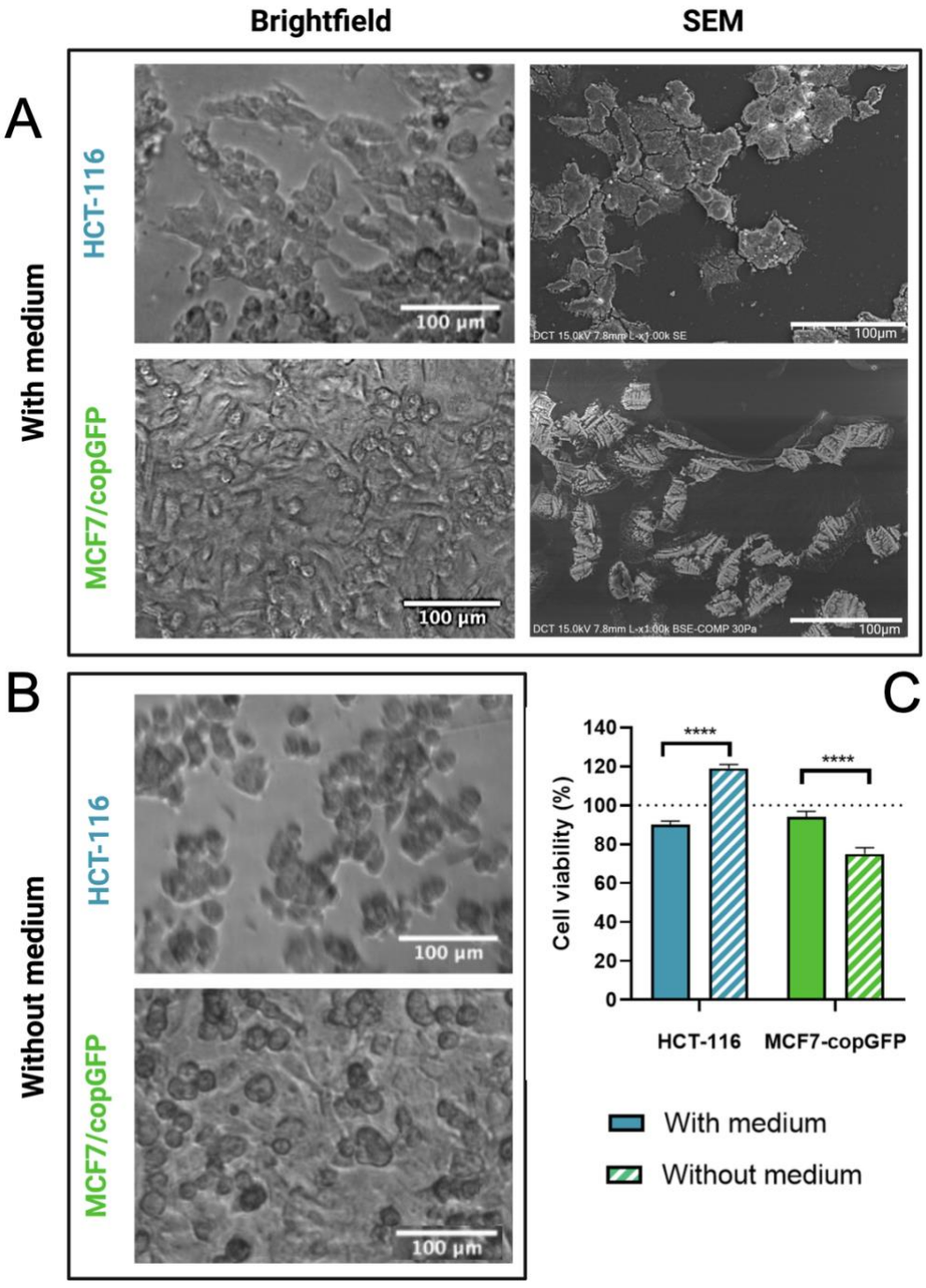

Figure 5.11. Effect of surface modification of the biochip on cell adhesion.
Microscopy images of HCT-116 and MCF-7/copGFP cells seeded into the biochip (**A**) with surface functionalization with DMEM + 10 % (v/v) FBS and (**B**) without surface functionalization. Brightfield images are on the left panel, and Scanning Electron Microscopy (SEM) images are on the right panel. (**C**) Viability results of HCT-116 (■) and MCF-7/copGFP (■) cells, 24 h after seeding on the biochip with (full bars) and without surface functionalization (stripped bars). Bars are the result of 3 independent biological replicate,s and the error bars are the respective Standard Error Mean. Statistical analysis was performed using Two-way ANOVA and Sidak's multiple comparison test. The results were considered statistically significant for p values < 0.05. (*) represents p < 0.0332, (**) represents p < 0.0021, (***) represents p < 0.0002 and (****) represents p<0.0001.

Results from the brightfield and electronic microscopy images and the MTS assay (**Figure 5.11**) showed significant differences in both cell viability and morphological features when the biochip was previously coated with medium (DMEM+10 % FBS). Cells seeded in the reservoirs previously incubated with DMEM+10% FBS display a spread-out morphology under monolayer conformation, with the presence of focal adhesions and the formation of junctions between neighboring cells, which are typical features of the cell adhesion processes (655,658) (**Figure 5.11,** panel A). Conversely, cells immediately seeded into the biochip, after the sterilization process, showed decreased cell spreading and a rounder morphology, which can be attributed to the reorganization of the cytoskeleton under stress (**Figure 5.11**, panel B) (659,660).

Furthermore, the results from the MTS assay show a decrease in the viability to 75 % of MCF-7/copGFP cells seeded into biochips without surface coating (**Figure 5.11,** panel C). The increase in cell viability (119 %) for HCT-116 cells can be attributed to adaptative response to stress, often promoting the mitochondrial activity and, therefore, resulting in higher metabolic conversion of the MTS reagent, leading to higher absorbance values at 490nm (**Figure 5.11**, panel C) (661). Together, these data corroborate the relevance of prior surface coating to prevent cellular stress and promote cell adherence.

5.4 Conclusions

In this chapter, we introduced a straightforward, rapid, and highly reproducible protocol for fabricating cell-culture platforms in under 10 minutes. Besides the rapid fabrication process, the biochip requires only a simple surface functionalization step to support cell viability comparable to that of standard plate-based cultures. The biochip was designed with eight independent reservoirs, each with a surface area comparable to the wells in standard 96-well plates (0.38cm^2). Relying on thermosensitive polystyrene, with its retractable nature, facilitates a 60 % reduction in the biochip's size relative to the original engraved dimensions. This shrinking property allows for engraving patterns with dimensions below the resolution capabilities of conventional engraving machines, such as laser printers (652). Achieving the final design involved several iterations, yet the only additional cost was the polystyrene slabs. By eliminating the need for masks, molds, and clean-room facilities, this process significantly accelerates the whole fabrication process while enabling on-demand design modifications to meet experimental requirements. These features effectively address the major limitations of ToC models: the high fabrication time and costs and the lack of design flexibility without incurring substantial expenses, which have hindered the transition from standard plate-based cultures to cutting-edge chip-based models.

Despite their immense potential, ToC models have faced limited adoption due to fabrication and operational complexities, especially in biology-oriented labs. So, simplifying the fabrication and

operation processes to enable rapid, economical modifications is crucial. This will facilitate the wider adoption of ToC models, leading to more successful cancer studies as researchers transition to more complex, physiologically relevant models. Ultimately, our novel fabrication process paves the way for more accessible ToC platforms, driving advancements in the field of cancer research.

6

ADVANCING CANCER RESEARCH BY TRANSITIONING GENE SILENCING ASSAYS TO TUMOR-ON-CHIP MODELS

Part of the data enclosed in this chapter was originally published in the following issue:

- **Oliveira, B.B**., Fernandes, A.R. and Baptista, P.V., (2024). Shrinking Cancer Research Barriers: Crafting Accessible Tumor-on-Chip Device for Gene Silencing Assays. *Advanced Engineering Materials,* 2402254. https://doi.org/10.1002/adem.202402254

I was responsible for designing and performing all the experiments. The optimization of growth conditions and silencing were also performed by me.

6.1 Introduction

Advancements in cancer biology, particularly the development of novel therapeutic approaches, hinge on the accuracy and relevance of the experimental models used (662). Traditional 2D cell cultures, though widely utilized in drug screening and toxicity studies (273–275,663), fall short in replicating the intricate conditions of the tumor microenvironment (664,665). *In vivo,* tumors are subjected to complex dynamics, including cell-cell and cell-matrix interactions, along with diffusion gradients of oxygen, nutrients, and signaling molecules, which are not accurately represented by 2D cultures (280,666).

Under the 2D conformation, cells grow in a monolayer, resulting in uniform exposure to nutrients, oxygen, and other molecules, thus failing to mimic the natural gradients found within a tumor (277,279,666). Additionally, the flat environment of 2D cultures forces cells to spread out and attach to the substrate rather than establish cell-cell interactions, which ends up altering their polarity, morphology, and behavior (579). These differences are likely the reason 2D cultures fail to provide accurate data on cell proliferation, differentiation, and drug responses (357,667).

In contrast, spheroids offer a more physiologically relevant model by forming three-dimensional cell aggregates that better resemble the tumor microenvironment (277,302,662). Spheroids exhibit diffusion gradients similar to those found in actual tumors. These gradients create a more realistic environment where cells in the spheroid periphery receive plenty of nutrients and oxygen, while those at the core experience hypoxic and nutrient-deprived conditions (275,668). This variation in exposure profiles influences cell behavior, proliferation rates, and gene expression patterns, contributing to a more accurate representation of tumor biology (283,284).

Research has shown that cancer cells grown in 3D conformations, such as spheroids, display different gene expression and mRNA splicing patterns compared to those grown in 2D cultures (283,357). For instance, genes related to cell cycle regulation, apoptosis, and drug resistance are often differentially expressed in 3D cultures (669–673). This discrepancy highlights the limitations of 2D models in predicting the *in vivo* behavior of cancer cells and underscores the importance of using 3D models for more accurate studies.

Tumor-on-chip models take the advantages of spheroids a step further by integrating microfluidic technology to simulate the dynamic environment of living tissues (353,662). These devices allow precise control over the microenvironment, including fluid flow, mechanical forces like shear stress, chemical gradients, and cellular interactions (674–679). This ability to mimic *in vivo* conditions more accurately makes Tumor-on-Chip models invaluable for studying cancer biology, particularly for exploring gene silencing and editing techniques and testing new drugs (445,466,622,680).

By providing a more realistic tumor microenvironment, Tumor-on-Chip models can improve the predictability of *in vitro* experiments and enhance the translational potential of research findings (356,360). This advancement is crucial for the successful development and testing of new cancer therapies, ultimately leading to better clinical outcomes (**Figure 6.1**) (356,358,361).

This chapter details the application of the previously developed biochip for modeling both 2D and 3D cancer cultures, as well as their subsequent use in gene silencing assays. The results demonstrate similar cell growth kinetics and gene silencing efficiency to those achieved with plate-based systems. This highlights the potential of simple chip devices to advance current modeling techniques, offering more sophisticated and realistic tumor modeling platforms.

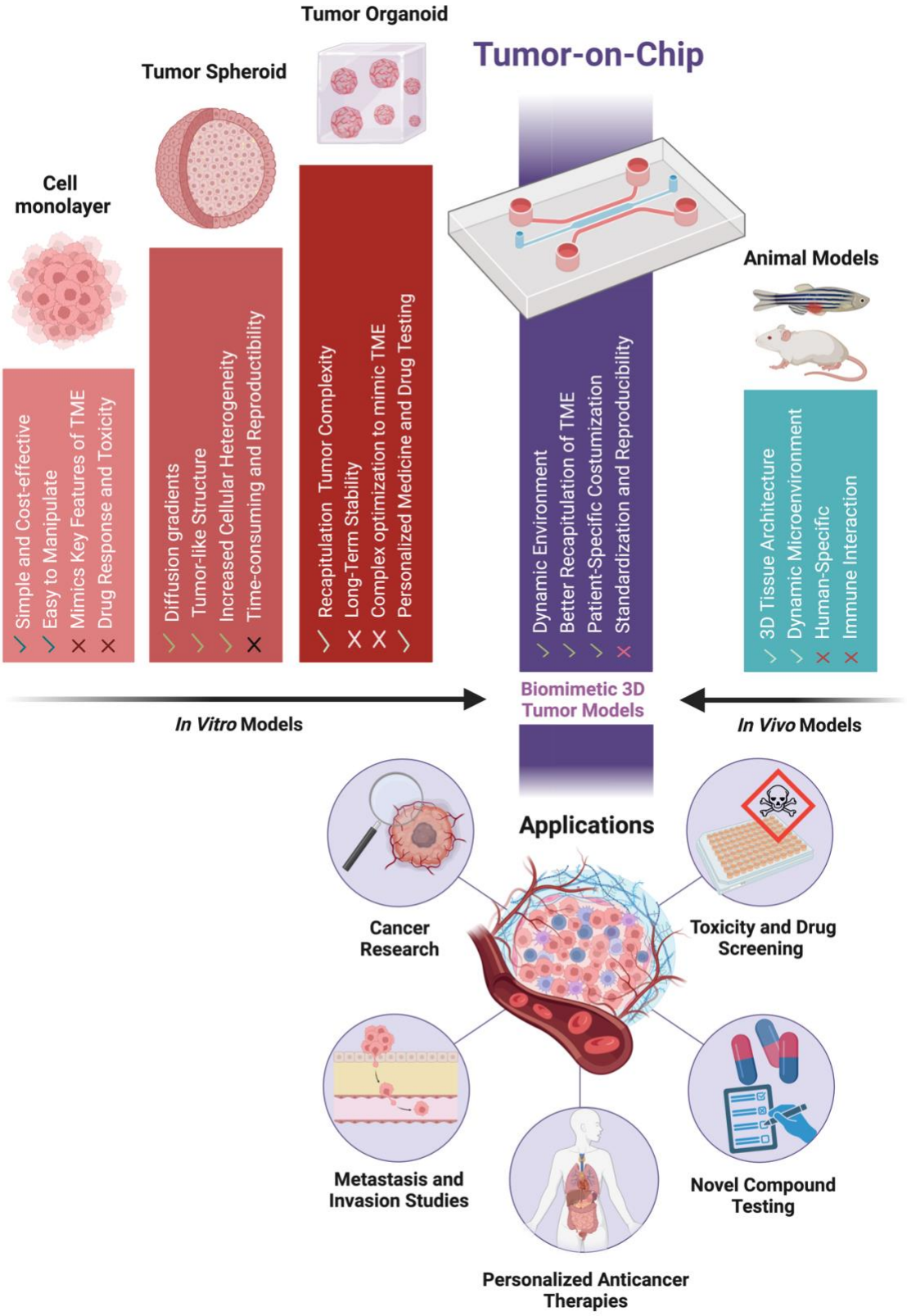

Figure 6.1. Bridging the gap in cancer research with Tumor-on-Chip models.
The recapitulative power of different cancer models: from *in vitro* cultures (cell monolayer, tumor spheroids, and tumor organoids) to *in vivo* models (animals). Advantages, hurdles, and main applications of Tumor-on-Chip

(cancer research, metastasis and invasion studies, personalized anticancer therapeutics, and drug development and screening).

6.2 Methods

To improve the readability of the present chapter, only the most relevant methods are detailed below. For detailed information regarding other methods and data treatment, see **Chapter Methods2.2.**

6.2.1 Cell Seeding and Growth on Biochip

Before cell seeding, the biochip surface was functionalized either with DMEM + 10%FBS to improve cell adherence (2D cell cultures) or with BIOFLOAT™ FLEX coating solution to prevent cell adherence (3D cultures) and incubated for 24 h at 37ºC on a CO_2 incubator. – For more details, see Chapter 2, Subsection **2.2.9Biochip Preparation.**

For cell seeding into the biochip, HCT-116 and MCF-7/copGFP cells are detached from the 25cm^2 culture flasks using Triple Express and centrifuged at 500 xg for 5 min. The pellet was resuspended in 1mL of DMEM medium, and the cells were counted using a hemacytometer. For on-chip 2D cell culture (HCT-116 and MCF-7/copGFP), each reservoir was incubated with 1x10^4 cells using an insulin syringe. For spheroid formation and growth, each reservoir was incubated with 5x10^3 HCT-116 cells. The biochips were then placed on a petri dish half-filled with distilled water at 37ºC in a CO_2 incubator. To promote spheroid formation, the biochips were placed in a circular shaker at 100 xg for 1.5 hours. This process was repeated for the length of spheroid growth (3 days).

For growth profiles, the cells were allowed to grow for 72 hours. After 24h periods, the cells were detached from the biochip for cell counting. For cell detachment, the cell medium was completely removed from the wells of the biochip, and cells were washed with PBS 1x. Following the removal of the PBS, the reservoirs were filled with Triple Express and incubated for 20 min at 37 ºC. After the incubation, the content from the 8 wells of the biochip was recovered to a 1.5 mL Eppendorf. The tube was centrifuged for 5 min at 750 xg. The pellet of cells was then resuspended in PBS 1x (100 uL). The cell suspension was then diluted 1:1 with Tripan Blue, and the solution was placed on a hemacytometer for cell counting.

6.2.2 Anti-copGFP Nanoconjugates Synthesis and Functionalization

The synthesis of AuNPs@Citrate and subsequent surface functionalization were performed as detailed in **Subsection 2.2.1.1**. Then, an ASOs sequence targeting the *copGFP* gene was added to the particles

in a 1:100 ratio, following the protocol used to produce the other ASOs-nanoconjugates as detailed in **Subsection 2.2.1.**

The obtained AuNPs@copGFP nanoconjugate was then characterized by UV-vis spectroscopy, DLS, and zeta potential.

6.2.3 *copGFP* Silencing Optimization on 2D-plate Cultures

The silencing effect of *copGFP* was performed using the MCF-7/copGFP cell line. These cells were seeded at a density of $0.5x10^5$ cells/well on a 24-well plate and allowed to adhere for 24h at 37 ºC in a CO_2 incubator. The optimal silencing condition was obtained by assessing different doses of the nanoconjugate (20nM, 50nM, and 100nM – concentration of ASOs, corresponding to 0.13nM, 0.32nM, and 0.64nM, of gold, respectively) and different incubation times (6h and 24h). Additionally, an AuNPs@PEG control matching the gold concentration to each of the silencing nanoconjugates was performed. All experiments also have a "Cells" control, where only DMEM medium was used.

The silencing of the *copGFP* gene was optimized following the conditions used by Daniela Ferreira for an siRNA (Nanomedicine Lab from NOVA School of Science and Technology).

6.2.4 Conditions for Chip-based Silencing Assays

Before incubating the cells/spheroids with the Au-nanoconjugates, the medium was withdrawn from the reservoirs using an insulin syringe, and then the respective concentration of each nanoconjugate was diluted in DMEM medium and infused back into the reservoirs of the biochip. During the challenge time, the biochips were incubated at 37ºC in a CO_2 incubator.

For the silencing assays on biochip, the cells, either 2D or 3D, were challenged for 6 hours using different gold nanoconjugates. HCT-116 cells (either 2D or spheroids) were incubated with 54nM of AuNPs@c-MYC (corresponding to 0.38nM of gold), for specific silencing of the *c-MYC* oncogene, while MCF-7/copGFP cells were incubated with 20nM of AuNPs@copGFP (corresponding to 0.13nM of gold) for specific silencing of *copGFP* gene. Additionally, both cell types were incubated with AuNPs@PEG, matching the gold concentration to each of the silencing nanoconjugates. All experiments also have "Cells" or "Spheroids" controls, where only DMEM medium was added to the wells. For each control, a total of 8 reservoirs were used.

6.2.5 RNA Extraction Protocol from Chip-based Cultures

A total of 8 reservoirs (1 biochip) were used per condition. The supernatant was removed from the reservoirs, and cells (and spheroids) were detached (or disintegrated) using TrypLE™ Express Enzyme (1X), which was incubated for 20 min at 37ºC. The cells were recovered from the reservoirs and placed in a 1.5mL Eppendorf. The pellets were then centrifuged for 5 min at 500xg (2D cells) or 1,000xg (spheroids), and then RNA was extracted using NZYol reagent, following the manufacturer's specifications.

Briefly, 250uL of TRIzol was added to the pellet of cells and then vigorously mixed in a vortex. Then, 50uL of chloroform was added and incubated at room temperature for 10 minutes. Following the incubation, the mixture was centrifuged at 12,000xg for 15 min at 4ºC. The upper phase was carefully recovered to a new Eppendorf tube, and an equal volume of isopropanol was added. Then, the solution was incubated overnight at -20ºC. Following the incubation, a 12,000xg centrifugation for 15 min at 4ºC was performed. The supernatant was discarded, and the pellet was washed with 70% ethanol (v/v) on DEPC-treated water. The ethanol was removed by centrifugation at 7,500xg for 10 min at 4ºC. This washing step was performed twice. Finally, the pellet was air-dried and then resuspended in DEPC-treated water. After extraction, the integrity of the RNA was assessed by electrophoresis in a 1% agarose gel, and the concentration of the RNA was quantified on NanoDrop.

6.2.6 mRNA Expression Analysis (RT-qPCR)

The RT-qPCR conditions for the detection of the mRNA expression of both *c-MYC* and c*opGFP* genes and subsequent data analysis are detailed in Section **2.2.5.2.**

6.2.7 Immunofluorescence

The silencing effect of the Au-nanoconjugates was also assessed at the c-MYC and copGFP protein levels via immunofluorescence microscopy. Following the challenge, cells were fixated either on the biochip or in a 24-well plate using a solution of 4% PFA in PBS 1X and incubated for 20 min at room temperature. Subsequently, cells were permeabilized with 0.1% (v/v) Triton X-100 solution for 10 minutes at room temperature. Next, the blocking step was performed with 1% (w/v) BSA in a PBS-Tween solution and incubated for 30 min at room temperature. For HCT-116 cells, the primary antibody, Rabbit anti-c-MYC antibody (1:100 dilution), was incubated overnight at 4ºC. After overnight incubation, cells were washed 3 times with PBST solution and then incubated with the respective secondary antibody: Anti-rabbit IgG (FITC) produced in goat (1:100 dilution) for 1 hour at room temperature. The secondary antibody was washed 3 times with PBS 1X. For MCF-7/copGFP, no

antibody was used since the copGFP protein is naturally fluorescent. Finally, both cell lines were stained with 7.5 µg/mL of Hoechst dye (nucleolus staining) for 15 min at room temperature. Following the incubation with Hoechst dye, cells were washed 3 times with PBS 1X.

6.2.8 Microscopy Imaging

The fluorescence images were acquired with an inverted microscope, using the DAPI filter with 200ms of exposure time for Hoechst dye, and the FITC filter with 2sec of exposure time for FITC beacon and copGFP fluorescent signals. ImageJ software was used to obtain the CTCF values of each fluorescence channel (Green for c-MYC and copGFP proteins; Blue for Hoechst dye). The CTCF values were obtained using the formula: CTCF= Integrated Density - (Area of selected cell x Mean fluorescence of the background). The final fluorescence ratio was obtained by dividing each condition by its control.

6.3 Results and Discussion

6.3.1 Cell Seeding on the Biochip

Assessing the therapeutic effects of novel compounds or systems typically involves growing cells in a controlled environment where their growth patterns, drug responses, and cellular interactions can be meticulously observed and compared to standard counterparts. Understanding the growth and proliferation dynamics of cancer models is crucial for accurately determining dosages and ensuring successful translation to more complex models or cell lines. Recent studies have shown that a comprehensive understanding of the growth dynamics of spheroids and Tumor-on-Chip models helps predict how cancer cells will behave in more advanced biological environments, leading to more reliable and consistent results (681–684). This highlights the necessity of previously assessed growing profiles when introducing new models or platforms. By doing so, these new platforms might start having a real shot at advancing applications in research phases for clinical settings.

Since the volume capacity of the biochip's reservoirs is comparable to that of a 96-well plate, the seeding and growth conditions were optimized to align with those of plate-based systems. For the initial assessments, MCF-7/copGFP cells were chosen because their intrinsic GFP expression allows for easy visualization and tracking of cell growth and confluency.

MCF-7/copGFP cells were seeded at a density of $1x10^4$ cells per reservoir, targeting approximately 80% confluency, akin to a standard 96-well plate. Cell density was monitored over three days at 24-hour intervals and further compared to that in a standard system (**Figure 6.2**). A preliminary analysis of the

results showed that the growing dynamics of cells cultured on the biochip closely mirrored those reported in the literature for 2D cultures growing in traditional well-plate systems (685).

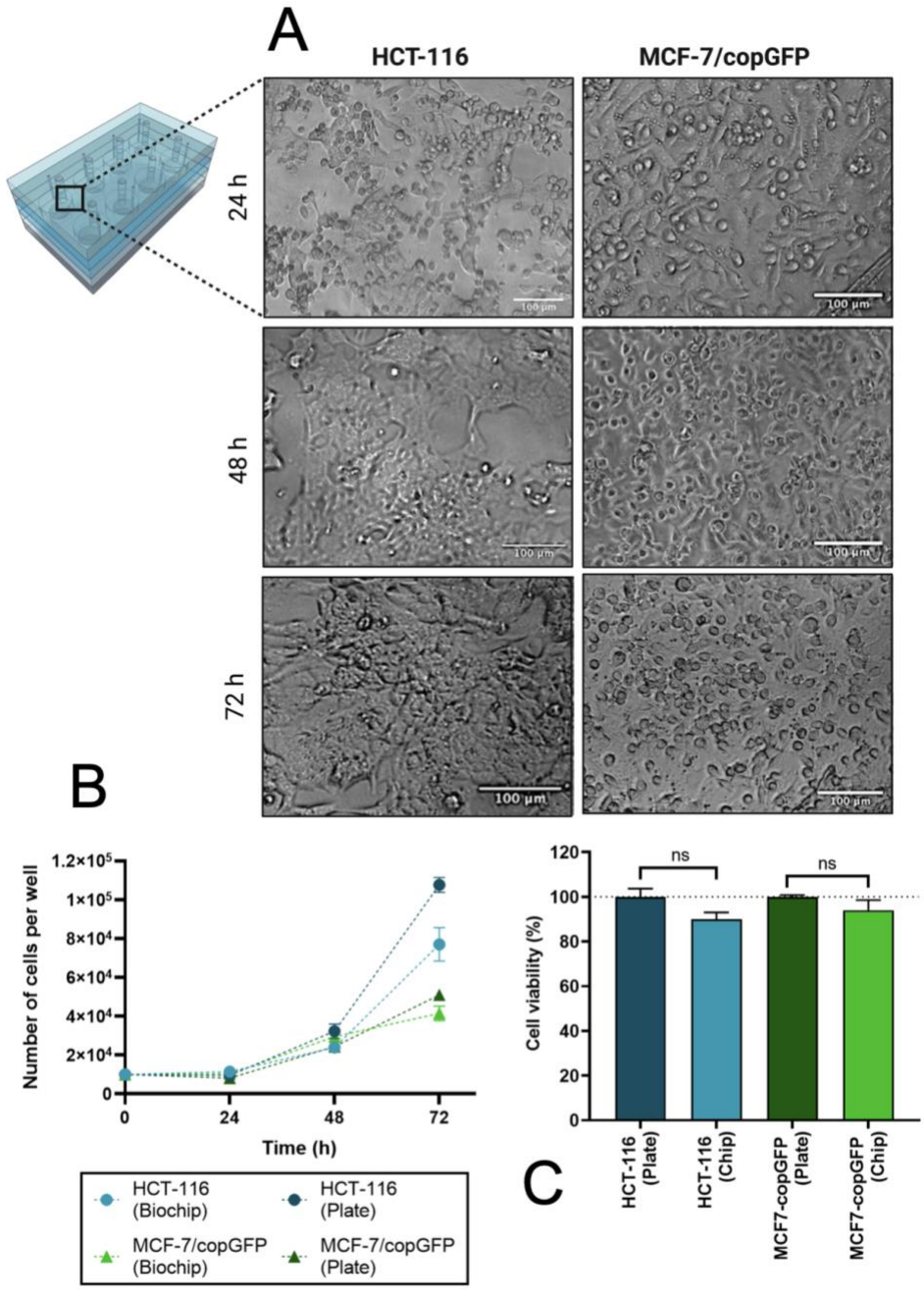

Figure 6.2. Cell growth on biochip.
(A) Brightfield microscopy images of HCT-116 and MCF-7/copGFP cells seeded on the biochip for 3 days of growth. The scale bar is 100µm. **(B)** Results of cell count on biochip and 96-well plates after 24h, 48h, and 72h of seeding. The initial seeding was performed using $1x10^4$ cells per well. The number of HCT-116 cells is represented by (●) on the biochip and (●) on the 96-well plate. For MCF-7/copGFP cells, (▲) represents the cells on the biochip and (▲) the cells on 96-wells. **(C)** HCT-116 and MCF-7/copGFP viability after 24h of seeding in the plate versus the biochip. The bars represent the average of 8 biological replicates, and the error bars are the standard

error mean. Statistical analysis was performed using One-way ANOVA and Sidak's multiple comparison test. The results were considered statistically significant for p values < 0.05.

It was necessary to ensure that the cells exhibited the expected morphology, proliferation rate, viability, and physiological behavior. Microscopy images corroborate that the biochip supports cell growth, which is denoted by the decrease in the gaps between cells, resulting in the formation of a 2D-cell monolayer, typical of adherent cells (**Figure 6.2,** panel A). Additionally, a shift in cell morphology is observed, transitioning from rounded shapes (commonly linked to non-adherent phenotypes and stress responses) to more elongated forms, potentially signaling the establishment of focal adhesions and improved cell adherence (686,687). Cell counting results also showed a comparable number of cells and duplication rate for both culture systems until 48 hours after seeding, once again denoting appropriate cell survival and growth. Afterward, the cells seeded into plates showed a continued increase in growth, probably due to the larger surface area and volume of medium in the microtiter plate, supporting more nutrients for cell growth (**Figure 6.2**, panel B). Finally, the cell viability results obtained with the MTS assay revealed no significant cytotoxic effects on cells growing in the biochip when compared to the plate (**Figure 6.2**, panel C). These findings demonstrate that the biochip offers a comparable microenvironment to standard plate-based systems, ensuring reliability and consistency when comparing experimental results across different models (688,689).

Still, to avoid any bias due to cell numbers and allow a seamless comparison of results between the biochip and plate-based systems, the subsequent experiments were performed 24 hours after seeding (when both systems hold an equivalent number of cells).

6.3.2 Gene Silencing on the Biochip

After confirming the biochip's ability to support 2D cell growth, its suitability for gene silencing experiments was further assessed. To this end, new Au-nanoconjugates targeting the *copGFP* gene in MCF-7/copGFP cells were developed and thoroughly characterized (**Figure 6.3**). The results revealed similar physicochemical properties, such as size, surface charge, and LSPR band, to those of the previously validated Au-nanoconjugates effective in silencing the *c-MYC* gene. These findings further confirm the suitability of the anti-copGFP nanoconjugates for future challenge assays.

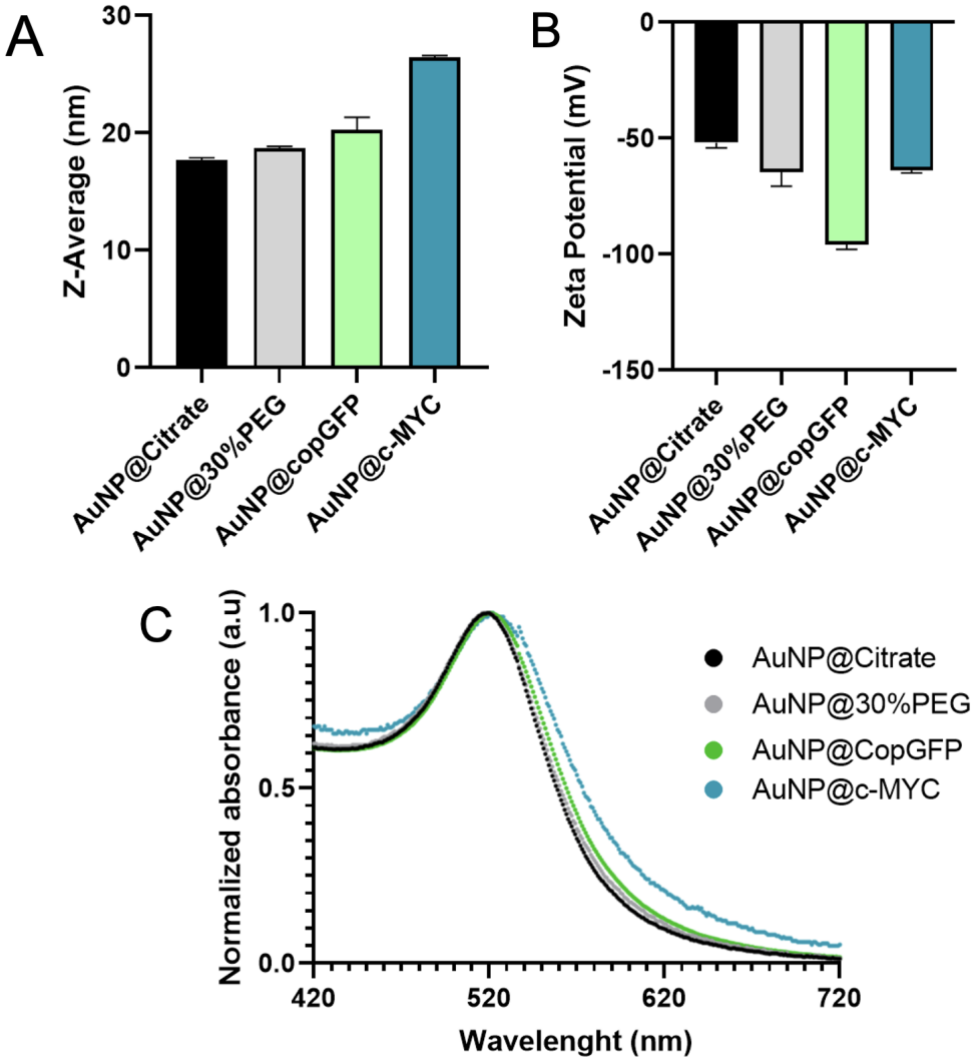

Figure 6.3. Characterization of Au-nanoconjugates for *copGFP* silencing assays.
(**A**) Dynamic Light Scattering (DLS) results were attained for the different nanoconjugates. (**B**) Zeta potential results were attained for the different nanoconjugates. The error bars represent the standard deviation for 3 different batches of particles, each with 3 independent measurements. (**C**) Normalized UV-vis spectroscopy results. All nanoconjugates showed the maximum peak corresponding to the Surface Plasmon Resonance (SPR) peak at 520 ± 2nm.

Similarly to what was performed for the other Au-nanoconjugate (see Chapter 3, *Subsection **3.3.2***), the optimal silencing condition was first assessed on cells cultured in a standard well-plate system (**Figure 6.4**). Based on work reporting the silencing of *copGFP* with a siRNA, three ASOs concentrations (20nM, 50nM, and 100nM) and two challenge times (6h and 24h) were evaluated (690,691), in terms of *copGFP* silencing efficiency and cell viability.

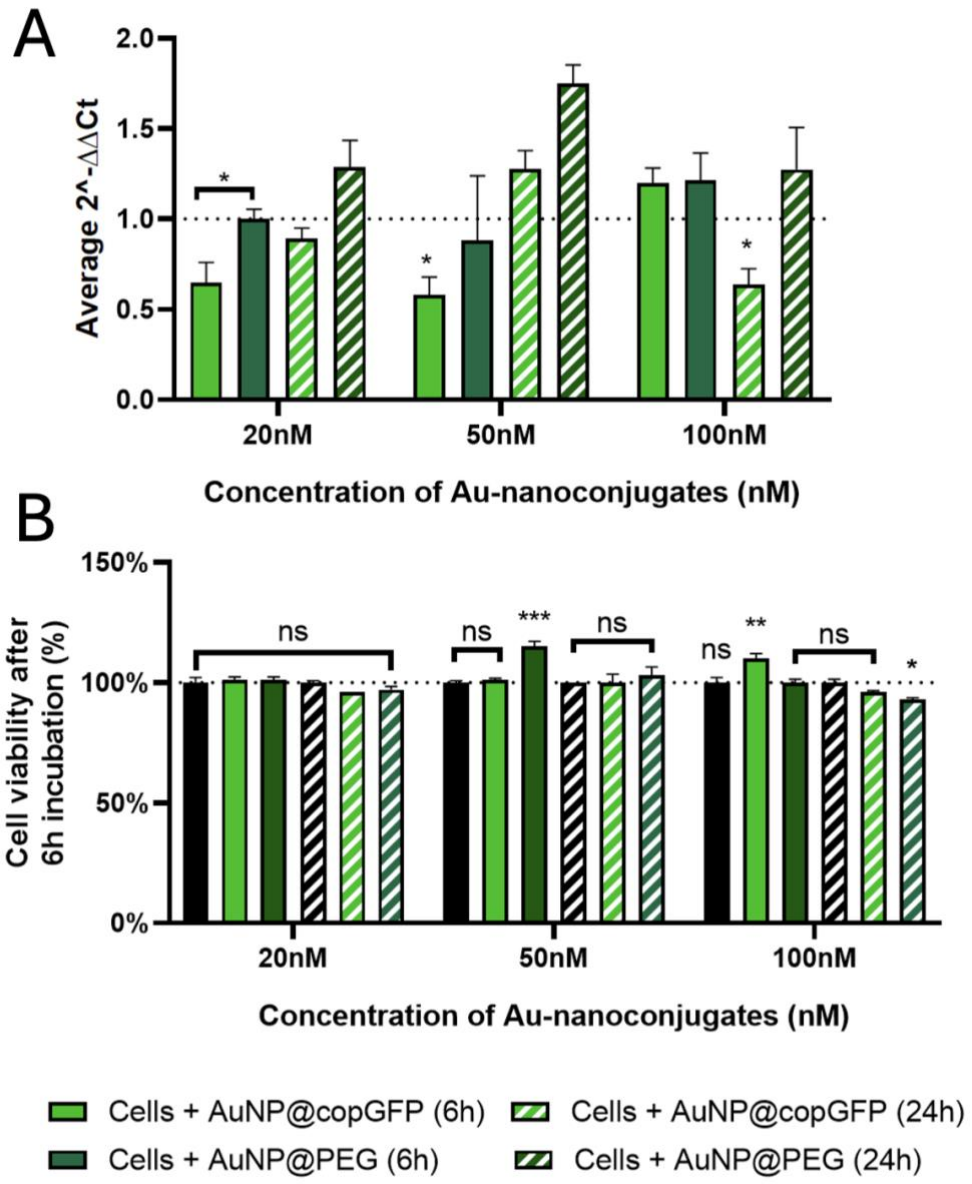

Figure 6.4. 2-△△CT and cell viability results of *copGFP* silencing conditions.
MCF-7/copGFP cells were challenged using concentrations of anti-copGFP oligonucleotide ranging between 20nM to 100nM for **(A)** Average $2^{-\Delta\Delta CT}$ results of *copGFP* silencing. Statistical analysis was performed using Two-way ANOVA and Sidak's multiple comparison test. The silencing results were considered statistically significant for p values < 0.1, corresponding to 90% confidence. (*) represents 0.1 < p values <0.05 and (**) 0.01 < p value < 0.001. **(B)** MTS assay results after the incubation of MCF-7/copGFP cells with different concentrations and challenge time points with each nanoconjugate. MCF-7/copGFP cells (■) were incubated with AuNPs@copGFP (■) and AuNPs@PEG (■) nanoconjugates. (Full bars) represent 6h of challenge, and (Crossed bars) represent 24h of challenge. Bars are the result of 3 independent biological replicates with 2 technical replicates, and the error bars are the respective Standard deviation. Statistical analysis was performed to assess cell viability differences to "Cells control using Two-way ANOVA, the results were considered statistically significant for p values < 0.05. (*) represents $p \leq 0.0323$, (**) represents $p \leq 0.0021$.

From the six conditions tested, only three showed effective gene downregulation, accounting for ~35% of suppression. (**Figure 6.4,** panel A). Most conditions did not significantly alter cell viability. In some conditions, only a very mild stress response (viability above 100%) or death (below 100%) was observed (**Figure 6.4,** panel B). Still, to minimize the impact on cells, while showing effective gene downregulation, the condition requiring the lower dose of Au-nanoconjugates (20nM) and incubation time (6 h) was then used for silencing the *copGFP* on-chip (**Figure 6.5**).

The results obtained for *copGFP* silencing on the biochip demonstrated equivalent silencing efficiencies to those obtained using standard well-plates (~32%) (**Figure 6.5,** panel A). Additionally, the protein-level analysis also confirmed this similarity, as GFP-associated fluorescence measurements revealed a comparable reduction in the fluorescence of cells cultured on the biochip (27%) and those in a standard 96-well plate (29%) (**Figure 6.5,** panels B and C). These findings indicate that the biochip successfully replicates the cell growth environment of standard plate-based systems, maintaining not only similar growth and survival rates but also consistent gene and protein expression patterns.

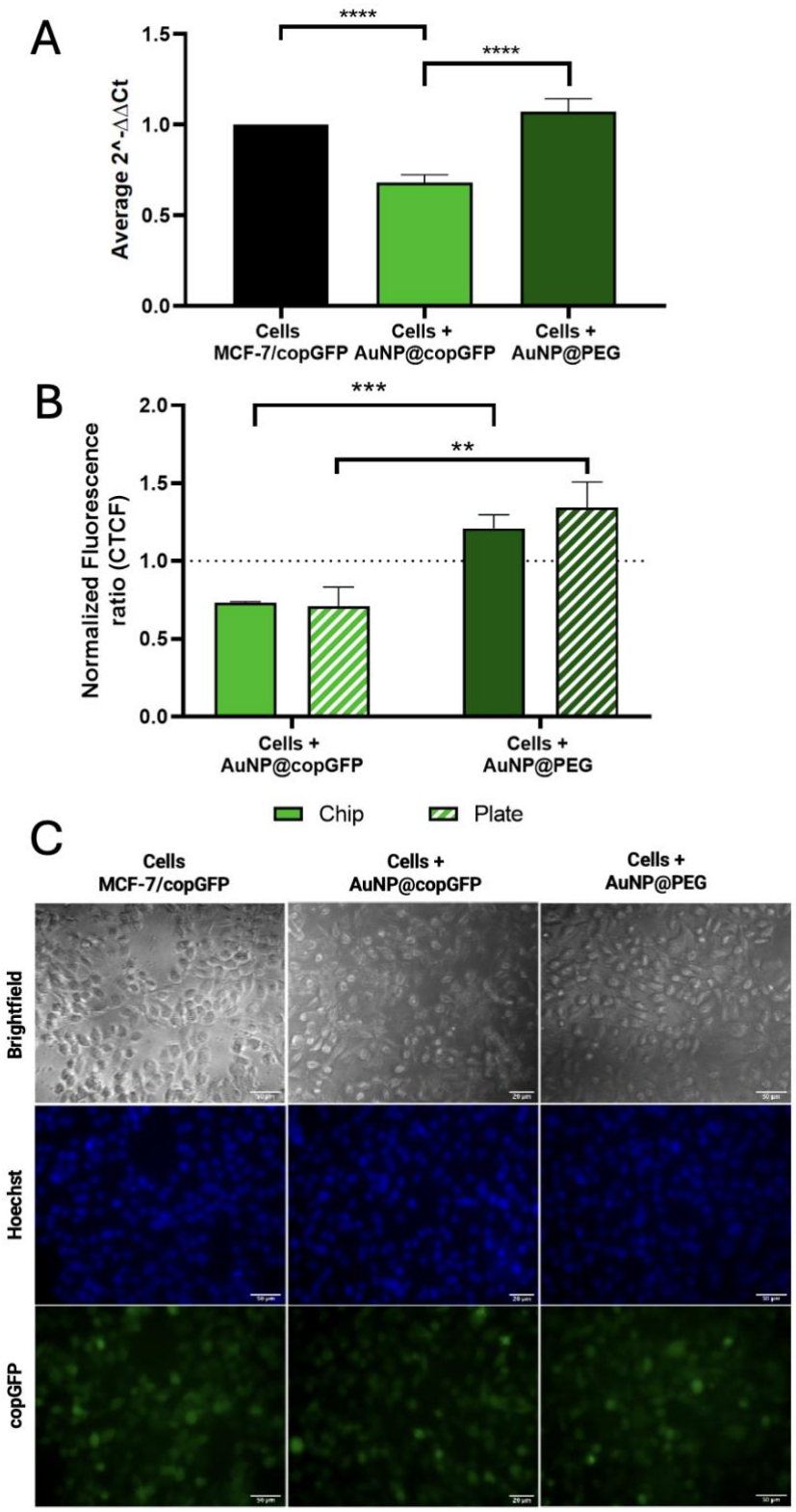

Figure 6.5. *copGFP* silencing on MCF-7/copGFP cells cultured on the biochip.
(A) Bars represent the average $2^{-\Delta\Delta CT}$ results and **(B)** average CTCF values obtained for the silencing of *copGFP* upon 6h of incubation with 20nM of oligonucleotide. MCF-7/copGFP controls were performed using only medium (■), 20nM of AuNPs@copGFP (■), and the respective control for AuNPs delivery is represented by AuNPs@PEG (■). Full bars represent the results obtained for cell cultures on the biochip and striped bars for the cells cultured on a plate. Bars are the result of 3 independent biological replicates, and the error bars are the respective Standard

Error Mean. Statistical analysis was performed using One-way ANOVA and Sidak's multiple comparison test. The results were considered statistically significant for p values < 0.05. (*) represents p < 0.0332, (**) represents p < 0.0021, (***) represents p < 0.0002 and (****) represents p<0.0001. (**C**) Fluorescence microscopy images of MCF-7/copGFP cells on the biochip. Each column shows a control used for the *copGFP* silencing: Column 1 – MCF-7/copGFP control; Column 2 – Cells incubated with AuNPs@copGFP; Column 3 - Cells incubated with AuNPs@PEG. On the top line are the brightfield images, the middle line shows the Blue channel (Hoescht dye), and the bottom line is the Green channel (copGFP protein) channels. The scale bar in the images represents 20 or 50μm.

Since the biochip has demonstrated the ability to replicate the results achieved with 2D cell cultures, it is now essential to apply it to more complex models. 3D models, including spheroids, more closely mimic the native tumor architecture, with features such as a proliferative outer layer and necrotic core that influence drug sensitivity, uptake dynamics, and cellular interactions (273,274,277,294,302), making them better predictors of therapeutic responses (277,330,692,693). By leveraging the biochip's ability to simulate the *in vivo* dynamic conditions of tumors (*e.g.*, shear forces, diffusion gradients, and external stimuli) (356,361,456,680), advancing the 3D-modeling to biochips can significantly enhance drug testing and therapy development.

Therefore, the potential of the proposed biochip to support spheroid cultures was further explored. While MCF-7/copGFP cells are valuable for assessing gene silencing in 2D cultures, their genetically engineered nature prevents the formation of 3D spheroids. Instead, the colorectal carcinoma cell line HCT-116, previously used for gene silencing studies, was utilized to demonstrate the biochip's suitability for 3D cell growth.

Initially, the biochip was applied to 2D cultures of HCT-116 cells, where conditions optimized for *c-MYC* silencing in plate-based systems (see Chapter 3, *Subsection* ***3.3.2***) were tested. The results confirmed that the biochip supports HCT-116 cell proliferation and efficient *c-MYC* gene silencing (**Figure 6.6**) (572,694). Specifically, under optimized conditions (54nM Au-nanoconjugates for 6 hours), *c-MYC* downregulation in the biochip reached approximately 33%, comparable to the 37% reduction observed in standard plate-based systems (**Figure 6.6,** panel A) (695). Similarly, c-MYC protein expression was reduced by 15% on the biochip and 13% in plate-based cultures (**Figure 6.6,** panels B and C).

These findings demonstrate that the proposed biochip successfully replicates outcomes achieved with standard plate-based cultures, suggesting it should be further evaluated for compatibility with more advanced cell models.

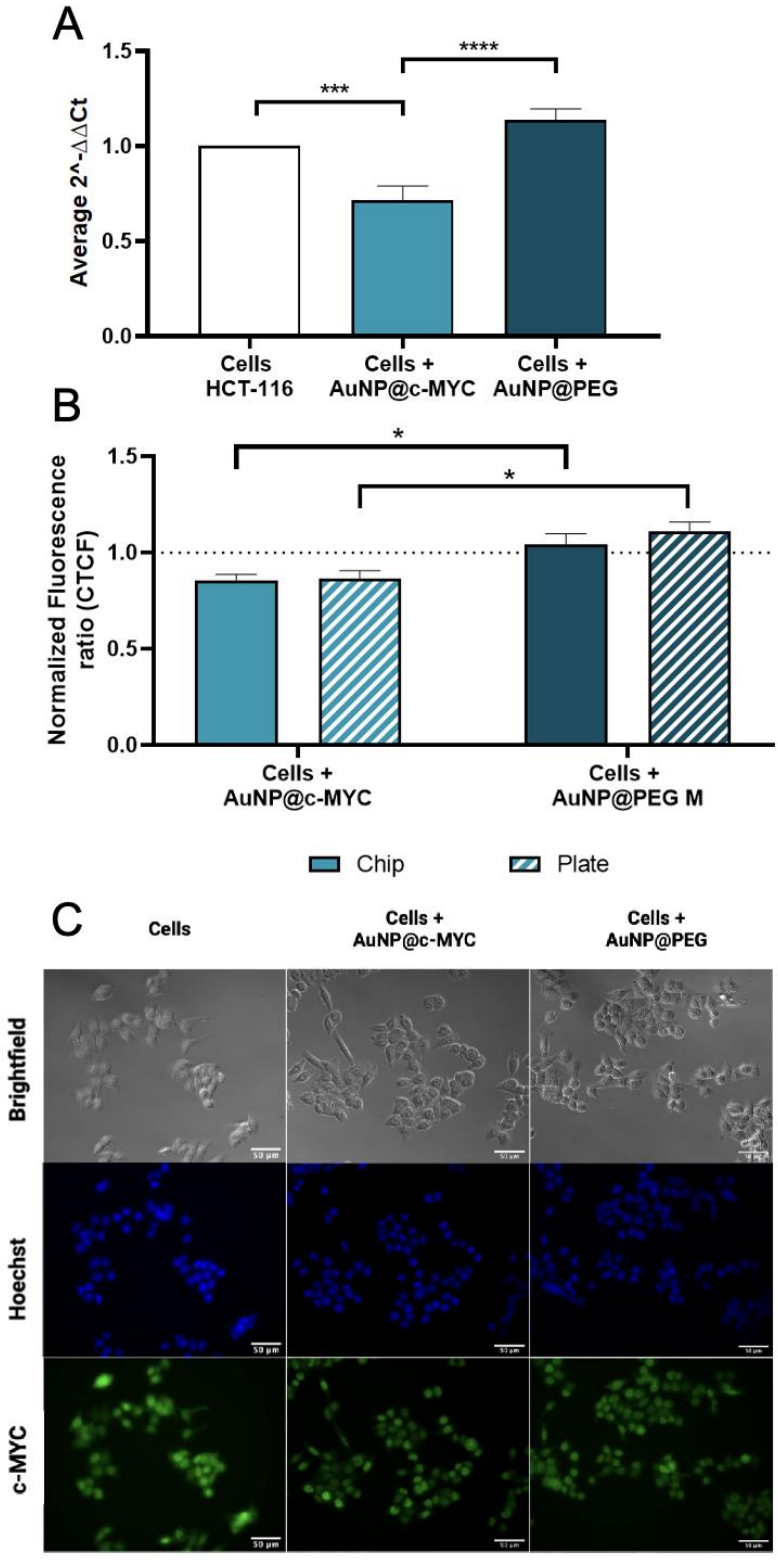

Figure 6.6. *c-MYC* silencing on HCT-116 cells cultured on the biochip.
(A) Bars represent the average $2^{-\Delta\Delta CT}$ results and (**B**) average CTCF values obtained for the silencing of c-MYC upon 6 h of incubation with 54nM of oligonucleotide, respectively. HCT-116 controls were performed using only medium (❑), with 54nM of AuNPs@c-MYC (■), and with the control for the AuNPs delivery represented by AuNPs@PEG (■). Bars are the result of 3 independent biological replicates, and the error bars are the respective Standard Error Mean. Statistical analysis was performed using One-way ANOVA and Sidak's multiple

comparison test. The results were considered statistically significant for p values < 0.05. (*) represents p < 0.0332, (**) represents p < 0.0021, (***) represents p < 0.0002 and (****) represents p<0.0001. (C) Fluorescence microscopy images of HCT-116 cells on biochip. Each column shows a control used for the c-MYC silencing: Column 1 – HCT-116 control; Column 2 – Cells incubated with AuNPs@c-MYC; Column 3 - Cells incubated with AuNPs@PEG. On the top line are the brightfield images, the middle line shows the Blue channel (Hoechst dye), and the bottom line is the Green channel (c-MYC protein) channels. The scale bar in the images represents 20 or 50 μm.

6.3.3 Spheroid Formation On-Chip

To promote the formation of cell aggregates, specific conditions regarding well geometry and material properties must be met. In this regard, U-shape or round bottoms have been pointed as the ideal geometries to promote a uniform spheroid formation, as they minimize cell adherence to the well walls and encourage cell aggregation (696,697). Additionally, the wells should be small to facilitate close cell-to-cell interactions but large enough to support the growth of spheroids over time, which is typically attained with diameters of 200-800μm (698). Finally, an adequate well depth of around 1mm is necessary to maintain sufficient nutrient and oxygen gradients, essential for spheroid viability (698).

Considering these requirements, a design featuring a single chamber with multiple microwells was envisioned (**Figure 6.7**) (699).

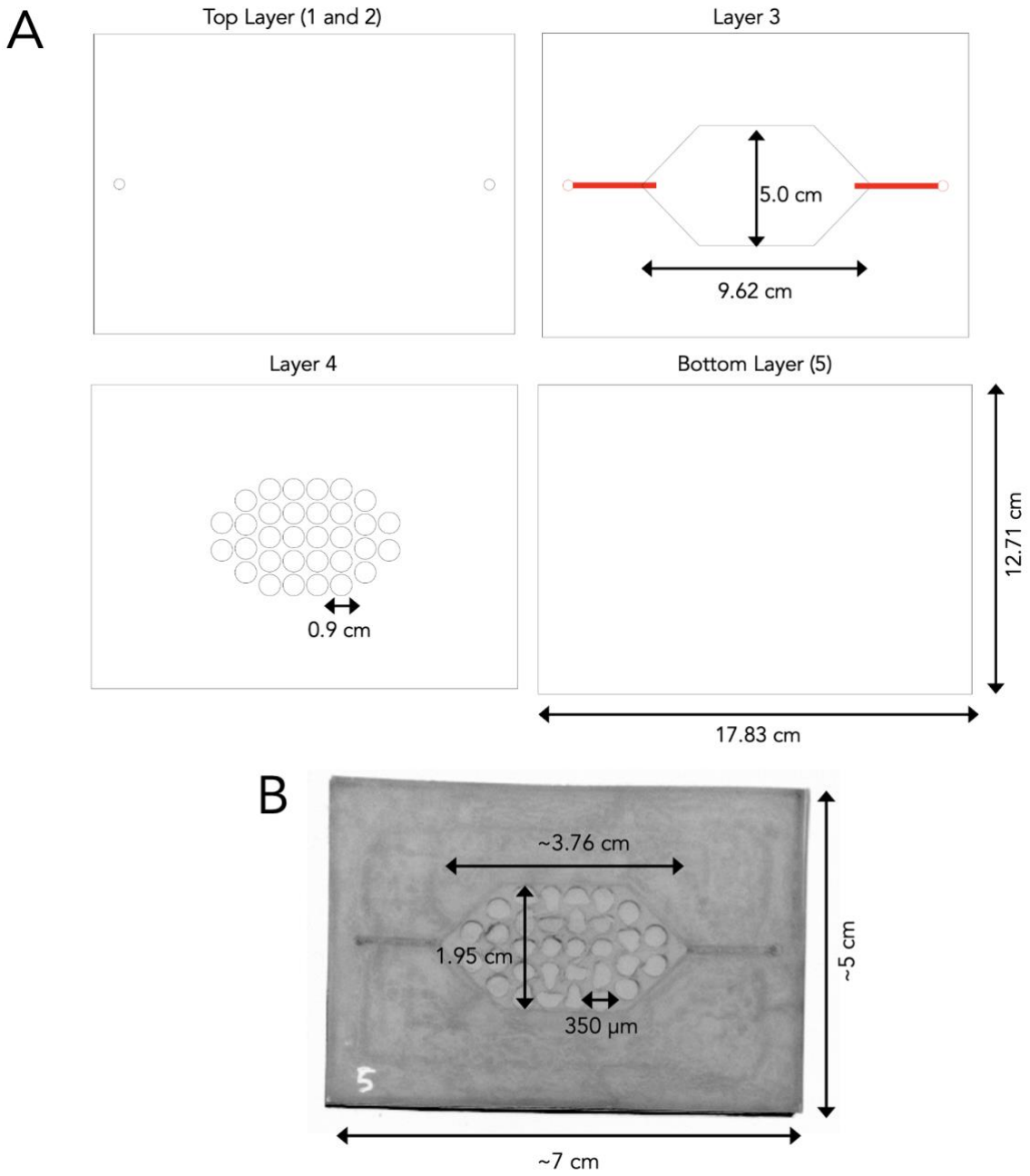

Figure 6.7. Initial design for spheroid formation on-chip.
Schematic representation of layer partnering and assemble order and engraved sizes. Layer 1 and 2 - Top layers (Layer 2 for enhanced stability) with a pair of inlet/outlet; Layer 3 – All in-depth wells and a microchannel for medium and cell infusion engraved for a final size of 930 µm; Layer 4 – All in-depth wells promote cell aggregation; Layer 5 – Sealer and surface for cell adherence. (**B**) Biochip size after shrinkage, entailing a volume capacity of 1.5 mL. The image was obtained on a transilluminator using the bright light mode.

Despite the reduced size of the microwells (~350µm), the cells adhered to the bottom rather than aggregating, which prevented spheroid formation (**Figure 6.8**). Given that the proposed design met the basic criteria for spheroid formation, other factors, such as surface properties, were investigated. The

literature suggests that hydrophobic surfaces and non-adherent coatings can prevent cells from sticking to the bottom and sides of the wells, thereby enhancing spheroid formation (700,701). To explore this, the device was functionalized with an ultra-low attachment solution. Although this treatment encouraged cells to attach to each other rather than to the chip surface, the low cell density relative to the well's dimensions still prevented the formation of spheroids comparable in size to those achieved in U-shaped 96-wells plates (600µm vs 50µm), even when the same cell seeding density was used ($5x10^3$ cells/well) (**Figure 6.8**).

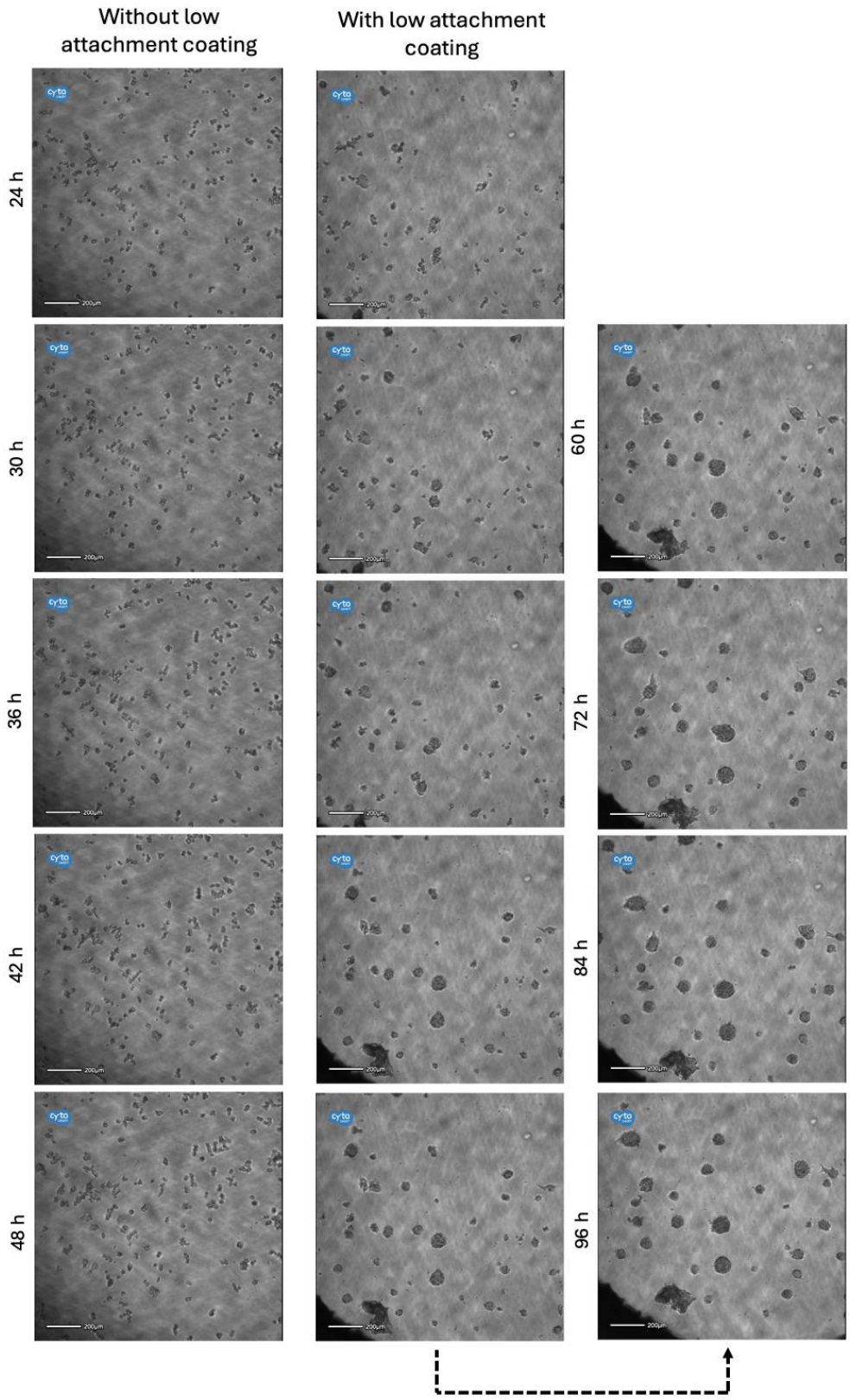

Figure 6.8. Effect of the biochip's surface modification on the spheroid formation of HCT-116 cells. Brightfield microscopy images of HCT-116 cells incubated on-chip without (left) and with (right) ultra-low attachment solution. Time-lapse images were obtained from videos recorded up to 96 hours after the seeding point. The scale bar in all images represents 200μm.

To further promote cell aggregation and spheroid growth, it was necessary to maximize the probability of cells encountering initial aggregates. This could be achieved in three ways. First, increasing the initial number of cells seeded on the biochip would enhance cell encounters and aggregate formation. However, this approach might alter spheroid growth kinetics and result in aggregates of different sizes and confluency compared to those in plate-based systems.

Second, the well geometry could be further optimized to resemble a U-shape. A similar chip was produced with the bottom of the microwells engraved at increasingly higher laser powers towards the center to create a curvature that would promote cell-cell contacts over cell-matrix interactions. However, the thermal sensitivity of the PS slabs caused excessive melting of the plastic, resulting in loss of transparency and significant optical defects that impaired cell visualization (**Figure 6.9**).

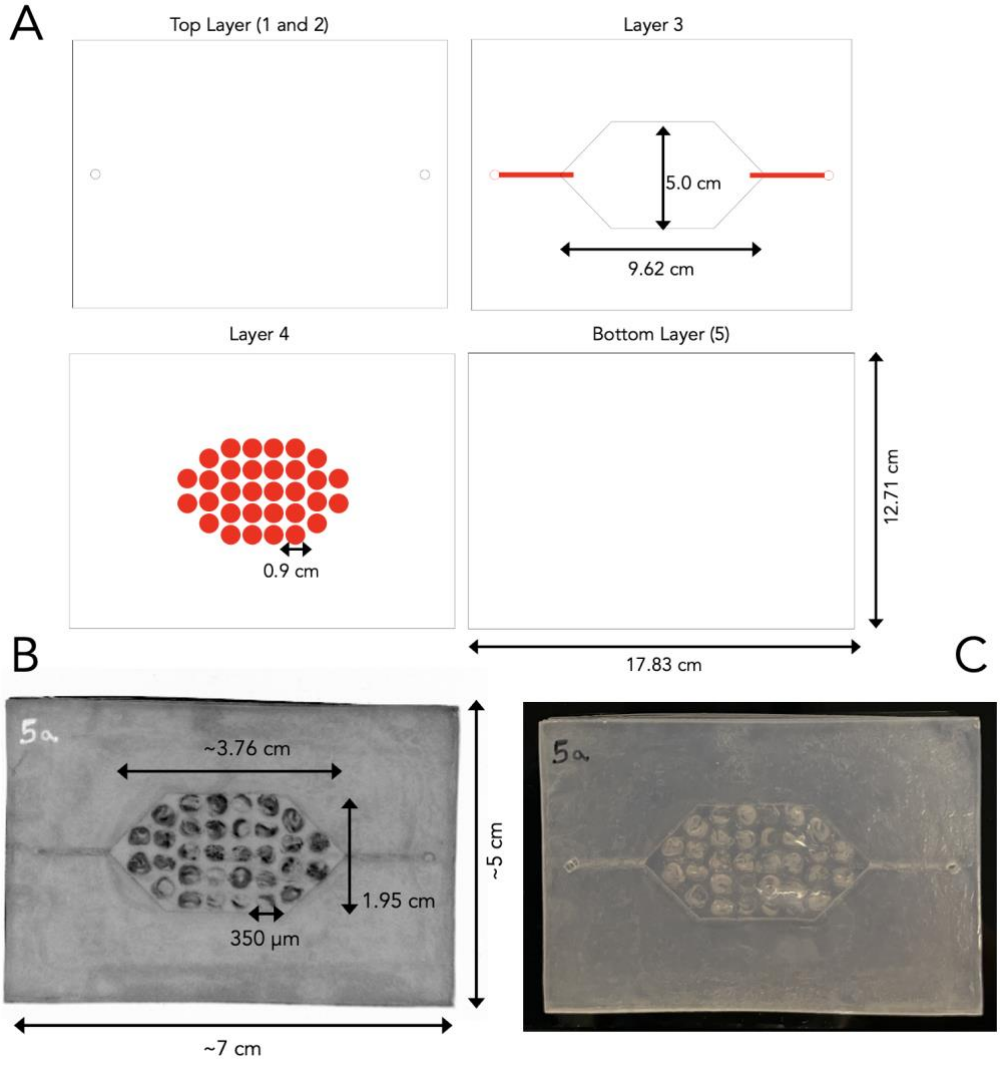

Figure 6.9. Second design for spheroid formation on-chip.
(**A**) Schematic representation of layer partnering and assemble order and engraved sizes. Layer 1 and 2 - Top layers (Layer 2 for enhanced stability) with a pair of inlet/outlet; Layer 3 – All in-depth well and a microchannel for medium and cell infusion engraved for a final size of 930 µm; Layer 4 – Laser patterned wells to promote cell

aggregation; Layer 5 – Sealer and surface for cell adherence. (**B**) Biochip size after shrinkage, entailing a volume capacity of 1.5mL. The image was obtained on a transilluminator using the bright light mode. (**C**) Biochip image after shrinkage obtained with the camera of an iPhone 12 Pro. The defects in the center of each culture chamber were caused by the laser engrave mode, causing the optical defects.

Since it was crucial to obtain spheroids with the same dimensions and cell density as those used in previous gene silencing assays (see Chapter 4, **Figure 4.9**), and the intrinsic nature of PS did not allow for curvature formation in the wells, a third approach was pursued: reducing the well size to increase cell contact. This involved adapting the previously developed biochip for 2D cell growth to support 3D cell cultures. This was accomplished by functionalizing the surface of the microwells with an ultra-low attachment solution (702). Then, HCT-116 cells were added to the biochip and allowed to grow for 3 days under circular agitation (703) to maximize cell aggregation into spheroids.

Data regarding the formation and growth of HCT-116 spheroids cultured on the biochip over three days showed a positive correlation with 3D spheroids grown in standard U-shaped 96-well plates (294,695). The spheroid morphology, size, and proliferation rates observed on the proposed platform were consistent with those documented in standard well-plate experiments (**Figure 6.10**).

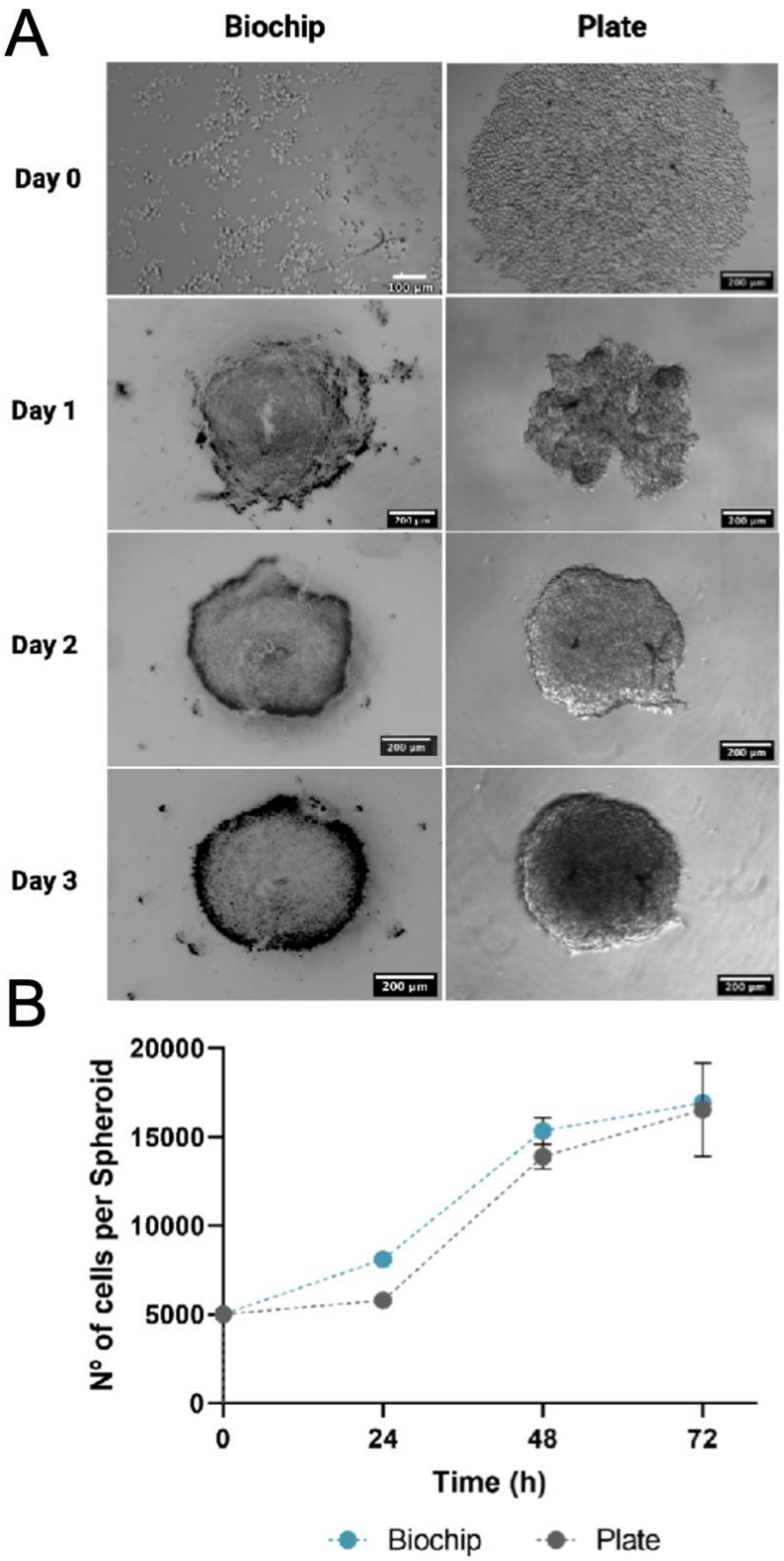

Figure 6.10. HCT-116 spheroids growth on the biochip.
(A) Brightfield microscopy images of spheroids growth in the biochip at 24, 48, and 72 hours. The scale bar represents 200 µm. **(B)** Number of cells per spheroid grown on the biochip (●) and U-shaped 96-well (●) on each day of growth. Dots are the average result of 3 biological replicates, and error bars represent the standard deviation.

Upon seeding, the cells on the 96-well plate quickly reorganized due to the U-shape curvature at the bottom of the wells, whereas cells on the biochip showed more dispersion, only attaching to each other due to the centripetal force caused by circular agitation (**Figure 6.10,** panel A). Nevertheless, on the third day of growth, the spheroids obtained with the developed biochip showed similar size, cell density, and shape as the ones obtained with the standard well-plate system.

Although the proposed design is simple and does not present innovations that significantly advance current spheroid culture methods, its key advantage lies in its adaptability. This device and fabrication process can be easily modified to include more complex geometries and control over spheroid growth. One crucial aspect for improving tumor-like models, and the reason microfluidic systems have gained increasing endorsement over the years, is their ability to control fluid flows to mimic the shear stress cells experience in their native microenvironment (704,705). To this end, the current design was further adapted to include microchannels that support medium perfusion, thereby simulating these fluid flow conditions (**Figure 6.11)**.

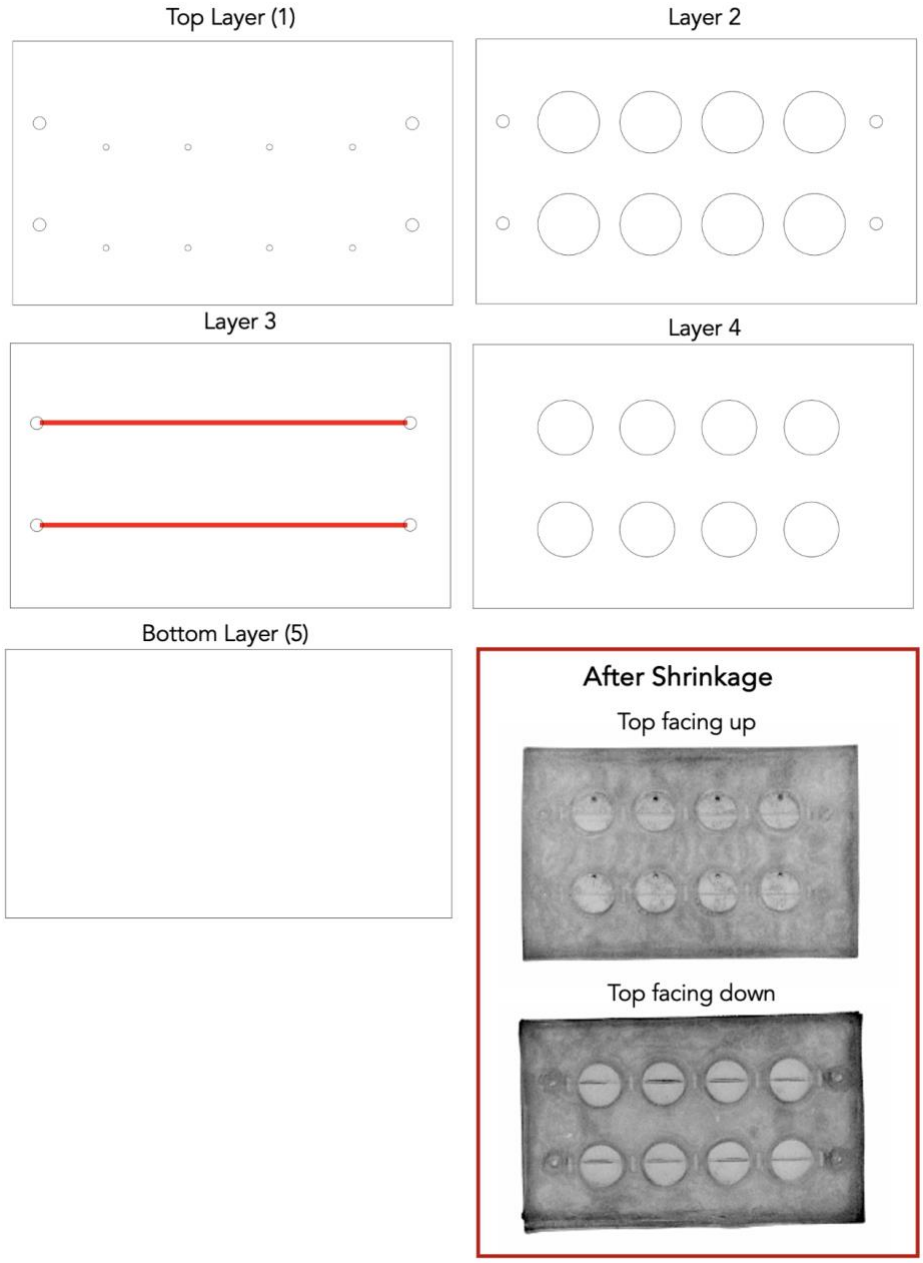

Figure 6.11. Biochip design for spheroid formation with channels for medium perfusion.
(**A**) Schematic representation of layer partnering and assemble order and engraved sizes. Layer 1: Top layers with two pairs of inlet/outlet and holes for air ventilation; Layer 2 and 4 – All in-depth wells for spheroid growth; Layer 3 – two microchannels for medium perfusion to simulate the shear stress that cells are exposed to. The channels were engraved for a final diameter of 500 µm (**B**) Biochip and microchannels after shrinkage. The image where the top of the chip is facing down better displays the microchannels since these were purposely engraved on a lower layer so that the medium perfusion touches the spheroids. The image was obtained on a transilluminator using the bright light mode.

This design was conceptualized to demonstrate the adaptability of the developed method, showing that the design can be easily modified to meet desired experimental settings and cell modeling conditions. However, the inclusion of microchannels increases the complexity of device operation and introduces

variations from the initial experimental settings used to optimize silencing conditions on plate-based systems. Therefore, the design without microchannels was used for subsequent silencing studies.

6.3.4 Gene Silencing Using Tumor Spheroids On-Chip

The same Au-nanoconjugates were used to assess if the 3D spheroids grown on the biochip behaved similarly to those cultured on traditional plates. The silencing of the *c-MYC* gene was performed on these 3D-cell models as previously optimized (see Chapter 4, *Subsection* **4.3.1**). Effective silencing of the *c-MYC* gene on spheroids grown on-chip was attained with a decrease in the expression of 41 % (**Figure 6.12**). This silencing is comparable to that reported for spheroids grown in plate (33 %) (695). Furthermore, the slight increase in the silencing efficiency accomplished on this Tumor-on-chip model can be attributed to the facility of performing several biological replicates in parallel, increasing the robustness of the results (445). Additionally, 3D growth on the chip is also impacted by differences in perfusion and nutrient apport, which can affect gene expression (706,707).

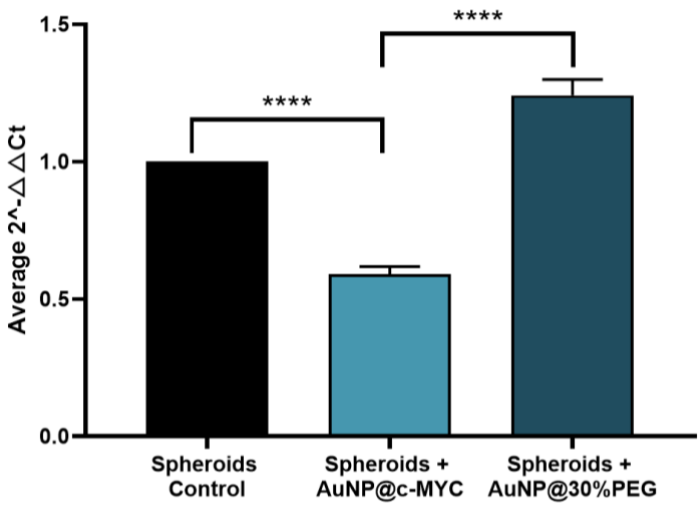

Figure 6.12. *c-MYC* silencing on HCT-116 spheroids cultured on the biochip.
Bars represent the average $2^{-\Delta\Delta CT}$ results obtained after incubating spheroids generated on biochip with medium (■), 54nM of AuNPs@c-MYC (■), and AuNPs@PEG Bars are the result of 3 independent biological replicates (with 8 spheroids per condition) and the error bars the respective Standard Error Mean. Statistical analysis was performed using One-way ANOVA and Sidak's multiple comparison test. The results were considered statistically significant for p values < 0.05. (****) represents p<0.0001.

6.4 Conclusions

This chapter assessed the suitability of the previously developed biochip to support the growth and maintenance of both 2D and 3D cancer cell models. The device successfully maintained cell

proliferation, viability, and gene/protein expression patterns comparable to those observed in traditional plate-based models. Gene silencing with Au-nanoconjugates further demonstrated that the biochip replicated silencing efficiencies, with a minor 4% difference in 2D cultures and an 8% improvement in 3D spheroids. These results highlight the effectiveness of the developed fabrication process for biochips, removing common barriers related to cost, time, and expertise. This approach accelerates the development of ToC platforms and lays a foundation for more complex systems.

However, it is important to note that the presented biochip currently lacks the microfluidic component, which is essential for mimicking tumor dynamics, such as shear forces and nutrient gradients. The absence of this feature likely contributed to the strong match between the biochip and standard well-plates.

Moving forward, integrating microfluidic channels should be prioritized to better replicate the complexity of the TME and enhance the physiological relevance of the biochip model. In the present study, the lack of microfluidic channels and the absence of commercially available chips made from the same polystyrene material led us to compare results with standard well plates due to their material similarity. Once refined to incorporate microchannels, the biochip should be compared with other ToC platforms and more advanced models, such as PDX, animal studies, and even clinical data, to further evaluate its potential in cancer research. Ultimately, ToC models bridge the gap between 2D cultures and *in vivo* systems, advancing cancer research and therapeutic testing. Still, the development of user-friendly, tailored platforms is crucial to realizing their full potential for clinical translation.

7

CONCLUSIONS AND FUTURE PERSPECTIVES

This thesis focused on the development and optimization of a straightforward and simplified approach to generate “Tumor-on-Chip" platforms and demonstrate their applicability for studying nanoparticle-mediated gene silencing in both 2D and 3D cancer models. By utilizing available over-the-counter materials and simple fabrication techniques, the generated platforms may be used as a substitute for traditional plate-based culture models for the optimization of more complex ToC systems. While plate-based cultures lack physiological relevance, ToC models often face limitations due to technical complexity and high fabrication costs.

The developed biochip successfully sustained the growth and maintenance of both 2D and 3D cell cultures, demonstrating cell viability rates above 85%, comparable to those achieved with conventional *in vitro* systems. Additionally, spheroids formed on-chip exhibited uniform size distribution and consistent morphology, ensuring stable culture conditions. These features confirm that the platform provides a suitable environment for long-term cell culture and experimental reproducibility.

In addition to supporting robust cell growth, the biochip demonstrated effective gene silencing capabilities using AuNPs@ASOs nanoconjugates targeting the *c-MYC* and *copGFP* genes. Experimental results showed a 33% reduction in *c-MYC* expression for 2D cultures and 41% in spheroids, while *copGFP* silencing efficiency reached 32%. These values closely mirrored the silencing efficiencies achieved in traditional plate cultures (*c-MYC*: 37% in 2D and 33% in spheroids; *copGFP*: 35% mRNA reduction). The observed silencing efficiencies align with previously reported nanoparticle-mediated gene silencing strategies, where reductions between 30–50% have been associated with significant phenotypic effects, such as reduced proliferation and increased apoptosis. The slightly enhanced silencing efficiency observed in biochip’s spheroids compared to conventional well-plate

cultures suggests that the biochip provides a more effective microenvironment for nanoparticle-cell interactions, likely due to improved nanoparticle retention and controlled exposure conditions.

One key factor enabling similar silencing efficiencies across both 2D and 3D models was the adjustment of nanoparticle dosing. The inherent differences in cell number, spatial organization, and diffusion constraints between 2D-cell monolayers and spheroids require careful dose optimization. In this study, the optimal nanoconjugate concentration for *c-MYC* silencing (54nM of oligonucleotide) resulted in approximately 2.6 times greater nanoparticle exposure per cell in spheroids compared to 2D cultures. This increase in the nanoparticle-to-cell ratio helped overcome the additional uptake barriers imposed by the dense extracellular matrix and diffusion limitations characteristic of spheroids. This underscores the necessity of precise dose calibration when transitioning from 2D to 3D models to achieve comparable biological effects.

At the molecular level, the observed reduction in gene expression was accompanied by a decrease in protein levels for both genes, in accordance with the well-established mechanism of action of antisense oligonucleotides. ASOs function by binding to complementary mRNA sequences, recruiting RNase H, which cleaves the RNA-DNA hybrid and degrades the target mRNA. This effectively reduces the transcript's availability for translation, leading to decreased protein expression. The consistency of protein reduction between biochip and plate-based cultures further validates the reliability of the model in replicating gene-silencing effects. Since the ASOs used in this study lacked chemical modifications, their silencing effect was solely dependent on RNase H recruitment. While effective, chemically modifying ASOs with 2'-O-methyl (2'-OMe), 2'-O-methoxyethyl (2'-MOE), or locked nucleic acids could enhance stability, binding affinity, and resistance to nuclease degradation, potentially improving silencing efficiency. Additionally, incorporating phosphorothioate backbone modifications could enhance cellular uptake and prolong the ASOs half-life, leading to more sustained knockdown effects. Future studies could explore the impact of such modifications on gene silencing efficiency in both 2D and 3D models to optimize therapeutic applications.

The design optimization process played a critical role in achieving these outcomes. The final ToC device featured a polystyrene-based microchamber system with transparent layers that facilitated real-time imaging and monitoring of cell growth and gene silencing effects. The chip dimensions measured 30 mm × 20 mm × 5 mm, with 6 individual culture chambers of 5 mm in diameter and 2 mm in depth, providing a volume capacity similar to that of wells in standard 96-well plates. These chambers were strategically designed to support 2D cell growth and facilitate the formation of uniformly sized spheroids while ensuring optimal nutrient diffusion. A later iteration of the chip incorporated perfusion channels

(500 μm in width) to allow controlled media exchange and nanoparticle delivery, mimicking physiological fluid dynamics. Additionally, the use of

The implementation of ToC technology provided several advantages. First, it enhanced reproducibility by enabling multiple replicates under controlled conditions, reducing experimental variability. Second, it allowed for a more physiologically relevant assessment of nanoparticle uptake and gene silencing efficiency, given the diffusion barriers inherent to 3D spheroids. Third, it demonstrated that integrating fluidic components could further improve the physiological accuracy of the model, making it a valuable tool for the preclinical screening of nanoparticle-based therapeutics.

Beyond its biological applications, the ToC platform also addressed key engineering challenges. The fabrication method optimized in this study proved to be scalable, cost-effective, and user-friendly while allowing for easy design changes, broadening the accessibility of ToC models beyond specialized research facilities. Additionally, the system successfully minimized material-related cytotoxicity while supporting robust cellular viability and proliferation, matching the performance of conventional well-plate systems.

However, despite these advances, certain limitations remain. The absence of integrated microfluidic flow restricted the ability to fully recapitulate the dynamic tumor microenvironment, particularly regarding nutrient and therapeutics perfusion. Additionally, the current model does not yet incorporate stromal or immune cell interactions, both of which play crucial roles in tumor progression and treatment response.

Traditional fabrication methods for ToC devices have encountered significant challenges, including high costs, the need for specialized equipment, and limited scalability. Many ToC platforms rely on complex lithographic or soft-lithography techniques, which, while offering precise microstructural control, require expensive cleanroom facilities and skilled personnel. These barriers have restricted widespread adoption, particularly in resource-limited settings. Additionally, commonly used materials, such as PDMS, present drawbacks, including drug absorption, mechanical instability, and inconsistencies in manufacturing. Developing alternative fabrication techniques that emphasize cost-efficiency, material stability, and reproducibility is essential for expanding the applicability of ToC platforms.

Similarly, conventional plate-based cancer models, despite their widespread use, present significant limitations in studying tumor biology and evaluating therapeutics. 2D cultures lack the structural complexity of native tumors, failing to replicate key cell-cell and cell-matrix interactions essential for tumor progression. While 3D cell models account for diffusion barriers present in solid tumors, the absence of flow dynamics makes them inadequate for assessing the full range of therapeutic effects

when transitioning from *in vitro* studies to clinical applications. Transitioning to ToC devices enables more accurate modeling of tumor heterogeneity and microenvironmental conditions, thereby improving the predictive power of preclinical studies.

Future improvements in the developed biochip ought to focus on integrating microfluidic components that enable continuous perfusion of media and therapeutic agents. Controlled flow dynamics would help maintain chemical gradients, regulate nutrient and oxygen distribution, and facilitate real-time monitoring of cellular responses, further mimicking the *in vivo* tumor microenvironment. Another critical area for development is the expansion to heterogeneous tumor models incorporating multiple cell types, such as fibroblasts and immune cells, to better simulate tumor-stroma interactions and immunomodulatory effects. Additionally, optimizing nanoparticle-based delivery strategies, functionalizing nanoparticles with targeting ligands, and incorporating automation for high-throughput screening could further enhance the platform's usability in drug discovery and precision medicine.

The development of an accessible, effective, and physiologically relevant ToC model represents a significant advancement in the preclinical evaluation of nanoparticle-based gene therapies. Continuous refinements, including advanced biomimetic features, improved nanoparticle delivery, and patient-specific tumor modeling, will be crucial for translating these platforms into clinical and industrial applications. ToC systems are poised to play an increasingly vital role in bridging the gap between conventional *in vitro* studies and complex *in vivo* models, ultimately accelerating the development of more effective cancer therapies.

BIBLIOGRAPHY

1. Cooper GM. The Cell: A Molecular Approach. 2nd edition [Internet]. Sinauer Associates 2000; 2000. Available from: http://lib.ugent.be/catalog/ebk01:3450000000002155

2. Hanahan D, Weinberg RA. Hallmarks of Cancer: The Next Generation. Cell [Internet]. 2011;144(5):646–74. Available from: https://www.sciencedirect.com/science/article/pii/S0092867411001279

3. Koeffler MHP, Mccormick DF, Denny C. Molecular Mechanisms of Cancer. West J Med. 1991;155(5):505–14.

4. Golemis EA, Scheet P, Beck TN, Scolnick EM, Hunter DJ, Hawk E, et al. Molecular mechanisms of the preventable causes of cancer in the United States. Vol. 32, Genes and Development. Cold Spring Harbor Laboratory Press; 2018. p. 868–902.

5. N HR. Cancer — Nature, Nurture, or Both. New England Journal of Medicine [Internet]. 2025 Jan 20;343(2):135–6. Available from: https://doi.org/10.1056/NEJM200007133430210

6. Anand P, Kunnumakara AB, Sundaram C, Harikumar KB, Tharakan ST, Lai OS, et al. Cancer is a preventable disease that requires major lifestyle changes. Vol. 25, Pharmaceutical Research. Springer New York LLC; 2008. p. 2097–116.

7. Zhu M, Wang T, Huang Y, Zhao X, Ding Y, Zhu M, et al. Genetic risk for overall cancer and the benefit of adherence to a healthy lifestyle. Cancer Res. 2021 Sep 1;81(17):4618–27.

8. Khan N, Afaq F, Mukhtar H. Lifestyle as risk factor for cancer: Evidence from human studies. Cancer Lett [Internet]. 2010;293(2):133–43. Available from: https://www.sciencedirect.com/science/article/pii/S0304383509007290

9. Weiderpass E. Lifestyle and Cancer Risk. J Prev Med Public Health. 2010 Nov 1;43:459–71.

10. Parsa N. Environmental Factors Inducing Human Cancers [Internet]. Vol. 41, Iranian J Publ Health. 2012. Available from: http://ijph.tums.ac.ir

11. Sandhu APS, Tanvir ., Singh K, Singh S, Antaal H, Luthra S, et al. Decoding Cancer Risk: Understanding Gene-Environment Interactions in Cancer Development. Cureus. 2024 Jul 19;

12. Bray F, Laversanne M, Sung H, Ferlay J, Siegel RL, Soerjomataram I, et al. Global cancer statistics 2022: GLOBOCAN estimates of incidence and mortality worldwide for 36 cancers in 185 countries. CA Cancer J Clin [Internet]. 2024 May 1;74(3):229–63. Available from: https://doi.org/10.3322/caac.21834

13. Hanahan D. Hallmarks of Cancer: New Dimensions. Cancer Discov [Internet]. 2022 Jan 12;12(1):31–46. Available from: https://doi.org/10.1158/2159-8290.CD-21-1059

14. Hanahan D, Weinberg RA. Hallmarks of Cancer: The Next Generation. Cell [Internet]. 2011 Mar 4;144(5):646–74. Available from: https://doi.org/10.1016/j.cell.2011.02.013

15. Hanahan D, Weinberg RA. The Hallmarks of Cancer. Cell [Internet]. 2000 Jan 7;100(1):57–70. Available from: https://doi.org/10.1016/S0092-8674(00)81683-9

16. Wang Q, Shao X, Zhang Y, Zhu M, Wang FXC, Mu J, et al. Role of tumor microenvironment in cancer progression and therapeutic strategy. Vol. 12, Cancer Medicine. John Wiley and Sons Inc; 2023. p. 11149–65.

17. Sükei T, Palma E, Urbani L. Interplay between cellular and non-cellular components of the tumour microenvironment in hepatocellular carcinoma. Cancers (Basel). 2021 Nov 1;13(21).

18. Zhao Y, Shen M, Wu L, Yang H, Yao Y, Yang Q, et al. Stromal cells in the tumor microenvironment: accomplices of tumor progression? Vol. 14, Cell Death and Disease. Springer Nature; 2023.

19. Xiao Y, Yu D. Tumor microenvironment as a therapeutic target in cancer. Pharmacol Ther [Internet]. 2021;221:107753. Available from: https://www.sciencedirect.com/science/article/pii/S0163725820302849

20. Mayer S, Milo T, Isaacson A, Halperin C, Miyara S, Stein Y, et al. The tumor microenvironment shows a hierarchy of cell-cell interactions dominated by fibroblasts. Nat Commun [Internet]. 2023;14(1):5810. Available from: https://doi.org/10.1038/s41467-023-41518-w

21. Winkler J, Abisoye-Ogunniyan A, Metcalf KJ, Werb Z. Concepts of extracellular matrix remodelling in tumour progression and metastasis. Nat Commun [Internet]. 2020;11(1):5120. Available from: https://doi.org/10.1038/s41467-020-18794-x

22. Henke E, Nandigama R, Ergün S. Extracellular Matrix in the Tumor Microenvironment and Its Impact on Cancer Therapy. Vol. 6, Frontiers in Molecular Biosciences. Frontiers Media S.A.; 2020.

23. Yuan Z, Li Y, Zhang S, Wang X, Dou H, Yu X, et al. Extracellular matrix remodeling in tumor progression and immune escape: from mechanisms to treatments. Vol. 22, Molecular Cancer. BioMed Central Ltd; 2023.

24. Qiong Huang, Xingbin Hu, Wanming He, Yang Zhao, Shihui Hao, Qijing Wu, et al. Fluid shear stress and tumor metastasis. Am J Cancer Res. 2018 May 1;5(8):763–77.

25. Mitchell MJ, King MR. Computational and experimental models of cancer cell response to fluid shear stress. Vol. 3 MAR, Frontiers in Oncology. 2013.

26. Wyld L, Audisio RA, Poston GJ. The evolution of cancer surgery and future perspectives. Nat Rev Clin Oncol [Internet]. 2015;12(2):115–24. Available from: https://doi.org/10.1038/nrclinonc.2014.191

27. Hyung WJ, Kim SS, Choi WH, Cheong JH, Choi SH, Kim CB, et al. Changes in treatment outcomes of gastric cancer surgery over 45 years at a single institution. Yonsei Med J. 2008 Jun;49(3):409–15.

28. Msika S, Benhamiche AM, Tazi MA, Rat P, Faivre J. Improvement of Operative Mortality after Curative Resection for Gastric Cancer: Population-based Study. World J Surg [Internet]. 2000 Sep 1;24(9):1137–42. Available from: https://doi.org/10.1007/s002680010185

29. OSAKI T, OYAMA T, TAKENOYAMA M, So T, YAMASHITA T, Aikawa M, et al. Results of Surgical Treatment for Primary Lung Cancer; Time Trends of Survival and Clinicopathologic Features. J UOEH. 2001 Oct 1;23:277–83.

30. Evans MD, Thomas R, Williams GL, Beynon J, Smith JJ, Stamatakis JD, et al. A comparative study of colorectal surgical outcome in a national audit separated by 15 years. Colorectal Disease [Internet]. 2013 May 1;15(5):608–12. Available from: https://doi.org/10.1111/codi.12065

31. Treasure T, Utley M. Surgical removal of asymptomatic pulmonary metastases: time for better evidence. BMJ : British Medical Journal [Internet]. 2013 Feb 21;346:f824. Available from: https://www.bmj.com/content/346/bmj.f824.abstract

32. Chua TC, Moran BJ, Sugarbaker PH, Levine EA, Glehen O, Gilly FN, et al. Early- and Long-Term Outcome Data of Patients With Pseudomyxoma Peritonei From Appendiceal Origin Treated by a Strategy of Cytoreductive Surgery and Hyperthermic Intraperitoneal Chemotherapy. Journal of Clinical Oncology [Internet]. 2012 May 21;30(20):2449–56. Available from: https://doi.org/10.1200/JCO.2011.39.7166

33. Alberts SR, Poston GJ. Treatment advances in liver-limited metastatic colorectal cancer. Clin Colorectal Cancer [Internet]. 2011;10(4):258–65. Available from: http://europepmc.org/abstract/MED/21820974

34. Eastley N, Newey M, Ashford RU. Skeletal metastases – The role of the orthopaedic and spinal surgeon. Surg Oncol [Internet]. 2012;21(3):216–22. Available from: https://www.sciencedirect.com/science/article/pii/S0960740412000242

35. Stättner S, Jones RP, Yip VS, Buchanan K, Poston GJ, Malik HZ, et al. Microwave ablation with or without resection for colorectal liver metastases. European Journal of Surgical Oncology (EJSO) [Internet]. 2013;39(8):844–9. Available from: https://www.sciencedirect.com/science/article/pii/S0748798313003661

36. Glazer ES, Hornbrook MC, Krouse RS. A meta-analysis of randomized trials: Immediate stent placement vs. surgical bypass in the palliative management of malignant biliary obstruction. Vol. 47, Journal of Pain and Symptom Management. 2014. p. 307–14.

37. Vahrmeijer AL, Hutteman M, van der Vorst JR, van de Velde CJH, Frangioni J V. Image-guided cancer surgery using near-infrared fluorescence. Nat Rev Clin Oncol [Internet]. 2013;10(9):507–18. Available from: https://doi.org/10.1038/nrclinonc.2013.123

38. Barone DG, Lawrie TA, Hart MG. Image guided surgery for the resection of brain tumours. Vol. 2014, Cochrane Database of Systematic Reviews. John Wiley and Sons Ltd; 2014.

39. Chi C, Du Y, Ye J, Kou D, Qiu J, Wang J, et al. Intraoperative imaging-guided cancer surgery: From current fluorescence molecular imaging methods to future multi-modality imaging technology. Vol. 4, Theranostics. Ivyspring International Publisher; 2014. p. 1072–84.

40. Jackson SP, Bartek J. The DNA-damage response in human biology and disease. Nature [Internet]. 2009;461(7267):1071–8. Available from: https://doi.org/10.1038/nature08467

41. Baskar R, Lee KA, Yeo R, Yeoh KW. Cancer and Radiation Therapy: Current Advances and Future Directions. Int J Med Sci [Internet]. 2012;9(3):193–9. Available from: https://www.medsci.org/v09p0193.htm

42. Eichenauer DA, Engert A. Advances in the treatment of Hodgkin lymphoma. Int J Hematol [Internet]. 2012;96(5):535–43. Available from: https://doi.org/10.1007/s12185-012-1199-2

43. Motzer RJ, Agarwal N, Beard C, Bolger GB, Boston B, Carducci MA, et al. Testicular Cancer. Journal of the National Comprehensive Cancer Network J Natl Compr Canc Netw [Internet]. 2009;7(6):672–93. Available from: https://jnccn.org/view/journals/jnccn/7/6/article-p672.xml

44. DeLaney TF. Radiation Therapy: Neoadjuvant, Adjuvant, or Not at All. Surgical Oncology Clinics [Internet]. 2012 Apr 1;21(2):215–41. Available from: https://doi.org/10.1016/j.soc.2011.12.005

45. Gunderson LL, Tepper J. Clinical Radiation Oncology: Third edition. 2011. 1–1638 p.

46. Brighton D, Johnston SRD, Wood M, Royal Marsden Hospital (London E. The Royal Marsden Hospital handbook of cancer chemotherapy : a guide for the multidisciplinary team [Internet]. Edinburgh: Elsevier Churchill Livingstone; 2005. Available from: http://books.google.com/books?id=tpNrAAAAMAAJ

47. Gill V. Treatment of Cancer (4th edn). Br J Cancer. 2003 May;88(10):1659–60.

48. Dickens E, Ahmed S. Principles of cancer treatment by chemotherapy. Surgery - Oxford International Edition [Internet]. 2018 Mar 1;36(3):134–8. Available from: https://doi.org/10.1016/j.mpsur.2017.12.002

49. Kciuk M, Gielecińska A, Mujwar S, Kołat D, Kałuzińska-Kołat Ż, Celik I, et al. Doxorubicin—An Agent with Multiple Mechanisms of Anticancer Activity. Vol. 12, Cells. MDPI; 2023.

50. Cree IA, Charlton P. Molecular chess? Hallmarks of anti-cancer drug resistance. Vol. 17, BMC Cancer. BioMed Central Ltd.; 2017.

51. Gill V. Treatment of Cancer (4th edn). Br J Cancer. 2003 May;88(10):1659–60.

52. Roland T. Skeel. Handbook of Cancer Chemotherapy. 11th ed. Philadelphia: Lippincott Williams & Wilkins; 2003.

53. Buchbinder EI, Desai A. CTLA-4 and PD-1 Pathways: Similarities, Differences, and Implications of Their Inhibition. Am J Clin Oncol [Internet]. 2016;39(1). Available from: https://journals.lww.com/amjclinicaloncology/fulltext/2016/02000/ctla_4_and_pd_1_pathways__similarities,.17.aspx

54. Walter HS, Ahmed S. Targeted therapies in cancer. Surgery (Oxford) [Internet]. 2018;36(3):122–7. Available from: https://www.sciencedirect.com/science/article/pii/S0263931917302752

55. CHMP. Yervoy, INN-ipilimumab [Internet]. Available from: www.ema.europa.eu/contact

56. Fukuhara H, Ino Y, Todo T. Oncolytic virus therapy: A new era of cancer treatment at dawn. Cancer Sci [Internet]. 2016 Oct 1;107(10):1373–9. Available from: https://doi.org/10.1111/cas.13027

57. Franke V, Berger DMS, Klop WMC, van der Hiel B, van de Wiel BA, ter Meulen S, et al. High response rates for T-VEC in early metastatic melanoma (stage IIIB/C-IVM1a). Int J Cancer [Internet]. 2019 Aug 15;145(4):974–8. Available from: https://doi.org/10.1002/ijc.32172

58. Nuhn P, De Bono JS, Fizazi K, Freedland SJ, Grilli M, Kantoff PW, et al. Update on Systemic Prostate Cancer Therapies: Management of Metastatic Castration-resistant Prostate Cancer in the Era of Precision Oncology. Eur Urol [Internet]. 2019;75(1):88–99. Available from: https://www.sciencedirect.com/science/article/pii/S030228381830246X

59. Cornelison AM, Kantarjian H, Cortes J, Jabbour E. Outcome of treatment of chronic myeloid leukemia with second-generation tyrosine kinase inhibitors after imatinib failure. In: Clinical Lymphoma, Myeloma and Leukemia. Elsevier Inc.; 2011.

60. Prat A, Perou C. Deconstructing the molecular portraits of breast cancer. Mol Oncol. 2011 Feb 1;5:5–23.

61. Walter H, Ahmed S. Targeted therapies in cancer. Surgery (Oxford). 2018 Feb 1;36.

62. Goel HL, Mercurio AM. VEGF targets the tumour cell. Vol. 13, Nature Reviews Cancer. 2013. p. 871–82.

63. Fardi M, Solali S, Farshdousti Hagh M. Epigenetic mechanisms as a new approach in cancer treatment: An updated review. Genes Dis [Internet]. 2018;5(4):304–11. Available from: https://www.sciencedirect.com/science/article/pii/S2352304218300746

64. European Medicines Agency. Azacitidine betapharm - EMA. 2024.

65. Gros C, Fahy J, Halby L, Dufau I, Erdmann A, Gregoire JM, et al. DNA methylation inhibitors in cancer: Recent and future approaches. Biochimie [Internet]. 2012;94(11):2280–96. Available from: https://www.sciencedirect.com/science/article/pii/S0300908412003070

66. Rath CM, Scaglione JB, Kittendorf JD, Sherman DH. 1.11 - NRPS/PKS Hybrid Enzymes and Their Natural Products. In: Liu HW (Ben), Mander L, editors. Comprehensive Natural Products II [Internet]. Oxford: Elsevier; 2010. p. 453–92. Available from: https://www.sciencedirect.com/science/article/pii/B9780080453828007255

67. Bubna AK. Vorinostat—An Overview. Indian J Dermatol [Internet]. 2015;60(4). Available from: https://journals.lww.com/ijd/fulltext/2015/60040/vorinostat_an_overview.31.aspx

68. Arabi F, Mansouri V, Ahmadbeigi N. Gene therapy clinical trials, where do we go? An overview. Biomedicine & Pharmacotherapy [Internet]. 2022;153:113324. Available from: https://www.sciencedirect.com/science/article/pii/S0753332222007132

69. Cesur-Ergün B, Demir-Dora D. Gene therapy in cancer. J Gene Med [Internet]. 2023 Nov 1;25(11):e3550. Available from: https://doi.org/10.1002/jgm.3550

70. Crooke ST, Witztum JL, Bennett CF, Baker BF. RNA-Targeted Therapeutics. Cell Metab [Internet]. 2018;27(4):714–39. Available from: https://www.sciencedirect.com/science/article/pii/S1550413118301827

71. Elbashir SM, Harborth J, Lendeckel W, Yalcin A, Weber K, Tuschl T. Duplexes of 21-nucleotide RNAs mediate RNA interference in cultured mammalian cells. Nature [Internet]. 2001;411(6836):494–8. Available from: https://doi.org/10.1038/35078107

72. Scanlon KJ, Ohta Y, Ishida H, Kijima H, Ohkawa T, Kaminski A, et al. Oligonucleotide-mediated modulation of mammalian gene expression. The FASEB Journal [Internet]. 1995 Oct 1;9(13):1288–96. Available from: https://doi.org/10.1096/fasebj.9.13.7557018

73. Crooke ST, Baker BF, Crooke RM, Liang X hai. Antisense technology: an overview and prospectus. Nat Rev Drug Discov [Internet]. 2021;20(6):427–53. Available from: https://doi.org/10.1038/s41573-021-00162-z

74. Mali P, Yang L, Esvelt KM, Aach J, Guell M, DiCarlo JE, et al. RNA-Guided Human Genome Engineering via Cas9. Science (1979) [Internet]. 2013 Feb 15;339(6121):823–6. Available from: https://doi.org/10.1126/science.1232033

75. Cong L, Ran FA, Cox D, Lin S, Barretto R, Habib N, et al. Multiplex genome engineering using CRISPR/Cas systems. Science (1979). 2013 Feb 15;339(6121):819–23.

76. Cox DBT, Platt RJ, Zhang F. Therapeutic genome editing: prospects and challenges. Nat Med [Internet]. 2015;21(2):121–31. Available from: https://doi.org/10.1038/nm.3793

77. Boch J, Scholze H, Schornack S, Landgraf A, Hahn S, Kay S, et al. Breaking the Code of DNA Binding Specificity of TAL-Type III Effectors. Science (1979) [Internet]. 2009;326(5959):1509–12. Available from: https://www.science.org/doi/abs/10.1126/science.1178811

78. Bogdanove AJ, Schornack S, Lahaye T. TAL effectors: finding plant genes for disease and defense. Curr Opin Plant Biol [Internet]. 2010;13(4):394–401. Available from: https://www.sciencedirect.com/science/article/pii/S1369526610000531

79. Diakun GP, Fairall L, Klug A. EXAFS study of the zinc-binding sites in the protein transcription factor IIIA. Nature [Internet]. 1986;324(6098):698–9. Available from: https://doi.org/10.1038/324698a0

80. Guo J, Gaj T, Barbas CF. Directed Evolution of an Enhanced and Highly Efficient FokI Cleavage Domain for Zinc Finger Nucleases. J Mol Biol [Internet]. 2010;400(1):96–107. Available from: https://www.sciencedirect.com/science/article/pii/S0022283610004481

81. LaFountaine JS, Fathe K, Smyth HDC. Delivery and therapeutic applications of gene editing technologies ZFNs, TALENs, and CRISPR/Cas9. Int J Pharm [Internet]. 2015;494(1):180–94. Available from: https://www.sciencedirect.com/science/article/pii/S0378517315301265

82. Chen XZ, Guo R, Zhao C, Xu J, Song H, Yu H, et al. A Novel Anti-Cancer Therapy: CRISPR/Cas9 Gene Editing. Vol. 13, Frontiers in Pharmacology. Frontiers Media S.A.; 2022.

83. Chehelgerdi M, Chehelgerdi M, Khorramian-Ghahfarokhi M, Shafieizadeh M, Mahmoudi E, Eskandari F, et al. Comprehensive review of CRISPR-based gene editing: mechanisms, challenges, and applications in cancer therapy. Vol. 23, Molecular Cancer. BioMed Central Ltd; 2024.

84. Ishida Y, Agata Y, Shibahara K, Honjo1 T. Induced expression of PD-1, a novel member of the immunoglobulin gene superfamily, upon programmed cell death. Vol. 1, The EMBO Journal. 1992.

85. Barber D, Wherry EJ, Masopust D, Zhu B, Allison J, Sharpe A, et al. Restoring function in exhausted CD8 T cells during chronic viral infection. Nature. 2006 Mar 1;439:682–7.

86. Blank C, Brown I, Peterson AC, Spiotto M, Iwai Y, Honjo T, et al. PD-L1/B7H-1 Inhibits the Effector Phase of Tumor Rejection by T Cell Receptor (TCR) Transgenic CD8+ T Cells. Cancer Res [Internet]. 2004 Feb 10;64(3):1140–5. Available from: https://doi.org/10.1158/0008-5472.CAN-03-3259

87. Menger L, Sledzinska A, Bergerhoff K, Vargas FA, Smith J, Poirot L, et al. TALEN-Mediated Inactivation of PD-1 in Tumor-Reactive Lymphocytes Promotes Intratumoral T-cell Persistence and Rejection of Established Tumors. Cancer Res [Internet]. 2016 Apr 14;76(8):2087–93. Available from: https://doi.org/10.1158/0008-5472.CAN-15-3352

88. Jing W, Gershan JA, Blitzer GC, Palen K, Weber J, McOlash L, et al. Adoptive cell therapy using PD-1+ myeloma-reactive T cells eliminates established myeloma in mice. J Immunother Cancer [Internet]. 2017 Dec 1;5(1):51. Available from: http://jitc.bmj.com/content/5/1/51.abstract

89. Chamberlain CA, Bennett EP, Kverneland AH, Svane IM, Donia M, Met Ö. Highly efficient PD-1-targeted CRISPR-Cas9 for tumor-infiltrating lymphocyte-based adoptive T cell therapy. Mol Ther Oncolytics [Internet]. 2022 Mar 17;24:417–28. Available from: https://doi.org/10.1016/j.omto.2022.01.004

90. ClinicalTrials.gov ID. Single Ascending Dose Study in Participants With LCA10. 2022. NCT03872479.

91. ClinicalTrials.gov ID. A Safety and Efficacy Study Evaluating CTX001 in Subjects With Transfusion-Dependent β-Thalassemia. 2024. NCT03655678.

92. ClinicalTrials.gov ID. NY-ESO-1-redirected CRISPR (TCRendo and PD1) Edited T Cells (NYCE T Cells). 2024. NCT03399448.

93. Maeder ML, Gersbach CA. Genome-editing Technologies for Gene and Cell Therapy. Molecular Therapy [Internet]. 2016;24(3):430–46. Available from: https://www.sciencedirect.com/science/article/pii/S1525001616309613

94. Martinez-Lage M, Puig-Serra P, Menendez P, Torres-Ruiz R, Rodriguez-Perales S. CRISPR/Cas9 for cancer therapy: Hopes and challenges. Vol. 6, Biomedicines. MDPI AG; 2018.

95. Chehelgerdi M, Chehelgerdi M, Khorramian-Ghahfarokhi M, Shafieizadeh M, Mahmoudi E, Eskandari F, et al. Comprehensive review of CRISPR-based gene editing: mechanisms, challenges, and applications in cancer therapy. Mol Cancer [Internet]. 2024;23(1):9. Available from: https://doi.org/10.1186/s12943-023-01925-5

96. Mirgayazova R, Khadiullina R, Chasov V, Mingaleeva R, Miftakhova R, Rizvanov A, et al. Therapeutic editing of the TP53 gene: Is crispr/CAS9 an option? Vol. 11, Genes. MDPI AG; 2020. p. 1–17.

97. Ohki R, Nemoto J, Murasawa H, Oda E, Inazawa J, Tanaka N, et al. Reprimo, a New Candidate Mediator of the p53-mediated Cell Cycle Arrest at the G2 Phase*. Journal of Biological Chemistry [Internet]. 2000;275(30):22627–30. Available from: https://www.sciencedirect.com/science/article/pii/S0021925819661077

98. Garcia-Bloj B, Moses C, Sgro A, Plani-Lam J, Arooj M, Duffy C, et al. Waking up dormant tumor suppressor genes with zinc fingers, TALEs and the CRISPR/dCas9 system. Oncotarget [Internet]. 2016 Aug 19;7(37):60535–54. Available from: www.impactjournals.com/oncotarget

99. Cheng Y, He C, Wang M, Ma X, Mo F, Yang S, et al. Targeting epigenetic regulators for cancer therapy: mechanisms and advances in clinical trials. Signal Transduct Target Ther [Internet]. 2019;4(1):62. Available from: https://doi.org/10.1038/s41392-019-0095-0

100. Dai W, Qiao X, Fang Y, Guo R, Bai P, Liu S, et al. Epigenetics-targeted drugs: current paradigms and future challenges. Signal Transduct Target Ther [Internet]. 2024;9(1):332. Available from: https://doi.org/10.1038/s41392-024-02039-0

101. Zhu Y, Zhu L, Wang X, Jin H. RNA-based therapeutics: an overview and prospectus. Vol. 13, Cell Death and Disease. Springer Nature; 2022.

102. Watts JK, Corey DR. Silencing disease genes in the laboratory and the clinic. Vol. 226, Journal of Pathology. 2012. p. 365–79.

103. Christie KN. Blocking Translation of Oncogenic mRNA. J Cancer Ther. 2023;14(06):233–56.

104. Castro N, Bjelic J, Malhotra G, Huang C, Alsaffar S. Comparison of the Feasibility, Efficiency, and Safety of Genome Editing Technologies. Int J Mol Sci. 2021 Sep 26;22:10355.

105. Khan SH. Genome-Editing Technologies: Concept, Pros, and Cons of Various Genome-Editing Techniques and Bioethical Concerns for Clinical Application. Mol Ther Nucleic Acids [Internet]. 2019 Jun 7;16:326–34. Available from: https://doi.org/10.1016/j.omtn.2019.02.027

106. Tian Z, Liang G, Cui K, Liang Y, Wang Q, Lv S, et al. Insight Into the Prospects for RNAi Therapy of Cancer. Vol. 12, Frontiers in Pharmacology. Frontiers Media S.A.; 2021.

107. Devi GR. siRNA-based approaches in cancer therapy. Cancer Gene Ther [Internet]. 2006;13(9):819–29. Available from: https://doi.org/10.1038/sj.cgt.7700931

108. Chen J, Xie J. Progress on RNAi-based molecular medicines. Vol. 7, International Journal of Nanomedicine. 2012. p. 3971–80.

109. Bäumer S, Bäumer N, Appel N, Terheyden L, Fremerey J, Schelhaas S, et al. Antibody-Mediated Delivery of Anti–KRAS-siRNA In Vivo Overcomes Therapy Resistance in Colon Cancer. Clinical Cancer Research [Internet]. 2015 Mar 12;21(6):1383–94. Available from: https://doi.org/10.1158/1078-0432.CCR-13-2017

110. Chandramohan K, Balan DJ, Devi KP, Nabavi SF, Reshadat S, Khayatkashani M, et al. Short interfering RNA in colorectal cancer: is it wise to shoot the messenger? Eur J Pharmacol [Internet]. 2023;949:175699. Available from: https://www.sciencedirect.com/science/article/pii/S0014299923002108

111. Devi GR. siRNA-based approaches in cancer therapy. Cancer Gene Ther [Internet]. 2006;13(9):819–29. Available from: https://doi.org/10.1038/sj.cgt.7700931

112. Lamb YN. BNT162b2 mRNA COVID-19 Vaccine: First Approval. Vol. 81, Drugs. Adis; 2021. p. 495–501.

113. R BL, M ESH, Brandon E, Karen K, Sharon F, Rick N, et al. Efficacy and Safety of the mRNA-1273 SARS-CoV-2 Vaccine. New England Journal of Medicine [Internet]. 2021 Feb 3;384(5):403–16. Available from: https://doi.org/10.1056/NEJMoa2035389

114. Corbett KS, Edwards DK, Leist SR, Abiona OM, Boyoglu-Barnum S, Gillespie RA, et al. SARS-CoV-2 mRNA vaccine design enabled by prototype pathogen preparedness. Nature [Internet]. 2020;586(7830):567–71. Available from: https://doi.org/10.1038/s41586-020-2622-0

115. Beck JD, Reidenbach D, Salomon N, Sahin U, Türeci Ö, Vormehr M, et al. mRNA therapeutics in cancer immunotherapy. Mol Cancer [Internet]. 2021;20(1):69. Available from: https://doi.org/10.1186/s12943-021-01348-0

116. Wang Y, Zhang Z, Luo J, Han X, Wei Y, Wei X. mRNA vaccine: a potential therapeutic strategy. Mol Cancer [Internet]. 2021;20(1):33. Available from: https://doi.org/10.1186/s12943-021-01311-z

117. Heine A, Juranek S, Brossart P. Clinical and immunological effects of mRNA vaccines in malignant diseases. Mol Cancer. 2021 Mar 15;20.

118. Leonetti C, Zupi G. Targeting Different Signaling Pathways with Antisense Oligonucleotides Combination for Cancer Therapy. Curr Pharm Des. 2007 Feb 1;13(5):463–70.

119. Setoguchi K, Cui L, Hachisuka N, Obchoei S, Shinkai K, Hyodo F, et al. Antisense Oligonucleotides Targeting Y-Box Binding Protein-1 Inhibit Tumor Angiogenesis by Downregulating Bcl-xL-VEGFR2/-Tie Axes. Mol Ther Nucleic Acids [Internet]. 2017;9:170–81. Available from: https://www.sciencedirect.com/science/article/pii/S2162253117302536

120. Hazan-Halevy I, Landesman-Milo D, Rosenblum D, Mizrahy S, Ng BD, Peer D. Immunomodulation of hematological malignancies using oligonucleotides based-nanomedicines. Journal of Controlled Release [Internet]. 2016;244:149–56. Available from: https://www.sciencedirect.com/science/article/pii/S0168365916304989

121. O'Brien SM, Cunningham CC, Golenkov AK, Turkina AG, Novick SC, Rai KR. Phase I to II Multicenter Study of Oblimersen Sodium, a Bcl-2 Antisense Oligonucleotide, in Patients With Advanced Chronic Lymphocytic Leukemia. Journal of Clinical Oncology [Internet]. 2025 Jan 20;23(30):7697–702. Available from: https://doi.org/10.1200/JCO.2005.02.4364

122. Rossor AM, Reilly MM, Sleigh JN. Antisense oligonucleotides and other genetic therapies made simple. Pract Neurol. 2018 Apr 1;18(2):126–31.

123. Liang XH, Sun H, Nichols JG, Crooke ST. RNase H1-Dependent Antisense Oligonucleotides Are Robustly Active in Directing RNA Cleavage in Both the Cytoplasm and the Nucleus. Molecular Therapy [Internet]. 2017;25(9):2075–92. Available from: https://www.sciencedirect.com/science/article/pii/S1525001617302629

124. Li D, Mastaglia FL, Fletcher S, Wilton SD. Precision Medicine through Antisense Oligonucleotide-Mediated Exon Skipping. Trends Pharmacol Sci [Internet]. 2018 Nov 1;39(11):982–94. Available from: https://doi.org/10.1016/j.tips.2018.09.001

125. Desterro J, Bak-Gordon P, Carmo-Fonseca M. Targeting mRNA processing as an anticancer strategy. Nat Rev Drug Discov [Internet]. 2020;19(2):112–29. Available from: https://doi.org/10.1038/s41573-019-0042-3

126. Kaczmarek JC, Kowalski PS, Anderson DG. Advances in the delivery of RNA therapeutics: from concept to clinical reality. Genome Med [Internet]. 2017;9(1):60. Available from: https://doi.org/10.1186/s13073-017-0450-0

127. ClinicalTrials.gov. Clinical Trials with Antisense Oligonucleotides. 2025.

128. de Smet MD, Meenken C, van den Horn GJ. Fomivirsen – a phosphorothioate oligonucleotide for the treatment of CMV retinitis. Ocul Immunol Inflamm [Internet]. 1999 Jan 1;7(3–4):189–98. Available from: https://doi.org/10.1076/ocii.7.3.189.4007

129. Anderson KP, Fox MC, Brown-Driver V, Martin MJ, Azad RF. Inhibition of Human Cytomegalovirus Immediate-Early Gene Expression by an Antisense Oligonucleotide Complementary to Immediate-Early RNA [Internet]. Vol. 40, ANTIMICROBIAL AGENTS AND CHEMOTHERAPY. 1996. Available from: https://journals.asm.org/journal/aac

130. Corey DR. Nusinersen, an antisense oligonucleotide drug for spinal muscular atrophy. Nat Neurosci [Internet]. 2017;20(4):497–9. Available from: https://doi.org/10.1038/nn.4508

131. Aartsma-Rus A. FDA Approval of Nusinersen for Spinal Muscular Atrophy Makes 2016 the Year of Splice Modulating Oligonucleotides. Nucleic Acid Ther [Internet]. 2017 Feb 21;27(2):67–9. Available from: https://doi.org/10.1089/nat.2017.0665

132. Aartsma-Rus A, Krieg AM. FDA Approves Eteplirsen for Duchenne Muscular Dystrophy: The Next Chapter in the Eteplirsen Saga. Nucleic Acid Ther [Internet]. 2016 Dec 8;27(1):1–3. Available from: https://doi.org/10.1089/nat.2016.0657

133. Shirley M. Casimersen: First Approval. Drugs [Internet]. 2021;81(7):875–9. Available from: https://doi.org/10.1007/s40265-021-01512-2

134. Aartsma-Rus A, Corey DR. The 10th Oligonucleotide Therapy Approved: Golodirsen for Duchenne Muscular Dystrophy. Vol. 30, Nucleic Acid Therapeutics. Mary Ann Liebert Inc.; 2020. p. 67–70.

135. Nakamura A, Takeda S. Exon-skipping therapy for Duchenne muscular dystrophy. The Lancet [Internet]. 2011 Aug 13;378(9791):546–7. Available from: https://doi.org/10.1016/S0140-6736(11)61028-3

136. Wu H, Lima WF, Zhang H, Fan A, Sun H, Crooke ST. Determination of the Role of the Human RNase H1 in the Pharmacology of DNA-like Antisense Drugs*. Journal of Biological Chemistry [Internet]. 2004;279(17):17181–9. Available from: https://www.sciencedirect.com/science/article/pii/S0021925819755409

137. Kim Y. Drug Discovery Perspectives of Antisense Oligonucleotides. Vol. 31, Biomolecules and Therapeutics. Korean Society of Applied Pharmacology; 2023. p. 241–52.

138. Kim J, Hu C, Achkar C, Black L, Douville J, Larson A, et al. Patient-Customized Oligonucleotide Therapy for a Rare Genetic Disease. New England Journal of Medicine. 2019 Oct 9;381.

139. Gerson SL, Caimi PF, William BM, Creger RJ. Chapter 57 - Pharmacology and Molecular Mechanisms of Antineoplastic Agents for Hematologic Malignancies. In: Hoffman R, Benz EJ, Silberstein LE, Heslop HE, Weitz JI, Anastasi J, et al., editors. Hematology (Seventh Edition) [Internet]. Elsevier; 2018. p. 849–912. Available from: https://www.sciencedirect.com/science/article/pii/B9780323357623000573

140. Hu J, Duan Z, Yu G, Wang S. Chapter 10 - Bcl-2 Inhibitors as Sensitizing Agents for Cancer Chemotherapy. In: Chen ZS, Yang DH, editors. Protein Kinase Inhibitors as Sensitizing Agents for Chemotherapy [Internet]. Academic Press; 2019. p. 151–68. Available from: https://www.sciencedirect.com/science/article/pii/B9780128164358000109

141. Walker AR, Marcucci G, Yin J, Blum W, Stock W, Kohlschmidt J, et al. Phase 3 randomized trial of chemotherapy with or without oblimersen in older AML patients: CALGB 10201 (Alliance). Blood Adv [Internet]. 2021 Jul 12;5(13):2775–87. Available from: https://doi.org/10.1182/bloodadvances.2021004233

142. Liu R, Yin L. Chapter 24 - Interventional therapy combined with molecular-targeted therapy for pancreatic cancer. In: Li M, Lu L, Xiao Y, Fu D, Zhang H, editors. Integrative Pancreatic Intervention Therapy [Internet]. Elsevier; 2021. p. 541–52. Available from: https://www.sciencedirect.com/science/article/pii/B9780128194027000243

143. Ciardiello D, Elez E, Tabernero J, Seoane J. Clinical development of therapies targeting TGFB: current knowledge and future perspectives. Annals of Oncology [Internet]. 2020 Oct 1;31(10):1336–49. Available from: https://doi.org/10.1016/j.annonc.2020.07.009

144. Oettle H, Hilbig A, Seufferlein T, Tsianakas A, Luger T, Schmid RM, et al. Phase I/II study with trabedersen (AP 12009) monotherapy for the treatment of patients with advanced pancreatic cancer, malignant melanoma, and colorectal carcinoma. Journal of Clinical Oncology [Internet]. 2025 Jan 20;29(15_suppl):2513. Available from: https://doi.org/10.1200/jco.2011.29.15_suppl.2513

145. Rodrigues ACB da C, Costa RGA, Silva SLR, Dias IRSB, Dias RB, Bezerra DP. Cell signaling pathways as molecular targets to eliminate AML stem cells. Crit Rev Oncol Hematol [Internet]. 2021;160:103277. Available from: https://www.sciencedirect.com/science/article/pii/S1040842821000652

146. Hong D, Kurzrock R, Kim Y, Woessner R, Younes A, Nemunaitis J, et al. AZD9150, a next-generation antisense oligonucleotide inhibitor of STAT3 with early evidence of clinical activity in lymphoma and lung cancer. Sci Transl Med. 2015 Nov 18;7(314).

147. Çakan E, Lara OD, Szymanowska A, Bayraktar E, Chavez-Reyes A, Lopez-Berestein G, et al. Therapeutic Antisense Oligonucleotides in Oncology: From Bench to Bedside. Vol. 16, Cancers. Multidisciplinary Digital Publishing Institute (MDPI); 2024.

148. Gagliardi M, Ashizawa AT. The challenges and strategies of antisense oligonucleotide drug delivery. Vol. 9, Biomedicines. MDPI AG; 2021.

149. Deleavey G, Damha MJ. Designing Chemically Modified Oligonucleotides for Targeted Gene Silencing. Chem Biol. 2012 Aug 24;19:937–54.

150. Lin A, Giuliano CJ, Palladino A, John KM, Abramowicz C, Yuan M Lou, et al. Off-target toxicity is a common mechanism of action of cancer drugs undergoing clinical trials. Sci Transl Med. 2019 Sep 11;11(509).

151. Veselov V, Nosyrev A, Jicsinszky L, Alyautdin R, Cravotto G. Targeted Delivery Methods for Anticancer Drugs. Cancers (Basel). 2022 Jan 26;14:622.

152. Chehelgerdi M, Chehelgerdi M, Allela OQB, Pecho RDC, Jayasankar N, Rao DP, et al. Progressing nanotechnology to improve targeted cancer treatment: overcoming hurdles in its clinical implementation. Vol. 22, Molecular Cancer. BioMed Central Ltd; 2023.

153. Lan H, Jamil M, Ke G, Dong N. The role of nanoparticles and nanomaterials in cancer diagnosis and treatment: a comprehensive review [Internet]. Vol. 13, Am J Cancer Res. 2023. Available from: www.ajcr.us/

154. Fan D, Cao Y, Cao M, Wang Y, Cao Y, Gong T. Nanomedicine in cancer therapy. Signal Transduct Target Ther [Internet]. 2023;8(1):293. Available from: https://doi.org/10.1038/s41392-023-01536-y

155. Cheng Z, Li M, Dey R, Chen Y. Nanomaterials for cancer therapy: current progress and perspectives. J Hematol Oncol [Internet]. 2021;14(1):85. Available from: https://doi.org/10.1186/s13045-021-01096-0

156. Sun L, Liu H, Ye Y, Lei Y, Islam R, Tan S, et al. Smart nanoparticles for cancer therapy. Signal Transduct Target Ther [Internet]. 2023;8(1):418. Available from: https://doi.org/10.1038/s41392-023-01642-x

157. Kurul F, Turkmen H, Cetin AE, Topkaya SN. Nanomedicine: How nanomaterials are transforming drug delivery, bio-imaging, and diagnosis. Next Nanotechnology [Internet]. 2025;7:100129. Available from: https://www.sciencedirect.com/science/article/pii/S2949829524000901

158. Shinde VR, Revi N, Murugappan S, Singh SP, Rengan AK. Enhanced permeability and retention effect: A key facilitator for solid tumor targeting by nanoparticles. Photodiagnosis Photodyn Ther [Internet]. 2022;39:102915. Available from: https://www.sciencedirect.com/science/article/pii/S1572100022002010

159. Bobo D, Robinson KJ, Islam J, Thurecht KJ, Corrie SR. Nanoparticle-Based Medicines: A Review of FDA-Approved Materials and Clinical Trials to Date. Pharm Res [Internet]. 2016;33(10):2373–87. Available from: https://doi.org/10.1007/s11095-016-1958-5

160. Barenholz Y (Chezy). Doxil® — The first FDA-approved nano-drug: Lessons learned. Journal of Controlled Release [Internet]. 2012;160(2):117–34. Available from: https://www.sciencedirect.com/science/article/pii/S0168365912002301

161. Batist G, Barton J, Chaikin P, Swenson C, Welles L. Myocet (liposome-encapsulated doxorubicin citrate): a new approach in breast cancer therapy. Expert Opin Pharmacother [Internet]. 2002 Dec 1;3(12):1739–51. Available from: https://doi.org/10.1517/14656566.3.12.1739

162. Frampton JE. Liposomal Irinotecan: A Review in Metastatic Pancreatic Adenocarcinoma. Drugs [Internet]. 2020;80(10):1007–18. Available from: https://doi.org/10.1007/s40265-020-01336-6

163. Silverman JA, Deitcher SR. Marqibo® (vincristine sulfate liposome injection) improves the pharmacokinetics and pharmacodynamics of vincristine. Cancer Chemother Pharmacol [Internet]. 2013;71(3):555–64. Available from: https://doi.org/10.1007/s00280-012-2042-4

164. Forssen EA. The design and development of DaunoXome® for solid tumor targeting in vivo. Adv Drug Deliv Rev [Internet]. 1997;24(2):133–50. Available from: https://www.sciencedirect.com/science/article/pii/S0169409X9600453X

165. Salehi B, Selamoglu Z, Mileski KS, Pezzani R, Redaelli M, Cho WC, et al. Liposomal cytarabine as cancer therapy: From chemistry to medicine. Vol. 9, Biomolecules. MDPI AG; 2019.

166. Mifamurtide. Drugs in R & D [Internet]. 2008;9(2):131–5. Available from: https://doi.org/10.2165/00126839-200809020-00007

167. Chou HH, Wang KL, Chen CA, Wei LH, Lai CH, Hsieh CY, et al. Pegylated liposomal doxorubicin (Lipo-Dox) for platinum-resistant or refractory epithelial ovarian carcinoma: A Taiwanese gynecologic oncology group study with long-term follow-up. Gynecol Oncol [Internet]. 2006 Jun 1;101(3):423–8. Available from: https://doi.org/10.1016/j.ygyno.2005.10.027

168. Heo YA, Syed YY, Keam SJ. Pegaspargase: A Review in Acute Lymphoblastic Leukaemia. Drugs [Internet]. 2019;79(7):767–77. Available from: https://doi.org/10.1007/s40265-019-01120-1

169. Masuda E, Maeda H. Antitumor resistance induced by zinostatin stimalamer (ZSS), a polymer-conjugated neocarzinostatin (NCS) derivative. Cancer Immunology, Immunotherapy [Internet]. 1995;40(5):329–38. Available from: https://doi.org/10.1007/BF01519634

170. Veronese FM, Pasut G. Drug–Polymer Conjugates. In: Taylor JB, Triggle DJ, editors. Comprehensive Medicinal Chemistry II [Internet]. Oxford: Elsevier; 2007. p. 1043–68. Available from: https://www.sciencedirect.com/science/article/pii/B008045044X001590

171. Wex J, Sidhu M, Odeyemi I, Abou-Setta AM, Retsa P, Tombal B. Leuprolide acetate 1-, 3- and 6-monthly depot formulations in androgen deprivation therapy for prostate cancer in nine European countries: Evidence review and economic evaluation. ClinicoEconomics and Outcomes Research. 2013 Jun 22;5(1):257–69.

172. Blair HA, Deeks ED. Albumin-Bound Paclitaxel: A Review in Non-Small Cell Lung Cancer. Drugs [Internet]. 2015;75(17):2017–24. Available from: https://doi.org/10.1007/s40265-015-0484-9

173. Werner ME, Cummings ND, Sethi M, Wang EC, Sukumar R, Moore DT, et al. Preclinical Evaluation of Genexol-PM, a Nanoparticle Formulation of Paclitaxel, as a Novel Radiosensitizer for the Treatment of Non-Small Cell Lung Cancer. Int J Radiat Oncol Biol Phys [Internet]. 2013 Jul 1;86(3):463–8. Available from: https://doi.org/10.1016/j.ijrobp.2013.02.009

174. Soetaert F, Korangath P, Serantes D, Fiering S, Ivkov R. Cancer therapy with iron oxide nanoparticles: Agents of thermal and immune therapies. Adv Drug Deliv Rev [Internet]. 2020;163–164:65–83. Available from: https://www.sciencedirect.com/science/article/pii/S0169409X20300715

175. Lamichhane N, Sharifabad ME, Hodgson B, Mercer T, Sen T. Chapter 13 - Superparamagnetic iron oxide nanoparticles (SPIONs) as therapeutic and diagnostic agents. In: Kesharwani P, Singh KK, editors. Nanoparticle Therapeutics [Internet]. Academic Press; 2022. p. 455–97. Available from: https://www.sciencedirect.com/science/article/pii/B978012820757400003X

176. Al-Thani AN, Jan AG, Abbas M, Geetha M, Sadasivuni KK. Nanoparticles in cancer theragnostic and drug delivery: A comprehensive review. Life Sci [Internet]. 2024;352:122899. Available from: https://www.sciencedirect.com/science/article/pii/S0024320524004892

177. Seidu TA, Kutoka PT, Asante DO, Farooq MA, Alolga RN, Bo W. Functionalization of Nanoparticulate Drug Delivery Systems and Its Influence in Cancer Therapy. Vol. 14, Pharmaceutics. MDPI; 2022.

178. Amreddy N, Babu A, Muralidharan R, Panneerselvam J, Srivastava A, Ahmed R, et al. Recent Advances in Nanoparticle-Based Cancer Drug and Gene Delivery. In: Advances in Cancer Research. Academic Press Inc.; 2018. p. 115–70.

179. Hsu CY, Rheima AM, Kadhim MM, Ahmed NN, Mohammed SH, Abbas FH, et al. An overview of nanoparticles in drug delivery: Properties and applications. S Afr J Chem Eng [Internet]. 2023;46:233–70. Available from: https://www.sciencedirect.com/science/article/pii/S102691852300080X

180. Mehta M, Bui TA, Yang X, Aksoy Y, Goldys EM, Deng W. Lipid-Based Nanoparticles for Drug/Gene Delivery: An Overview of the Production Techniques and Difficulties Encountered in Their Industrial Development. ACS Materials Au [Internet]. 2023 Nov 8;3(6):600–19. Available from: https://doi.org/10.1021/acsmaterialsau.3c00032

181. Wu X, Wu M, Zhao JX. Recent development of silica nanoparticles as delivery vectors for cancer imaging and therapy. Nanomedicine [Internet]. 2014;10(2):297–312. Available from: https://www.sciencedirect.com/science/article/pii/S154996341300470X

182. Wagner AM, Knipe JM, Orive G, Peppas NA. Quantum dots in biomedical applications. Acta Biomater [Internet]. 2019;94:44–63. Available from: https://www.sciencedirect.com/science/article/pii/S1742706119303393

183. Mody V V, Siwale R, Singh A, Mody HR. Introduction to metallic nanoparticles. J Pharm Bioallied Sci [Internet]. 2010;2(4). Available from: https://journals.lww.com/jpbs/fulltext/2010/02040/introduction_to_metallic_nanoparticles.2.aspx

184. Rahman M. Magnetic Resonance Imaging and Iron-oxide Nanoparticles in the era of Personalized Medicine. Vol. 7, Nanotheranostics. Ivyspring International Publisher; 2023. p. 424–49.

185. Bruna T, Maldonado-Bravo F, Jara P, Caro N. Silver nanoparticles and their antibacterial applications. Vol. 22, International Journal of Molecular Sciences. MDPI; 2021.

186. Tiwari PM, Vig K, Dennis VA, Singh SR. Functionalized gold nanoparticles and their biomedical applications. Vol. 1, Nanomaterials. MDPI; 2011. p. 31–63.

187. Bansal SA, Kumar V, Karimi J, Singh AP, Kumar S. Role of gold nanoparticles in advanced biomedical applications. Vol. 2, Nanoscale Advances. Royal Society of Chemistry; 2020. p. 3764–87.

188. Yeh YC, Creran B, Rotello VM. Gold nanoparticles: preparation, properties, and applications in bionanotechnology. Nanoscale [Internet]. 2012;4(6):1871–80. Available from: http://dx.doi.org/10.1039/C1NR11188D

189. Carnovale C, Bryant G, Shukla R, Bansal V. Identifying Trends in Gold Nanoparticle Toxicity and Uptake: Size, Shape, Capping Ligand, and Biological Corona. ACS Omega [Internet]. 2019 Jan 31;4(1):242–56. Available from: https://doi.org/10.1021/acsomega.8b03227

190. Desai N. Challenges in development of nanoparticle-based therapeutics. Vol. 14, AAPS Journal. 2012. p. 282–95.

191. X. The Bakerian Lecture. —Experimental relations of gold (and other metals) to light. Philos Trans R Soc Lond. 1857 Dec 31;147:145–81.

192. Turkevich J, Stevenson PC, Hillier J. A study of the nucleation and growth processes in the synthesis of colloidal gold. Discuss Faraday Soc [Internet]. 1951;11(0):55–75. Available from: http://dx.doi.org/10.1039/DF9511100055

193. Sakamoto M, Fujistuka M, Majima T. Light as a construction tool of metal nanoparticles: Synthesis and mechanism. Journal of Photochemistry and Photobiology C: Photochemistry Reviews [Internet]. 2009;10(1):33–56. Available from: https://www.sciencedirect.com/science/article/pii/S1389556708000865

194. Tangeysh B, Moore Tibbetts K, Odhner JH, Wayland BB, Levis RJ. Gold Nanoparticle Synthesis Using Spatially and Temporally Shaped Femtosecond Laser Pulses: Post-Irradiation Auto-Reduction of Aqueous [AuCl4]−. The Journal of Physical Chemistry C [Internet]. 2013 Sep 12;117(36):18719–27. Available from: https://doi.org/10.1021/jp4056494

195. Birtcher RC, Kirk MA, Furuya K, Lumpkin GR, Ruault MO. In situ transmission electron microscopy investigation of radiation effects. J Mater Res [Internet]. 2005;20(7):1654–83. Available from: https://doi.org/10.1557/JMR.2005.0242

196. Mandal R, Baranwal A, Srivastava A, Chandra P. Evolving trends in bio/chemical sensor fabrication incorporating bimetallic nanoparticles. Biosens Bioelectron [Internet].

2018;117:546–61. Available from: https://www.sciencedirect.com/science/article/pii/S0956566318304718

197. Brust M, Walker M, Bethell D, Schiffrin DJ, Whyman R. Synthesis of thiol-derivatised gold nanoparticles in a two-phase Liquid–Liquid system. J Chem Soc Chem Commun [Internet]. 1994;(7):801–2. Available from: http://dx.doi.org/10.1039/C39940000801

198. Mahato K, Nagpal S, Shah MA, Srivastava A, Maurya PK, Roy S, et al. Gold nanoparticle surface engineering strategies and their applications in biomedicine and diagnostics. 3 Biotech [Internet]. 2019;9(2):57. Available from: https://doi.org/10.1007/s13205-019-1577-z

199. Baranwal A, Mahato K, Srivastava A, Maurya P, Chandra DrP. Phytofabricated metallic nanoparticles and their clinical applications. RSC Adv. 2016 Oct 26;6.

200. Korbekandi H, Iravani S, Abbasi S. Production of nanoparticles using organisms. Crit Rev Biotechnol [Internet]. 2009 Dec 1;29(4):279–306. Available from: https://doi.org/10.3109/07388550903062462

201. He S, Guo Z, Zhang Y, Zhang S, Wang J, Gu N. Biosynthesis of gold nanoparticles using the bacteria Rhodopseudomonas capsulata. Mater Lett [Internet]. 2007;61(18):3984–7. Available from: https://www.sciencedirect.com/science/article/pii/S0167577X07000171

202. Castro-Longoria E, Vilchis-Nestor AR, Avalos-Borja M. Biosynthesis of silver, gold and bimetallic nanoparticles using the filamentous fungus Neurospora crassa. Colloids Surf B Biointerfaces [Internet]. 2011;83(1):42–8. Available from: https://www.sciencedirect.com/science/article/pii/S0927776510006004

203. Singaravelu G, Arockiamary JS, Kumar VG, Govindaraju K. A novel extracellular synthesis of monodisperse gold nanoparticles using marine alga, Sargassum wightii Greville. Colloids Surf B Biointerfaces [Internet]. 2007;57(1):97–101. Available from: https://www.sciencedirect.com/science/article/pii/S0927776507000252

204. Arcos Rosero WA, Bueno Barbezan A, Daruich de Souza C, Chuery Martins Rostelato ME. Review of Advances in Coating and Functionalization of Gold Nanoparticles: From Theory to Biomedical Application. Vol. 16, Pharmaceutics. Multidisciplinary Digital Publishing Institute (MDPI); 2024.

205. Huang H, Liu R, Yang J, Dai J, Fan S, Pi J, et al. Gold Nanoparticles: Construction for Drug Delivery and Application in Cancer Immunotherapy. Vol. 15, Pharmaceutics. Multidisciplinary Digital Publishing Institute (MDPI); 2023.

206. Astruc D, Editor. Nanoparticles and Catalysis. 2008. 640 pp.

207. Khlebtsov B, Burov A, Pylaev T, Khlebtsov N. Polydopamine-coated Au nanorods for targeted fluorescent cell imaging and photothermal therapy. Beilstein Journal of Nanotechnology. 2019 Apr 1;10:794–803.

208. Li P, Wu Y, Li D, Su X, Luo C, Wang Y, et al. Seed-Mediated Synthesis of Tunable-Aspect-Ratio Gold Nanorods for Near-Infrared Photoacoustic Imaging. Nanoscale Res Lett [Internet]. 2018;13(1):313. Available from: https://doi.org/10.1186/s11671-018-2734-8

209. Zhou B, Guo X, Yang N, Huang Z, Huang L, Fang Z, et al. Surface engineering strategies of gold nanomaterials and their applications in biomedicine and detection. Vol. 9, Journal of Materials Chemistry B. 2021. p. 5583–98.

210. Zhou B, Xiong Z, Wang P, Peng C, Shen M, Shi X. Acetylated Polyethylenimine-Entrapped Gold Nanoparticles Enable Negative Computed Tomography Imaging of Orthotopic Hepatic Carcinoma. Langmuir. 2018 Jul 24;34(29):8701–7.

211. Wei SC, Hsu PH, Lee YF, Lin YW, Huang CC. Selective Detection of Iodide and Cyanide Anions Using Gold-Nanoparticle-Based Fluorescent Probes. ACS Appl Mater Interfaces. 2012 Apr 23;4:2652–8.

212. Behi M, Naficy S, Chandrawati R, Dehghani F. Nanoassembled Peptide Biosensors for Rapid Detection of Matrilysin Cancer Biomarker. Small [Internet]. 2020 Apr 1;16(16):1905994. Available from: https://doi.org/10.1002/smll.201905994

213. Dongying Q, Lan L, Qian D. Targeting of ovarian cancer cell through functionalized gold nanoparticles by novel glypican-3- binding peptide as a ultrasound contrast agents. Process Biochemistry [Internet]. 2020;98:51–8. Available from: https://www.sciencedirect.com/science/article/pii/S1359511320308886

214. Endzeliņš E, Berger A, Melne V, Bajo-Santos C, Soboļevska K, Ābols A, et al. Detection of circulating miRNAs: comparative analysis of extracellular vesicle-incorporated miRNAs and cell-free miRNAs in whole plasma of prostate cancer patients. BMC Cancer [Internet]. 2017;17(1):730. Available from: https://doi.org/10.1186/s12885-017-3737-z

215. Zhao J, Liu C, Li Y, Ma Y, Deng J, Li L, et al. Thermophoretic Detection of Exosomal microRNAs by Nanoflares. J Am Chem Soc [Internet]. 2020 Mar 18;142(11):4996–5001. Available from: https://doi.org/10.1021/jacs.9b13960

216. Arcos Rosero WA, Bueno Barbezan A, Daruich de Souza C, Chuery Martins Rostelato ME. Review of Advances in Coating and Functionalization of Gold Nanoparticles: From Theory to Biomedical Application. Vol. 16, Pharmaceutics. Multidisciplinary Digital Publishing Institute (MDPI); 2024.

217. Yin H, Kanasty RL, Eltoukhy AA, Vegas AJ, Dorkin JR, Anderson DG. Non-viral vectors for gene-based therapy. Nat Rev Genet [Internet]. 2014;15(8):541–55. Available from: https://doi.org/10.1038/nrg3763

218. Li W, Cao Z, Liu R, Liu L, Li H, Li X, et al. AuNPs as an important inorganic nanoparticle applied in drug carrier systems. Artif Cells Nanomed Biotechnol [Internet]. 2019 Dec 4;47(1):4222–33. Available from: https://doi.org/10.1080/21691401.2019.1687501

219. Suk JS, Xu Q, Kim N, Hanes J, Ensign LM. PEGylation as a strategy for improving nanoparticle-based drug and gene delivery. Vol. 99, Advanced Drug Delivery Reviews. Elsevier B.V.; 2016. p. 28–51.

220. Thiruppathi R, Mishra S, Ganapathy M, Padmanabhan P, Gulyás B. Nanoparticle Functionalization and Its Potentials for Molecular Imaging. Advanced Science [Internet]. 2017 Mar 1;4(3):1600279. Available from: https://doi.org/10.1002/advs.201600279

221. Mahato K, Nagpal S, Shah MA, Srivastava A, Maurya PK, Roy S, et al. Gold nanoparticle surface engineering strategies and their applications in biomedicine and diagnostics. 3 Biotech [Internet]. 2019;9(2):57. Available from: https://doi.org/10.1007/s13205-019-1577-z

222. Park C, Youn H, Kim H, Noh T, Kook Y, Oh E, et al. Cyclodextrin-covered gold nanoparticles for targeted delivery of an anti-cancer drug. J Mater Chem. 2009 Apr 28;19:2310–5.

223. Naahidi S, Jafari M, Edalat F, Raymond K, Khademhosseini A, Chen P. Biocompatibility of engineered nanoparticles for drug delivery. Journal of Controlled Release [Internet]. 2013;166(2):182–94. Available from: https://www.sciencedirect.com/science/article/pii/S0168365912008553

224. Baidya S, Hassan AM. SARS-CoV-2 Detection Using Colorimetric Plasmonic Sensors: A Proof-of-Concept Computational Study. IEEE Trans Nanobioscience. 2023 Jan 1;22(1):71–7.

225. Sepúlveda B, Angelomé PC, Lechuga LM, Liz-Marzán LM. LSPR-based nanobiosensors. Nano Today [Internet]. 2009;4(3):244–51. Available from: https://www.sciencedirect.com/science/article/pii/S1748013209000280

226. Guo J, Rahme K, He Y, Li LL, Holmes JD, O'Driscoll CM. Gold nanoparticles enlighten the future of cancer theranostics. Int J Nanomedicine [Internet]. 2017 Aug 22 [cited 2021 Dec 15];12:6131–52. Available from: https://pubmed.ncbi.nlm.nih.gov/28883725/

227. Shanmugam V, Selvakumar S, Yeh CS. Near-infrared light-responsive nanomaterials in cancer therapeutics. Chem Soc Rev [Internet]. 2014;43(17):6254–87. Available from: http://dx.doi.org/10.1039/C4CS00011K

228. Cole JT, Holland NB. Multifunctional nanoparticles for use in theranostic applications. Drug Deliv Transl Res [Internet]. 2015;5(3):295–309. Available from: https://doi.org/10.1007/s13346-015-0218-2

229. Lee H, Lee K, Kim IK, Park TG. Synthesis, characterization, and in vivo diagnostic applications of hyaluronic acid immobilized gold nanoprobes. Biomaterials [Internet]. 2008;29(35):4709–18. Available from: https://www.sciencedirect.com/science/article/pii/S0142961208006479

230. Li W, Chen X. Gold Nanoparticles for Photoacoustic Imaging. Nanomedicine [Internet]. 2015 Jan 1;10(2):299–320. Available from: https://doi.org/10.2217/nnm.14.169

231. Wu Y, Ali MRK, Chen K, Fang N, El-Sayed MA. Gold nanoparticles in biological optical imaging. Nano Today [Internet]. 2019;24:120–40. Available from: https://www.sciencedirect.com/science/article/pii/S1748013218305735

232. Link S, El-Sayed M. Optical Properties and Ultrafast Dynamics of Metallic Nanocrystals. Annu Rev Phys Chem. 2003 Feb 1;54:331–66.

233. Kneipp K, Kneipp H, Manoharan R, Hanlon EB, Itzkan I, Dasari RR, et al. Extremely Large Enhancement Factors in Surface-Enhanced Raman Scattering for Molecules on Colloidal Gold Clusters. Appl Spectrosc [Internet]. 1998 Dec 1;52(12):1493–7. Available from: https://doi.org/10.1366/0003702981943059

234. Cole LE, Ross RD, Tilley JMR, Vargo-Gogola T, Roeder RK. Gold Nanoparticles as Contrast Agents in x-ray Imaging and Computed Tomography. Nanomedicine [Internet]. 2015 Jan 1;10(2):321–41. Available from: https://doi.org/10.2217/nnm.14.171

235. Kumalasari MR, Alfanaar R, Andreani AS. Gold nanoparticles (AuNPs): A versatile material for biosensor application. Talanta Open [Internet]. 2024;9:100327. Available from: https://www.sciencedirect.com/science/article/pii/S2666831924000419

236. Cordeiro M, Carlos FF, Pedrosa P, Lopez A, Baptista PV. Gold nanoparticles for diagnostics: Advances towards points of care. Vol. 6, Diagnostics. Multidisciplinary Digital Publishing Institute (MDPI); 2016.

237. Grubisha D, Lipert R, Park HY, Driskell J, Porter M. Femtomolar Detection of Prostate-Specific Antigen: An Immunoassay Based on Surface-Enhanced Raman Scattering and Immunogold Labels. Anal Chem. 2003 Dec 1;75:5936–43.

238. Yao Y, Zhou Y, Liu L, Xu Y, Chen Q, Wang Y, et al. Nanoparticle-Based Drug Delivery in Cancer Therapy and Its Role in Overcoming Drug Resistance. Front Mol Biosci [Internet]. 2020;7. Available from: https://www.frontiersin.org/journals/molecular-biosciences/articles/10.3389/fmolb.2020.00193

239. Attia MF, Anton N, Wallyn J, Omran Z, Vandamme TF. An overview of active and passive targeting strategies to improve the nanocarriers efficiency to tumour sites. Journal of Pharmacy and Pharmacology [Internet]. 2019 Aug 1;71(8):1185–98. Available from: https://doi.org/10.1111/jphp.13098

240. Clemons TD, Singh R, Sorolla A, Chaudhari N, Hubbard A, Iyer KS. Distinction Between Active and Passive Targeting of Nanoparticles Dictate Their Overall Therapeutic Efficacy. Langmuir [Internet]. 2018 Dec 18;34(50):15343–9. Available from: https://doi.org/10.1021/acs.langmuir.8b02946

241. Dreaden EC, Austin LA, Mackey MA, El-Sayed MA. Size Matters: Gold Nanoparticles in Targeted Cancer Drug Delivery. Ther Deliv [Internet]. 2012 Apr 1;3(4):457–78. Available from: https://doi.org/10.4155/tde.12.21

242. Patel JK, Patel AP. Passive Targeting of Nanoparticles to Cancer. In: Pathak Y V, editor. Surface Modification of Nanoparticles for Targeted Drug Delivery [Internet]. Cham: Springer International Publishing; 2019. p. 125–43. Available from: https://doi.org/10.1007/978-3-030-06115-9_6

243. Sykes EA, Chen J, Zheng G, Chan WCW. Investigating the Impact of Nanoparticle Size on Active and Passive Tumor Targeting Efficiency. ACS Nano [Internet]. 2014 Jun 24;8(6):5696–706. Available from: https://doi.org/10.1021/nn500299p

244. Goddard ZR, Marín MJ, Russell DA, Searcey M. Active targeting of gold nanoparticles as cancer therapeutics. Chem Soc Rev [Internet]. 2020;49(23):8774–89. Available from: http://dx.doi.org/10.1039/D0CS01121E

245. Kumar A, Ma H, Zhang X, Huang K, Jin S, Liu J, et al. Gold nanoparticles functionalized with therapeutic and targeted peptides for cancer treatment. Biomaterials [Internet]. 2012;33(4):1180–9. Available from: https://www.sciencedirect.com/science/article/pii/S0142961211012622

246. Maus L, Dick O, Bading H, Spatz JP, Fiammengo R. Conjugation of Peptides to the Passivation Shell of Gold Nanoparticles for Targeting of Cell-Surface Receptors. ACS Nano [Internet]. 2010 Nov 23;4(11):6617–28. Available from: https://doi.org/10.1021/nn101867w

247. Bhattacharyya S, Khan JA, Curran GL, Robertson JD, Bhattacharya R, Mukherjee P. Efficient Delivery of Gold Nanoparticles by Dual Receptor Targeting. Advanced Materials [Internet]. 2011 Nov 16;23(43):5034–8. Available from: https://doi.org/10.1002/adma.201102287

248. Mi P. Stimuli-responsive nanocarriers for drug delivery, tumor imaging, therapy and theranostics. Vol. 10, Theranostics. Ivyspring International Publisher; 2020. p. 4557–88.

249. Mariadoss AVA, Saravanakumar K, Sathiyaseelan A, Karthikkumar V, Wang MH. Smart drug delivery of p-Coumaric acid loaded aptamer conjugated starch nanoparticles for effective triple-negative breast cancer therapy. Int J Biol Macromol [Internet]. 2022;195:22–9. Available from: https://www.sciencedirect.com/science/article/pii/S0141813021025757

250. Trabbic KR, Kleski KA, Barchi JJ. Stable Gold-Nanoparticle-Based Vaccine for the Targeted Delivery of Tumor-Associated Glycopeptide Antigens. ACS Bio and Med Chem Au. 2021 Dec 15;1(1):31–43.

251. Cai H, Degliangeli F, Palitzsch B, Gerlitzki B, Kunz H, Schmitt E, et al. Glycopeptide-functionalized gold nanoparticles for antibody induction against the tumor associated mucin-1 glycoprotein. Bioorg Med Chem [Internet]. 2016;24(5):1132–5. Available from: https://www.sciencedirect.com/science/article/pii/S096808961630044X

252. Kanu GA, Parambath JBM, Abu Odeh RO, Mohamed AA. Gold Nanoparticle-Mediated Gene Therapy. Vol. 14, Cancers. MDPI; 2022.

253. Cuciniello R, Filosa S, Crispi S. Novel approaches in cancer treatment: preclinical and clinical development of small non-coding RNA therapeutics. Journal of Experimental & Clinical Cancer Research [Internet]. 2021;40(1):383. Available from: https://doi.org/10.1186/s13046-021-02193-1

254. Żelechowska-Matysiak K, Wawrowicz K, Wierzbicki M, Budlewski T, Bilewicz A, Majkowska-Pilip A. Doxorubicin- and Trastuzumab-Modified Gold Nanoparticles as Potential Multimodal Agents for Targeted Therapy of HER2+ Cancers. Molecules. 2023 Mar 1;28(6).

255. WANG Z, DONG J, ZHAO Q, YING Y, ZHANG L, ZOU J, et al. Gold nanoparticle-mediated delivery of paclitaxel and nucleic acids for cancer therapy (Review). Mol Med Rep. 2020 Dec 1;22(6):4475–84.

256. Conde J, Oliva N, Artzi N. Implantable hydrogel embedded dark-gold nanoswitch as a theranostic probe to sense and overcome cancer multidrug resistance. Proceedings of the National Academy of Sciences [Internet]. 2015 Mar 17;112(11):E1278–87. Available from: https://doi.org/10.1073/pnas.1421229112

257. González-López MA, Gutiérrez-Cárdenas EM, Sánchez-Cruz C, Hernández-Paz JF, Pérez I, Olivares-Trejo JJ, et al. Reducing the effective dose of cisplatin using gold nanoparticles as carriers. Cancer Nanotechnol [Internet]. 2020;11(1):4. Available from: https://doi.org/10.1186/s12645-020-00060-w

258. Sadalage PS, Patil R V, Havaldar D V, Gavade SS, Santos AC, Pawar KD. Optimally biosynthesized, PEGylated gold nanoparticles functionalized with quercetin and camptothecin enhance potential anti-inflammatory, anti-cancer and anti-angiogenic activities. J Nanobiotechnology [Internet]. 2021;19(1):84. Available from: https://doi.org/10.1186/s12951-021-00836-1

259. Libutti SK, Paciotti GF, Byrnes AA, Alexander HR, Gannon WE, Walker M, et al. Phase I and pharmacokinetic studies of CYT-6091, a novel PEGylated colloidal gold-rhTNF nanomedicine. Clinical Cancer Research. 2010 Dec 15;16(24):6139–49.

260. Tamarkin L, Myer L, Haynes R, Paciotti G. CYT6091 (Aurimune): a colloidal gold-based tumor-targeted nanomedicine. Nanomedicine-nanotechnology Biology and Medicine - NANOMED-NANOTECHNOL BIOL MED. 2006 Dec 1;2:273–4.

261. Mendes R, Fernandes AR, Baptista P V. Gold nanoparticle approach to the selective delivery of gene silencing in cancer-The case for combined delivery? Vol. 8, Genes. MDPI AG; 2017.

262. Lee K, Conboy M, Park HM, Jiang F, Kim HJ, Dewitt MA, et al. Nanoparticle delivery of Cas9 ribonucleoprotein and donor DNA in vivo induces homology-directed DNA repair. Nat Biomed Eng [Internet]. 2017;1(11):889–901. Available from: https://doi.org/10.1038/s41551-017-0137-2

263. Lee B, Lee K, Panda S, Gonzales-Rojas R, Chong A, Bugay V, et al. Nanoparticle delivery of CRISPR into the brain rescues a mouse model of fragile X syndrome from exaggerated repetitive behaviours. Nat Biomed Eng. 2018 Jul 1;2.

264. Kesharwani P, Ma R, Sang L, Fatima M, Sheikh A, Abourehab MAS, et al. Gold nanoparticles and gold nanorods in the landscape of cancer therapy. Mol Cancer [Internet]. 2023;22(1):98. Available from: https://doi.org/10.1186/s12943-023-01798-8

265. Siddique S, Chow JCL. Gold nanoparticles for drug delivery and cancer therapy. Vol. 10, Applied Sciences (Switzerland). MDPI AG; 2020.

266. Foglizzo V, Cocco E, Marchiò S. Advanced Cellular Models for Preclinical Drug Testing: From 2D Cultures to Organ-on-a-Chip Technology. Vol. 14, Cancers. MDPI; 2022.

267. Crouigneau R, Li YF, Auxillos J, Goncalves-Alves E, Marie R, Sandelin A, et al. Mimicking and analyzing the tumor microenvironment. Cell reports methods [Internet]. 2024 Sep 25;100866. Available from: http://www.ncbi.nlm.nih.gov/pubmed/39353424

268. Sajjad H, Imtiaz S, Noor T, Siddiqui YH, Sajjad A, Zia M. Cancer models in preclinical research: A chronicle review of advancement in effective cancer research. Vol. 4, Animal Models and Experimental Medicine. John Wiley and Sons Inc; 2021. p. 87–103.

269. Zhang C, Sui Y, Liu S, Yang M. In vitro and in vivo experimental models for cancer immunotherapy study. Curr Res Biotechnol [Internet]. 2024;7:100210. Available from: https://www.sciencedirect.com/science/article/pii/S2590262824000364

270. Katt ME, Placone AL, Wong AD, Xu ZS, Searson PC. In vitro tumor models: Advantages, disadvantages, variables, and selecting the right platform. Vol. 4, Frontiers in Bioengineering and Biotechnology. Frontiers Media S.A.; 2016.

271. Bartlett R, Everett W, Lim S, G N, Loizidou M, Jell G, et al. Personalized In Vitro Cancer Modeling — Fantasy or Reality? Transl Oncol [Internet]. 2014;7(6):657–64. Available from: https://www.sciencedirect.com/science/article/pii/S1936523314001193

272. Ferreira LP, Gaspar VM, Mano JF. Design of spherically structured 3D in vitro tumor models - Advances and prospects. Acta Biomater [Internet]. 2018;75:11–34. Available from: https://www.sciencedirect.com/science/article/pii/S1742706118303106

273. Manduca N, Maccafeo E, De Maria R, Sistigu A, Musella M. 3D cancer models: One step closer to in vitro human studies. Vol. 14, Frontiers in Immunology. Frontiers Media S.A.; 2023.

274. Tosca EM, Ronchi D, Facciolo D, Magni P. Replacement, Reduction, and Refinement of Animal Experiments in Anticancer Drug Development: The Contribution of 3D In Vitro Cancer Models in the Drug Efficacy Assessment. Biomedicines [Internet]. 2023;11(4). Available from: https://www.mdpi.com/2227-9059/11/4/1058

275. Nayak P, Bentivoglio V, Varani M, Signore A. Three-Dimensional In Vitro Tumor Spheroid Models for Evaluation of Anticancer Therapy: Recent Updates. Vol. 15, Cancers. Multidisciplinary Digital Publishing Institute (MDPI); 2023.

276. Jiang X, Oyang L, Peng Q, Liu Q, Xu X, Wu N, et al. Organoids: opportunities and challenges of cancer therapy. Front Cell Dev Biol [Internet]. 2023;11. Available from: https://www.frontiersin.org/journals/cell-and-developmental-biology/articles/10.3389/fcell.2023.1232528

277. Li W, Zhou Z, Zhou X, Khoo BL, Gunawan R, Chin YR, et al. 3D Biomimetic Models to Reconstitute Tumor Microenvironment In Vitro: Spheroids, Organoids, and Tumor-on-a-Chip. Adv Healthc Mater. 2023;12(18).

278. Sharma R, Restan Perez M, da Silva VA, Thomsen J, Bhardwaj L, Andrade TAM, et al. 3D bioprinting complex models of cancer. Biomater Sci [Internet]. 2023;11(10):3414–30. Available from: http://dx.doi.org/10.1039/D2BM02060B

279. Sharma K, Dey S, Karmakar R, Rengan AK. A comprehensive review of 3D cancer models for drug screening and translational research. Cancer Innovation [Internet]. 2024;3(1):e102–e102. Available from: https://doi.org/10.1002/cai2.102

280. Barbosa MAG, Xavier CPR, Pereira RF, Petrikaitė V, Vasconcelos MH. 3D Cell Culture Models as Recapitulators of the Tumor Microenvironment for the Screening of Anti-Cancer Drugs. Cancers (Basel). 2021;14(1):190.

281. Atat O El, Farzaneh Z, Pourhamzeh M, Taki F, Abi-Habib R, Vosough M, et al. 3D modeling in cancer studies. Hum Cell [Internet]. 2022;35(1):23–36. Available from: https://doi.org/10.1007/s13577-021-00642-9

282. Brooks A, Liang X, Zhang Y, Zhao CX, Roberts MS, Wang H, et al. Liver organoid as a 3D in vitro model for drug validation and toxicity assessment. Pharmacol Res [Internet]. 2021;169:105608. Available from: https://www.sciencedirect.com/science/article/pii/S1043661821001924

283. Arutyunyan I V., Soboleva AG, Kovtunov EA, Kosyreva AM, Kudelkina V V., Alekseeva AI, et al. Gene Expression Profile of 3D Spheroids in Comparison with 2D Cell Cultures and Tissue Strains of Diffuse High-Grade Gliomas. Bull Exp Biol Med. 2023 Aug 1;175(4):576–84.

284. Miller CP, Fung M, Jaeger-Ruckstuhl CA, Xu Y, Warren EH, Akilesh S, et al. Therapeutic targeting of tumor spheroids in a 3D microphysiological renal cell carcinoma-on-a-chip system. Neoplasia [Internet]. 2023;46:100948. Available from: https://www.sciencedirect.com/science/article/pii/S1476558623000726

285. Sun M, Liu A, Yang X, Gong J, Yu M, Yao X, et al. 3D Cell Culture—Can It Be As Popular as 2D Cell Culture? Adv Nanobiomed Res [Internet]. 2021 May 1;1(5):2000066. Available from: https://doi.org/10.1002/anbr.202000066

286. Booij TH, Cattaneo CM, Hirt CK. Tumor Organoids as a Research Tool: How to Exploit Them. Cells. 2022;11, 3440(21).

287. S.5002—117th Congress (2021–2022): FDA Modernization Act 2.0. [Internet]. 2022. Available from: https://www.congress.gov/bill/117th-congress/senate-bill/5002

288. Wanigasekara J, Cullen PJ, Bourke P, Tiwari B, Curtin JF. Advances in 3D culture systems for therapeutic discovery and development in brain cancer. Drug Discov Today. 2023;28(2):103426.

289. Heinrich MA, Mostafa AMRH, Morton JP, Hawinkels LJAC, Prakash J. Translating complexity and heterogeneity of pancreatic tumor: 3D in vitro to in vivo models. Adv Drug Deliv Rev. 2021;174:265–93.

290. Ahvaraki A, Gheytanchi E, Behroodi E, Latifi H, Vakhshiteh F, Bagheri Z, et al. Advanced co-culture 3D breast cancer model to study cell death and nanodrug sensitivity of tumor spheroids. Biochem Eng J. 2024;209:109400.

291. Ascheid D, Baumann M, Pinnecker J, Friedrich M, Szi-Marton D, Medved C, et al. A vascularized breast cancer spheroid platform for the ranked evaluation of tumor microenvironment-targeted drugs by light sheet fluorescence microscopy. Nat Commun [Internet]. 2024;15(1):3599. Available from: https://doi.org/10.1038/s41467-024-48010-z

292. Kumar R, Iden M, Tsaih SW, Schmidt R, Ojesina AI, Rader JS. Deciphering the divergent transcriptomic landscapes of cervical cancer cells grown in 3D and 2D cell culture systems. Front Cell Dev Biol. 2024;12.

293. Xu X, Shen L, Li W, Liu X, Yang P, Cai J. ITGA5 promotes tumor angiogenesis in cervical cancer. Cancer Med. 2023;12(10):11983–99.

294. Valente R, Cordeiro S, Luz A, Melo MC, Rodrigues CR, Baptista P V., et al. Doxorubicin-sensitive and -resistant colorectal cancer spheroid models: assessing tumor microenvironment features for therapeutic modulation. Front Cell Dev Biol. 2023;11.

295. Heydari Z, Moeinvaziri F, Agarwal T, Pooyan P, Shpichka A, Maiti TK, et al. Organoids: a novel modality in disease modeling. Biodes Manuf [Internet]. 2021;4(4):689–716. Available from: https://doi.org/10.1007/s42242-021-00150-7

296. Batista JE dos S, Rodrigues MB, Bristot IJ, Silva V, Bernardy S, Rodrigues OED, et al. Systematic screening of synthetic organochalcogen compounds with anticancer activity using human lung adenocarcinoma spheroids. Chem Biol Interact. 2024;396:111047.

297. Li X, Zhou Y, Luo L, Zheng S, Deng J, Luan T. Chlorinated Anthracenes Induced Pulmonary Immunotoxicity in 3D Coculture Spheroids Simulating the Lung Microenvironment. Environ Sci Technol [Internet]. 2024;58(27):11923–34. Available from: https://doi.org/10.1021/acs.est.4c02957

298. Bano S, Alburquerque JQ, Roberts HJ, Pang S, Huang HC, Hasan T. Minocycline and photodynamic priming significantly improve chemotherapy efficacy in heterotypic spheroids of pancreatic ductal adenocarcinoma. J Photochem Photobiol B. 2024;255:112910.

299. Struth E, Labaf M, Karimnia V, Liu Y, Cramer G, Dahl JB, et al. Drug resistant pancreatic cancer cells exhibit altered biophysical interactions with stromal fibroblasts in imaging studies of 3D

co-culture models. Sci Rep [Internet]. 2024;14(1):20698. Available from: https://doi.org/10.1038/s41598-024-71372-9

300. Song WH, Lim YS, Kim JE, Kang HY, Lee C, Rajbongshi L, et al. A Marine Collagen-Based 3D Scaffold for In Vitro Modeling of Human Prostate Cancer Niche and Anti-Cancer Therapeutic Discovery. Mar Drugs [Internet]. 2024;22(7). Available from: https://www.mdpi.com/1660-3397/22/7/295

301. Rakhmatullina AR, Zolotykh MA, Filina Y V, Mingaleeva RN, Sagdeeva AR, Boulygina EA, et al. Development of a novel prostate Cancer-Stroma Sphere (CSS) model for In Vitro tumor microenvironment studies. Transl Oncol [Internet]. 2024;44:101930. Available from: https://www.sciencedirect.com/science/article/pii/S1936523324000573

302. Lee SY, Koo IS, Hwang HJ, Lee DW. In Vitro three-dimensional (3D) cell culture tools for spheroid and organoid models. SLAS Discovery [Internet]. 2023;28(4):119–37. Available from: https://www.sciencedirect.com/science/article/pii/S247255522300028X

303. Rodrigues T, Kundu B, Silva-Correia J, Kundu SC, Oliveira JM, Reis RL, et al. Emerging tumor spheroids technologies for 3D in vitro cancer modeling. Pharmacol Ther. 2018;184:201–11.

304. Fang G, Chen YC, Lu H, Jin D. Advances in Spheroids and Organoids on a Chip. Adv Funct Mater. 2023;33(19):2215043.

305. Wood LD, Ewald AJ. Organoids in cancer research: a review for pathologist-scientists. J Pathol [Internet]. 2021;254(4):395–404. Available from: https://doi.org/10.1002/path.5684

306. Corrò C, Novellasdemunt L, Li VSW. A brief history of organoids. American Journal of Physiology-Cell Physiology [Internet]. 2020;319(1):C151–65. Available from: https://doi.org/10.1152/ajpcell.00120.2020

307. Kim J, Koo BK, Knoblich JA. Human organoids: model systems for human biology and medicine. Nat Rev Mol Cell Biol [Internet]. 2020;21(10):571–84. Available from: https://doi.org/10.1038/s41580-020-0259-3

308. Tang XY, Wu S, Wang D, Chu C, Hong Y, Tao M, et al. Human organoids in basic research and clinical applications. Signal Transduct Target Ther [Internet]. 2022;7(1):168. Available from: https://doi.org/10.1038/s41392-022-01024-9

309. Zhao Z, Chen X, Dowbaj AM, Sljukic A, Bratlie K, Lin L, et al. Organoids. Nature Reviews Methods Primers [Internet]. 2022;2(1):94. Available from: https://doi.org/10.1038/s43586-022-00174-y

310. Verduin M, Hoeben A, De Ruysscher D, Vooijs M. Patient-Derived Cancer Organoids as Predictors of Treatment Response. Vol. 11, Frontiers in Oncology. Frontiers Media S.A.; 2021.

311. Kaushik G, Ponnusamy MP, Batra SK. Concise Review: Current Status of Three-Dimensional Organoids as Preclinical Models. Stem Cells [Internet]. 2018;36(9):1329–40. Available from: https://doi.org/10.1002/stem.2852

312. Huang Y, Huang Z, Tang Z, Chen Y, Huang M, Liu H, et al. Research Progress, Challenges, and Breakthroughs of Organoids as Disease Models. Front Cell Dev Biol [Internet]. 2021;9. Available from: https://www.frontiersin.org/journals/cell-and-developmental-biology/articles/10.3389/fcell.2021.740574

313. Kozlowski MT, Crook CJ, Ku HT. Towards organoid culture without Matrigel. Commun Biol [Internet]. 2021;4(1):1387. Available from: https://doi.org/10.1038/s42003-021-02910-8

314. Matano M, Date S, Shimokawa M, Takano A, Fujii M, Ohta Y, et al. Modeling colorectal cancer using CRISPR-Cas9–mediated engineering of human intestinal organoids. Nat Med [Internet]. 2015;21(3):256–62. Available from: https://doi.org/10.1038/nm.3802

315. Sun J, Liu W, Li Y, Gholamipour-Shirazi A, Abdulla A, Ding X. An on-chip cell culturing and combinatorial drug screening system. Microfluid Nanofluidics. 2017 Jul 1;21(7):125.

316. Takeda H, Kataoka S, Nakayama M, Ali MAE, Oshima H, Yamamoto D, et al. CRISPR-Cas9–mediated gene knockout in intestinal tumor organoids provides functional validation for colorectal cancer driver genes. Proceedings of the National Academy of Sciences [Internet]. 2019;116(31):15635–44. Available from: https://doi.org/10.1073/pnas.1904714116

317. Truong VA, Hsu MN, Kieu Nguyen NT, Lin MW, Shen CC, Lin CY, et al. CRISPRai for simultaneous gene activation and inhibition to promote stem cell chondrogenesis and calvarial bone regeneration. Nucleic Acids Res [Internet]. 2019;47(13). Available from: https://doi.org/10.1093/nar/gkz267

318. Shegekar T, Vodithala S, Juganavar A. The emerging role of liquid biopsies in revolutionising cancer diagnosis and therapy. Cureus. 2023;15(8).

319. Martins I, Ribeiro IP, Jorge J, Gonçalves AC, Sarmento-Ribeiro AB, Melo JB, et al. Liquid Biopsies: Applications for Cancer Diagnosis and Monitoring. Genes (Basel) [Internet]. 2021;12(3). Available from: https://www.mdpi.com/2073-4425/12/3/349

320. Bex A, Mathon B. Advances, technological innovations, and future prospects in stereotactic brain biopsies. Neurosurg Rev [Internet]. 2022;46(1):5. Available from: https://doi.org/10.1007/s10143-022-01918-w

321. Kim D, Hwang KS, Seo EU, Seo S, Lee BC, Choi N, et al. Vascularized Lung Cancer Model for Evaluating the Promoted Transport of Anticancer Drugs and Immune Cells in an Engineered Tumor Microenvironment. Adv Healthc Mater [Internet]. 2022 Jun 1;11(12):2102581. Available from: https://doi.org/10.1002/adhm.202102581

322. Qiao Z, Teng X, Liu A, Yang W. Novel Isolating Approaches to Circulating Tumor Cell Enrichment Based on Microfluidics: A Review. Micromachines (Basel) [Internet]. 2024;15(6). Available from: https://www.mdpi.com/2072-666X/15/6/706

323. Broutier L, Mastrogiovanni G, Verstegen MMA, Francies HE, Gavarró LM, Bradshaw CR, et al. Human primary liver cancer–derived organoid cultures for disease modeling and drug screening. Nat Med [Internet]. 2017;23(12):1424–35. Available from: https://doi.org/10.1038/nm.4438

324. Qu S, Xu R, Yi G, Li Z, Zhang H, Qi S, et al. Patient-derived organoids in human cancer: a platform for fundamental research and precision medicine. Molecular Biomedicine [Internet]. 2024;5(1):6. Available from: https://doi.org/10.1186/s43556-023-00165-9

325. Kita Y, Hamada A, Saito R, Teramoto Y, Tanaka R, Takano K, et al. Systematic chemical screening identifies disulfiram as a repurposed drug that enhances sensitivity to cisplatin in bladder cancer: a summary of preclinical studies. Br J Cancer [Internet]. 2019;121(12):1027–38. Available from: https://doi.org/10.1038/s41416-019-0609-0

326. Huang L, Bockorny B, Paul I, Akshinthala D, Frappart PO, Gandarilla O, et al. PDX-derived organoids model in vivo drug response and secrete biomarkers. JCI Insight. 2020;5(21).

327. Low RRJ, Lim WW, Nguyen PM, Lee B, Christie M, Burgess AW, et al. The Diverse Applications of Pancreatic Ductal Adenocarcinoma Organoids. Cancers (Basel). 2021;13(19):4979.

328. Ukai S, Honma R, Sakamoto N, Yamamoto Y, Pham QT, Harada K, et al. Molecular biological analysis of 5-FU-resistant gastric cancer organoids; KHDRBS3 contributes to the attainment of features of cancer stem cell. Oncogene. 2020;39(50):7265–78.

329. Qu J, Kalyani FS, Liu L, Cheng T, Chen L. Tumor organoids: synergistic applications, current challenges, and future prospects in cancer therapy. Cancer Commun [Internet]. 2021;41(12):1331–53. Available from: https://doi.org/10.1002/cac2.12224

330. Beutel AK, Schütte L, Scheible J, Roger E, Müller M, Perkhofer L, et al. A Prospective Feasibility Trial to Challenge Patient–Derived Pancreatic Cancer Organoids in Predicting Treatment Response. Cancers (Basel). 2021;13(11):2539.

331. Schwank G, Koo BK, Sasselli V, Dekkers JF, Heo I, Demircan T, et al. Functional Repair of CFTR by CRISPR/Cas9 in Intestinal Stem Cell Organoids of Cystic Fibrosis Patients. Cell Stem Cell. 2013;13(6):653–8.

332. El Harane S, Zidi B, El Harane N, Krause KH, Matthes T, Preynat-Seauve O. Cancer Spheroids and Organoids as Novel Tools for Research and Therapy: State of the Art and Challenges to Guide Precision Medicine. Cells. 2023;12(7):1001.

333. Dekkers JF, Alieva M, Cleven A, Keramati F, Wezenaar AKL, van Vliet EJ, et al. Uncovering the mode of action of engineered T cells in patient cancer organoids. Nat Biotechnol. 2023;41(1):60–9.

334. Nowak-Sliwinska P, Segura T, Iruela-Arispe ML. The chicken chorioallantoic membrane model in biology, medicine and bioengineering. Vol. 17, Angiogenesis. Kluwer Academic Publishers; 2014. p. 779–804.

335. Mosna MJ, Garde FJ, Stinson MG, Pastore CD, Carcagno AL. The chorioallantoic membrane (CAM) model: From its origins in developmental biology to its role in cancer research. Dev Biol [Internet]. 2025;519:79–95. Available from: https://www.sciencedirect.com/science/article/pii/S0012160624002793

336. Kennedy DC, Coen B, Wheatley AM, McCullagh KJA. Microvascular experimentation in the chick chorioallantoic membrane as a model for screening angiogenic agents including from gene-modified cells. Vol. 23, International Journal of Molecular Sciences. MDPI; 2022.

337. Liu Y, Lang F, Xie X, Prabhu S, Xu J, Sampath D, et al. Efficacy of adenovirally expressed soluble TRAIL in human glioma organotypic slice culture and glioma xenografts. Cell Death Dis [Internet]. 2011;2(2):e121–e121. Available from: https://doi.org/10.1038/cddis.2010.95

338. Kirby TO, Rivera A, Rein D, Wang M, Ulasov I, Breidenbach M, et al. A Novel Ex vivo Model System for Evaluation of Conditionally Replicative Adenoviruses Therapeutic Efficacy and Toxicity. Clinical Cancer Research [Internet]. 2004 Dec 28;10(24):8697–703. Available from: https://doi.org/10.1158/1078-0432.CCR-04-1166

339. Khalili A, Rivera A, Mathis J. Gene transfer to carcinoma of the breast with fiber-modified adenoviral vectors in a tissue slice model system. Cancer Biol Ther. 2005 Nov 1;4:1203–10.

340. Zimmermann M, Armeanu S, Smirnow I, Kupka S, Wagner S, Wehrmann M, et al. Human precision-cut liver tumor slices as a tumor patient-individual predictive test system for oncolytic measles vaccine viruses. Int J Oncol. 2009 Jun 1;34:1247–56.

341. van Geer MA, Kuhlmann KFD, Bakker CT, ten Kate FJW, Oude Elferink RPJ, Bosma PJ. Ex-vivo evaluation of gene therapy vectors in Human pancreatic (cancer) tissue slices. World J Gastroenterol. 2009 Mar 21;15(11):1359–66.

342. Pennington K, Chu QD, Curiel DT, Li BDL, Mathis JM. The Utility of a Tissue Slice Model System to Determine Breast Cancer Infectivity by Oncolytic Adenoviruses[1]. Journal of Surgical Research [Internet]. 2010 Oct 1;163(2):270–5. Available from: https://doi.org/10.1016/j.jss.2010.03.072

343. Weissinger D, Tagscherer K, Macher-Göppinger S, Haferkamp A, Wagener N, Roth W. The soluble Decoy Receptor 3 is regulated by a PI3K-dependent mechanism and promotes migration and invasion in renal cell carcinoma. Mol Cancer. 2013 Oct 10;12:120.

344. Meijer A, Kruyt FAE, van der Zee AGJ, Hollema H, Le P, ten Hoor KA, et al. Nutlin-3 preferentially sensitises wild-type p53-expressing cancer cells to DR5-selective TRAIL over rhTRAIL. Br J Cancer [Internet]. 2013;109(10):2685–95. Available from: https://doi.org/10.1038/bjc.2013.636

345. Séveno C, Loussouarn D, Bréchet S, Campone M, Juin P, Barillé-Nion S. γ-Secretase inhibition promotes cell death, Noxa upregulation, and sensitization to BH3 mimetic ABT-737 in human breast cancer cells. Breast Cancer Research [Internet]. 2012;14(3):R96. Available from: https://doi.org/10.1186/bcr3214

346. Masters JRW. Human cancer cell lines: fact and fantasy. Nat Rev Mol Cell Biol [Internet]. 2000;1(3):233–6. Available from: https://doi.org/10.1038/35043102

347. Sonnenberg M, van der Kuip H, Haubeiß S, Fritz P, Schroth W, Friedel G, et al. Highly variable response to cytotoxic chemotherapy in carcinoma-associated fibroblasts (CAFs) from lung and breast. BMC Cancer. 2008 Dec 11;8.

348. Schmid JO, Dong M, Haubeiss S, Friedel G, Bode S, Grabner A, et al. Cancer Cells Cue the p53 Response of Cancer-Associated Fibroblasts to Cisplatin. Cancer Res [Internet]. 2012 Nov 14;72(22):5824–32. Available from: https://doi.org/10.1158/0008-5472.CAN-12-1201

349. Vaira V, Fedele G, Pyne S, Fasoli E, Zadra G, Bailey D, et al. Preclinical model of organotypic culture for pharmacodynamic profiling of human tumors. Proceedings of the National Academy of Sciences [Internet]. 2010 May 4;107(18):8352–6. Available from: https://doi.org/10.1073/pnas.0907676107

350. Williams ST, Wells G, Conroy S, Gagg H, Allen R, Rominiyi O, et al. Precision oncology using ex vivo technology: a step towards individualised cancer care? Vol. 24, Expert Reviews in Molecular Medicine. Cambridge University Press; 2022.

351. Bouquerel C, Dubrova A, Hofer I, Phan DTT, Bernheim M, Ladaigue S, et al. Bridging the gap between tumor-on-chip and clinics: a systematic review of 15 years of studies. Vol. 23, Lab on a Chip. Royal Society of Chemistry; 2023. p. 3906–35.

352. Balkwill FR, Capasso M, Hagemann T. The tumor microenvironment at a glance. J Cell Sci. 2012;125(23):5591–6.

353. Giannitelli SM, Peluzzi V, Raniolo S, Roscilli G, Trombetta M, Mozetic P, et al. On-chip recapitulation of the tumor microenvironment: A decade of progress. Biomaterials. 2024;306:122482.

354. Dsouza VL, Kuthethur R, Kabekkodu SP, Chakrabarty S. Organ-on-Chip platforms to study tumor evolution and chemosensitivity. Biochimica et Biophysica Acta (BBA) - Reviews on Cancer. 2022;1877(3):188717.

355. Liu X, Su Q, Zhang X, Yang W, Ning J, Jia K, et al. Recent Advances of Organ-on-a-Chip in Cancer Modeling Research. Biosensors (Basel). 2022 Nov 1;12(11):1045.

356. Lovitt C, Shelper T, Avery V. Advanced Cell Culture Techniques for Cancer Drug Discovery. Biology (Basel). 2014;3(2):345–67.

357. Riedl A, Schlederer M, Pudelko K, Stadler M, Walter S, Unterleuthner D, et al. Comparison of cancer cells in 2D vs 3D culture reveals differences in AKT–mTOR–S6K signaling and drug responses. Ewald A, editor. J Cell Sci [Internet]. 2017;130(1):203–18. Available from: https://doi.org/10.1242/jcs.188102

358. Schuster B, Junkin M, Kashaf SS, Romero-Calvo I, Kirby K, Matthews J, et al. Automated microfluidic platform for dynamic and combinatorial drug screening of tumor organoids. Nat Commun. 2020;11(1):5271.

359. Chaicharoenaudomrung N, Kunhorm P, Noisa P. Three-dimensional cell culture systems as an in vitro platform for cancer and stem cell modeling. World J Stem Cells. 2019;11(12):1065–83.

360. Vulto P, Joore J. Adoption of organ-on-chip platforms by the pharmaceutical industry. Nat Rev Drug Discov. 2021;20(12):961–2.

361. Liu X, Fang J, Huang S, Wu X, Xie X, Wang J, et al. Tumor-on-a-chip: from bioinspired design to biomedical application. Microsyst Nanoeng. 2021 Dec 1;7(1).

362. Chen YA, King AD, Shih HC, Peng CC, Wu CY, Liao WH, et al. Generation of oxygen gradients in microfluidic devices for cell culture using spatially confined chemical reactions. Lab Chip. 2011;11(21):3626–33.

363. Brennan MD, Rexius-Hall ML, Elgass LJ, Eddington DT. Oxygen control with microfluidics. Lab Chip. 2014;14(22):4305–18.

364. Purkayastha P, Jaiswal MK, Lele TP. Molecular cancer cell responses to solid compressive stress and interstitial fluid pressure. Cytoskeleton [Internet]. 2021 Jun 1;78(6):312–22. Available from: https://doi.org/10.1002/cm.21680

365. Menon N V, Chuah YJ, Cao B, Lim M, Kang Y. A microfluidic co-culture system to monitor tumor-stromal interactions on a chip. Biomicrofluidics. 2014;8(6).

366. Zou H, Yue W, Yu WK, Liu D, Fong CC, Zhao J, et al. Microfluidic Platform for Studying Chemotaxis of Adhesive Cells Revealed a Gradient-Dependent Migration and Acceleration of Cancer Stem Cells. Anal Chem [Internet]. 2015;87(14):7098–108. Available from: https://doi.org/10.1021/acs.analchem.5b00873

367. Manoharan TJM, Ravi K, Suresh AP, Acharya AP, Nikkhah M. Engineered Tumor–Immune Microenvironment On A Chip to Study T Cell–Macrophage Interaction in Breast Cancer Progression. Adv Healthc Mater. 2024;13(14).

368. Nia HT, Munn LL, Jain RK. Physical traits of cancer. Science (1979) [Internet]. 2020 Oct 30;370(6516):eaaz0868. Available from: https://doi.org/10.1126/science.aaz0868

369. Anderson NM, Simon MC. The tumor microenvironment. Current Biology [Internet]. 2020 Aug 17;30(16):R921–5. Available from: https://doi.org/10.1016/j.cub.2020.06.081

370. Richter M, Piwocka O, Musielak M, Piotrowski I, Suchorska WM, Trzeciak T. From Donor to the Lab: A Fascinating Journey of Primary Cell Lines. Front Cell Dev Biol [Internet]. 2021;9. Available from: https://www.frontiersin.org/journals/cell-and-developmental-biology/articles/10.3389/fcell.2021.711381

371. Close D, Wang A, Kochanek S, Shun T, Eiseman J, Johnston P. Implementation of the NCI-60 Human Tumor Cell Line Panel to Screen 2260 Cancer Drug Combinations to Generate >3 Million Data Points Used to Populate a Large Matrix of Anti-Neoplastic Agent Combinations (ALMANAC) Database. SLAS DISCOVERY: Advancing Life Sciences R&D. 2018 Nov 30;24:247255521881242.

372. Boussommier-Calleja A, Atiyas Y, Haase K, Headley M, Lewis C, Kamm RD. The effects of monocytes on tumor cell extravasation in a 3D vascularized microfluidic model. Biomaterials [Internet]. 2019;198:180–93. Available from: https://www.sciencedirect.com/science/article/pii/S0142961218301649

373. Hassell BA, Goyal G, Lee E, Sontheimer-Phelps A, Levy O, Chen CS, et al. Human Organ Chip Models Recapitulate Orthotopic Lung Cancer Growth, Therapeutic Responses, and Tumor Dormancy In Vitro. Cell Rep [Internet]. 2017 Oct 10;21(2):508–16. Available from: https://doi.org/10.1016/j.celrep.2017.09.043

374. Gerigk M, Bulstrode H, Shi HH, Tönisen F, Cerutti C, Morrison G, et al. On-chip perivascular niche supporting stemness of patient-derived glioma cells in a serum-free, flowable culture. Lab Chip [Internet]. 2021;21(12):2343–58. Available from: http://dx.doi.org/10.1039/D1LC00271F

375. Humayun M, Ayuso JM, Brenneke RA, Virumbrales-Muñoz M, Lugo-Cintrón K, Kerr S, et al. Elucidating cancer-vascular paracrine signaling using a human organotypic breast cancer cell

extravasation model. Biomaterials [Internet]. 2021;270:120640. Available from: https://www.sciencedirect.com/science/article/pii/S0142961220308875

376. Papapetrou EP. Patient-derived induced pluripotent stem cells in cancer research and precision oncology. Nat Med [Internet]. 2016;22(12):1392–401. Available from: https://doi.org/10.1038/nm.4238

377. Jeibouei S, Monfared AK, Hojat A, Aref AR, Shams F, Dolati M, et al. Human-derived Tumor-On-Chip model to study the heterogeneity of breast cancer tissue. Biomaterials Advances [Internet]. 2024;162:213915. Available from: https://www.sciencedirect.com/science/article/pii/S2772950824001584

378. Matsuda K, Ohga N, Hida Y, Muraki C, Tsuchiya K, Kurosu T, et al. Isolated tumor endothelial cells maintain specific character during long-term culture. Biochem Biophys Res Commun [Internet]. 2010;394(4):947–54. Available from: https://www.sciencedirect.com/science/article/pii/S0006291X10005401

379. Bouquerel C, Dubrova A, Hofer I, Phan DTT, Bernheim M, Ladaigue S, et al. Bridging the gap between tumor-on-chip and clinics: a systematic review of 15 years of studies. Lab Chip [Internet]. 2023;23(18):3906–35. Available from: http://dx.doi.org/10.1039/D3LC00531C

380. Adjei-Sowah EA, O'Connor SA, Veldhuizen J, Lo Cascio C, Plaisier C, Mehta S, et al. Investigating the Interactions of Glioma Stem Cells in the Perivascular Niche at Single-Cell Resolution using a Microfluidic Tumor Microenvironment Model. Advanced Science [Internet]. 2022 Jul 1;9(21):2201436. Available from: https://doi.org/10.1002/advs.202201436

381. Pelon F, Bourachot B, Kieffer Y, Magagna I, Mermet-Meillon F, Bonnet I, et al. Cancer-associated fibroblast heterogeneity in axillary lymph nodes drives metastases in breast cancer through complementary mechanisms. Nat Commun. 2020 Dec 1;11(1).

382. Yavvari P, Laporte A, Elomaa L, Schraufstetter F, Pacharzina I, Daberkow AD, et al. 3D-Cultured Vascular-Like Networks Enable Validation of Vascular Disruption Properties of Drugs In Vitro. Front Bioeng Biotechnol. 2022 Jun 13;10.

383. Sleeboom JJF, Eslami Amirabadi H, Nair P, Sahlgren CM, den Toonder JMJ. Metastasis in context: modeling the tumor microenvironment with cancer-on-a-chip approaches. Dis Model Mech [Internet]. 2018 Mar 16;11(3):dmm033100. Available from: https://doi.org/10.1242/dmm.033100

384. Adjei-Sowah EA, O'Connor SA, Veldhuizen J, Lo Cascio C, Plaisier C, Mehta S, et al. Investigating the Interactions of Glioma Stem Cells in the Perivascular Niche at Single-Cell Resolution using a Microfluidic Tumor Microenvironment Model. Advanced Science [Internet]. 2022 Jul 1;9(21):2201436. Available from: https://doi.org/10.1002/advs.202201436

385. Campisi M, Shin Y, Osaki T, Hajal C, Chiono V, Kamm RD. 3D self-organized microvascular model of the human blood-brain barrier with endothelial cells, pericytes and astrocytes. Biomaterials [Internet]. 2018;180:117–29. Available from: https://www.sciencedirect.com/science/article/pii/S0142961218304915

386. Han W, Chen S, Yuan W, Fan Q, Tian J, Wang X, et al. Oriented collagen fibers direct tumor cell intravasation. Proceedings of the National Academy of Sciences [Internet]. 2016 Oct 4;113(40):11208–13. Available from: https://doi.org/10.1073/pnas.1610347113

387. Drifka CR, Eliceiri KW, Weber SM, Kao WJ. A bioengineered heterotypic stroma–cancer microenvironment model to study pancreatic ductal adenocarcinoma. Lab Chip [Internet]. 2013;13(19):3965–75. Available from: http://dx.doi.org/10.1039/C3LC50487E

388. Azadi S, Tafazzoli Shadpour M, Warkiani ME. Characterizing the effect of substrate stiffness on the extravasation potential of breast cancer cells using a 3D microfluidic model. Biotechnol Bioeng [Internet]. 2021 Feb 1;118(2):823–35. Available from: https://doi.org/10.1002/bit.27612

389. Bi Y, Shirure VS, Liu R, Cunningham C, Ding L, Meacham JM, et al. Tumor-on-a-chip platform to interrogate the role of macrophages in tumor progression. Integrative Biology [Internet]. 2020 Sep 30;12(9):221–32. Available from: https://doi.org/10.1093/intbio/zyaa017

390. Frenkel N, Poghosyan S, Alarcón C, García S, Queiroz K, Bent L, et al. Long-Lived Human Lymphatic Endothelial Cells to Study Lymphatic Biology and Lymphatic Vessel/Tumor Coculture in a 3D Microfluidic Model. ACS Biomater Sci Eng. 2021 Jun 29;7.

391. Lee S, Lim J, Yu J, Ahn J, Lee Y, Jeon NL. Engineering tumor vasculature on an injection-molded plastic array 3D culture (IMPACT) platform. Lab Chip [Internet]. 2019;19(12):2071–80. Available from: http://dx.doi.org/10.1039/C9LC00148D

392. Bersini S, Jeon JS, Dubini G, Arrigoni C, Chung S, Charest JL, et al. A microfluidic 3D in vitro model for specificity of breast cancer metastasis to bone. Biomaterials [Internet]. 2014;35(8):2454–61. Available from: https://www.sciencedirect.com/science/article/pii/S0142961213014038

393. Bai J, Tu TY, Kim C, Thiery JP, Kamm RD. Oncotarget 36603 www.impactjournals.com/oncotarget Identification of drugs as single agents or in combination to prevent carcinoma dissemination in a microfluidic 3D environment [Internet]. Vol. 6, Oncotarget. 2015. Available from: www.impactjournals.com/oncotarget/

394. Chi CW, Lao YH, Ahmed AHR, Benoy EC, Li C, Dereli-Korkut Z, et al. High-Throughput Tumor-on-a-Chip Platform to Study Tumor–Stroma Interactions and Drug Pharmacokinetics. Adv Healthc Mater [Internet]. 2020 Nov 1;9(21):2000880. Available from: https://doi.org/10.1002/adhm.202000880

395. Prince E, Kheiri S, Wang Y, Xu F, Cruickshank J, Topolskaia V, et al. Microfluidic Arrays of Breast Tumor Spheroids for Drug Screening and Personalized Cancer Therapies. Adv Healthc Mater [Internet]. 2022 Jan 1;11(1):2101085. Available from: https://doi.org/10.1002/adhm.202101085

396. Azizipour N, Avazpour R, Weber MH, Sawan M, Ajji A, Rosenzweig DH. Uniform Tumor Spheroids on Surface-Optimized Microfluidic Biochips for Reproducible Drug Screening and Personalized Medicine. Micromachines (Basel). 2022 Apr 1;13(4).

397. An D, Kim K, Kim J. Microfluidic system based high throughput drug screening system for curcumin/TRAIL combinational chemotherapy in human prostate cancer PC3 cells. Biomol Ther (Seoul). 2014;22(4):355–62.

398. Jiang X, Ren L, Tebon P, Wang C, Zhou X, Qu M, et al. Cancer-on-a-Chip for Modeling Immune Checkpoint Inhibitor and Tumor Interactions. Small [Internet]. 2021 Feb 1;17(7):2004282. Available from: https://doi.org/10.1002/smll.202004282

399. Ao Z, Cai H, Wu Z, Hu L, Li X, Kaurich C, et al. Evaluation of cancer immunotherapy using mini-tumor chips. Theranostics [Internet]. 2022;12(8):3628–36. Available from: https://www.thno.org/v12p3628.htm

400. Jiang X, Ren L, Tebon P, Wang C, Zhou X, Qu M, et al. Cancer-on-a-Chip for Modeling Immune Checkpoint Inhibitor and Tumor Interactions. Small [Internet]. 2021 Feb 1;17(7):2004282. Available from: https://doi.org/10.1002/smll.202004282

401. Bouquerel C, César W, Barthod L, Arrak S, Battistella A, Gropplero G, et al. Precise and fast control of the dissolved oxygen level for tumor-on-chip. Lab Chip [Internet]. 2022;22(22):4443–55. Available from: http://dx.doi.org/10.1039/D2LC00696K

402. Calibasi Kocal G, Güven S, Foygel K, Goldman A, Chen P, Sengupta S, et al. Dynamic Microenvironment Induces Phenotypic Plasticity of Esophageal Cancer Cells Under Flow. Sci Rep [Internet]. 2016;6(1):38221. Available from: https://doi.org/10.1038/srep38221

403. Haque MR, Wessel CR, Leary DD, Wang C, Bhushan A, Bishehsari F. Patient-derived pancreatic cancer-on-a-chip recapitulates the tumor microenvironment. Microsyst Nanoeng [Internet]. 2022;8(1):36. Available from: https://doi.org/10.1038/s41378-022-00370-6

404. Huang R, Zheng W, Liu W, Zhang W, Long Y, Jiang X. Investigation of Tumor Cell Behaviors on a Vascular Microenvironment-Mimicking Microfluidic Chip. Sci Rep. 2015 Dec 3;5.

405. Ao M, Brewer BM, Yang L, Franco Coronel OE, Hayward SW, Webb DJ, et al. Stretching fibroblasts remodels fibronectin and alters cancer cell migration. Sci Rep. 2015;5:8334.

406. Huh D, Matthews BD, Mammoto A, Montoya-Zavala M, Hsin HY, Ingber DE. Reconstituting Organ-Level Lung Functions on a Chip. Science (1979) [Internet]. 2010 Jun 25;328(5986):1662–8. Available from: https://doi.org/10.1126/science.1188302

407. Choi Y, Hyun E, Seo J, Blundell C, Kim HC, Lee E, et al. A microengineered pathophysiological model of early-stage breast cancer. Lab Chip [Internet]. 2015;15(16):3350–7. Available from: http://dx.doi.org/10.1039/C5LC00514K

408. Gioeli D, Snow CJ, Simmers MB, Hoang SA, Figler RA, Allende JA, et al. Development of a multicellular pancreatic tumor microenvironment system using patient-derived tumor cells. Lab Chip [Internet]. 2019;19(7):1193–204. Available from: http://dx.doi.org/10.1039/C8LC00755A

409. Chakrabarty S, Quiros-Solano WF, Kuijten MMP, Haspels B, Mallya S, Lo CSY, et al. A Microfluidic Cancer-on-Chip Platform Predicts Drug Response Using Organotypic Tumor Slice Culture. Cancer Res [Internet]. 2022 Feb 1;82(3):510–20. Available from: https://doi.org/10.1158/0008-5472.CAN-21-0799

410. Ayuso JM, Rehman S, Virumbrales-Munoz M, McMinn PH, Geiger P, Fitzgerald C, et al. Microfluidic tumor-on-a-chip model to evaluate the role of tumor environmental stress on NK cell exhaustion. Sci Adv [Internet]. 2025 Jan 21;7(8):eabc2331. Available from: https://doi.org/10.1126/sciadv.abc2331

411. Kwak TJ, Lee E. Rapid multilayer microfabrication for modeling organotropic metastasis in breast cancer. Biofabrication [Internet]. 2021;13(1):015002. Available from: https://dx.doi.org/10.1088/1758-5090/abbd28

412. Miller CP, Tsuchida C, Zheng Y, Himmelfarb J, Akilesh S. A 3D Human Renal Cell Carcinoma-on-a-Chip for the Study of Tumor Angiogenesis. Neoplasia [Internet]. 2018;20(6):610–20. Available from: https://www.sciencedirect.com/science/article/pii/S1476558617304852

413. Nothdurfter D, Ploner C, Coraça-Huber DC, Wilflingseder D, Müller T, Hermann M, et al. 3D bioprinted, vascularized neuroblastoma tumor environment in fluidic chip devices for precision medicine drug testing. Biofabrication [Internet]. 2022;14(3):035002. Available from: https://dx.doi.org/10.1088/1758-5090/ac5fb7

414. Holle AW, Young JL, Spatz JP. In vitro cancer cell–ECM interactions inform in vivo cancer treatment. Adv Drug Deliv Rev [Internet]. 2016;97:270–9. Available from: https://www.sciencedirect.com/science/article/pii/S0169409X1500232X

415. Davidov T, Efraim Y, Hayam R, Oieni J, Baruch L, Machluf M. Extracellular matrix hydrogels originated from different organs mediate tissue-specific properties and function. Int J Mol Sci. 2021 Nov 1;22(21).

416. Brown BN, Barnes CA, Kasick RT, Michel R, Gilbert TW, Beer-Stolz D, et al. Surface characterization of extracellular matrix scaffolds. Biomaterials. 2010 Jan;31(3):428–37.

417. Li ZL, Wang ZJ, Wei GH, Yong Y, Wang XW. Changes in extracellular matrix in different stages of colorectal cancer and their effects on proliferation of cancer cells. World J Gastrointest Oncol. 2020 Mar 15;12(3):267–75.

418. Kopanska KS, Alcheikh Y, Staneva R, Vignjevic D, Betz T. Tensile forces originating from cancer spheroids facilitate tumor invasion. PLoS One. 2016 Jun 1;11(6).

419. Langhans SA. Three-dimensional in vitro cell culture models in drug discovery and drug repositioning. Vol. 9, Frontiers in Pharmacology. Frontiers Media S.A.; 2018.

420. Bonnans C, Chou J, Werb Z. Remodelling the extracellular matrix in development and disease. Nat Rev Mol Cell Biol [Internet]. 2014;15(12):786–801. Available from: https://doi.org/10.1038/nrm3904

421. Rajan N, Habermehl J, Coté MF, Doillon CJ, Mantovani D. Preparation of ready-to-use, storable and reconstituted type I collagen from rat tail tendon for tissue engineering applications. Nat Protoc [Internet]. 2006;1(6):2753–8. Available from: https://doi.org/10.1038/nprot.2006.430

422. Aisenbrey EA, Murphy WL. Synthetic alternatives to Matrigel. Nat Rev Mater [Internet]. 2020;5(7):539–51. Available from: https://doi.org/10.1038/s41578-020-0199-8

423. Price KJ, Tsykin A, Giles KM, Sladic RT, Epis MR, Ganss R, et al. Matrigel Basement Membrane Matrix influences expression of microRNAs in cancer cell lines. Biochem Biophys Res Commun [Internet]. 2012;427(2):343–8. Available from: https://www.sciencedirect.com/science/article/pii/S0006291X12017998

424. Ayuso JM, Virumbrales-Munoz M, McMinn PH, Rehman S, Gomez I, Karim MR, et al. Tumor-on-a-chip: a microfluidic model to study cell response to environmental gradients. Lab Chip [Internet]. 2019;19(20):3461–71. Available from: http://dx.doi.org/10.1039/C9LC00270G

425. Brennan MD, Rexius-Hall ML, Elgass LJ, Eddington DT. Oxygen control with microfluidics. Lab Chip [Internet]. 2014;14(22):4305–18. Available from: http://dx.doi.org/10.1039/C4LC00853G

426. Tovar M, Mahler L, Buchheim S, Roth M, Rosenbaum MA. Monitoring and external control of pH in microfluidic droplets during microbial culturing. Microb Cell Fact. 2020 Jan 29;19(1).

427. Purkayastha P, Jaiswal MK, Lele TP. Molecular cancer cell responses to solid compressive stress and interstitial fluid pressure. Cytoskeleton [Internet]. 2021 Jun 1;78(6):312–22. Available from: https://doi.org/10.1002/cm.21680

428. McKeown SR. Defining normoxia, physoxia and hypoxia in tumours—implications for treatment response. Br J Radiol. 2014;87(1035):20130676.

429. Petrova V, Annicchiarico-Petruzzelli M, Melino G, Amelio I. The hypoxic tumour microenvironment. Oncogenesis. 2018;7(1):10.

430. Ward C, Meehan J, Gray ME, Murray AF, Argyle DJ, Kunkler IH, et al. The impact of tumour pH on cancer progression: strategies for clinical intervention. Explor Target Antitumor Ther [Internet]. 2020;1(2):71–100. Available from: https://www.explorationpub.com/Journals/etat/Article/10025

431. Dey S, Kinoshita M, Puttick S, Rose S, Trau M, Roberts MJ, et al. Cancer-on-Chip and Integrative Tumor Microenvironment Sensor Technologies for Progressing Precision Radiotherapy. Advanced Sensor Research [Internet]. 2024 Jul 1;3(7):2300193. Available from: https://doi.org/10.1002/adsr.202300193

432. Purkayastha P, Jaiswal MK, Lele TP. Molecular cancer cell responses to solid compressive stress and interstitial fluid pressure. Cytoskeleton [Internet]. 2021 Jun 1;78(6):312–22. Available from: https://doi.org/10.1002/cm.21680

433. Gong F, Yang Y, Wen L, Wang C, Li J, Dai J. An Overview of the Role of Mechanical Stretching in the Progression of Lung Cancer. Vol. 9, Frontiers in Cell and Developmental Biology. Frontiers Media S.A.; 2021.

434. Rizzuti IF, Mascheroni P, Arcucci S, Ben-Mériem Z, Prunet A, Barentin C, et al. Mechanical Control of Cell Proliferation Increases Resistance to Chemotherapeutic Agents. Phys Rev Lett [Internet]. 2020 Sep 18;125(12):128103. Available from: https://link.aps.org/doi/10.1103/PhysRevLett.125.128103

435. Delarue M, Montel F, Vignjevic D, Prost J, Joanny JF, Cappello G. Compressive Stress Inhibits Proliferation in Tumor Spheroids through a Volume Limitation. Biophys J [Internet]. 2014 Oct 21;107(8):1821–8. Available from: https://doi.org/10.1016/j.bpj.2014.08.031

436. Kim D, Hwang KS, Seo EU, Seo S, Lee BC, Choi N, et al. Vascularized Lung Cancer Model for Evaluating the Promoted Transport of Anticancer Drugs and Immune Cells in an Engineered Tumor Microenvironment. Adv Healthc Mater [Internet]. 2022 Jun 1;11(12):2102581. Available from: https://doi.org/10.1002/adhm.202102581

437. Onal S, Alkaisi MM, Nock V. A Flexible Microdevice for Mechanical Cell Stimulation and Compression in Microfluidic Settings. Front Phys. 2021 May 25;9.

438. Ronaldson-Bouchard K, Vunjak-Novakovic G. Organs-on-a-Chip: A Fast Track for Engineered Human Tissues in Drug Development. Cell Stem Cell [Internet]. 2018;22(3):310–24. Available from: https://www.sciencedirect.com/science/article/pii/S1934590918300730

439. Whitesides GM. The origins and the future of microfluidics. Nature. 2006;442(7101):368–73.

440. Xu Z, Li E, Guo Z, Yu R, Hao H, Xu Y, et al. Design and Construction of a Multi-Organ Microfluidic Chip Mimicking the in vivo Microenvironment of Lung Cancer Metastasis. ACS Appl Mater Interfaces [Internet]. 2016;8(39):25840–7. Available from: https://doi.org/10.1021/acsami.6b08746

441. Silverio V, Cardoso de Freitas S. Microfabrication Techniques for Microfluidic Devices. In: Complex Fluid-Flows in Microfluidics. Cham: Springer International Publishing; 2018. p. 25–51.

442. Xia Y, Whitesides GM. Soft Lithography. Angewandte Chemie International Edition [Internet]. 1998 Mar 16;37(5):550–75. Available from: https://doi.org/10.1002/(SICI)1521-3773(19980316)37:5<550::AID-ANIE550>3.0.CO

443. Lee H, Cho DW. One-step fabrication of an organ-on-a-chip with spatial heterogeneity using a 3D bioprinting technology. Lab Chip. 2016;16(14):2618–25.

444. Yang Q, Lian Q, Xu F. Perspective: Fabrication of integrated organ-on-a-chip via bioprinting. Biomicrofluidics. 2017;11(3):31301.

445. Steinberg E, Friedman R, Goldstein Y, Friedman N, Beharier O, Demma JA, et al. A fully 3D-printed versatile tumor-on-a-chip allows multi-drug screening and correlation with clinical outcomes for personalized medicine. Commun Biol. 2023 Dec 1;6(1):1157.

446. Hsieh YK, Chen SC, Huang WL, Hsu KP, Gorday K, Wang T, et al. Direct Micromachining of Microfluidic Channels on Biodegradable Materials Using Laser Ablation. Polymers (Basel). 2017;9(7):242.

447. Mansour H, Soliman EA, El-Bab AMF, Matsushita Y, Abdel-Mawgood AL. Fabrication and characterization of microfluidic devices based on boron-modified epoxy resin using CO2 laser ablation for bio-analytical applications. Sci Rep. 2023;13(1):12623.

448. Ng JMK, Gitlin I, Stroock AD, Whitesides GM. Components for integrated poly(dimethylsiloxane) microfluidic systems. Electrophoresis [Internet]. 2002;23(20):3461–73. Available from: https://doi.org/10.1002/1522-2683(200210)23:20<3461::AID-ELPS3461>3.0.CO

449. Hoch E, Hirth T, Tovar GEM, Borchers K. Chemical tailoring of gelatin to adjust its chemical and physical properties for functional bioprinting. J Mater Chem B. 2013;1(41):5675–85.

450. Ren K, Zhou J, Wu H. Materials for Microfluidic Chip Fabrication. Acc Chem Res [Internet]. 2013;46(11):2396–406. Available from: https://doi.org/10.1021/ar300314s

451. Terrell JA, Jones CG, Kabandana GKM, Chen C. From cells-on-a-chip to organs-on-a-chip: scaffolding materials for 3D cell culture in microfluidics. J Mater Chem B. 2020;8(31):6667–85.

452. McDonald JC, Whitesides GM. Poly(dimethylsiloxane) as a Material for Fabricating Microfluidic Devices. Acc Chem Res [Internet]. 2002;35(7):491–9. Available from: https://doi.org/10.1021/ar010110q

453. Auner AW, Tasneem KM, Markov DA, McCawley LJ, Hutson MS. Chemical-PDMS binding kinetics and implications for bioavailability in microfluidic devices. Lab Chip. 2019 Mar 7;19(5):864–74.

454. Altmann B, Steinberg T, Giselbrecht S, Gottwald E, Tomakidi P, Bächle-Haas M, et al. Promotion of osteoblast differentiation in 3D biomaterial micro-chip arrays comprising fibronectin-coated poly(methyl methacrylate) polycarbonate. Biomaterials [Internet]. 2011;32(34):8947–56. Available from: https://www.sciencedirect.com/science/article/pii/S0142961211009288

455. Palacio-Castañeda V, Kooijman L, Venzac B, Verdurmen W, Le Gac S. Metabolic Switching of Tumor Cells under Hypoxic Conditions in a Tumor-on-a-chip Model. Micromachines (Basel). 2020;11(4):382.

456. Bērziņa S, Harrison A, Taly V, Xiao W. Technological Advances in Tumor-On-Chip Technology: From Bench to Bedside. Cancers (Basel). 2021;13(16):4192.

457. Song HHG, Park KM, Gerecht S. Hydrogels to model 3D in vitro microenvironment of tumor vascularization. Adv Drug Deliv Rev. 2014;79–80:19–29.

458. Chen Z, Wang F, Zhang J, Sun X, Yan Y, Wang Y, et al. Study on Development of Composite Hydrogels With Tunable Structures and Properties for Tumor-on-a-Chip Research. Front Bioeng Biotechnol. 2020;8.

459. Aralekallu S, Boddula R, Singh V. Development of glass-based microfluidic devices: A review on its fabrication and biologic applications. Mater Des. 2023;225:111517.

460. Ren K, Chen Y, Wu H. New materials for microfluidics in biology. Curr Opin Biotechnol. 2014 Feb 1;25:78–85.

461. Berthier E, Young EWK, Beebe D. Engineers are from PDMS-land, Biologists are from Polystyrenia. Lab Chip [Internet]. 2012;12(7):1224–37. Available from: http://dx.doi.org/10.1039/C2LC20982A

462. Mastrangeli M, Millet S, van den Eijnden-van Raaij J. Organ-on-chip in development: Towards a roadmap for organs-on-chip. ALTEX. 2019;36:650–68.

463. Mittal R, Woo FW, Castro CS, Cohen MA, Karanxha J, Mittal J, et al. Organ-on-chip models: Implications in drug discovery and clinical applications. J Cell Physiol. 2019;234(6):8352–80.

464. Park SE, Georgescu A, Huh D. Organoids-on-a-chip. Science (1979). 2019;364(6444):960–5.

465. Thompson CL, Fu S, Heywood HK, Knight MM, Thorpe SD. Mechanical Stimulation: A Crucial Element of Organ-on-Chip Models. Front Bioeng Biotechnol. 2020;8.

466. Hachey SJ, Hughes CCW. Applications of tumor chip technology. Lab Chip. 2018 Oct 7;18(19):2893–912.

467. Portillo-Lara R, Annabi N. Microengineered cancer-on-a-chip platforms to study the metastatic microenvironment. Lab Chip [Internet]. 2016;16(21):4063–81. Available from: http://dx.doi.org/10.1039/C6LC00718J

468. Wong AHH, Li H, Jia Y, Mak PI, Martins RP da S, Liu Y, et al. Drug screening of cancer cell lines and human primary tumors using droplet microfluidics. Sci Rep [Internet]. 2017;7(1):9109. Available from: https://doi.org/10.1038/s41598-017-08831-z

469. Acosta MA, Jiang X, Huang PK, Cutler KB, Grant CS, Walker GM, et al. A microfluidic device to study cancer metastasis under chronic and intermittent hypoxia. Biomicrofluidics. 2014 Oct 17;8(5):054117.

470. Zervantonakis IK, Hughes-Alford SK, Charest JL, Condeelis JS, Gertler FB, Kamm RD. Three-dimensional microfluidic model for tumor cell intravasation and endothelial barrier function. Proceedings of the National Academy of Sciences [Internet]. 2012;109(34):13515–20. Available from: https://doi.org/10.1073/pnas.1210182109

471. Zhao Y, Wang D, Xu T, Liu P, Cao Y, Wang Y, et al. Bladder cancer cells re-educate TAMs through lactate shuttling in the microfluidic cancer microenvironment. Oncotarget. 2015;6(36):39196–210.

472. Sung KE, Yang N, Pehlke C, Keely PJ, Eliceiri KW, Friedl A, et al. Transition to invasion in breast cancer: a microfluidic in vitro model enables examination of spatial and temporal effects. Integrative Biology [Internet]. 2011;3(4):439–50. Available from: https://doi.org/10.1039/c0ib00063a

473. Zhang H, Xiao L, Li Q, Qi X, Zhou A. Microfluidic chip for non-invasive analysis of tumor cells interaction with anti-cancer drug doxorubicin by AFM and Raman spectroscopy. Biomicrofluidics [Internet]. 2018;12(2). Available from: https://doi.org/10.1063/1.5024359

474. Dhiman N, Kingshott P, Sumer H, Sharma CS, Rath SN. On-chip anticancer drug screening – Recent progress in microfluidic platforms to address challenges in chemotherapy. Biosens Bioelectron [Internet]. 2019;137:236–54. Available from: https://www.sciencedirect.com/science/article/pii/S0956566319302209

475. Gao Y, Peng H, Li L, Wang F, Meng J, Huang H, et al. Screening of high-efficiency and low-toxicity antitumor active components in Macleaya cordata seeds based on the competitive effect of drugs on double targets by a new laminar flow chip. Analyst [Internet]. 2021;146(15):4934–44. Available from: http://dx.doi.org/10.1039/D1AN00754H

476. Rosa R, Monteleone F, Zambrano N, Bianco R. In Vitro and In Vivo Models for Analysis of Resistance to Anticancer Molecular Therapies. Curr Med Chem. 2014;21(14):1595–606.

477. Patel D, Gao Y, Son K, Siltanen C, Neve RM, Ferrara K, et al. Microfluidic co-cultures with hydrogel-based ligand trap to study paracrine signals giving rise to cancer drug resistance. Lab Chip [Internet]. 2015;15(24):4614–24. Available from: http://dx.doi.org/10.1039/C5LC00948K

478. Chen Y, Gao D, Liu H, Lin S, Jiang Y. Drug cytotoxicity and signaling pathway analysis with three-dimensional tumor spheroids in a microwell-based microfluidic chip for drug screening. Anal Chim Acta [Internet]. 2015;898:85–92. Available from: https://www.sciencedirect.com/science/article/pii/S0003267015012404

479. Jeong SY, Lee JH, Shin Y, Chung S, Kuh HJ. Co-Culture of Tumor Spheroids and Fibroblasts in a Collagen Matrix-Incorporated Microfluidic Chip Mimics Reciprocal Activation in Solid Tumor Microenvironment. PLoS One. 2016;11(7):e0159013.

480. Ashley EA. Towards precision medicine. Nat Rev Genet [Internet]. 2016;17(9):507–22. Available from: https://doi.org/10.1038/nrg.2016.86

481. Mathur A, Loskill P, Shao K, Huebsch N, Hong S, Marcus SG, et al. Human iPSC-based Cardiac Microphysiological System For Drug Screening Applications. Sci Rep [Internet]. 2015;5(1):8883. Available from: https://doi.org/10.1038/srep08883

482. Huebsch N, Loskill P, Deveshwar N, Spencer CI, Judge LM, Mandegar MA, et al. Miniaturized iPS-Cell-Derived Cardiac Muscles for Physiologically Relevant Drug Response Analyses. Sci Rep [Internet]. 2016;6(1):24726. Available from: https://doi.org/10.1038/srep24726

483. Takebe T, Zhang B, Radisic M. Synergistic Engineering: Organoids Meet Organs-on-a-Chip. Cell Stem Cell [Internet]. 2017;21(3):297–300. Available from: https://doi.org/10.1016/j.stem.2017.08.016

484. Huh D, Kim HJ, Fraser JP, Shea DE, Khan M, Bahinski A, et al. Microfabrication of human organs-on-chips. Nat Protoc [Internet]. 2013;8(11):2135–57. Available from: https://doi.org/10.1038/nprot.2013.137

485. Edington CD, Chen WLK, Geishecker E, Kassis T, Soenksen LR, Bhushan BM, et al. Interconnected Microphysiological Systems for Quantitative Biology and Pharmacology Studies. Sci Rep. 2018;8(1):4530.

486. Bhatia SN, Ingber DE. Microfluidic organs-on-chips. Nat Biotechnol [Internet]. 2014;32(8):760–72. Available from: https://doi.org/10.1038/nbt.2989

487. Pedrosa P, Mendes R, Cabral R, Martins LMDRS, Baptista P V., Fernandes AR. Combination of chemotherapy and Au-nanoparticle photothermy in the visible light to tackle doxorubicin resistance in cancer cells. Sci Rep. 2018 Dec 1;8(1).

488. Sousa DP, Conde J. Using gold nanobeacons as a theranostic technique to recognize, detect, and inhibit specific nucleic acids. STAR Protoc. 2022 Dec 16;3(4).

489. Baptista P, Conde J, Rosa J, Baptista P. Gold-Nanobeacons as a theranostic system for the detection and inhibition of specific genes. Protoc Exch. 2013 Nov 27;

490. Conde J, Tian F, Hernández Y, Bao C, Cui D, Janssen KP, et al. In vivo tumor targeting via nanoparticle-mediated therapeutic siRNA coupled to inflammatory response in lung cancer mouse models. Biomaterials [Internet]. 2013;34(31):7744–53. Available from: https://www.sciencedirect.com/science/article/pii/S0142961213007564

491. Susnik E, Bazzoni A, Taladriz-Blanco P, Balog S, Moreno-Echeverri AM, Glaubitz C, et al. Epidermal growth factor alters silica nanoparticle uptake and improves gold-nanoparticle-mediated gene silencing in A549 cells. Frontiers in Nanotechnology. 2023;5.

492. Baek NH, Seo OW, Kim MS, Hulme J, An SSA. Monitoring the effects of doxorubicin on 3D-spheroid tumor cells in real-time. Onco Targets Ther. 2016 Nov 22;9:7207–18.

493. Chiaraviglio L, Kirby JE. Evaluation of impermeant, DNA-binding dye fluorescence as a real-time readout of eukaryotic cell toxicity in a high throughput screening format. Assay Drug Dev Technol. 2014 May 1;12(4):219–28.

494. Bittremieux M, Gerasimenko J V, Schuermans M, Luyten T, Stapleton E, Alzayady KJ, et al. DPB162-AE, an inhibitor of store-operated Ca2+ entry, can deplete the endoplasmic reticulum Ca2+ store. Cell Calcium [Internet]. 2017;62:60–70. Available from: https://www.sciencedirect.com/science/article/pii/S014341601630207X

495. Schmittgen TD, Livak KJ. Analyzing real-time PCR data by the comparative CT method. Nat Protoc [Internet]. 2008;3(6):1101–8. Available from: https://doi.org/10.1038/nprot.2008.73

496. Bromma K, Chithrani DB. Advances in gold nanoparticle-based combined cancer therapy. Vol. 10, Nanomaterials. MDPI AG; 2020. p. 1–25.

497. Daraee H, Eatemadi A, Abbasi E, Aval SF, Kouhi M, Akbarzadeh A. Application of gold nanoparticles in biomedical and drug delivery. Vol. 44, Artificial Cells, Nanomedicine and Biotechnology. Taylor and Francis Ltd.; 2016. p. 410–22.

498. Cho WS, Cho M, Jeong J, Choi M, Han BS, Shin HS, et al. Size-dependent tissue kinetics of PEG-coated gold nanoparticles. Toxicol Appl Pharmacol [Internet]. 2010;245(1):116–23. Available from: https://www.sciencedirect.com/science/article/pii/S0041008X10000724

499. Lipka J, Semmler-Behnke M, Sperling RA, Wenk A, Takenaka S, Schleh C, et al. Biodistribution of PEG-modified gold nanoparticles following intratracheal instillation and intravenous injection. Biomaterials [Internet]. 2010;31(25):6574–81. Available from: https://www.sciencedirect.com/science/article/pii/S0142961210006277

500. Kanu GA, Parambath JBM, Abu Odeh RO, Mohamed AA. Gold Nanoparticle-Mediated Gene Therapy. Vol. 14, Cancers. MDPI; 2022.

501. Wu L, Zhou W, Lin L, Chen A, Feng J, Qu X, et al. Delivery of therapeutic oligonucleotides in nanoscale. Bioact Mater [Internet]. 2022;7:292–323. Available from: https://www.sciencedirect.com/science/article/pii/S2452199X21002589

502. Miller DM, Thomas SD, Islam A, Muench D, Sedoris K. c-Myc and cancer metabolism. Vol. 18, Clinical Cancer Research. 2012. p. 5546–53.

503. Dhanasekaran R, Deutzmann A, Mahauad-Fernandez WD, Hansen AS, Gouw AM, Felsher DW. The MYC oncogene — the grand orchestrator of cancer growth and immune evasion. Vol. 19, Nature Reviews Clinical Oncology. Nature Research; 2022. p. 23–36.

504. Tolcher AW, Papadopoulos KP, Patnaik A, Rasco DW, Martinez D, Wood DL, et al. Safety and activity of DCR-MYC, a first-in-class Dicer-substrate small interfering RNA (DsiRNA) targeting MYC, in a phase I study in patients with advanced solid tumors. Journal of clinical oncology. 2015;33(15_suppl):11006.

505. Yahya SMM, Hamed AR, Emara M, Soltan MM, Abd-Ellatef GEF, Abdelnasser SM. Differential effects of c-myc and ABCB1 silencing on reversing drug resistance in HepG2/Dox cells. Tumor Biology [Internet]. 2016;37(5):5925–32. Available from: https://doi.org/10.1007/s13277-015-4426-7

506. Kabilova TO, Chernolovskaya EL, Vladimirova A V, Vlassov V V. Silencing of c-myc Expression in Tumor Cells by siRNA. Nucleosides Nucleotides Nucleic Acids [Internet]. 2004 Dec 31;23(6–7):867–72. Available from: https://doi.org/10.1081/NCN-200026033

507. Wang YH, Liu S, Zhang G, Zhou CQ, Zhu HX, Zhou XB, et al. Knockdown of c-Myc expression by RNAi inhibits MCF-7 breast tumor cells growth in vitro and in vivo. 2004; Available from: http://breast-cancer-research.com/content/7/2/R220

508. Zhao Y, Jian W, Gao W, Zheng YX, Wang YK, Zhou ZQ, et al. RNAi silencing of c-Myc inhibits cell migration, invasion, and proliferation in HepG2 human hepatocellular carcinoma cell line: C-Myc silencing in hepatocellular carcinoma cell. Cancer Cell Int. 2013 Mar 8;13(1).

509. Habib S, Ariatti M, Singh M. Anti-c-myc rnai-based onconanotherapeutics. Vol. 8, Biomedicines. MDPI AG; 2020. p. 1–15.

510. Ferreira D, Fontinha D, Martins C, Pires D, Fernandes AR, Baptista P V. Gold nanoparticles for vectorization of nucleic acids for cancer therapeutics. Vol. 25, Molecules. MDPI AG; 2020.

511. Song Z, Tao Y, Liu Y, Li J. Advances in delivery systems for CRISPR/Cas-mediated cancer treatment: a focus on viral vectors and extracellular vesicles. Vol. 15, Frontiers in Immunology. Frontiers Media SA; 2024.

512. Crooke ST. Progress in antisense technology: The end of the beginning. In: Methods in Enzymology [Internet]. Academic Press; 2000. p. 3–45. Available from: https://www.sciencedirect.com/science/article/pii/S0076687900130034

513. Crooke ST. Molecular mechanisms of action of antisense drugs. Biochimica et Biophysica Acta (BBA) - Gene Structure and Expression [Internet]. 1999;1489(1):31–43. Available from: https://www.sciencedirect.com/science/article/pii/S0167478199001487

514. Watts JK, Corey DR. Silencing disease genes in the laboratory and the clinic. Vol. 226, Journal of Pathology. 2012. p. 365–79.

515. Chan JHP, Lim S, Wong WSF. ANTISENSE OLIGONUCLEOTIDES: FROM DESIGN TO THERAPEUTIC APPLICATION. Clin Exp Pharmacol Physiol [Internet]. 2006 May 1;33(5–6):533–40. Available from: https://doi.org/10.1111/j.1440-1681.2006.04403.x

516. Lauffer MC, van Roon-Mom W, Aartsma-Rus A. Possibilities and limitations of antisense oligonucleotide therapies for the treatment of monogenic disorders. Vol. 4, Communications Medicine. Springer Nature; 2024.

517. Lee PC, Meisel D. Adsorption and surface-enhanced Raman of dyes on silver and gold sols. J Phys Chem [Internet]. 1982 Aug 1;86(17):3391–5. Available from: https://doi.org/10.1021/j100214a025

518. Pedrosa P, Mendes R, Cabral R, Martins LMDRS, Baptista P V., Fernandes AR. Combination of chemotherapy and Au-nanoparticle photothermy in the visible light to tackle doxorubicin resistance in cancer cells. Sci Rep. 2018 Dec 1;8(1).

519. Sousa DP, Conde J. Using gold nanobeacons as a theranostic technique to recognize, detect, and inhibit specific nucleic acids. STAR Protoc [Internet]. 2022;3(4):101916. Available from: https://www.sciencedirect.com/science/article/pii/S2666166722007961

520. Conde J, Dias JT, Grazú V, Moros M, Baptista P V., de la Fuente JM. Revisiting 30 years of biofunctionalization and surface chemistry of inorganic nanoparticles for nanomedicine. Vol. 2, Frontiers in Chemistry. Frontiers Media S. A; 2014.

521. Baek NH, Seo OW, Kim MS, Hulme J, An SSA. Monitoring the effects of doxorubicin on 3D-spheroid tumor cells in real-time. Onco Targets Ther. 2016 Nov 22;9:7207–18.

522. Roma-Rodrigues C, Pombo I, Fernandes AR, Baptista P V. Hyperthermia induced by gold nanoparticles and visible light photothermy combined with chemotherapy to tackle doxorubicin sensitive and resistant colorectal tumor 3D spheroids. Int J Mol Sci. 2020 Nov 1;21(21):1–13.

523. Conde J, Tian F, Hernández Y, Bao C, Cui D, Janssen KP, et al. In vivo tumor targeting via nanoparticle-mediated therapeutic siRNA coupled to inflammatory response in lung cancer mouse models. Biomaterials [Internet]. 2013;34(31):7744–53. Available from: https://www.sciencedirect.com/science/article/pii/S0142961213007564

524. Oliveira BB, Fernandes AR, Baptista P V. Advances in Cancer Nanotheranostics for Experimental and Personalized Medicine. 2020.

525. Vinhas R, Fernandes AR, Baptista P V. Gold Nanoparticles for BCR-ABL1 Gene Silencing: Improving Tyrosine Kinase Inhibitor Efficacy in Chronic Myeloid Leukemia. Mol Ther Nucleic Acids. 2017 Jun 1;7:408–16.

526. Cabral RM, Baptista P V. Anti-cancer precision theranostics: a focus on multifunctional gold nanoparticles. Expert Rev Mol Diagn [Internet]. 2014 Nov 1;14(8):1041–52. Available from: https://doi.org/10.1586/14737159.2014.965683

527. Zhang P, Wang TY, Xiong HM, Kong JL. In situ tracking the intracellular delivery of antisense oligonucleotides by fluorescein doped silica nanoparticles. Talanta [Internet]. 2014;127:43–50. Available from: https://www.sciencedirect.com/science/article/pii/S0039914014002264

528. Schubert J, Chanana M. Coating Matters: Review on Colloidal Stability of Nanoparticles with Biocompatible Coatings in Biological Media, Living Cells and Organisms. Curr Med Chem. 2018 Jun 4;25(35):4553–86.

529. Carone A, Emilsson S, Mariani P, Désert A, Parola S. Gold nanoparticle shape dependence of colloidal stability domains. Nanoscale Adv. 2023 Feb 27;5(7):2017–26.

530. Doane TL, Chuang CH, Hill RJ, Burda C. Nanoparticle ζ -Potentials. Acc Chem Res [Internet]. 2012 Mar 20;45(3):317–26. Available from: https://doi.org/10.1021/ar200113c

531. Chopada R, Sarwate R, Kumar V. Effect of mild to extreme pH, temperature, and ionic strength on the colloidal stability of differentially capped gold nanoparticles. J Mol Struct [Internet]. 2025;1323:140751. Available from: https://www.sciencedirect.com/science/article/pii/S0022286024032599

532. Burns C, Spendel WU, Puckett S, Pacey GE. Solution ionic strength effect on gold nanoparticle solution color transition. Talanta [Internet]. 2006;69(4):873–6. Available from: https://www.sciencedirect.com/science/article/pii/S0039914005007666

533. Dalal C, Saha A, Jana NR. Nanoparticle Multivalency Directed Shifting of Cellular Uptake Mechanism. The Journal of Physical Chemistry C [Internet]. 2016 Mar 31;120(12):6778–86. Available from: https://doi.org/10.1021/acs.jpcc.5b11059

534. Bae Y, Liu X. Unveiling the effects of protein corona formation on the aggregation kinetics of gold nanoparticles in monovalent and divalent electrolytes. Environmental Pollution [Internet]. 2024;346:123552. Available from: https://www.sciencedirect.com/science/article/pii/S0269749124002665

535. Amina SJ, Guo B. A review on the synthesis and functionalization of gold nanoparticles as a drug delivery vehicle. Vol. 15, International Journal of Nanomedicine. Dove Medical Press Ltd; 2020. p. 9823–57.

536. Zhang G, Yang Z, Lu W, Zhang R, Huang Q, Tian M, et al. Influence of anchoring ligands and particle size on the colloidal stability and in vivo biodistribution of polyethylene glycol-coated gold nanoparticles in tumor-xenografted mice. Biomaterials [Internet]. 2009;30(10):1928–36. Available from: https://www.sciencedirect.com/science/article/pii/S0142961208010223

537. Persengiev SP, Zhu X, Green MR. Nonspecific, concentration-dependent stimulation and repression of mammalian gene expression by small interfering RNAs (siRNAs). RNA. 2004 Jan;10(1):12–8.

538. Vinhas RPGS;, Baptista PMRV;, Limão-Vieira PMAL; Gold nanoparticles for nanotheranostics in leukemia-Addressing Chronic Myeloid Leukemia [PhD thesis]. Faculdade de Ciências da Universidade Nova de Lisboa; 2018.

539. Livak KJ, Schmittgen TD. Analysis of Relative Gene Expression Data Using Real-Time Quantitative PCR and the 2−ΔΔCT Method. Methods [Internet]. 2001;25(4):402–8. Available from: https://www.sciencedirect.com/science/article/pii/S1046202301912629

540. Fernandes AR, Jesus J, Martins P, Figueiredo S, Rosa D, Martins LMRDRS, et al. Multifunctional gold-nanoparticles: A nanovectorization tool for the targeted delivery of novel chemotherapeutic agents. Journal of Controlled Release. 2017 Jan 10;245:52–61.

541. Alabi CA, Sahay G, Langer R, Anderson DG. Development of siRNA-probes for studying intracellular trafficking of siRNA nanoparticles. Integrative Biology (United Kingdom). 2013;5(1):224–30.

542. Shukla R, Bansal V, Chaudhary M, Basu A, Bhonde RR, Sastry M. Biocompatibility of Gold Nanoparticles and Their Endocytotic Fate Inside the Cellular Compartment: A Microscopic Overview. Langmuir [Internet]. 2005 Nov 1;21(23):10644–54. Available from: https://doi.org/10.1021/la0513712

543. Marano F, Hussain S, Rodrigues-Lima F, Baeza-Squiban A, Boland S. Nanoparticles: molecular targets and cell signalling. Arch Toxicol [Internet]. 2011;85(7):733–41. Available from: https://doi.org/10.1007/s00204-010-0546-4

544. Li B, Tang M. Research progress of nanoparticle toxicity signaling pathway. Life Sci [Internet]. 2020;263:118542. Available from: https://www.sciencedirect.com/science/article/pii/S0024320520312959

545. Rambanapasi C, Zeevaart JR, Buntting H, Bester C, Kotze D, Hayeshi R, et al. Bioaccumulation and subchronic toxicity of 14 nm gold nanoparticles in rats. Molecules. 2016 Jun 1;21(6).

546. Conde J, Ambrosone A, Hernandez Y, Tian F, McCully M, Berry CC, et al. 15 years on siRNA delivery: Beyond the State-of-the-Art on inorganic nanoparticles for RNAi therapeutics. Nano Today [Internet]. 2015;10(4):421–50. Available from: https://www.sciencedirect.com/science/article/pii/S174801321500078X

547. Rosi NL, Giljohann DA, Thaxton CS, Lytton-Jean AKR, Han MS, Mirkin CA. Oligonucleotide-Modified Gold Nanoparticles for Intracellular Gene Regulation. Science (1979) [Internet]. 2006 May 19;312(5776):1027–30. Available from: https://doi.org/10.1126/science.1125559

548. Gerber A, Bundschuh M, Klingelhofer D, Groneberg DA. Gold nanoparticles: recent aspects for human toxicology [Internet]. 2013. Available from: http://www.occup-med.com/content/8/1/32

549. Gerber A, Bundschuh M, Klingelhofer D, Groneberg DA. Gold nanoparticles: recent aspects for human toxicology [Internet]. 2013. Available from: http://www.occup-med.com/content/8/1/32

550. Chen YS, Hung YC, Liau I, Huang GS. Assessment of the In Vivo Toxicity of Gold Nanoparticles. Nanoscale Res Lett [Internet]. 2009;4(8):858. Available from: https://doi.org/10.1007/s11671-009-9334-6

551. Conde J, Larguinho M, Cordeiro A, Raposo LR, Costa PM, Santos S, et al. Gold-nanobeacons for gene therapy: evaluation of genotoxicity, cell toxicity and proteome profiling analysis. Nanotoxicology [Internet]. 2014 Aug 1;8(5):521–32. Available from: https://doi.org/10.3109/17435390.2013.802821

552. Connor EE, Mwamuka J, Gole A, Murphy CJ, Wyatt MD. Gold Nanoparticles Are Taken Up by Human Cells but Do Not Cause Acute Cytotoxicity. Small [Internet]. 2005 Mar 1;1(3):325–7. Available from: https://doi.org/10.1002/smll.200400093

553. Trickler WJ, Lantz SM, Murdock RC, Schrand AM, Robinson BL, Newport GD, et al. Brain microvessel endothelial cells responses to gold nanoparticles: In vitro pro-inflammatory mediators and permeability. Nanotoxicology [Internet]. 2011 Dec 1;5(4):479–92. Available from: https://doi.org/10.3109/17435390.2010.540356

554. Khan JA, Pillai B, Das TK, Singh Y, Maiti S. Molecular Effects of Uptake of Gold Nanoparticles in HeLa Cells. ChemBioChem [Internet]. 2007 Jul 23;8(11):1237–40. Available from: https://doi.org/10.1002/cbic.200700165

555. Senut MC, Zhang Y, Liu F, Sen A, Ruden DM, Mao G. Size-Dependent Toxicity of Gold Nanoparticles on Human Embryonic Stem Cells and Their Neural Derivatives. Small. 2016 Feb 3;12(5):631–46.

556. Alkilany AM, Murphy CJ. Toxicity and cellular uptake of gold nanoparticles: What we have learned so far? Journal of Nanoparticle Research. 2010 Sep;12(7):2313–33.

557. ISO (the International Organization for Standardization). Biological evaluation of medical devices — Part 5: Tests for in vitro cytotoxicity. In: ISO 10993-5:2009(en) Biological evaluation of medical devices. 2009. p. 1–34.

558. Tournebize J, Sapin-Minet A, Bartosz G, Leroy P, Boudier A. Pitfalls of assays devoted to evaluation of oxidative stress induced by inorganic nanoparticles. Talanta [Internet]. 2013;116:753–63. Available from: https://www.sciencedirect.com/science/article/pii/S0039914013006504

559. Ghasemi M, Turnbull T, Sebastian S, Kempson I. The mtt assay: Utility, limitations, pitfalls, and interpretation in bulk and single-cell analysis. Int J Mol Sci. 2021 Dec 1;22(23).

560. Wang P, Henning SM, Heber D. Limitations of MTT and MTS-Based Assays for Measurement of Antiproliferative Activity of Green Tea Polyphenols. PLoS One [Internet]. 2010 Apr 16;5(4):e10202-. Available from: https://doi.org/10.1371/journal.pone.0010202

561. Braissant O, Astasov-Frauenhoffer M, Waltimo T, Bonkat G. A Review of Methods to Determine Viability, Vitality, and Metabolic Rates in Microbiology. Vol. 11, Frontiers in Microbiology. Frontiers Media S.A.; 2020.

562. Ekaterina Olegovna T, Zaynat Sattarovna K, Umida Bakhriddin Kizi K, Mukaddas Rustamovna U, Nigora Arziyevna T, Orzigul Bakhrievna A, et al. Cytotoxicity Is the Key Test for In Vitro Toxicity. In: Cytotoxicity - A Crucial Toxicity Test for In Vitro Experiments [Working Title]. IntechOpen; 2024.

563. Wątroba M, Bednarczyk W, Szewczyk PK, Kawałko J, Mech K, Grünewald A, et al. In vitro cytocompatibility and antibacterial studies on biodegradable Zn alloys supplemented by a critical assessment of direct contact cytotoxicity assay. J Biomed Mater Res B Appl Biomater. 2023 Feb 1;111(2):241–60.

564. Strober W. Trypan Blue Exclusion Test of Cell Viability. Curr Protoc Immunol [Internet]. 2015 Nov 1;111(1):A3.B.1-A3.B.3. Available from: https://doi.org/10.1002/0471142735.ima03bs111

565. Conde J, Ambrosone A, Sanz V, Hernandez Y, Marchesano V, Tian F, et al. Design of multifunctional gold nanoparticles for in vitro and in vivo gene silencing. ACS Nano. 2012 Sep 25;6(9):8316–24.

566. Gill T, Wang H, Bandaru R, Lawlor M, Lu C, Nieman LT, et al. Selective targeting of MYC mRNA by stabilized antisense oligonucleotides. Oncogene. 2021 Nov 25;40(47):6527–39.

567. Shen L, Zhang C, Ambrus JL, Wang JH. Silencing of Human c-myc Oncogene Expression by Poly-DNP-RNA. Vol. 15, OLIGONUCLEOTIDES. 2005.

568. Zhao Y, Jian W, Gao W, Zheng YX, Wang YK, Zhou ZQ, et al. RNAi silencing of c-Myc inhibits cell migration, invasion, and proliferation in HepG2 human hepatocellular carcinoma cell line: C-Myc silencing in hepatocellular carcinoma cell. Cancer Cell Int. 2013 Mar 8;13(1).

569. E. Wickstrom, T. A. Bacon, C. M. Werking, R. D. Palmiter, R. L. Brinster, E. P. Sandgren. Antisense oligodeoxynucleoside methylphosphonate inhibition of mouse c-myc p65 protein expression in E mu-c-myc transgenic mice. Nucleic Acids Symp Ser. 1991;24:151–4.

570. Crooke ST, Wang S, Vickers TA, Shen W, Liang XH. Cellular uptake and trafficking of antisense oligonucleotides. Vol. 35, Nature Biotechnology. Nature Publishing Group; 2017. p. 230–7.

571. Simonsson T, Henriksson M. c-myc Suppression in Burkitt's Lymphoma Cells. Biochem Biophys Res Commun [Internet]. 2002;290(1):11–5. Available from: https://www.sciencedirect.com/science/article/pii/S0006291X01960966

572. Miller DM, Thomas SD, Islam A, Muench D, Sedoris K. c-Myc and cancer metabolism. Clinical Cancer Research. 2012 Oct 15;18(20):5546–53.

573. Liang XH, Nichols JG, Hsu CW, Vickers TA, Crooke ST. MRNA levels can be reduced by antisense oligonucleotides via no-go decay pathway. Nucleic Acids Res. 2019 Jul 26;47(13):6900–16.

574. Paul A, Muralidharan A, Biswas A, Kamath BV, Joseph A, Alex AT. siRNA therapeutics and its challenges: Recent advances in effective delivery for cancer therapy. OpenNano [Internet]. 2022;7:100063. Available from: https://www.sciencedirect.com/science/article/pii/S2352952022000251

575. Sambale F, Lavrentieva A, Stahl F, Blume C, Stiesch M, Kasper C, et al. Three dimensional spheroid cell culture for nanoparticle safety testing. J Biotechnol. 2015 Jul 1;205:120–9.

576. Da Rocha EL, Porto LM, Rambo CR. Nanotechnology meets 3D in vitro models: Tissue engineered tumors and cancer therapies. Vol. 34, Materials Science and Engineering C. 2014. p. 270–9.

577. Breslin S, O'Driscoll L. Three-dimensional cell culture: The missing link in drug discovery. Vol. 18, Drug Discovery Today. 2013. p. 240–9.

578. Juarez-Moreno K, Chávez-García D, Hirata G, Vazquez-Duhalt R. Monolayer (2D) or spheroids (3D) cell cultures for nanotoxicological studies? Comparison of cytotoxicity and cell internalization of nanoparticles. Toxicology in Vitro. 2022 Dec;85:105461.

579. Kapałczyńska M, Kolenda T, Przybyła W, Zajączkowska M, Teresiak A, Filas V, et al. 2D and 3D cell cultures – a comparison of different types of cancer cell cultures. Archives of Medical Science. 2018;14(4):910–9.

580. Hickman JA, Graeser R, de Hoogt R, Vidic S, Brito C, Gutekunst M, et al. Three-dimensional models of cancer for pharmacology and cancer cell biology: Capturing tumor complexity in vitro/ex vivo. Vol. 9, Biotechnology Journal. Wiley-VCH Verlag; 2014. p. 1115–28.

581. Baker BM, Chen CS. Deconstructing the third dimension-how 3D culture microenvironments alter cellular cues. Vol. 125, Journal of Cell Science. 2012. p. 3015–24.

582. Riedl A, Schlederer M, Pudelko K, Stadler M, Walter S, Unterleuthner D, et al. Comparison of cancer cells in 2D vs 3D culture reveals differences in AKT-mTOR-S6K signaling and drug responses. J Cell Sci. 2017;130(1):203–18.

583. Huh D, Hamilton GA, Ingber DE. From 3D cell culture to organs-on-chips. Vol. 21, Trends in Cell Biology. 2011. p. 745–54.

584. Mehta G, Hsiao AY, Ingram M, Luker GD, Takayama S. Opportunities and challenges for use of tumor spheroids as models to test drug delivery and efficacy. Journal of Controlled Release. 2012 Dec 10;164(2):192–204.

585. Schmeichel KL, Bissell MJ. Modelling tissue-specific signaling and organ function in three dimensions. Vol. 116, Journal of Cell Science. 2003. p. 2377–88.

586. Friedrich J, Seidel C, Ebner R, Kunz-Schughart LA. Spheroid-based drug screen: Considerations and practical approach. Nat Protoc. 2009;4(3):309–24.

587. Roberts TC, Langer R, Wood MJA. Advances in oligonucleotide drug delivery. Vol. 19, Nature Reviews Drug Discovery. Nature Research; 2020. p. 673–94.

588. Barata P, Sood AK, Hong DS. RNA-targeted therapeutics in cancer clinical trials: Current status and future directions. Cancer Treat Rev [Internet]. 2016;50:35–47. Available from: https://www.sciencedirect.com/science/article/pii/S0305737216300743

589. Belli V, Guarnieri D, Biondi M, della Sala F, Netti PA. Dynamics of nanoparticle diffusion and uptake in three-dimensional cell cultures. Colloids Surf B Biointerfaces [Internet]. 2017;149:7–15. Available from: https://www.sciencedirect.com/science/article/pii/S0927776516307007

590. Belli V, Guarnieri D, Biondi M, della Sala F, Netti PA. Dynamics of nanoparticle diffusion and uptake in three-dimensional cell cultures. Colloids Surf B Biointerfaces. 2017 Jan 1;149(1):7–15.

591. Goodman TT, Chee PN, Suzie HP. 3-D tissue culture systems for the evaluation and optimization of nanoparticle-based drug carriers. Vol. 19, Bioconjugate Chemistry. American Chemical Society; 2008. p. 1951–9.

592. Van Zundert I, Fortuni B, Rocha S. From 2d to 3d cancer cell models—the enigmas of drug delivery research. Vol. 10, Nanomaterials. MDPI AG; 2020. p. 1–30.

593. Bhise NS, Gray RS, Sunshine JC, Htet S, Ewald AJ, Green JJ. The relationship between terminal functionalization and molecular weight of a gene delivery polymer and transfection efficacy in mammary epithelial 2-D cultures and 3-D organotypic cultures. Biomaterials. 2010 Nov;31(31):8088–96.

594. Abbas ZN, Al-Saffar AZ, Jasim SM, Sulaiman GM. Comparative analysis between 2D and 3D colorectal cancer culture models for insights into cellular morphological and transcriptomic variations. Sci Rep. 2023 Dec 1;13(1).

595. Hoarau-Véchot J, Rafii A, Touboul C, Pasquier J. Halfway between 2D and animal models: Are 3D cultures the ideal tool to study cancer-microenvironment interactions? Vol. 19, International Journal of Molecular Sciences. MDPI AG; 2018.

596. Xu FX, Sun R, Owens R, Hu K, Fu D. Assessing Drug Uptake and Response Differences in 2D and 3D Cellular Environments Using Stimulated Raman Scattering Microscopy. Anal Chem [Internet]. 2024 Sep 10;96(36):14480–9. Available from: https://doi.org/10.1021/acs.analchem.4c02592

597. Behzadi S, Serpooshan V, Tao W, Hamaly MA, Alkawareek MY, Dreaden EC, et al. Cellular uptake of nanoparticles: Journey inside the cell. Vol. 46, Chemical Society Reviews. Royal Society of Chemistry; 2017. p. 4218–44.

598. Stylianopoulos T, Jain RK. Design considerations for nanotherapeutics in oncology. Vol. 11, Nanomedicine: Nanotechnology, Biology, and Medicine. Elsevier Inc.; 2015. p. 1893–907.

599. Musielak M, Boś-Liedke A, Piwocka O, Kowalska K, Markiewicz R, Szymkowiak B, et al. The Role of Functionalization and Size of Gold Nanoparticles in the Response of MCF-7 Breast Cancer Cells to Ionizing Radiation Comparing 2D and 3D In Vitro Models. Pharmaceutics. 2023 Mar 1;15(3).

600. Dimitrijevic D, Fabian E, Nicol B, Funk-Weyer D, Landsiedel R. Toward Realistic Dosimetry In Vitro: Determining Effective Concentrations of Test Substances in Cell Culture and Their Prediction by an In Silico Mass Balance Model. Chem Res Toxicol [Internet]. 2022 Nov 21;35(11):1962–73. Available from: https://doi.org/10.1021/acs.chemrestox.2c00128

601. Wheeler GM, Mander AP, Bedding A, Brock K, Cornelius V, Grieve AP, et al. How to design a dose-finding study using the continual reassessment method. BMC Med Res Methodol. 2019 Jan 18;19(1).

602. Tamargo J, Le Heuzey JY, Mabo P. Narrow therapeutic index drugs: A clinical pharmacological consideration to flecainide. Eur J Clin Pharmacol. 2015 May 1;71(5):549–67.

603. Ferreira-Silva M, Faria-Silva C, Baptista PV, Fernandes E, Fernandes AR, Corvo ML. Drug delivery nanosystems targeted to hepatic ischemia and reperfusion injury. Drug Deliv Transl Res [Internet]. 2021;11(2):397–410. Available from: https://doi.org/10.1007/s13346-021-00915-8

604. Amacher DE. The discovery and development of proteomic safety biomarkers for the detection of drug-induced liver toxicity. Toxicol Appl Pharmacol [Internet]. 2010;245(1):134–42. Available from: https://www.sciencedirect.com/science/article/pii/S0041008X10000700

605. Musuamba FT, Manolis E, Holford N, Cheung SYA, Friberg LE, Ogungbenro K, et al. Advanced methods for dose and regimen finding during drug development: Summary of the EMA/EFPIA workshop on dose finding (London 4-5 December 2014). CPT Pharmacometrics Syst Pharmacol. 2017 Jul 1;6(7):418–29.

606. Ferreira GS, Dijkstra FM, Veening-Griffioen DH, Boon WPC, Schellekens H, Moors EHM, et al. Translatability of preclinical to early clinical tolerable and pharmacologically active dose ranges for central nervous system active drugs. Vol. 13, Translational Psychiatry. Springer Nature; 2023.

607. Chithrani BD, Ghazani AA, Chan WCW. Determining the size and shape dependence of gold nanoparticle uptake into mammalian cells. Nano Lett. 2006 Apr;6(4):662–8.

608. Mironava T, Hadjiargyrou M, Simon M, Jurukovski V, Rafailovich MH. Gold nanoparticles cellular toxicity and recovery: Effect of size, concentration and exposure time. Nanotoxicology. 2010 Mar;4(1):120–37.

609. Imanis Life Sciences. HCT116 (Colorectal Carcinoma).

610. Conner SD, Schmid SL. Regulated portals of entry into the cell. Vol. 422, Nature. 2003. p. 37–44.

611. Saha K, Kim ST, Yan B, Miranda OR, Alfonso FS, Shlosman D, et al. Surface functionality of nanoparticles determines cellular uptake mechanisms in mammalian cells. Small. 2013 Jan 28;9(2):300–5.

612. Chithrani BD, Chan WCW. Elucidating the mechanism of cellular uptake and removal of protein-coated gold nanoparticles of different sizes and shapes. Nano Lett. 2007 Jun;7(6):1542–50.

613. Dobrovolskaia MA, Mcneil E. Immunological properties of engineered nanomaterials [Internet]. 2007. Available from: www.orthobiotech.com;

614. Xie X, Liao J, Shao X, Li Q, Lin Y. The Effect of shape on Cellular Uptake of Gold Nanoparticles in the forms of Stars, Rods, and Triangles. Sci Rep. 2017 Dec 1;7(1).

615. Shukla R, Bansal V, Chaudhary M, Basu A, Bhonde RR, Sastry M. Biocompatibility of Gold Nanoparticles and Their Endocytotic Fate Inside the Cellular Compartment: A Microscopic Overview. Langmuir. 2005 Nov 1;21(23):10644–54.

616. Nativo P, Prior IA, Brust M. Uptake and intracellular fate of surface-modified gold nanoparticles. ACS Nano. 2008 Aug;2(8):1639–44.

617. Bonilla-Vidal L, Esteruelas G, Souto EB, Espina M, García ML, Sánchez López E. The role of blood–brain and blood–retinal barriers in drug delivery. In: Nanotechnology and Regenerative Medicine. Elsevier; 2023. p. 133–54.

618. Gao H, Shi W, Freund LB. Mechanics of receptor-mediated endocytosis [Internet]. 2005. Available from: www.pnas.orgcgidoi10.1073pnas.0503879102

619. Alkilany AM, Murphy CJ. Toxicity and cellular uptake of gold nanoparticles: What we have learned so far? Journal of Nanoparticle Research. 2010 Sep;12(7):2313–33.

620. Cree IA. Principles of Cancer Cell Culture. In: Cree IA, editor. Cancer Cell Culture: Methods and Protocols [Internet]. Totowa, NJ: Humana Press; 2011. p. 13–26. Available from: https://doi.org/10.1007/978-1-61779-080-5_2

621. Mirabelli P, Coppola L, Salvatore M. Cancer cell lines are useful model systems for medical research. Cancers (Basel). 2019 Aug 1;11(8):1098.

622. Tian C, Zheng S, Liu X, Kamei K ichiro. Tumor-on-a-chip model for advancement of anti-cancer nano drug delivery system. J Nanobiotechnology. 2022 Dec 1;20(1):338.

623. Fontana F, Marzagalli M, Sommariva M, Gagliano N, Limonta P. In vitro 3D cultures to model the tumor microenvironment. Cancers (Basel). 2021 Jun 2;13(12):2970.

624. Chang CW, Cheng YJ, Tu M, Chen YH, Peng CC, Liao WH, et al. A polydimethylsiloxane-polycarbonate hybrid microfluidic device capable of generating perpendicular chemical and oxygen gradients for cell culture studies. Lab Chip. 2014;14(19):3762–72.

625. Orcheston-Findlay L, Hashemi A, Garrill A, Nock V. A microfluidic gradient generator to simulate the oxygen microenvironment in cancer cell culture. Microelectron Eng. 2018 Aug 5;195:107–13.

626. Neto JP, Mota A, Lopes G, Coelho BJ, Frazão J, Moura AT, et al. Open-source tool for real-time and automated analysis of droplet-based microfluidic. Lab Chip [Internet]. 2023;23(14):3238–44. Available from: http://dx.doi.org/10.1039/D3LC00327B

627. Bernacka-Wojcik I, Lopes P, Catarina Vaz A, Veigas B, Jerzy Wojcik P, Simoes P, et al. Bio-microfluidic platform for gold nanoprobe based DNA detection-application to Mycobacterium tuberculosis. Biosens Bioelectron. 2013 Oct 5;48:87–93.

628. Martynova L, Locascio LE, Gaitan M, Kramer GW, Christensen RG, Maccrehan WA. Fabrication of Plastic Microfluid Channels by Imprinting Methods. Anal Chem [Internet]. 1997;69(23):4783–9. Available from: https://pubs.acs.org/sharingguidelines

629. Gerlach A, Knebel G, Guber AE, Heckele M, Herrmann D, Muslija A, et al. Microfabrication of single-use plastic microfluidic devices for high-throughput screening and DNA analysis. Microsystem Technologies. 2002;7(5–6):265–8.

630. Rötting O, Röpke W, Becker H, Gärtner C. Polymer microfabrication technologies. Microsystem Technologies. 2002 Mar;8(1):32–6.

631. Regmi S, Poudel C, Adhikari R, Luo KQ. Applications of Microfluidics and Organ-on-a-Chip in Cancer Research. Biosensors (Basel). 2022 Jul 1;12(7):459.

632. Nguyen T, Jung SH, Lee MS, Park TE, Ahn SK, Kang JH. Robust chemical bonding of PMMA microfluidic devices to porous PETE membranes for reliable cytotoxicity testing of drugs. Lab Chip. 2019 Nov 7;19(21):3706–13.

633. Kumar D, Nadda R, Repaka R. Advances and challenges in organ-on-chip technology: toward mimicking human physiology and disease in vitro. Med Biol Eng Comput. 2024;

634. van der Meer AD, van den Berg A. Organs-on-chips: breaking the in vitro impasse. Integrative Biology [Internet]. 2012 May 1;4(5):461–70. Available from: https://doi.org/10.1039/c2ib00176d

635. Bhise NS, Ribas J, Manoharan V, Zhang YS, Polini A, Massa S, et al. Organ-on-a-chip platforms for studying drug delivery systems. Journal of Controlled Release [Internet]. 2014;190:82–93. Available from: https://www.sciencedirect.com/science/article/pii/S0168365914002958

636. Zhou W, Dou M, Timilsina SS, Xu F, Li XJ. Recent innovations in cost-effective polymer and paper hybrid microfluidic devices. Lab Chip. 2021 Jul 21;21(14):2658–83.

637. Li H, Fan Y, Kodzius R, Foulds IG. Fabrication of polystyrene microfluidic devices using a pulsed CO 2 laser system. Microsystem Technologies. 2012 Mar;18(3):373–9.

638. Chen CS, Breslauer DN, Luna JI, Grimes A, Chin WC, Lee LP, et al. Shrinky-Dink microfluidics: 3D polystyrene chips. Lab Chip. 2008;8(4):622–4.

639. Kodzius R, Xiao K, Wu J, Yi X, Gong X, Foulds IG, et al. Inhibitory effect of common microfluidic materials on PCR outcome. Sens Actuators B Chem. 2012 Jan 3;161(1):349–58.

640. Nayak NC, Lam YC, Yue CY, Sinha AT. CO2-laser micromachining of PMMA: The effect of polymer molecular weight. Journal of Micromechanics and Microengineering. 2008 Sep 1;18(9):095020.

641. Yi X, Kodzius R, Gong X, Xiao K, Wen W. A simple method of fabricating mask-free microfluidic devices for biological analysis. Biomicrofluidics. 2010;4(3):036503.

642. Fan Y, Wang H, Liu S, Liu J, Gao K, Zhang Y. Rapid prototyping of shrinkable BOPS-based microfluidic devices. Microfluid Nanofluidics. 2018 Dec 1;22(12).

643. Lim J, Ching H, Yoon JK, Jeon NL, Kim YT. Microvascularized tumor organoids-on-chips: advancing preclinical drug screening with pathophysiological relevance. Nano Converg. 2021 Dec 1;8(1):12.

644. Yang Y, Kong Y, Cui J, Hou Y, Gu Z, Ma C. Advances and Applications of Cancer Organoids in Drug Screening and Personalized Medicine. Stem Cell Rev Rep. 2024;

645. Gelfand Center. Shrinky Dinks ® [Internet]. [cited 2024 May 23]. Available from: https://www.cmu.edu/gelfand/lgc-educational-media/polymers/molecular-rearrangement/shrinky-dinks.html

646. Powell J. CO2 Laser Cutting. 2nd ed. Vol. 2. London: Springer London; 1998. 205–229 p.

647. Kameyama N, Yoshida H, Fukagawa H, Yamada K, Fukuda M. Thin-film processing of polypropylene and polystyrene sheets by a continuous wave CO2 laser with the Cu cooling base. Polymers (Basel). 2021 May 1;13(9):1448.

648. Mark J. E. Polymer Data Handbook, 2nd edition [Internet]. Vol. 131, Journal of the American Chemical Society. 2009. 16330–16330 p. Available from: https://pubs.acs.org/doi/10.1021/ja907879q

649. Greene JP. 3 - Microstructures of Polymers. In: Greene JP, editor. Automotive Plastics and Composites [Internet]. William Andrew Publishing; 2021. p. 27–37. Available from: https://www.sciencedirect.com/science/article/pii/B978012818008200009X

650. Nguyen D, Taylor D, Qian K, Norouzi N, Rasmussen J, Botzet S, et al. Better shrinkage than Shrinky-Dinks. Lab Chip. 2010;10(12):1623–6.

651. Grimes A, Breslauer DN, Long M, Pegan J, Lee LP, Khine M. Shrinky-Dink microfluidics: Rapid generation of deep and rounded patterns. Lab Chip. 2007;8(1):170–2.

652. Oliveira B, Veigas B, Fernandes AR, Águas H, Martins R, Fortunato E, et al. Fast prototyping microfluidics: Integrating droplet digital lamp for absolute quantification of cancer biomarkers. Sensors (Switzerland). 2020 Mar 2;20(6):1624.

653. Bakhtiari A, Kähler CJ. A method to prevent clogging and clustering in microfluidic systems using microbubble streaming. Biomicrofluidics. 2024 Jul 1;18(4).

654. Cai S, Wu C, Yang W, Liang W, Yu H, Liu L. Recent advance in surface modification for regulating cell adhesion and behaviors. Nanotechnol Rev. 2020 Jan 1;9(1):971–89.

655. Kim K, Thorp H, Bou-Ghannam S, Grainger DW, Okano T. Stable cell adhesion affects mesenchymal stem cell sheet fabrication: Effects of fetal bovine serum and human platelet lysate. J Tissue Eng Regen Med. 2020 May 1;14(5):741–53.

656. Miller DC, Haberstroh KM, Webster TJ. Mechanism(s) of increased vascular cell adhesion on nanostructured poly(lactic-co-glycolic acid) films. J Biomed Mater Res A. 2005 Jun 15;73(4):476–84.

657. Azizipour N, Avazpour R, Sawan M, Rosenzweig DH, Ajji A. Uniformity of spheroids-on-a-chip by surface treatment of PDMS microfluidic platforms. Cite this: Sens Diagn. 2022;1:750.

658. Schlie-Wolter S, Ngezahayo A, Chichkov BN. The selective role of ECM components on cell adhesion, morphology, proliferation and communication in vitro. Exp Cell Res. 2013 Jun 10;319(10):1553–61.

659. Fulda S, Gorman AM, Hori O, Samali A. Cellular stress responses: Cell survival and cell death. Int J Cell Biol. 2010;2010(1):214074.

660. Chen Y, Li X, Yang M, Liu SB. Research progress on morphology and mechanism of programmed cell death. Cell Death Dis. 2024 May 1;15(5):327.

661. Wang P, Henning SM, Heber D. Limitations of MTT and MTS-based assays for measurement of antiproliferative activity of green tea polyphenols. PLoS One. 2010;5(4):e10202.

662. Cordeiro S, Oliveira BB, Valente R, Ferreira D, Luz A, Baptista P V., et al. Breaking the mold: 3D cell cultures reshaping the future of cancer research. Vol. 12, Frontiers in Cell and Developmental Biology. Frontiers Media SA; 2024.

663. Drost J, van Jaarsveld RH, Ponsioen B, Zimberlin C, van Boxtel R, Buijs A, et al. Sequential cancer mutations in cultured human intestinal stem cells. Nature [Internet]. 2015;521(7550):43–7. Available from: https://doi.org/10.1038/nature14415

664. Baghy K, Ladányi A, Reszegi A, Kovalszky I. Insights into the Tumor Microenvironment—Components, Functions and Therapeutics. Int J Mol Sci [Internet]. 2023;24(24). Available from: https://www.mdpi.com/1422-0067/24/24/17536

665. Roma-Rodrigues C, Mendes R, Baptista P V, Fernandes AR. Targeting Tumor Microenvironment for Cancer Therapy. Int J Mol Sci [Internet]. 2019;20(4). Available from: https://www.mdpi.com/1422-0067/20/4/840

666. Kapałczyńska M, Kolenda T, Przybyła W, Zajączkowska M, Teresiak A, Filas V, et al. 2D and 3D cell cultures – a comparison of different types of cancer cell cultures. Archives of Medical Science. 2018;14(4):910–9.

667. Fontoura JC, Viezzer C, dos Santos FG, Ligabue RA, Weinlich R, Puga RD, et al. Comparison of 2D and 3D cell culture models for cell growth, gene expression and drug resistance. Materials Science and Engineering: C [Internet]. 2020;107:110264. Available from: https://www.sciencedirect.com/science/article/pii/S0928493119305934

668. Brooks A, Zhang Y, Chen J, Zhao CX. Cancer Metastasis-on-a-Chip for Modeling Metastatic Cascade and Drug Screening. Adv Healthc Mater [Internet]. 2024;13(21):2302436. Available from: https://doi.org/10.1002/adhm.202302436

669. Birgersdotter A, Sandberg R, Ernberg I. Gene expression perturbation in vitro—A growing case for three-dimensional (3D) culture systems. Semin Cancer Biol [Internet]. 2005;15(5):405–12. Available from: https://www.sciencedirect.com/science/article/pii/S1044579X05000416

670. Li C, Kato M, Shiue L, Shively JE, Ares M, Lin RJ. Cell type and culture condition-dependent alternative splicing in human breast cancer cells revealed by splicing-sensitive microarrays. Cancer Res. 2006 Feb 15;66(4):1990–9.

671. Fuchs E, Tumbar T, Guasch G. Socializing with the Neighbors: Stem Cells and Their Niche. Cell [Internet]. 2004;116(6):769–78. Available from: https://www.sciencedirect.com/science/article/pii/S0092867404002557

672. Gómez-Lechón MJ, Jover R, Donato T, Ponsoda X, Rodriguez C, Stenzel KG, et al. Long-term expression of differentiated functions in hepatocytes cultured in three-dimensional collagen matrix. J Cell Physiol [Internet]. 1998 Dec 1;177(4):553–62. Available from: https://doi.org/10.1002/(SICI)1097-4652(199812)177:4<553::AID-JCP6>3.0.CO

673. Ghosh S, Spagnoli GC, Martin I, Ploegert S, Demougin P, Heberer M, et al. Three-dimensional culture of melanoma cells profoundly affects gene expression profile: A high density oligonucleotide array study. J Cell Physiol [Internet]. 2005 Aug 1;204(2):522–31. Available from: https://doi.org/10.1002/jcp.20320

674. Moghimi N, Hosseini SA, Dalan AB, Mohammadrezaei D, Goldman A, Kohandel M. Controlled tumor heterogeneity in a co-culture system by 3D bio-printed tumor-on-chip model. Sci Rep. 2023 Dec 1;13(1).

675. Zou H, Yue W, Yu WK, Liu D, Fong CC, Zhao J, et al. Microfluidic Platform for Studying Chemotaxis of Adhesive Cells Revealed a Gradient-Dependent Migration and Acceleration of

Cancer Stem Cells. Anal Chem [Internet]. 2015 Jul 21;87(14):7098–108. Available from: https://doi.org/10.1021/acs.analchem.5b00873

676. Menon N V., Chuah YJ, Cao B, Lim M, Kang Y. A microfluidic co-culture system to monitor tumor-stromal interactions on a chip. Biomicrofluidics. 2014 Dec 5;8(6).

677. Lanz HL, Saleh A, Kramer B, Cairns J, Ng CP, Yu J, et al. Therapy response testing of breast cancer in a 3D high-throughput perfused microfluidic platform. BMC Cancer. 2017 Nov 2;17(1).

678. Brennan MD, Rexius-Hall ML, Elgass LJ, Eddington DT. Oxygen control with microfluidics. Lab Chip [Internet]. 2014;14(22):4305–18. Available from: http://dx.doi.org/10.1039/C4LC00853G

679. Chen YA, King AD, Shih HC, Peng CC, Wu CY, Liao WH, et al. Generation of oxygen gradients in microfluidic devices for cell culture using spatially confined chemical reactions. Lab Chip [Internet]. 2011;11(21):3626–33. Available from: http://dx.doi.org/10.1039/C1LC20325H

680. Chi CW, Lao YH, Ahmed AHR, Benoy EC, Li C, Dereli-Korkut Z, et al. High-Throughput Tumor-on-a-Chip Platform to Study Tumor–Stroma Interactions and Drug Pharmacokinetics. Adv Healthc Mater. 2020;9(21):2000880.

681. Huh D, Hamilton GA, Ingber DE. From 3D cell culture to organs-on-chips. Trends Cell Biol [Internet]. 2011 Dec 1;21(12):745–54. Available from: https://doi.org/10.1016/j.tcb.2011.09.005

682. Friedrich J, Ebner R, Kunz-Schughart LA. Experimental anti-tumor therapy in 3-D: Spheroids – old hat or new challenge? Int J Radiat Biol [Internet]. 2007 Jan 1;83(11–12):849–71. Available from: https://doi.org/10.1080/09553000701727531

683. Edmondson R, Broglie JJ, Adcock AF, Yang L. Three-dimensional cell culture systems and their applications in drug discovery and cell-based biosensors. Vol. 12, Assay and Drug Development Technologies. Mary Ann Liebert Inc.; 2014. p. 207–18.

684. Verjans ET, Doijen J, Luyten W, Landuyt B, Schoofs L. Three-dimensional cell culture models for anticancer drug screening: Worth the effort? J Cell Physiol [Internet]. 2018 Apr 1;233(4):2993–3003. Available from: https://doi.org/10.1002/jcp.26052

685. Sutherland RL, Hall RE, Taylor IW. Cell Proliferation Kinetics of MCF-7 Human Mammary Carcinoma Cells in Culture and Effects of Tamoxifen on Exponentially Growing and Plateau-

Phase Cells1. Cancer Res [Internet]. 1983;43(9):3998–4006. Available from: http://aacrjournals.org/cancerres/article-pdf/43/9/3998/2417028/cr0430093998.pdf

686. Wozniak MA, Modzelewska K, Kwong L, Keely PJ. Focal adhesion regulation of cell behavior. Biochimica et Biophysica Acta (BBA) - Molecular Cell Research [Internet]. 2004;1692(2):103–19. Available from: https://www.sciencedirect.com/science/article/pii/S0167488904000990

687. Hakkinen KM, Harunaga JS, Doyle AD, Yamada KM. Direct comparisons of the morphology, migration, cell adhesions, and actin cytoskeleton of fibroblasts in four different three-dimensional extracellular matrices. Tissue Eng Part A. 2011 Mar 1;17(5–6):713–24.

688. Song K, Zu X, Du Z, Hu Z, Wang J, Li J. Diversity models and applications of 3d breast tumor-on-a-chip. Micromachines (Basel). 2021 Jul 1;12(7).

689. Shirure VS, Bi Y, Curtis MB, Lezia A, Goedegebuure MM, Goedegebuure SP, et al. Tumor-on-a-chip platform to investigate progression and drug sensitivity in cell lines and patient-derived organoids. Lab Chip. 2018 Dec 7;18(23):3687–702.

690. Ferreira D, Fernandes AR, Baptista P V. Mild hyperthermia via gold nanoparticles and visible light irradiation for enhanced siRNA and ASO delivery in 2D and 3D tumour spheroids. Cancer Nanotechnol. 2024 Dec 1;15(1):19.

691. Persengiev SP, Zhu X, Green MR. Nonspecific, concentration-dependent stimulation and repression of mammalian gene expression by small interfering RNAs (siRNAs). RNA. 2004 Jan;10(1):12–8.

692. Wang HM, Zhang CY, Peng KC, Chen ZX, Su JW, Li YF, et al. Using patient-derived organoids to predict locally advanced or metastatic lung cancer tumor response: A real-world study. Cell Rep Med [Internet]. 2023;4(2). Available from: https://doi.org/10.1016/j.xcrm.2022.100911

693. Al-Hamaly MA, Turner LT, Rivera-Martinez A, Rodriguez A, Blackburn JS. Zebrafish Cancer Avatars: A Translational Platform for Analyzing Tumor Heterogeneity and Predicting Patient Outcomes. Int J Mol Sci [Internet]. 2023;24(3). Available from: https://www.mdpi.com/1422-0067/24/3/2288

694. Trop-Steinberg S, Azar Y. Is Myc an Important Biomarker? Myc Expression in Immune Disorders and Cancer. Am J Med Sci [Internet]. 2018;355(1):67–75. Available from: https://www.sciencedirect.com/science/article/pii/S0002962917303038

695. Oliveira BB, Fernandes AR, Baptista PV. Assessing the gene silencing potential of AuNP-based approaches on conventional 2D cell culture versus 3D tumor spheroid. Front Bioeng Biotechnol. 2024;12(1):1320729.

696. Buentello DC, Koch LS, Trujillo-De Santiago G, Alvarez MM, Broersen K. Use of standard U-bottom and V-bottom well plates to generate neuroepithelial embryoid bodies. PLoS One. 2022 May 1;17(5 May).

697. Howes AL, Richardson RD, Finlay D, Vuori K. 3-Dimensional culture systems for anti-cancer compound profiling and high-Throughput screening reveal increases in EGFR inhibitor-mediated Cytotoxicity compared to monolayer culture systems. PLoS One. 2014 Sep 23;9(9).

698. Singh SK, Abbas S, Saxena AK, Tiwari S, Sharma LK, Tiwari M. Critical Role of Three-Dimensional Tumorsphere Size on Experimental Outcome. Biotechniques [Internet]. 2020 Nov 1;69(5):333–8. Available from: https://doi.org/10.2144/btn-2020-0081

699. Jun Y, Lee J, Choi S, Yang JH, Sander M, Chung S, et al. In vivo-mimicking microfluidic perfusion culture of pancreatic islet spheroids. Vol. 5, Sci. Adv. 2019.

700. Morán M del C, Cirisano F, Ferrari M. Spheroid Formation and Recovery Using Superhydrophobic Coating for Regenerative Purposes. Pharmaceutics. 2023 Sep 1;15(9).

701. Luca AC, Mersch S, Deenen R, Schmidt S, Messner I, Schäfer KL, et al. Impact of the 3D Microenvironment on Phenotype, Gene Expression, and EGFR Inhibition of Colorectal Cancer Cell Lines. PLoS One. 2013 Mar 26;8(3).

702. Raghavan S, Mehta P, Horst EN, Ward MR, Rowley KR, Mehta G. Comparative analysis of tumor spheroid generation techniques for differential in vitro drug toxicity. Oncotarget [Internet]. 2016;7(13):16948–61. Available from: www.impactjournals.com/oncotarget/

703. Tuan RS, Lo CW. Developmental Biology Protocols: Overview III. In: Developmental Biology Protocols [Internet]. New Jersey: Humana Press; 2000. p. 3–5. Available from: http://link.springer.com/10.1385/1-59259-066-7:3

704. Xie H, Appelt JW, Jenkins RW. Going with the flow: Modeling the tumor microenvironment using microfluidic technology. Vol. 13, Cancers. MDPI; 2021.

705. Ozcelikkale A, Moon HR, Linnes M, Han B. In vitro microfluidic models of tumor microenvironment to screen transport of drugs and nanoparticles. Vol. 9, Wiley Interdisciplinary Reviews: Nanomedicine and Nanobiotechnology. Wiley-Blackwell; 2017.

706. Ishida-Ishihara S, Takada R, Furusawa K, Ishihara S, Haga H. Improvement of the cell viability of hepatocytes cultured in three-dimensional collagen gels using pump-free perfusion driven by water level difference. Sci Rep. 2022 Dec 1;12(1):20269.

707. Romero-López M, Trinh AL, Sobrino A, Hatch MMS, Keating MT, Fimbres C, et al. Recapitulating the human tumor microenvironment: Colon tumor-derived extracellular matrix promotes angiogenesis and tumor cell growth. Biomaterials. 2017 Feb 1;116:118–29.

2025

ANA BEATRIZ BRITO DE OLIVEIRAA

SIMPLIFIED CHIP PROTOTYPING FOR IMPROVED SCREENING OF GENE SILENCING THERAPEUTICS USING